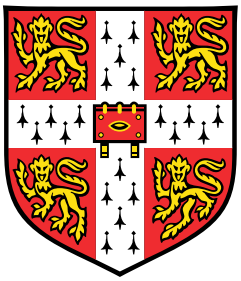

Propulsion, navigation and control of biological and artificial microswimmers

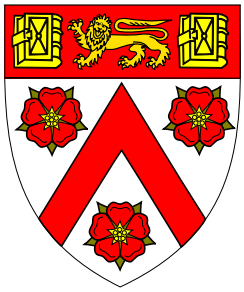

Alexander Joachim Chamolly

Department of Applied Mathematics and Theoretical Physics
University of Cambridge

This dissertation is submitted for the degree of
Doctor of Philosophy

Trinity College May 2020

Declaration

This dissertation is the result of my own work and includes nothing which is the outcome of work done in collaboration except as declared in the Preface and specified in the text. It is not substantially the same as any that I have submitted, or, is being concurrently submitted for a degree or diploma or other qualification at the University of Cambridge or any other University or similar institution except as declared in the Preface and specified in the text. I further state that no substantial part of my thesis has already been submitted, or, is being concurrently submitted for any such degree, diploma or other qualification at the University of Cambridge or any other University or similar institution except as declared in the Preface and specified in the text. It does not exceed the prescribed word limit for the relevant Degree Committee.

The research presented in chapters 2, 3, 4, 5 and 6 has been published, or submitted for publication, in Refs. [36–40] respectively. I am the primary investigator and author of all these manuscripts.

The work in chapter 2 was in part carried out under the supervision of Prof. Takuji Ishikawa at Tohoku University, Sendai, during a visit in the summer of 2016. In particular, I am indebted to him for allowing me to adapt the numerical code used in Ref. [110] and for providing the computational resources necessary to perform the simulations.

The research presented in chapter 6 is the result of a collaboration initiated by Dr Soichiro Tottori, who completed his PhD under the supervision of Prof. Ulrich Keyser at the Cavendish Laboratory in 2019. Soichiro performed and validated the finite-element simulations that are described in section §6.2.2, and produced Fig. 6.2a, Fig. 6.3 and Fig. 6.4. The remainder of that chapter is my own work.

Everything presented in this thesis has been discussed with my supervisor Prof. Eric Lauga, who has given me helpful comments on draft versions of all chapters.

For convenience, I will use the author's "we" throughout.

Alexander Joachim Chamolly
May 2020

Propulsion, navigation and control of biological and artificial microswimmers

Alexander Joachim Chamolly

This dissertation contains original research on a range of problems involving the locomotion of different types of microswimmers, including both biological microorganisms and artificial colloids. Due to the physical constraints imposed by the inertialess hydrodynamics at these small scales, these swimmers rely on multiple locomotion strategies that are unfamiliar from the macroscale. The results presented here answer several theoretical questions concerning the fundamentals of specific propulsion mechanisms, as well as the interactions of a wide range of different microswimmers with geometrically complex environments.

For a general spherical squirmer-type microswimmer we first analyse the swimming dynamics in a periodic three-dimensional lattice of obstacles numerically, and obtain a phase diagram detailing qualitatively different kinds of trajectories. These range from nearly straight over diffusive to trapped, depending on the squirming parameter and the lattice packing density. We then explain these results theoretically using a combination of near- and far-field hydrodynamic arguments. Importantly, we predict qualitatively different dynamics of 'pusher'-type swimmers, such as bacteria, and 'puller'-type swimmers, such as algae, in a geometry that is representative for soil as a biologically relevant domain.

Next, we derive the singularity representation for the solution of the Stokes equations in the two cases of a point torque outside a rigid sphere, and a point torque outside a spherical bubble. In the axisymmetric case outside a rigid sphere, the solution takes an extremely simple form that is reminiscent of the solution for a point charge outside a grounded sphere in electrostatics, and is rationalised with a similar geometrical argument. In addition, we repeat the analysis for a point source.

We apply these results to an analysis of the swimming dynamics of a single peritrichous bacterium, specifically the physical mechanisms that lead to the formation of a flagellar bundle behind the cell during its forward motion. We categorise the forces at play into 'direct' and 'indirect' depending on whether they are due to hydrodynamic interactions between the flagellar filaments, or triggered by flows around the cell body due to its motion, and demonstrate using a minimal theoretical model that under very general conditions the latter dominate in all but the final stages of bundle formation. For parameter values that are representative for the model bacterium *Escherichia Coli* we perform a full dynamic elastohydrodynamic simulation to analyse the relative strength of hydrodynamic and elastic effects along the full length of the flagella during the bundling process.

On the topic of artificial microswimmers we next examine theoretically the stochastic dynamics of a self-propelled colloid that is dissolving over time, as motivated by recent experiments aimed at the design of active particles suitable for biomedical applications. We present two models that differ in the details of the dissolution mechanism, and in each case derive analytical expressions for the particle life time and mean squared displacement due to active diffusion. A new dimensionless parameter emerges, classifying trajectories into globally ballistic and globally diffusive depending on the ratio of particle life time to rotational diffusivity, and we obtain a hierarchy of our models in all regimes that quantifies the limit of control that can be exerted on the motion of dissolving colloids.

Expanding on the topic of control and manipulation on the microscale, we finally analyse the entrapment of passive cargo by a magnetically actuated spheroidal roller near a rigid wall. We predict that as such a roller propels along an interface, it is able to collect and transport passive cargo particles in its path by entrapping them inside a vortex to its side. This apparent violation of the Stokes flow reversibility is facilitated through irreversible steric interactions between the cargo and the interface, and analogous to the microfluidic technique of deterministic lateral displacement. We combine finite element simulations of the flow field due to the roller with an effective model for cargo migration to generate a phase diagram of entrapment as a function of roller aspect ratio, cargo size and cargo location, and predict that flat rollers are able to trap cargo for the largest range of parameter values.

Acknowledgements

The list of people that I have and want to thank for their support in the last four years is long. It begins with my supervisor, Eric. There were times of great uncertainty when I ineluctably stretched his patience to the limit, and I am infinitely grateful to him for holding on to me, both pushing me to do the right thing when I doubted myself and giving me the freedom I needed to develop my identity as a scientist (a process which I liken to *Zarathustra*'s three transformations). I have enjoyed working with him greatly and it is my goal to take his humour, creativity and humanity forward in my own career as a researcher.

Next I thank my parents, and my late grandparents, for giving me the opportunity to pursue my dreams and giving me unconditional support when I had nowhere else to go. I have always worked hard for what I set out to do, but it is due to them that I have had the privilege to choose.

I am indebted to the incredibly kind Takuji Ishikawa for hosting me in his lab and providing guidance and supervision on my first research project. I would also like to thank my collaborators Soichiro Tottori for our work together on the roller project, and Sébastien Michelin for our work on bubble-propelled swimmers. I thank the members of DAMTP for providing an environment that has felt more akin to a family than a workplace during my time here. In particular I would like to thank John Lister for mentoring me for the last 6 years, Ray Goldstein for many insightful and stimulating questions during our seminars, and George Fortune for the fun and productive co-supervision of our wonderful summer student Richard Moulange. My thanks extend to Julia Gog and her dedication to the undergraduate maths café, which I gladly sacrificed my Saturday afternoons for, and Thomas Forster from DPMMS for invaluable advice on how to complete a thesis ("just write it"). It has been a great pleasure also to teach and mentor over one hundred undergraduate students over the years, many of whom have become friends, and it is my hope that they have been given the tools to eclipse the success of their teacher.

I thank the current and past members of the Lauga and Goldstein groups for creating the stimulating and welcoming environment that I have been so proud to be a part of. These include my officemates Ivan Tanasijević and Panayiota Katsamba, and Maciek Lisicki, Justas Dauparas, Lyndon Koens, Maria Tătulea-Codrean, Debasish Das, Albane Théry, Christian Esparza-López, Masha Dvoriashyna, Tamsin Spelman, Emily Riley, Yi Man, Weida Liao, and Pierre Haas,

Hélène de Maleprade, Mazi Jalaal, Anne Herrmann, Rafa Martínez-Avial, Kyriacos Leptos, Stephanie Höhn, Francesco Boselli, Nuno Oliveira, Sumit Birwa, Julius Kirkegaard, François Peaudecerf and Kirsty Wan, as well as Theresa Jakuszeit from the group of Ottavio Croze.

One of the greatest adventures I had the pleasure to participate in was the foundation and administration of the Cambridge University Ethics in Mathematics Society. I would like to thank Maurice Chiodo and Piers Bursill-Hall for their dedication to this endeavour, and Matthew Priddin, the fantastic Hannah Fox, Clément Mouhot, Grae Worster, Aimeric Malter, John Helsby and Toby Clifton for their associated support.

Trinity College has been my home for the last eight years, and I harbour a deeply felt love for the place and the people that have made it such a special environment for me over the years. These include but are not limited to Herschel Chawdhry, Artjoms Iškovs, Andrew McClement, James Rickards, Allan Gerrard, Kasia Warburton, Aaron Wienkers, Lukas Gast and the Trinity BA Society committee 2019-20, Irene Li, Oliver Feng, Will Gao, Matthew Maitra, Filip Murár, Stan Fořt, Michal Buráň, Dan Šafka, Jitka Štollová, Gunnar Peng, Filip Wronowski, Jason Han, Monica Bilbao and Jeremy Butterfield, who can take credit for being the kindest man in existence.

Finally, I thank my friends from the Cambridge University Olympic Gymnastics Club, among them Harvey Klyne, Leo Ferrari, Jack Neill and Claudio Castelnovo, for completing my understanding of run-and-tumble mechanics, and Ludwig van Beethoven, Jean Sibelius, Ryuichi Sakamoto, Alva Noto, Brian Eno, Jeremy Soule, Austin Wintory, Steve Reich and Philip Glass for providing the soundtrack to which this thesis was written.

My work has been funded by the European Research Council (through an ERC Consolidator Grant to Eric), and Trinity College (through a Rouse Ball Travelling Studentship in Mathematics).

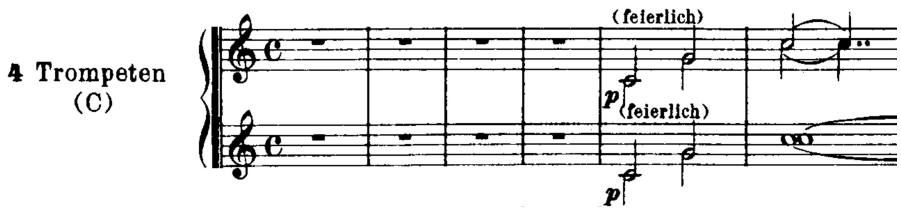

The *Sonnenaufgang* motif [224]

Drei Verwandlungen nenne ich euch des Geistes: wie der Geist zum Kamele wird, und zum Löwen das Kamel, und zum Kinde zuletzt der Löwe.

Vieles Schwere gibt es dem Geiste, dem starken, tragsamen Geiste, dem Ehrfurcht innewohnt: nach dem Schweren und Schwersten verlangt seine Stärke.

Was ist schwer? so fragt der tragsame Geist, so kniet er nieder, dem Kamele gleich, und will gut beladen sein. (...)

Alles dies Schwerste nimmt der tragsame Geist auf sich: dem Kamele gleich, das beladen in die Wüste eilt, also eilt er in seine Wüste.

Aber in der einsamsten Wüste geschieht die zweite Verwandlung: zum Löwen wird hier der Geist, Freiheit will er sich erbeuten und Herr sein in seiner eignen Wüste. (...)

Neue Werte schaffen – das vermag auch der Löwe noch nicht: aber Freiheit sich schaffen zu neuem Schaffen – das vermag die Macht des Löwen. (...)

Aber sagt, meine Brüder, was vermag noch das Kind, das auch der Löwe nicht vermochte? Was muß der raubende Löwe auch noch zum Kinde werden?

Unschuld ist das Kind und Vergessen, ein Neubeginnen, ein Spiel, ein aus sich rollendes Rad, eine erste Bewegung, ein heiliges Ja-sagen.

Ja, zum spiele des Schaffens, meine Brüder, bedarf es eines heiligen Ja-sagens: s e i n e n Willen will nun der Geist, s e i n e Welt gewinnt sich den Weltverlorene.

Drei Verwandlungen nannte ich euch des Geistes: wie der Geist zum Kamele ward, und zum Löwen das Kamel, und der Löwe zuletzt zum Kinde. –

Also sprach Zarathustra.

Friedrich Nietzsche [172]

Table of Contents

List of Figures xv

List of Tables xvii

1 Introduction 1
- 1.1 Historical development . . . 1
- 1.2 Fundamental physical principles and models . . . 3
- 1.3 Structure of the thesis . . . 5

2 Active particles in periodic lattices 9
- 2.1 Introduction . . . 9
- 2.2 Model and Simulations . . . 11
- 2.3 Computational results . . . 13
  - 2.3.1 Phenomenology of trajectories . . . 13
  - 2.3.2 Phase diagram . . . 15
- 2.4 Theory . . . 19
  - 2.4.1 Straight swimming vs. random walks . . . 19
  - 2.4.2 Unbounded vs. trapped trajectories . . . 23
  - 2.4.3 Stuck swimmer vs. orbiting . . . 27
- 2.5 Discussion . . . 28
- 2.A Details of the numerical method . . . 29

3 Stokes flow due to point torques and sources in a spherical geometry 33
- 3.1 Introduction . . . 33
- 3.2 Geometry and setup . . . 35
  - 3.2.1 Geometry . . . 35
  - 3.2.2 Problem setup . . . 36
  - 3.2.3 Method of solution . . . 37

3.3 The axisymmetric rotlet . . . 38
3.3.1 No-slip boundary condition (rigid sphere) . . . 38
3.3.2 No tangential stress boundary condition (spherical bubble) . . . 41
3.4 The transverse rotlet . . . 44
3.4.1 No-slip boundary condition (rigid sphere) . . . 44
3.4.2 No tangential stress boundary condition (spherical bubble) . . . 48
3.5 The point source . . . 51
3.5.1 The multipole expansion for a source . . . 51
3.5.2 No-slip boundary condition (rigid sphere) . . . 52
3.5.3 No tangential stress boundary condition (spherical bubble) . . . 55
3.6 Discussion . . . 57

4 Direct vs indirect hydrodynamic interactions in bacterial flagellar bundling 61
4.1 Introduction . . . 61
4.2 Minimal model of flagellar bundling . . . 63
4.2.1 Hydrodynamics of flagellar propulsion . . . 63
4.2.2 Modelling flagellar filaments by flow singularities . . . 65
4.2.3 Direct vs indirect interactions . . . 66
4.3 Advection induced by flagellar thrust . . . 67
4.3.1 Direct polar advection between flagella . . . 67
4.3.2 Cell kinematics and indirect polar advection between flagella . . . 70
4.3.3 Direct vs indirect interactions . . . 71
4.4 Advection induced by flagellar rotation . . . 73
4.5 Dynamic elastohydrodynamic model . . . 75
4.5.1 Motivation . . . 75
4.5.2 Computational modelling . . . 76
4.5.3 Numerically simulated filament dynamics . . . 79
4.6 Discussion . . . 84

5 Stochastic dynamics of dissolving active particles 87
5.1 Introduction . . . 87
5.2 Dissolution models . . . 88
5.2.1 Non-reacting swimmer . . . 89
5.2.2 Dissolution through reaction . . . 95
5.3 Passive dynamics of dissolving colloids . . . 100
5.3.1 Mathematical model . . . 101
5.3.2 Total root mean squared displacement . . . 102

5.4 Active motion of dissolving colloids . . . 103
5.4.1 Mathematical model . . . 105
5.4.2 Computational results . . . 108
5.5 Discussion . . . 112
5.A Details of the asymptotics for active MSD . . . 114
5.A.1 Diffusive limit ($\gamma \to \infty$) . . . 114
5.A.2 Ballistic limit ($\gamma \to 0$) . . . 116

6 Irreversible hydrodynamic trapping by surface rollers 119
6.1 Introduction . . . 119
6.2 Computational model . . . 121
6.2.1 Setup . . . 121
6.2.2 The finite-element routine . . . 122
6.2.3 Simulating cargo trajectories . . . 123
6.3 Computational results . . . 125
6.3.1 Phase diagram for cargo entrapment . . . 125
6.3.2 Illustration of cargo migration . . . 126
6.3.3 Pure translation does not lead to trapping . . . 128
6.4 Theoretical models . . . 128
6.4.1 Vortex flow surrounding a translating and rotating rigid disc . . . 128
6.4.2 Physical mechanism of trapping by the squeezing of streamlines . . . 131
6.5 Discussion . . . 133
6.A Analysis of the flow disturbance due to finite cargo size . . . 135
6.B Derivation of the streamfunction for a rotating rigid disc . . . 138
6.C Details of the 2D singularity model . . . 140
6.C.1 Derivation . . . 140
6.C.2 No force, $\eta = 0$ . . . 142
6.C.3 With force, $\eta > 0$ . . . 144

7 Summary 147

References 153

List of Figures

2.1 Sketch of the model geometry of a spherical squirmer moving through a BCC lattice . . . 11
2.2 Sample trajectories for a swimmer moving in a BCC lattice . . . 14
2.3 Phase diagram of squirmer trajectories . . . 16
2.4 Macroscopic trajectories of intermediate-strength pushers . . . 17
2.5 Probability of straight trajectories as a function of lattice packing density . . . 18
2.6 Sketch of the far-field stability model . . . 20
2.7 Instantaneous perturbation growth and decay for a pusher in a channel . . . 22
2.8 Oscillatory decay of the perturbation for a moving pusher . . . 24
2.9 Sketch of the two-dimensional lubrication argument . . . 25

3.1 Illustration of the geometrical setup for flow singularities in a spherical geometry 35
3.2 Flow due to an axisymmetric rotlet outside and inside a rigid spherical shell . 42
3.3 Flow due to an axisymmetric rotlet outside a spherical bubble . . . 44
3.4 Flow due to a transverse rotlet outside a rigid sphere . . . 47
3.5 Flow due to a transverse rotlet outside a spherical bubble . . . 50
3.6 Flow due to a point source outside a rigid sphere . . . 54
3.7 Flow due to a point source outside a spherical bubble . . . 56
3.8 Illustration of two model systems . . . 58

4.1 Snapshots of the bundling process . . . 62
4.2 Minimal hydrodynamic model sketch . . . 64
4.3 Illustration of the flow due to a point force . . . 69
4.4 Contour plot of the ratio of direct to indirect polar advection . . . 72
4.5 Contour plot of the ratio between direct and indirect azimuthal advection . . . 74
4.6 Sketch of the computational model . . . 76
4.7 Snapshots of the bundling dynamics for $L = 6\,\mu\text{m}$ and $\theta = \pi/2$ viewed in the laboratory frame . . . 81

4.8 Ratio of direct and indirect interactions along the filament axis during the bundling process . . . 82
4.9 Computed bundling dynamics for various filament axial lengths and base separation angles . . . 83

5.1 Schematic presentation of non-reacting dissolution dynamics . . . 89
5.2 Schematic presentation of the molecular dynamics near the boundary of a reacting colloid . . . 95
5.3 Comparison of the decay dynamics between the three models . . . 100
5.4 2D-projections of sample trajectories for different values of γ . . . 104
5.5 Normalised active mean squared displacement as a function of γ for the non-reacting model . . . 108
5.6 Normalised active mean squared displacement as a function of γ for the slow reaction limit of the reacting model . . . 109
5.7 Normalised active mean squared displacement against γ for the fast reaction limit of the reacting model . . . 110
5.8 Distribution of the root mean squared displacement for different values of γ . . . 111
5.9 Cloud scatter plot of lateral displacement vs. lateral displacement . . . 112

6.1 Examples of entrapment by rotating micro-objects . . . 120
6.2 Sketches of the model roller geometry . . . 121
6.3 Rotation-translation coupling rates for different aspect ratios and gap widths . . . 123
6.4 Verification of the finite element method . . . 124
6.5 Phase diagram for cargo entrapment . . . 125
6.6 Illustration of sample cargo trajectories . . . 127
6.7 Illustration of the rotating disc model . . . 130
6.8 Illustration of the 2D singularity model . . . 131
6.9 Illustration of the squeezing of streamlines in the 2D singularity model . . . 134
6.10 Schematic illustration of deterministic lateral displacement . . . 135
6.11 Distortion of streamlines in the full simulation . . . 137
6.12 Sketch of the 2D singularity model . . . 140
6.13 Squeezing of streamlines in the 2D singularity model with no force . . . 143
6.14 Squeezing of streamlines in the 2D singularity model with force . . . 145

List of Tables

4.1 Experimentally-obtained physical parameters for our computational elastohydrodynamic model 79

6.1 Parameter values for the model verification tests 136

Chapter 1

Introduction

1.1 Historical development

It is often said that scientists today, and in particular those at the beginning of their careers, stand on the shoulders of giants. In the case of the study of microorganisms, the first of these giants lived in the seventeenth century AD. Although their existence was conjectured as early as 30 BC by the Roman scholar Marcus Varro [240], it was not until after the invention of the compound microscope in the Netherlands around 1620 [239] that scientists discovered the motion of objects invisible to the naked eye. In 1665, Robert Hooke published a treatise including a famously detailed drawing of the anatomy of a flea [101] and the observations made by Antonie van Leeuwenhoek in the 1670s are the first documented observations of unicellular organisms such as bacteria, spermatozoa and other microbes [140].

In 1827 the Scottish botanist Robert Brown observed the motion of pollen in water, finding it to be erratic and unpredictable [30]. Though he was not the first to observe it [105], the phenomenon became named after him as Brownian motion and remained unexplained for the remainder of the 19th century. Indeed it was first postulated by nobody less than Albert Einstein [63, 64] that this motion was due to the perpetual bombardment of the pollen grains by fluid molecules actuated by thermal fluctuations – controversial at the time as it relied on the concept of dividing matter into atoms and molecules. An appropriate mathematical formalism was subsequently presented by Marian Smoluchowski [246] and Paul Langevin [134]. This led to the development of kinetic theory, and ultimately a statistical approach to the understanding of active matter [157, 193, 241].

Meanwhile in the subject of fluid dynamics, George Gabriel Stokes realised the importance of 'tangential action called into play by the sliding of one portion of fluid along another', giving rise to internal friction, in 1845 [222]. Stokes later derived the time-dependent version of what is known today as the Stokes equations in the context of the damped motion of pendulums

[223]. Due to their relatively simple mathematical structure and wide applicability to creeping flow as well as flow on small scales, many properties and solutions to these equations were studied and derived in the first half of the 20th century [94, 133, 176]. However, it was not until 1951 that Geoffrey Ingram Taylor realised that they also apply to the swimming of microorganisms, and hence that the physics at heart of their locomotion is qualitatively different from the inertial propulsion of fish [231]. In 1976, Edward Purcell gave an influential lecture titled 'Life at low Reynolds number' [189] in which he disseminated significant physical insight into the constraints of inertia-less locomotion, culminating in his 'scallop theorem' that gives a necessary condition to achieve propulsion, namely that the motion is non-reciprocal, i.e. that the sequence of geometric configurations that a microswimmer attains is not symmetric under time reversal. In the decades since, the locomotion of microorganisms has been investigated extensively [26, 135, 136], aided by advances both in numerical and experimental techniques. The most commonly investigated mechanisms are based on breaking reciprocity by introducing chirality, such as the rotation of one or more helical filaments in the case of many bacterial species including *Escherichia Coli* (*E. coli*) [17, 136], or by generating travelling waves, such as along the appendages of spermatozoa [26, 231], or metachronal waves over the surface of ciliated organisms such as *Volvox carteri* [31, 85, 180] and *Paramecium* [27, 213]. Some algae, such as *Chlamydomonas reinhardtii* [186, 198] and *Gonium* [55], are also known to perform a coordinated breast-stroke motion with two flagella.

In parallel to this, the field of nanotechnology and nanoengineering emerged following Richard Feynman's landmark 1959 lecture 'There's Plenty of Room at the Bottom: An Invitation to Enter a New Field of Physics' [68]. Among advances in computing and microscopy he envisioned what manufacturing processes would be required for the production of small machines. In particular, he correctly predicted that the process used to build automobiles would be unsuitable for miniaturisation, instead advocating for evaporation techniques. Indeed, with this method it has since been possible to manufacture a wide array of different self-propelled micro- and nanoparticles [103, 249]. This is often achieved through the asymmetrical patterning of a colloid, which can then self-propel due to phoretic effects, eliminating the need for moving parts but often requiring external fuel. Due to their asymmetric design, they are commonly referred to as Janus particles, in reference to the Roman double-faced god. Many other designs also exist, including chiral propellers [80], cell-colloid hybrids [61], droplets [113, 232], microjets [203] and electric or magnetic rollers [28, 233]. The research interest in these artificial microswimmers is primarily fuelled by their promise in health care [2, 168, 178, 250] and environmental applications [77].

The overarching themes of this thesis are microswimmer propulsion mechanisms, their navigation through complex environments, and the external control of swimmer behaviour,

either through their design or through external influence. In §1.2 we will briefly summarise the most important underlying physical principles and classical models that are used in later chapters. We then conclude with an outline of the thesis structure in §1.3.

1.2 Fundamental physical principles and models

The dynamics of incompressible Newtonian fluids (such as liquid water) are described by the Navier-Stokes equations [94],

$$\rho\left(\frac{\partial \boldsymbol{u}}{\partial t} + \boldsymbol{u}\cdot\boldsymbol{\nabla}\boldsymbol{u}\right) = \boldsymbol{\nabla}\cdot\boldsymbol{\sigma} + \boldsymbol{f}, \quad \boldsymbol{\nabla}\cdot\boldsymbol{u} = 0, \tag{1.1}$$

where $\boldsymbol{u}(\boldsymbol{x},t)$ is the fluid velocity, ρ its mass density, $\boldsymbol{f}(\boldsymbol{x},t)$ a body force density and the hydrodynamic stress tensor $\boldsymbol{\sigma}$ is defined as

$$\boldsymbol{\sigma} = -p\boldsymbol{I} + \mu\left(\boldsymbol{\nabla}\boldsymbol{u} + (\boldsymbol{\nabla}\boldsymbol{u})^T\right), \tag{1.2}$$

where $p(\boldsymbol{x},t)$ is the dynamic pressure field and μ the dynamic viscosity of the fluid. For general $\boldsymbol{\sigma}$ Eq. (1.1) is known as the Cauchy equation and valid for any (incompressible) continuum while the relation in Eq. (1.2) defines the character of a Newtonian fluid. Commonly applied boundary conditions are continuity of velocity at interfaces (reducing to no-slip if the interface is rigid), and continuity of stress. By considering the characteristic scales involved in the inertial terms on the left-hand side and the viscous term on the right-hand side of Eq. (1.1), it is possible to define a dimensionless ratio called the Reynolds number,

$$\mathrm{Re} = \frac{\rho U L}{\mu}, \tag{1.3}$$

where U is a velocity and L a length scale. For microswimmers it is typically the case that $L = O(10\,\mu\mathrm{m})$ and $U = O(10\,\mu\mathrm{m\,s^{-1}})$ [26, 189], while for water at room temperature $\rho \approx 10^3\,\mathrm{kg\,m^{-3}}$ and $\mu \approx 10^{-3}\,\mathrm{Pa\,s}$ [96], so

$$\mathrm{Re} \approx 10^{-4} \ll 1, \tag{1.4}$$

which means that inertia is negligible. This leads to the incompressible *Stokes equations*,

$$\boldsymbol{\nabla}p = \mu\nabla^2\boldsymbol{u} + \boldsymbol{f}, \quad \boldsymbol{\nabla}\cdot\boldsymbol{u} = 0. \tag{1.5}$$

The Stokes equations enjoy a number of useful properties that are fundamental to the propulsion of microswimmers, and that we will exploit numerous times in this thesis. Firstly, they are *instantaneous*, which means that the global flow is affected immediately by changes to the forcing or the boundary conditions. Physically this means that the motion is overdamped, making propulsion strategies such as coasting impossible, as they rely on inertia [189]. Second, they are *linear*, which means that solution techniques involving superposition, such as Fourier transforms or the method of images, may be applied. The Green's function corresponds physically to a point force, and is commonly called the Stokeslet [127]. Many solution approaches rely on representing the flow in terms of the Stokeslet and its derivatives (corresponding to force dipoles, quadrupoles etc) whose magnitudes decay increasingly fast. Most importantly for numerical computations, it is possible to represent any Stokes flow in terms of integrals over the domain boundary using Stokeslet kernels [188], reducing a three-dimensional problem to a two-dimensional one. Powerful numerical techniques rely on either discretising these integrals directly, or first performing mathematical simplifications. For instance, it is possible to expand the flow field due to the motion of a moving rigid body as a multipole expansion of flow singularities [127]. With this technique it is then possible to obtain analytical expressions for the leading-order dynamics due to hydrodynamic interactions at long distances. In chapter 3 we will use this method to explore the flows generated by point torques and point sources in a spherical geometry, and will apply some of the results therein to a model of bacterial flagellar filaments in 4.

Another property, obtained by integrating Eq. (1.5) and applying the divergence theorem, is that in the absence of a body force the total force and torque on a body in Stokes flow vanish [94]. Combined with the expansion described above, this means that the multipole expansion for a microswimmer cannot contain either a Stokeslet or an anti-symmetric force dipole (known as a rotlet). Instead, the leading-order flow is determined by the symmetric force dipole, or stresslet. Here there are then two possibilities, as the dipole can appear either extensile or contractile. This gives rise to a general classification of microswimmers called, respectively, pushers and pullers [136]. *Pushers*, that is microswimmers appearing as extensile dipoles, generally include organisms that generate thrust behind their body. This applies to peritrichous bacteria such as *E. coli* during their 'run' gait [135], and spermatozoa [26]. *Pullers* on the other hand include algae such as *C. reinhardtii* that generate thrust in front of their bodies by pulling the cell body forward [186]. Artificial colloids can fall in either category, depending on their patterning [249]. It has been confirmed by many studies that the behaviour of suspensions, including the formation of coherent structures and their stability, depends qualitatively on the pusher-puller nature of the swimmers [200–202]. The same is true for their interactions with boundaries [216, 217]. In a similar vein, we discover in chapter 2 that a microswimmer's ability

to navigate through the complex geometry of a lattice of obstacles depends on its pusher-puller characterisation.

Related to this notion is another well-established general model for the locomotion of a microswimmer: the *spherical squirmer* [181]. This model was proposed by James Lighthill [142] and then corrected and extended by John Blake [21], who applied it to the motion of ciliates. The central idea is to introduce an axisymmetric slip velocity boundary condition that replicates the motion generated by a ciliated envelope. In spherical polar co-ordinates (r, θ), fixed at the centre of the swimmer, its components can be written as [21]

$$u_r(\theta, t) = \sum_{n=0}^{\infty} A_n(t) P_n(\cos\theta), \tag{1.6}$$

$$u_\theta(\theta, t) = \sum_{n=1}^{\infty} B_n(t) \frac{2\sin\theta}{n(n+1)} P_n'(\cos\theta), \tag{1.7}$$

where P_n is the nth Legendre polynomial. For a non-deforming body the A_n are zero and the requirement that the swimmer is force-free determines its velocity U as

$$U = \frac{2}{3} B_1. \tag{1.8}$$

Furthermore, the ratio $\beta = B_2/B_1$ corresponds to the strength of the dipolar flow, with $\beta > 0$ indicating a puller, and $\beta < 0$ indicating a pusher. The squirmer model has been widely applied and extended [110, 132, 147, 180, 232], and we will use it ourselves in chapter 2.

Finally, the Stokes equations are *reversible*, in the sense that the global flow history may be reversed by changing the direction of any forcing. This is in stark contrast to mixing and chaotic turbulence in macroscale flows, and leads to considerable practical challenges that need to be overcome when mixing is desired in microfluidic systems [225]. However, multiple methods exist that break reversibility, either by injecting energy into an active system [157], or by introducing steric interactions [104, 184]. In chapter 6, we will explore a system exploiting the latter to trap and transport a passive cargo particle.

1.3 Structure of the thesis

The common themes of this thesis are microswimmer propulsion mechanisms, their navigation through complex environments, and the external control of swimmer behaviour, either through their design or through external influence. The research presented in each chapter discusses individual problems related to one or more of these themes.

We begin in chapter 2 with an analytical and numerical study of a spherical squirmer in a complex geometry. While most past theoretical work on low-Reynolds number locomotion addressed idealised geometrical situations, not much is known about the motion of swimmers in heterogeneous environments. As a first theoretical model, we investigate numerically the behaviour of a single spherical microswimmer located in an infinite, periodic body-centred cubic lattice consisting of rigid inert spheres of the same size as the swimmer. Running a large number of simulations, we uncover the phase diagram of possible trajectories as a function of the strength of the swimming actuation and the packing density of the lattice. We then use hydrodynamic theory to rationalise our computational results and show in particular how the far-field nature of the swimmer (pusher vs. puller) governs the behaviour at high volume fractions.

In contrast, chapter 3 is of a purely mathematical nature. Here we extend the catalogue of known solutions to the Stokes equations by deriving the flow expressions due to a general point torque and point source in the presence of a stationary sphere with either a no-slip or a stress-free (no shear) boundary condition. For an axisymmetric point torque and a no-slip sphere the image system simplifies to a single image point torque, reminiscent of the solution in electrostatics for a point charge outside a grounded sphere. By symmetry, this also gives a simple representation of the solution due to an axisymmetric point torque inside a rigid spherical shell. In all remaining cases, the solution can be described by a collection of physically intuitive point and line singularities. These results will be useful for the theoretical modelling of the propulsion of microswimmers and efficient numerical implementation of far-field hydrodynamic interactions in this geometry.

Indeed, the first such application is presented in chapter 4. In this chapter we focus on the early stages of bundle formation in peritrichous bacteria, aiming to understand the fundamental physical process behind it. To this end, we define a general notion of direct and indirect hydrodynamic interactions, allowing us to categorise and compare the relative importance of various physical mechanisms that have previously been identified to contribute to the bundling process. Based on general physical principles we find that generation of thrust by flagellar filaments is sufficient to trigger the formation of a bundle, and that indirect effects due to the cell body kinematics dominate at the early stages of the process. We supplement our theory with an elastic spring-and-rod model of a biflagellate bacterium and perform a detailed analysis of the forces at each point along the filaments throughout the bundling process.

The remaining chapters are devoted to artificial microswimmers. First, we present in chapter 5 a theoretical study on the dynamics of dissolving active particles. Many current designs

suffer from a common problem for biomedical applications, namely that the swimmers remain in the fluid indefinitely, posing risks of clogging and damage. Inspired by recently proposed experimental designs, we develop and compare two distinct chemical models for the decay of a microswimmer, taking into account the material composition and nature of the chemical or enzymatic reaction at its surface. These include a model for dissolution without a reaction, as well as models for a reacting swimmer studied in the limit of large and small Damköhler number. A new dimensionless parameter emerges that permits the classification of colloids into ballistic and diffusive type. Using this parameter, we perform an asymptotic analysis to derive expressions for colloid lifetimes and their total mean-squared displacement from release before validating these using numerical Brownian dynamics simulations of the associated Langevin equations. Supported by general scaling relationships, our theoretical results provide new and valuable insight into the experimental applicability of a wide range of designs for degradable active colloids.

Finally, we analyse in chapter 6 a system composed of a colloidal roller, driven by externally actuated rotation, and a passive cargo particle. The roller can self-propel parallel to a rigid boundary by exploiting the hydrodynamic coupling that surfaces induce between translation and rotation. As it moves along the boundary, it generates local vortical flows, which can be used to facilitate trapping and transport of the cargo particle. However, the details and conditions for this trapping mechanism have not yet been fully understood. Here we show that the trapping is accomplished through time-irreversible interactions between the cargo and the boundary, leading to its migration across streamlines into a steady flow vortex next to the roller. The trapping mechanism is explained analytically with a two dimensional model, investigated numerically in three dimensions for a wide range of parameters, and is shown to be analogous to the deterministic lateral displacement (DLD) technique used in microfluidics for the separation of differently sized particles. The several geometrical parameters of the problem are analysed and we predict that thin, disc-like rollers offer the most favourable trapping conditions.

We conclude with a brief summary in chapter 7.

Chapter 2

Active particles in periodic lattices

2.1 Introduction

Swimming microorganisms live in a variety of natural and industrial environments, including the ocean, soil, intestinal tract and bioreactors, and they play diverse and important roles in environmental, agricultural and health issues [43, 107, 248]. Understanding the spreading of cells in various environments is therefore a fundamental problem, and this knowledge can be exploited for predicting and controlling the distribution of cells and their growth [89, 182].

From a physical point of view, the simplest environment for swimming cells is an unbounded fluid in the absence of background flow or the biological responses to stimulus, including chemotaxis, phototaxis or gravitaxis. The spreading of individual cells in such a simple environment has already been studied thoroughly. Early work investigated run and tumble motions of individual *Escherichia coli* (*E. coli*) bacteria and showed that the motion of the cells could be described by random walk models with the entire population displaying diffusive behaviour [17]. Similar results were also found for the unicellular alga *Chlamydomonas*, and cell populations displayed long-time diffusive behaviour [97, 100, 186, 244].

The behaviour of swimming microorganisms in the presence of a planar wall has also been investigated extensively. The first such report was by Rothschild who observed a significant increase of cell density near a glass wall using bull spermatozoa [197]. A similar accumulation of cells near a wall was also found for human spermatozoa [256] and *E. coli* bacteria [19, 71]. The mechanism of attraction to a wall may be in part explained by far-field hydrodynamics [136]. When a swimming cell is a so-called pusher, i.e. its thrust is generated behind the cell body like for spermatozoa or flagellated bacteria, the cell tends to direct itself towards the wall due to far-field hydrodynamic interactions. In contrast, when a swimming cell is a puller, i.e. when its thrust is generated in front of the cell body, cells swimming parallel to the wall tend to be repelled by it hydrodynamically.

Some swimming microorganisms can be trapped by planar walls. For instance, swimming *E. coli* cells are drawn to a stable circular trajectory, and the physical mechanism underlying the entrapment has been explained by hydrodynamic and steric effects [60, 81, 137, 242]. Spermatozoa can also be trapped by a planar wall, and the entrapment mechanism can again be explained by hydrodynamic and steric effects [67, 119, 215]. Such entrapment phenomena may reduce the spreading of cells near surfaces considerably.

Other types of surface-related behaviour have also been reported for both biological and artificial swimmers. *Chlamydomonas* algae cells scatter from flat walls due to contact between their flagella and the surface, and exhibit billard-like motion in polygonal geometries [218]. The collective behaviour of *Bacillus subtilis* swarms and their interactions has been also shown to depend on the geometry of the enclosing cavities [257]. Chemically propelled rods tend to move on a surface along large circles with stochastic changes in the sign of the orbit curvature [226] and may be captured around solid spheres of various radii and materials [227]. Colloidal particles rolling along a planar wall display a transition to macroscopic directed motion for large populations [28]. Finally, swimming *E. coli* cells have been observed experimentally to be trapped along convex walls provided the wall curvature was sufficiently small [211]. This result has been explained by a theoretical analysis of the entrapment mechanism that shows that a swimmer approaching a spherical colloid can be captured hydrodynamically when the colloid is larger than a critical size [217].

In nature many microorganisms live in environments subject to complex geometrical constraints. Bacteria in soil, for instance, swim in heterogeneous granular matter, and their habitat is influenced by physical parameters including granular size and shape [35, 95, 175, 247, 263]. While locomotion of organisms in granular media with particle size smaller than the body length has been investigated widely [102, 155], only a few studies have addressed the spreading of microswimmers in complex geometries [165]. A study on the motion of Janus particles in a two-dimensional (2D) periodic pattern of ellipsoidal pillars arranged in a triangular lattice showed that microswimmers can even navigate perpendicularly to an applied force in the periodic pattern [245]. Swimming Janus particles and *E. coli* cells in a two-dimensional colloidal crystal demonstrate that artificial particles orbit individual colloids with occasional hops while the circular orbits, while bacterial trajectories were rectified into long, straight runs [29].

Given the potential environmental complexity encountered by both natural and artificial swimmers, a lot remains to be explored. In particular, the role played by both the type of swimmer and its environment in dictating how the swimmers spread on average is of fundamental interest. To this end, we consider here a model system for swimming in a periodic environment. The swimmer is a spherical squirmer [21, 142], one of the simplest models of low-Reynolds

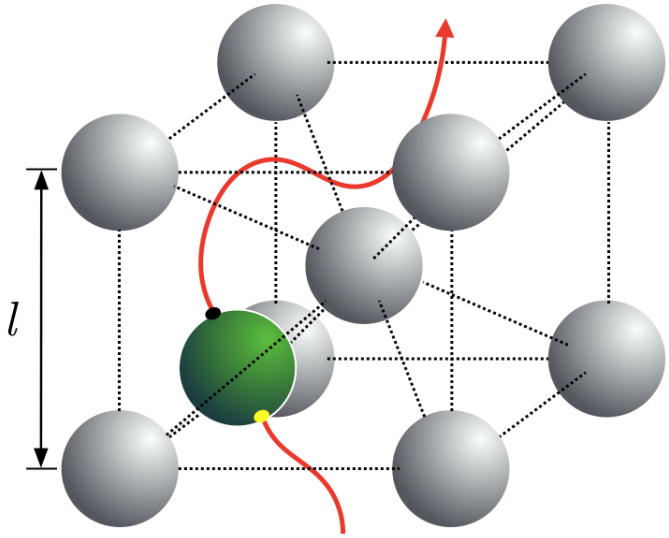

Figure 2.1 Sketch of a unit lattice cell. The squirmer (green sphere with front indicated in black and back in yellow) navigates between rigid spheres (grey) forming a BCC lattice with period l. The computational domain consists of $4 \times 4 \times 2$ such unit lattice cells with periodic boundary conditions, and contains a single squirmer.

number swimmers that allows us to compute the hydrodynamics precisely. The squirmer is placed in an infinite three-dimensional body-centred cubic (BCC) lattice of passive, rigid spheres of the same radius, and its trajectory is computed numerically by considering both far- and near-field hydrodynamic interactions with the lattice [110]. Running a large number of simulations, we are able to address three main questions in our study: (1) which qualitative types of trajectories arise in periodic lattices, (2) how these depend on the strength of the swimmer and the packing density of the lattice and (3) how to explain these results with hydrodynamic arguments.

We begin by explaining the model and the numerical method in §2.2. Following that, we present the results of our numerical computations in §2.3. These will then be explained analytically by two different models that we describe in §2.4. We finish with a concluding discussion in §2.5.

2.2 Model and Simulations

Our computations are carried using a modified version of the code used and validated in Ref. [110] to model a suspension of squirming microswimmers. A detailed explanation of the method is provided in §2.A. For the purposes of this chapter we consider a single spherical squirmer, and 64 identical rigid spheres arranged as a rigid stationary BCC lattice. The flow

satisfies the no-slip boundary condition on their surface. Lengths are scaled so that all spheres have unit radius. A unit lattice cell has side length l, while the computational cell consists of $4 \times 4 \times 2$ unit cells. The squirmer moves through the space between the lattice spheres (see Fig. 2.1). At the edge of the computational cell, periodic boundary conditions for the flow are applied. The volume fraction occupied by the lattice ϕ, which we alternatively call packing density, is related to l by $\phi = 8\pi/3l^3$.

As explained in §1.2, the squirmer induces an effective slip velocity tangential to its surface in order to propel forward. Specifically, in spherical coordinates measured from its centre, the velocity boundary conditions applied by the squirmer in the swimming frame are given by [21, 142]

$$u_r(1,\theta) = u_\phi(1,\theta) = 0, \quad u_\theta(1,\theta) = \frac{3}{2}\sin\theta\,(1+\beta\cos\theta)\,, \tag{2.1}$$

where θ is the azimuthal angle measured from the squirmer orientation vector $\boldsymbol{e}$, and β is the so-called squirming parameter dictating the nature of the far-field flow. A swimmer with $\beta > 0$ is a puller, like the alga *Chlamydomonas*, whereas one with $\beta < 0$ is a pusher, similar to most flagellated bacteria and spermatozoa.

The boundary conditions in Eq. (2.1) have been chosen such that an individual squirmer would swim with unit speed in absence of the lattice [21]. The characteristic time scale of the problem is thus the time it takes for the squirmer to move as far as its own radius. With this scaling, the simulation uses a timestep of 10^{-3} and runs for a total of 10^6 steps, equivalent to 1000 dimensionless time units. The viscosity of the fluid, μ, is also scaled to unity.

The squirmer is initialised at the centre of a face of a unit lattice cell, with random orientation. We note that through the periodic boundary conditions our model really is that of an infinite lattice with an infinite number of squirmers in it. However, the separation between the swimmers is large enough to make any hydrodynamic interactions negligible compared to those with the surrounding lattice spheres, making this an appropriate model for a single swimmer in an infinite lattice.

In what follows, we examine volume fractions between 1% and 13%. The theoretical maximum to allow space for a squirmer to pass through the lattice along one of its axes (i.e. such that $l \geq 4$) is $\phi = \pi/24 \approx 13.1\%$, so the examined parameter range extends from the very dilute limit up to almost the densest possible lattices that the swimmer could theoretically traverse. We also vary the strength of the squirming parameter by considering the range $-3 \leq \beta \leq 2$ and thus include both pullers and pushers.

2.3 Computational results

2.3.1 Phenomenology of trajectories

We performed 338 simulations in the parameter range $-3 \leq \beta \leq 2$, $1\% \leq \phi \leq 13\%$ with random initial orientations and observed qualitatively different features of the resulting trajectories, originating from a complex interplay of both far-field and near-field interactions with the lattice (see illustration in Fig. 2.2 and the supplementary material [1]). In order to classify the various different kinds of behaviour rigorously and systematically, we first introduce some definitions.

Definition #1: Turns and straight trajectories

A squirmer is said to make a turn every time its orientation changes by more than 60° from when it last made a turn (or from its initial orientation in case of the first turn). If a squirmer makes no turn during the entire simulation, or more than 500 time units elapse between two subsequent turns, then we say the trajectory is straight. The last condition is added to discount transients occurring at the beginning of the simulation and to account for trajectories with very long straight segments. The results are not sensitive to the exact value of the threshold, which has therefore just been chosen to be much larger than the time scale of scattering from the lattice. The value of the angular threshold can be motivated by the typical behaviour observed in our numerical simulations: the swimmers do not perform U-turns, but often tend to wiggle around an otherwise straight path. The particular angular value we have chosen reflects these observations and has proven to capture the intuitive idea of a turn (as opposed to a wiggle) correctly in all cases considered. We note that the translational velocity direction and the orientation of the squirmer need not coincide and we may also have chosen this as a criterion for the definition (although it did perform not as effectively as the angular criterion). We note furthermore that our criterion does not distinguish between a sharp turn and a long trajectory with small curvature; however the latter does not occur in our simulations since the swimmer only changes its orientation substantially in the neighbourhood of a lattice sphere, so there is no ambiguity.

Definition #2: Entrapment

Writing the position of the centre of the squirmer as $\boldsymbol{r}(t)$, we define a squirmer to be trapped if there is a time $t^\star$ such that $|\boldsymbol{r}(t^\star + t) - \boldsymbol{r}(t^\star)| \leq 5$ for all times $0 < t < 100$. This means that a swimmer is considered trapped if it does not move further than 5 radii in 20 times the time it would require to traverse that distance at full speed. In this case, $t^\star$ is then the moment of entrapment. The spatial threshold here is chosen to identify squirmers trapped by (and so

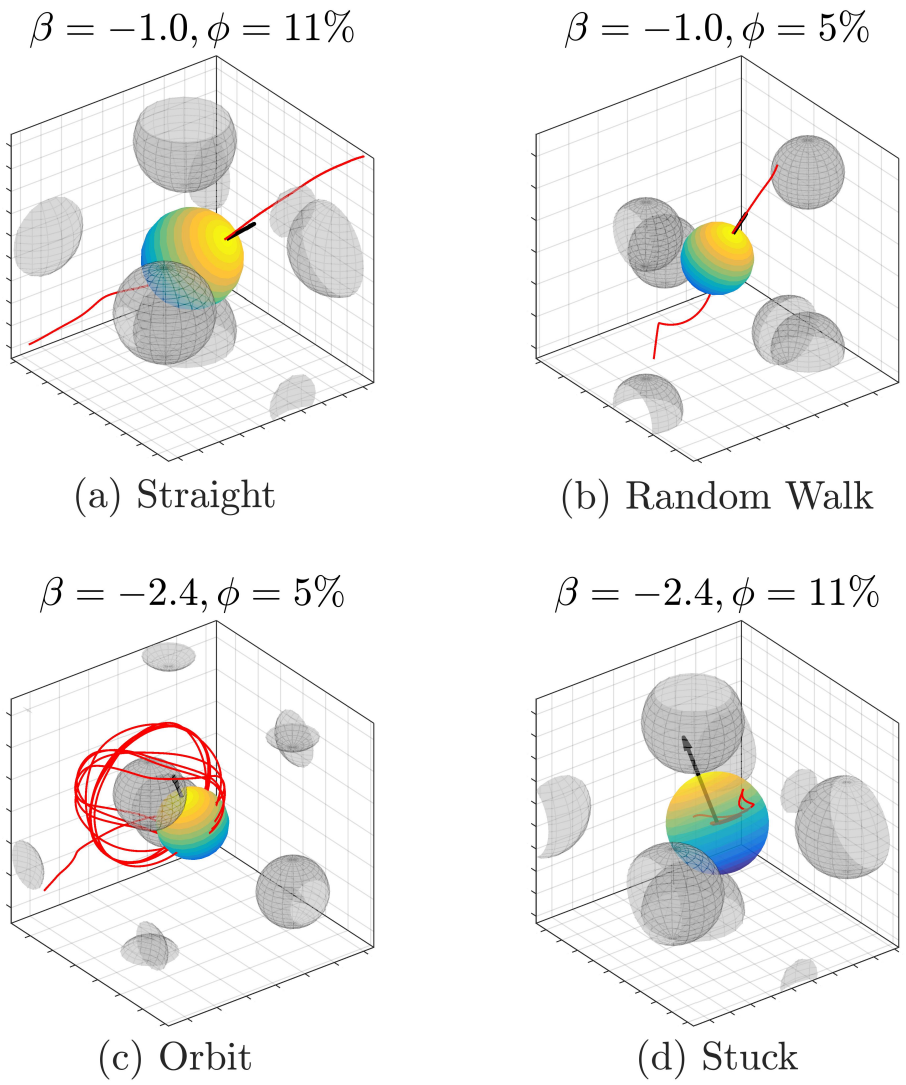

Figure 2.2 Sample trajectories for a swimmer moving in a BCC lattice for various values of the squirming parameter β and the lattice volume fraction ϕ: (a) Weak pusher ($\beta = -1.0$) swimming straight ($\phi = 11\%$); (b) Weak pusher ($\beta = -1.0$) moving on a random walk through the lattice ($\phi = 5\%$); (c) Strong pusher ($\beta = -2.4$) orbiting one of the obstacles ($\phi = 5\%$); (d) Strong pusher ($\beta = -2.4$) stuck ($\phi = 11\%$). See also the supplementary material [1] for animated versions of these and for pullers at $\beta = 1.0$.

remaining in contact with) a single lattice sphere, in which case the displacement is limited to slightly more than 4 radii. The temporal threshold is chosen to be much larger than the time required for the free case, and is not sensitive to the precise value as squirmers tend to get caught early in the simulations.

Definition #3: Stuck vs. Orbiting

For the case that a swimmer is trapped, we introduce two further definitions to distinguish swimmers that stay in place from those that move on confined periodic or chaotic trajectories. A trapped trajectory is called stuck if it remains straight according to definition #1, and orbiting if it does not.

Definition #4: Random walks

If a swimmer's trajectory is neither straight nor trapped, it resembles a random walk. Generically with periods of straight swimming followed by reorientations after collisions with lattice spheres. When a swimmer follows a random walk, we measure the total number of turns of the swimmer trajectory over the entire course of the simulation.

2.3.2 Phase diagram

With these definitions we can now summarise our computational results in a phase diagram. This is shown in Fig. 2.3 for parameters β and ϕ. Four qualitatively different behaviours can be distinguished: straight trajectories; random walks (with a colour scheme indicating the total number of turns that occur during the 1000 non-dimensional time units of the computation); orbiting swimmers; and stuck swimmers. The red line around $\beta \approx -1.8$ to -1.6 represents the boundary between trapped swimmers (strong pushers) and those which are not trapped (pullers and weak pushers).

Pullers

All pullers ($\beta > 0$) considered in our simulations move through the lattice on nearly straight trajectories at almost unit speed. The pullers appear to be repelled by the obstacles, and the trajectories only feature some small wiggles due small perturbations of the swimmer orientation. A simple far-field theoretical approach in §2.4 will allow us to rationalise these observations.

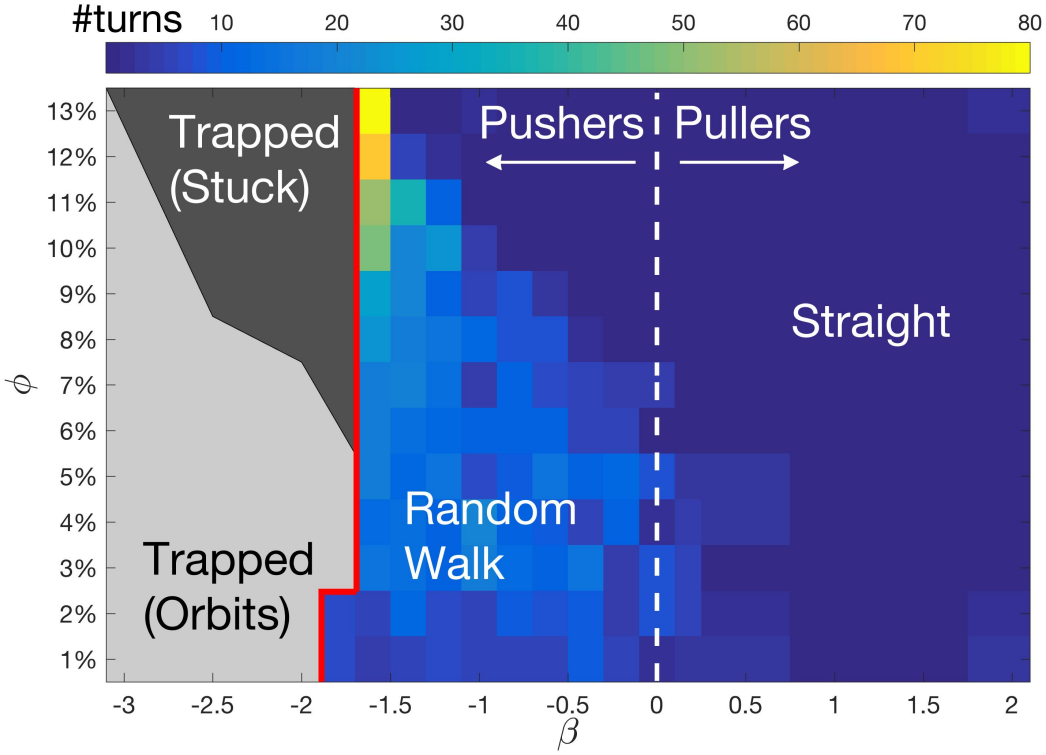

Figure 2.3 Phase diagram of squirmer trajectories for parameters β and ϕ based on 338 simulations with random initial orientations, showing four qualitatively different kinds of trajectories. The red line indicates the transition between a trapped behaviour for strong pushers to a random walk and straight trajectories for weak pushers and pullers. Coloured cells quantify the number of turns exhibited by a trajectory of 1000 non-dimensional time units as defined in §2.2.

Pushers

For weak pushers ($-1.6 \lesssim \beta < 0$) similarly straight trajectories are observed at small volume fractions, although the perturbations of the orientation are larger (Fig. 2.2a). However, when the volume fraction is increased, the active particles are deflected through interactions with the lattice, leading to random walks, or weakly diffusive behaviour (Fig. 2.2b). Most of these random walks only feature at most ≈ 20 turns over the course of the 10^3 time units, corresponding to only one turn every couple of lattice cells (see coloured cells in Fig. 2.3). Furthermore we observe that the number of turns in the random walks increase with the volume fraction of the lattice (ϕ) and with the strength of the flow imposed by the swimmer (β), leading to a spike in the number of turns when the packing density is very high and the squirming parameter is close to the entrapment threshold. In contrast, for very small values of ϕ the interactions become weaker and the number of turns reduces to a small non-zero value for

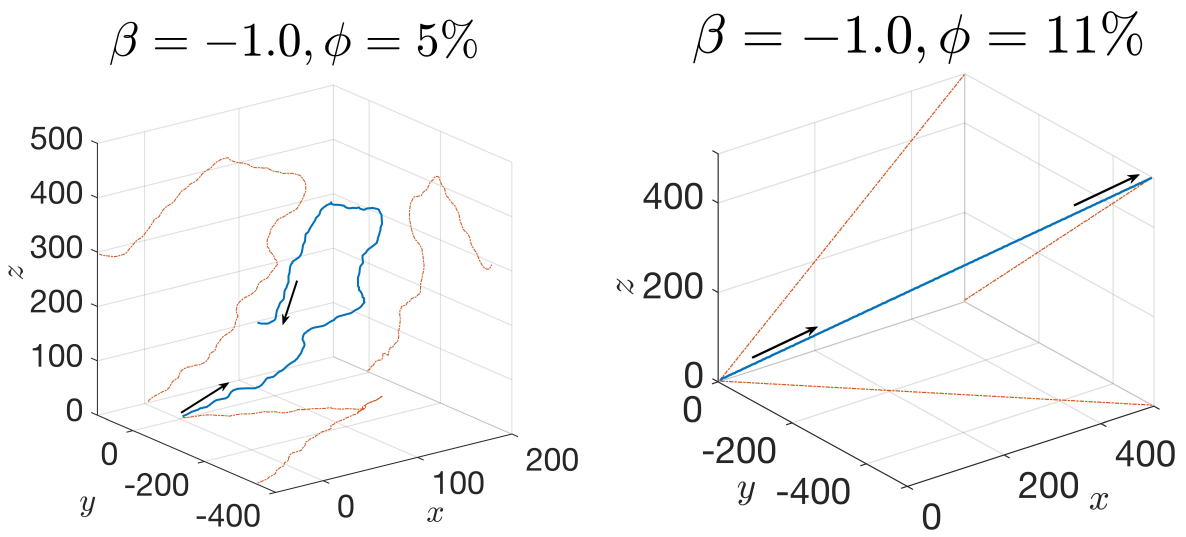

(a) Random Walk

(b) Straight

Figure 2.4 Macroscopic trajectories (blue solid lines) of intermediate-strength pushers ($\beta = -1$) transitioning from random walks at low volume fraction (a, $\phi = 5\%$) to straight swimming at high volume fractions (b, $\phi = 11\%$). Shadows on the $x-y$, $x-z$ and $y-z$ planes are drawn to help the eye (red dash-dotted lines), and arrows indicate the direction of motion (lengths scales are scaled by the swimmer radius).

a wide range of values for β. Interestingly, for intermediate-strength pushers a high packing density tends to stabilise the trajectories again, leading to a region of straight pusher trajectories in Fig. 2.4.

When the squirming parameter exceeds a critical threshold, found to be approximately $\beta_c \approx -1.6$ in our simulations we observe a sharp transition to trapped states which appears to be largely independent of the volume fraction in the lattice. Only in the very dilute limit the threshold decreases to $\beta_c \approx -1.8$. In the trapped region of the phase diagram we observe orbiting behaviour for low packing densities (Fig. 2.2c) and stuck swimmers at high packing densities Fig. 2.2d). The range of values of β leading to a stuck swimmer shrinks as β is decreased further until all trajectories are orbits at $\beta = -3$. Interestingly, these orbits are nearly periodic circles for small volume fractions, but become chaotic for larger values of ϕ, apparently due to hydrodynamic repulsion but not steric interactions with the surrounding obstacles. In all cases that orbiting behaviour is observed, the squirmer is tilted from the normal to the obstacle surface by a small acute angle that increases with $|\beta|$, effectively making it slide around the obstacle.

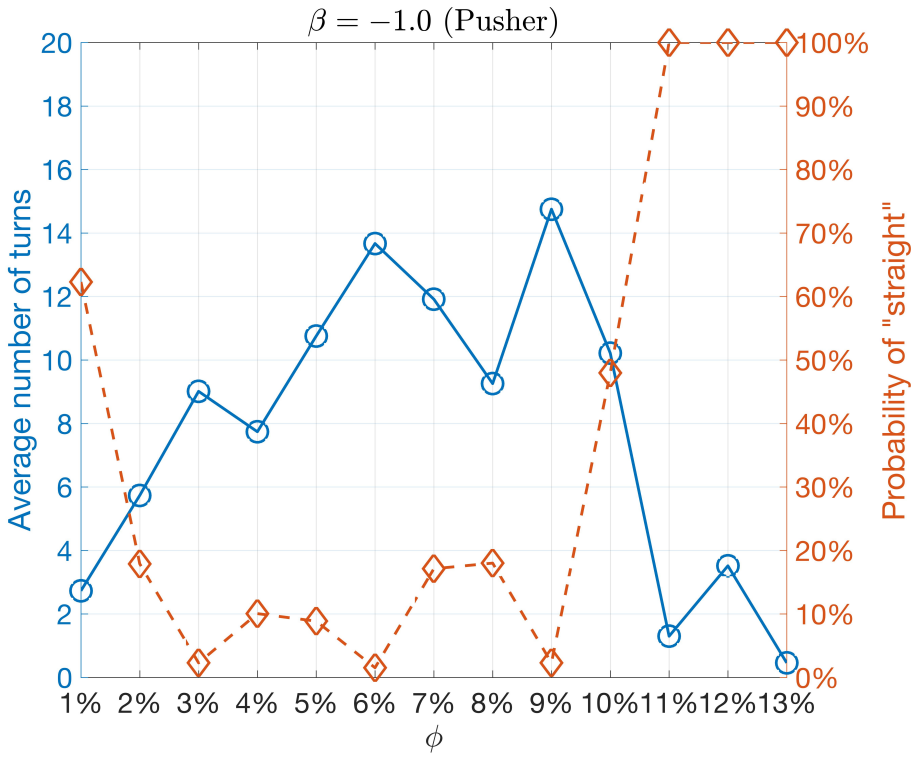

Figure 2.5 Characteristics of trajectories for a weak pusher ($\beta = -1.0$) calculated using Lebedev quadrature from 12 sample initial orientations: expected number of turns (blue solid line) and probability that a trajectory is straight (dashed red line). The transition from random walk to straight occurs at a volume fraction around $\phi = 10\%$.

Dependence on initial orientation

While the results presented so far are representative of the characteristic dynamics of squirmers in this geometry due to the long simulations times, the exact nature of the random-walk like diffusive behaviour inevitably depends sensitively on the initial conditions due to the complexity of the geometry. Therefore, in order to analyse the dependence of these random walks on the volume fraction of the lattice in more detail we performed multiple runs for selected values of the parameters using judiciously chosen initial orientations of the swimmer. In particular, we consider the transition from straight to weakly diffusive behaviour for fixed $\beta = -1$ and varying packing density ϕ.

The space of orientations is suitable for Lebedev quadrature, which allows the numerical computation of integrals using only a finite set of orientations [138]. We choose 17th-degree quadrature which ordinarily requires 110 sample points but this can be reduced to 12 by exploiting the symmetries of the lattice, leading to a substantial reduction of the computational

effort. However, we recognise that due to the sensitive dependence on the initial orientation, the results can still only give a qualitative indication of the dynamics.

In Fig. 2.5 we plot for a given intermediate strength pusher ($\beta = -1.0$) the expected number of turns (blue solid line) and the probability that a trajectory is straight (dashed red line). Strikingly, the probability to obtain a straight trajectory rises sharply to unity at volume fractions greater or equal to 10%, along with a corresponding sharp decrease in the number turns (that need not be zero, see §2.3.1). Likewise, we see that trajectories are on average more straight at very low volume fractions, which is what one would expect for the case of free swimmer. Similar computations for values of β in the trapped regime also reveal that the average distance travelled by swimmers through the lattice decreases as either the volume fraction and or the squirming parameter increase.

2.4 Theory

Our simulations reveal a number of remarkable features of the locomotion of an active particle in a lattice. In this section, we provide theoretical arguments in order to rationalise these observations. We focus below on three main questions arising from the phase diagram in Fig. 2.3: (1) Why are pullers able to swim straight while weak pushers tend to perform a random walks? (2) Why is there a threshold in β for the entrapment of pushers? (3) How can we understand the transition, in the trapped regime, between an orbiting and a stuck state as a function of the volume fraction of the lattice?

2.4.1 Straight swimming vs. random walks

In order to understand why pullers swim straight though the lattice while weak pushers tend to perform random walks, we use a far-field analysis of the hydrodynamic interactions between the swimmer and the stationary obstacles of the lattice. In this limit, the interactions can be calculated using the method of reflections [94, 127]. Below we show analytically that squirmers swimming through a channel of spheres are stabilised and destabilised along their otherwise straight trajectory in approximately equal intervals but with varying strength and in a manner that depends on the sign of the squirming parameter.

The leading-order flow induced by the squirmer is that of a stresslet (force-dipole) which can be written as [10, 21]

$$\boldsymbol{u}(\boldsymbol{r}) = -\frac{3}{4}\beta\left(3\frac{\boldsymbol{r}(\boldsymbol{e}\cdot\boldsymbol{r})^2}{r^5} - \frac{\boldsymbol{r}}{r^3}\right), \tag{2.2}$$

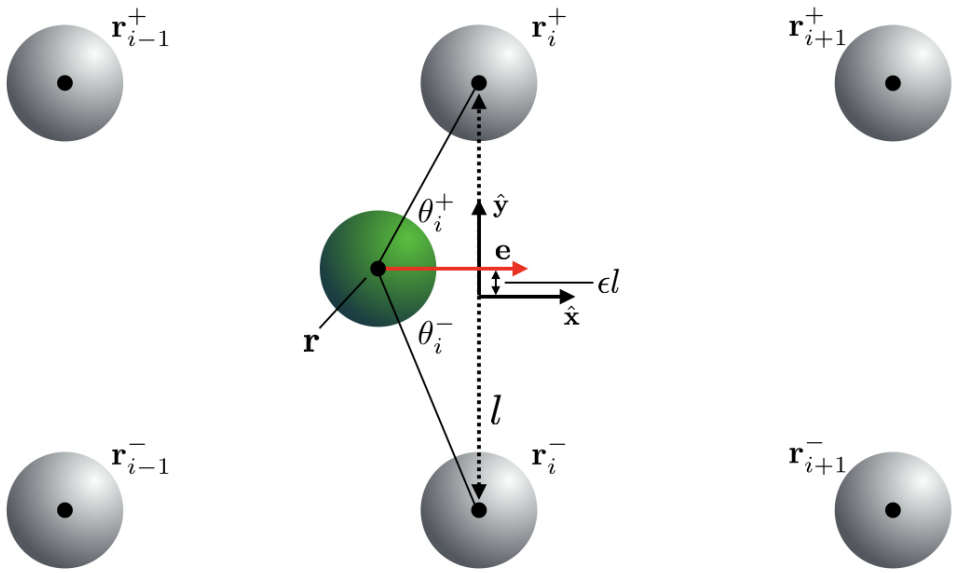

Figure 2.6 Simplified model used to explain the transition from straight swimming (pullers) to random walks (pushers). The squirmer moves through a planar channel of width l made of unit rigid spheres. The position of the swimmer is denoted $\boldsymbol{r} = (xl, \epsilon l)$ and those of the fixed spheres by $\boldsymbol{r}_i^{\pm} = il\hat{\boldsymbol{x}} \pm l/2\hat{\boldsymbol{y}}$ where i is an integer. $\theta_i^{\pm}$ denotes the angle between $\boldsymbol{e}$, $\boldsymbol{r}$ and $\boldsymbol{r}_i^{\pm}$.

where the squirmer is instantaneously centred at the origin and has orientation $\boldsymbol{e}$. It decays as $1/r^2$. The leading-order hydrodynamic response to this flow by a lattice sphere located at $\boldsymbol{r}_0$ is a Stokeslet (point force) that can be calculated using Faxèn relations [127]. The response of the squirmer to this Stokeslet is then a perturbation, $\boldsymbol{u}_{\text{Stokes}}$, to its swimming velocity as

$$\boldsymbol{u}_{\text{Stokes}} = \frac{9}{8}\beta(3\cos^2\theta - 1)\frac{\boldsymbol{r}_0}{r_0^4} + O\left(r_0^{-4}\right), \quad \cos\theta := \boldsymbol{e}\cdot\hat{\boldsymbol{r}}_0, \tag{2.3}$$

which decays as $1/r^3$ because it is the $1/r$ Stokeslet response to a perturbation that decays as $1/r^2$. Higher-order terms are then due to faster decaying flow singularities and their responses. Importantly, the sign of this velocity perturbation depends both on the squirming parameter, β, and on the angle that $\boldsymbol{e}$ makes with the displacement vector to the lattice sphere; this is a consequence of the dipolar nature of the flow in Eq. (2.2). From this, it is clear that the geometry of the lattice and the position and orientation of the squirmer within it determine its behaviour in a very non-trivial fashion.

Further progress can be made however by considering a simplified geometry, illustrated in Fig. 2.6. Here we consider a squirmer confined to a two-dimensional plane moving through a 'channel' of lattice spheres positioned at $\boldsymbol{r}_i^{\pm} = il\hat{\boldsymbol{x}} \pm l/2\hat{\boldsymbol{y}}$ where i is an integer. Such a channel is a common feature of regular lattices such as cubic, BCC and FCC, which can all be thought of as assembled from interlaced channels at different orientations. In particular, by linearity of the flow in the dilute limit the results obtained from this model gives qualitatively predictions for the three-dimensional case at sufficiently low volume fractions.

Since the Stokeslet responses are directed towards the centre of the squirmer, they do not exert any net torque on it. For this reason the rate of change of its orientation $\boldsymbol{e}$ is with $O(r^{-5})$ at least two orders of magnitude smaller than the rate of change of ϵ (one order from the higher-order response and another due to the fact that torques arise from vorticity which is the curl of the response flow). At leading order we may therefore assume that the orientation of a swimmer remains unchanged. We focus on the case $\boldsymbol{e} = \hat{\boldsymbol{x}}$ and quantify the role of hydrodynamic interactions on the motion of the sphere. The squirmer position is denoted by $\boldsymbol{r} = (x(t)l, \epsilon(t)l)$ where $|\epsilon| \ll 1$. Neglecting all but the leading-order interactions we then obtain the dynamical system for (x, ϵ) as

$$\frac{\mathrm{d}x}{\mathrm{d}\tau} = 1 + O(\epsilon), \quad \frac{\mathrm{d}\epsilon}{\mathrm{d}\tau} \approx \frac{9\beta}{8l^3} \sum_{i,\pm} \frac{3\cos^2\theta_i^{\pm} - 1}{|\boldsymbol{r}_i^{\pm} - \boldsymbol{r}|^3} \sin\theta_i^{\pm}, \tag{2.4}$$

where $\tau = t/l$ and $\theta_i^{\pm}$ is the angle between the vectors $\boldsymbol{e}$ and $\boldsymbol{r}_i^{\pm} - \boldsymbol{r}$. Upon linearising in ϵ the terms in the sum we obtain the differential equation for the off-axis location of the swimmer as

$$\frac{\mathrm{d}\epsilon}{\mathrm{d}x} = -\frac{36\beta}{l^3} \left\{ \sum_{n=-\infty}^{\infty} \frac{3 - 52(n-x)^2 + 32(n-x)^4}{[1 + 4(n-x)^2]^4} \right\} \epsilon + O(\epsilon^2). \tag{2.5}$$

which integrates to

$$\ln\left(\frac{\epsilon}{\epsilon_0}\right) \approx -\frac{36\beta}{l^3} \sum_{n=-\infty}^{\infty} \left\{ \frac{11(x-n) + 16(x-n)^5}{4(1 + 4(x-n)^2)^3} + \frac{1}{8}\tan^{-1}\left(2(x-n)\right) \right\} \tag{2.6}$$

Each term in the sum represents a kink in $\ln\epsilon$ of magnitude $\pi/8$ and width $O(1)$, centred around $x = n$. Taking the average over the period of the channel we can therefore deduce that the mean growth rate of the perturbation satisfies

$$\langle \ln(\epsilon/\epsilon_0) \rangle \approx -\frac{9\pi\beta}{2l^3} x = -\frac{27}{16}\beta\phi\tau \quad \Rightarrow \quad \epsilon(\tau) \sim e^{-(27/16)\beta\phi\tau}. \tag{2.7}$$

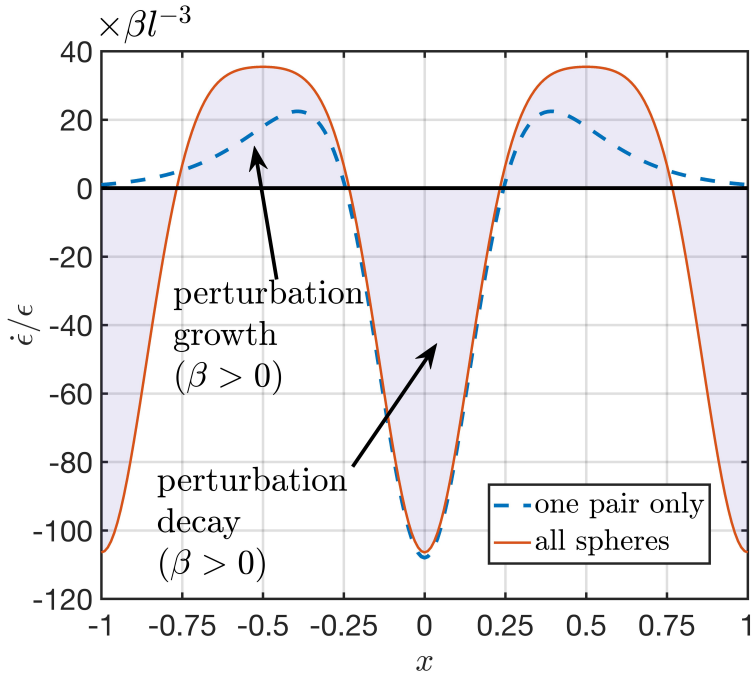

Figure 2.7 Instantaneous growth/decay of a perturbation ϵ away from a trajectory through the middle of a two-dimensional channel of rigid spheres. Results are shown in the case of a puller ($\beta > 0$); for a pusher the stability properties are reversed via a change of sign. The contribution from a single $\pm$-pair of spheres is displayed for illustrative purposes (dashed blue line) while the total effect of all spheres is a superposition of such pair effects (solid red line).

From this we see that puller trajectories ($\beta > 0$) are stable, whereas pushers ($\beta < 0$) are not. Moreover, the growth rate depends linearly on the packing density.

In Fig. 2.7 we plot the effect of a single pair of spheres at $y = \pm l/2$, corresponding to one term in the series ($n = 0$), on a puller squirmer ($\beta > 0$) depending on its position relative to them (dashed blue line). We also plot the influence of all spheres in the channel (solid red line). We note that the dynamics are essentially entirely controlled by contributions from spheres less than $\approx 0.75l$ away from the swimmer. The dynamics of the swimmer are therefore controlled by the local geometry of the lattice only, which justifies our use of a periodic numerical scheme to model an individual swimmer.

As the swimmer moves through the channel, the perturbation of its position away from the central axis of the channel, ϵ, features alternating periods of growth (positive regions in Fig. 2.7) and decay (negative regions). We observe that the perturbations grow in one direction when the swimmer is roughly between a $\pm$-pair of spheres and grow in the other when it is roughly in the middle between two such pairs. Importantly, the rate of change is considerably greater in the decay region than in the growth region. This is illustrated in Fig. 2.8 where we plot the spatial variation of the perturbation, ϵ with dimensionless time τ, as well as the log-average from

Eq. (2.7). As a consequence, the perturbation is subject to oscillating decay for a puller and the straight trajectory is therefore stable, consistent with our numerical simulations. In contrast, for a pusher the decay/growth regions in Fig. 2.7 are reversed and the swimmer is ultimately unstable, as observed in our simulations at low volume fractions. Furthermore we note that the force with which the squirmer is stabilised or destabilised in this dilute model scales as $\sim \beta\phi$. Therefore the effect becomes very small at low volume fractions; in particular, when the orientation of the squirmer is not aligned with an axis of the lattice, trajectories become more complex and are impacted by scattering from lattice spheres.

Conversely, as ϕ is increased for pushers, there is less space for them to turn and reorient, forcing them on an effectively straight trajectory. This is what is observed in Fig. 2.2a. The clear jump in the probability that pushers go straight in Fig. 2.5 can therefore be explained by the existence of a critical volume fraction ϕ_c increasing with $|\beta|$, above which the squirmers cannot reorient quickly enough to leave an effectively straight path through the lattice.

In this theoretical argument we make two simplifying assumptions: We assume that the lattice is planar, and we exploit a symmetry which allows to pair up lattice spheres as pairs and consider their joint contribution. However, as shown in the supplementary material [1], neither of these restrictions are in fact necessary. Eq. (2.3) shows that pullers are generally repelled by obstacles to their side, while pushers are attracted towards them. This is sufficient to determine the stability of trajectories at low densities even for an irregular lattice arrangement. Nonetheless, at high densities it is observed that pusher trajectories are also stable. This is because the geometry of the lattice becomes sufficiently compact that the pushers do not have sufficient space to reorient. Since the strenght of interaction is linear in β, and hence increases as $|\beta|$ is increased, the threshold is larger for strong pushers. Due to geometric exclusion, it will also depend on the lattice type and swimmer shape.

2.4.2 Unbounded vs. trapped trajectories

In order to understand the transition from unbounded to trapped trajectories we present both a far-field and near-field model, each leading to a prediction for the entrapment threshold in β. The numerically observed value lies between these values, which hints at a balance of global and local effects.

For the far-field calculation we make use of a recent study which analysed the swimming of force dipoles near rigid spheres using the method of hydrodynamic images [217]. In that study, it was shown that for a pusher swimmer of unit radius creating a dipolar flow of strength α,

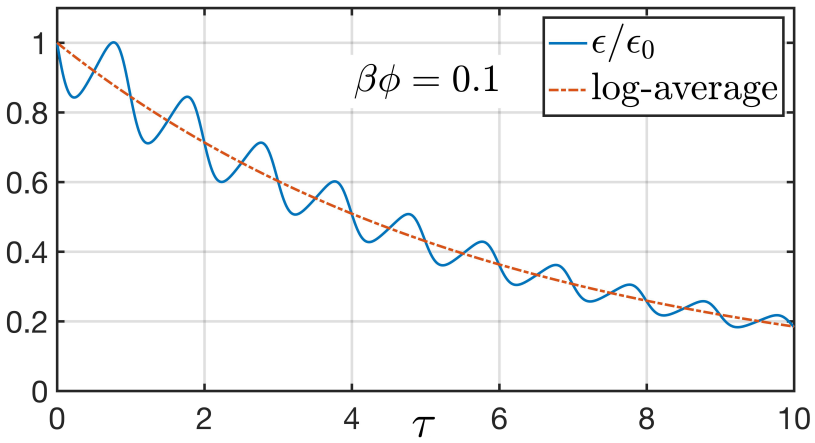

Figure 2.8 Decay of a perturbation for the off-axis position of the swimmer in a two-dimensional channel of rigid spheres (setup in Fig. 2.6) in the case of puller ($\beta > 0$) and $\beta\phi = 0.1$ over 10 unit lattice lengths (blue solid line). The shape of the curve is generic for a puller. While the deviation of the swimmer away from the axis features periods of both growth and decay, overall the latter dominates the dynamics, leading to exponential decay of the perturbation on average (Eq. (2.7), red dashed line).

trapping would occur along colloids whose radius, A, exceed a critical value A_c given by

$$A_c = \frac{64}{9\alpha^2}. \tag{2.8}$$

Swimmers near colloids for which $A < A_c$ will continue swimming (possibly with some scattering) while in the case $A > A_c$ pushers would all be predicted to be trapped.

Since the passive spheres of the lattice are of radius 1, this means that trapping would be predicted to occur for strong pushers, $|\alpha| > |\alpha_c|$, with

$$\alpha_c = \left(\frac{64}{9}\right)^{1/2} = \frac{8}{3}. \tag{2.9}$$

In our model, Eq. (2.2) indicates that the strength of the dipolar flow is given by

$$\alpha = -\frac{3}{4}\beta, \tag{2.10}$$

and thus trapping is predicted to occur for this far-field model for strong pushers satisfying

$$\beta < \beta_c^{\mathrm{FF}}, \quad \beta_c^{\mathrm{FF}} = -\frac{32}{9} \approx -3.56. \tag{2.11}$$

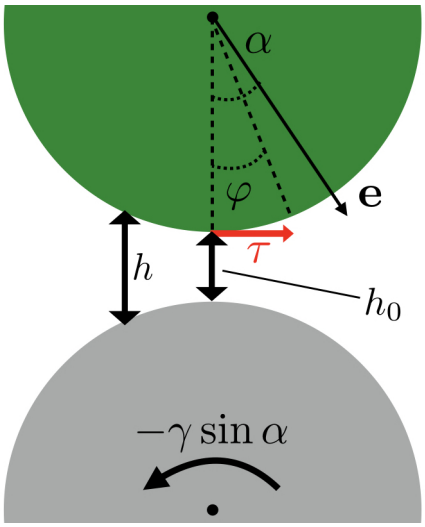

Figure 2.9 Sketch of the two-dimensional lubrication argument giving rise to a viscous torque, τ, acting on the squirmer (green, top) sliding around an inert lattice 'sphere' (grey, bottom), as viewed in the frame where the squirmer is stationary and the sphere rotates with an angular velocity of $-\gamma \sin\alpha$ where α is the angle that the squirmer orientation $\boldsymbol{e}$ makes to the normal to the sphere and γ a constant. For an angle φ from the normal $h(\varphi)$ denotes the gap width, which has its minimum h_0 at $\phi = 0$.

In order to model near-field effects, we now derive an argument based on lubrication theory (i.e. the equations of hydrodynamics valid in thin geometries [11]) to derive an expression for the torque experienced by a squirmer near an inert sphere as a function of its orientation (assuming that the swimmer is already in contact with a lattice sphere).

To simplify the calculation, we consider the two-dimensional case of two cylinders, which although they exhibit different scalings for the forces and torques, capture the same flow physics (see sketch in Fig. 2.9). Because the dynamics are overdamped there is no inertia, and hence no frame depended forces such as centrifugal forces. For this reason it is valid and convenient to consider a frame in which the squirmer is stationary and next to a uniformly rotating cylinder, i.e. the body frame of the squirmer. In this frame we can directly apply the squirming boundary condition, Eq. (2.1). Furthermore we assume that in steady state the squirmer maintains a constant distance h_0 from the inert 'sphere' surface and that its swimming direction, $\boldsymbol{e}$, makes an acute angle α with the normal to it. The gap width is thus written as

$$h(\varphi) = h_0 + 2(1 - \cos\varphi), \tag{2.12}$$

where φ is the angle between the normal and a point on the squirmer. We assume that the speed at which the surface is rotating is constant and write it as $u_{\text{slide}} = -\gamma \sin\alpha$ where γ is a constant

between 0 and 1 that reflects the fact that the squirmer is slowed down by its interaction with the obstacle.

From Eq. (2.1) we have that the tangential velocity on the squirmer is given by

$$u_{\text{Squirmer}} = -\frac{3}{2}\sin(\alpha-\varphi)(1+\beta\cos(\alpha-\varphi)) \tag{2.13}$$

in the direction of increasing φ (see Fig. 2.9). Since there is no external pressure gradient, the flow in the gap is a pure shear flow and therefore the total tangential stress on the squirmer is given by

$$\tau = -\int_{-\varphi_0}^{\varphi_0} \frac{u_{\text{Squirmer}} - u_{\text{slide}}}{h}\cos^2\varphi\,\mathrm{d}\varphi \tag{2.14}$$

$$= -\int_{-\varphi_0}^{\varphi_0} \left(\frac{-\frac{3}{2}\sin(\alpha-\varphi)(1+\beta\cos(\alpha-\varphi)) - (-\gamma\sin\alpha)}{h}\right)\cos^2\varphi\,\mathrm{d}\varphi, \tag{2.15}$$

where φ_0 is a cut-off angle for the region in which lubrication theory is valid ($\sqrt{h} \ll 1$) and the factor of $\cos^2\varphi$ arises from the need to project integrand and integration measure into the direction perpendicular to the gap. Carrying out the integration leads to

$$\tau = \sin\alpha\frac{3\pi}{2\sqrt{h_0}}\left(1-\frac{2}{3}\gamma+\beta\cos\alpha\right), \tag{2.16}$$

at leading order in h_0 as $h_0 \to 0$. We note that $\tau \sim h_0^{-1/2}$ in this two-dimensional setting while for spheres one finds $\tau \sim \ln h_0^{-1}$ [84, 109].

This traction results in a torque on the squirmer, and we are interested in the consequences of this torque on the dynamics of trapped swimmers. Analysing Eq. (2.16) for equilibrium points in α we find that $\alpha = 0$ is unstable for $\beta > \beta_c^{\text{NF}}$ and stable for $\beta < \beta_c^{\text{NF}}$ where

$$\beta_c^{\text{NF}} = -1 + \frac{2}{3}\gamma. \tag{2.17}$$

and $0 < \gamma < 1$ implies $-1 < \beta_c^{\text{NF}} < -1/3$. Compared with Eq. (2.11) we see that the threshold for entrapment predicted from considering near field effects only is much lower than that expected from far field effects. As the lubrication forces scale rather weakly with h_0 in three dimensions and higher order effects from the global geometry will matter, we conclude that a theoretical prediction for the critical squirming strength should lie between those two extremes, as is the case with our numerical observed value of $\beta_c \approx -1.8$. Recent studies of squirmers near curved boundaries using the Lattice-Boltzmann methods support this conclusion [131].

One of the characteristics of pushers and pullers is that the flow fields they generate contain vortices for $|\beta| > 1$, since in this case there exists a non-zero angle θ on their surface at which the velocity u_θ in Eq. (2.1) changes direction. For pullers this vortex is located in the wake of the swimmer, while for pushers it is located in front. The more complex dynamics observed for pushers may hence also be understood as the interaction of the lattice with these vortices. In particular, these vortices are fully captured by neither of the two models above, which may be the reason for the under- and overestimation of β_c respectively. Finally, we note that the reason why β_c is independent of the lattice packing density may be seen as due to the fact that it only depends on the hydrodynamic interaction with a single lattice obstacle, as long as the lattice is not so dilute that the probability of approach to a lattice obstacle is approaching zero.

2.4.3 Stuck swimmer vs. orbiting

So far we have provided mathematical arguments for two of the main numerical observations, namely the qualitative difference between pushers and pullers as well as the transition, for the case of pushers, between a trapped and non-trapped regime. The transition from stuck to orbiting for trapped pushers is due to an increase in the lattice packing density, and hence due to the interaction of the squirmer with multiple lattice spheres. This is very difficult to model quantitatively, but insight may still be gained by an argument based on the structure of the flow that a pusher generates.

By definition, a pusher expels fluid at its front and back, while pulling in fluid around its equator. A pusher that is trapped by a given lattice sphere will therefore be repelled by obstacles in its wake, and attracted by obstacles to its side, as may also be seen from Eq. (2.2). In the case of a dilute lattice these interactions are very weak, allowing the pusher to slide around the trapping obstacle on approximately a great circle. As the lattice becomes more compact, these interactions become stronger. In particular, since the swimmer is a pusher oriented towards the trapping sphere, it is repelled by the lattice spheres at its rear (Eq. (2.3)). When the lattice becomes sufficiently dense, these repulsive interactions are sufficiently strong to keep the squirmer in place, leading to the observed stuck behaviour.

We observe numerically that strong pushers are only trapped at very large packing densities. We postulate that the reason for this is that the interactions with the trapping obstacle depend more strongly on the squirming strength β than the long-distance interactions with the surrounding lattice.

2.5 Discussion

Using extensive numerical simulations we computed the trajectories of spherical squirmers through BCC lattices for a broad range of both the squirming parameter, β, and the lattice packing density, ϕ. We found a rich array of different qualitative behaviours, ranging from straight trajectories over weakly diffusive random walks to instant entrapment by the lattice.

We further demonstrated that much of this behaviour can be explained, at least qualitatively, using a combination of relatively simple hydrodynamic near-field and far-field arguments for the squirmer and its interactions with individual spheres in the lattice. Specifically, pullers tend to be stabilised and pushers destabilised on trajectories far from lattice elements. Close to lattice spheres, near-field and far-field hydrodynamic effects compete. There is a clear threshold in the squirming strength for entrapment, indicating that strong pushers are trapped, whereas weak pushers and pullers navigate through the lattice more or less unhindered. This may then result either in a trajectory resembling a weak random walk or, if too constrained by the lattice packing density, again a straight path. For a given squirming strength, there appears to be a clear threshold in packing density above which all trajectories are straight regardless of initial conditions.

In the parameter range for which the swimmer performs a random walk, it would be interesting to quantify the effective diffusive motion of the active particles. However, because reorientation events occur very infrequently, it is currently too computationally expensive to quantify it accurately from our simulations. A recent study has investigated this for a random Lorentz gas [165], and future work with more powerful numerical algorithms may shed more light on this issue taking hydrodynamics into account. Similarly, the effects of lattice geometry warrant further investigation: while test runs that we performed for a cubic lattice reveal the same generic behaviour of squirmers in the far field, the question to what extent the stuck-to-orbiting and unbounded-to-trapped transitions depend on the lattice geometry remains to be answered. Recently, simulations using Lattice-Boltzmann methods have revealed a rich behaviour of squirmer dynamics near flat and curved surfaces, which add to the complexity of the dynamics [130, 131]. The phenomenology of straight puller trajectories and deflected pusher trajectories is also reminiscent of the stability behaviour of suspensions of such model microswimmers, where pushers generically interact chaotically while pullers tend to form stable or isotropic structures [200–202].

Future studies could address how additional properties of the squirmer can affect the dynamics, for example potential phoretic effects. In a setup with a chemically-patterned lattice, a passive particle may propel through phoretic interactions, or in the case of a weakly charged lattice a charged swimmer may be affected through electromagnetic effects. Practical

applications in which our results may be put into use include the design of porous filters for swimmers of different types and strengths.

2.A Details of the numerical method

In this chapter we employ numerical code that was originally developed to model the dynamics of a suspension of squirmer microswimmers. Here we give a brief overview of the procedure and how we adapted it. The full mathematical details may be found in Ref. [110].

In essence, the default mode of calculating the interaction between the squirmer and the lattice is by means of a far-field expansion, which is computed using Ewald summation. In the event that the distance between the squirmer and an obstacle falls below a predetermined threshold, the pairwise interaction with that obstacle is computed using a precompiled database of lubrication interactions.

The fluid velocity $\boldsymbol{u}(\boldsymbol{x})$ at any point external to the swimmer or the lattice may be written in terms of a boundary integral as [188]

$$\boldsymbol{u}(\boldsymbol{x}) - \langle \boldsymbol{u} \rangle = -\frac{1}{8\pi\mu} \sum_{\text{spheres}} \int_S \boldsymbol{J}(\boldsymbol{x} - \boldsymbol{y}) \cdot \boldsymbol{q}(\boldsymbol{y}) \, \mathrm{d}S, \tag{2.18}$$

where $\langle \boldsymbol{u} \rangle$ is the average flow velocity in the computational domain, the sum is performed over all 65 spheres within (64 lattice spheres and the squirmer) and the integral is calculated over the surface of each sphere. The integrand consists of $\boldsymbol{J}$, which is the Green's function for a triply periodic lattice of spheres, and $\boldsymbol{q}$, which is the single-layer potential. At each time step $\boldsymbol{J}$ is calculated by Ewald summation as detailed in Ref. [13]. The right-hand side may be expanded in moments about the centre of each sphere as

$$\boldsymbol{u}(\boldsymbol{x}) - \langle \boldsymbol{u} \rangle = \frac{1}{8\pi\mu} \sum_{\text{sphere centres}} [\text{ monopole of } \boldsymbol{q} + \text{ dipole } + \text{ quadrupole } + \dots], \tag{2.19}$$

where each term is contracted with a propagator that is calculated from $\boldsymbol{J}$ and its gradients. The monopole and antisymmetric dipole correspond to the force and torque on each sphere respectively.

In order to determine the swimmer kinematics, Faxén's laws are applied for each sphere i located at $\boldsymbol{x}_i$ in the domain as

$$\boldsymbol{U}_i - \langle \boldsymbol{u} \rangle = \frac{\boldsymbol{F}_i}{6\pi\mu} + \boldsymbol{e} + \left(1 + \frac{1}{6}\nabla^2\right) \boldsymbol{u}'(\boldsymbol{x}_i), \tag{2.20}$$

$$\boldsymbol{\Omega}_i - \langle \boldsymbol{\omega} \rangle = \frac{\boldsymbol{G}_i}{8\pi\mu} + \frac{1}{2}\boldsymbol{\nabla} \times \boldsymbol{u}'(\boldsymbol{x}_i), \tag{2.21}$$

$$\boldsymbol{0} = \frac{\boldsymbol{S}_i}{\frac{20}{3}\pi\mu} + \frac{3}{10}\beta\,(3\boldsymbol{e}\boldsymbol{e} - \boldsymbol{I}) + \frac{1}{2\mu}\left(1 + \frac{1}{10}\nabla^2\right) \boldsymbol{\sigma}'_{\text{dev}}(\boldsymbol{x}_i), \tag{2.22}$$

where $\boldsymbol{U}_i$, $\boldsymbol{\Omega}_i$ are the translational and rotational velocity of the ith sphere, $\boldsymbol{F}_i$, $\boldsymbol{G}_i$ and $\boldsymbol{S}_i$ are the force, torque and stresslet that the ith sphere exert on the fluid, $\boldsymbol{u}'$ and $\boldsymbol{\sigma}'_{\text{dev}}$ are the velocity and deviatoric stress due to the other spheres, and $\langle \boldsymbol{u} \rangle$ and $\langle \boldsymbol{\omega} \rangle$ are the domain-averaged velocity and vorticity respectively. The terms in blue are present only for the squirmer, which has the orientation vector $\boldsymbol{e}$.

The method then proceeds by substituting Eq. (2.19) into the right-hand side of Eqs. (2.20)-(2.22) and truncating the expansion after the dipole (with an approximating expression substituting for the quadrupole). This leads to a linear system of the form

$$\begin{pmatrix} \boldsymbol{U} - \langle \boldsymbol{u} \rangle - \boldsymbol{e} + \boldsymbol{Q}_{\text{sq}} \\ \boldsymbol{\Omega} - \langle \boldsymbol{\omega} \rangle \\ -\frac{3}{10}\beta(3\boldsymbol{e}\boldsymbol{e} - \boldsymbol{I}) \end{pmatrix} = \boldsymbol{M}^{\text{far}} \cdot \begin{pmatrix} \boldsymbol{F} \\ \boldsymbol{G} \\ \boldsymbol{S} \end{pmatrix}, \tag{2.23}$$

where $\boldsymbol{Q}_{\text{sq}}$ is a quadrupole term due to squirming that is only experienced by the lattice spheres. $\boldsymbol{M}^{\text{far}}$ is the far-field grand mobility matrix, which is the same as the one for inert spheres [25] – the effect of swimming is contained in the blue and red terms on the left-hand side. For each of the lattice spheres it is given that $\boldsymbol{U}_i = \boldsymbol{\Omega}_i = \boldsymbol{0}$, while for the squirmer it is given that $\boldsymbol{F}_i = \boldsymbol{G}_i = \boldsymbol{0}$, and the system may hence be solved to find the kinematics of the swimmer.

In the case that the distance between the swimmer and an obstacle falls below 0.1 sphere radii, Eq. (2.23) is modified to account for near-field interactions. This is achieved by a system of the form

$$\begin{aligned} \begin{pmatrix} \boldsymbol{F} \\ \boldsymbol{G} \\ \boldsymbol{S} \end{pmatrix} = \left[\boldsymbol{R}^{\text{far}} - \boldsymbol{R}^{\text{far}}_{\text{2B}} + \boldsymbol{R}^{\text{near}}_{\text{2B}}\right] \begin{pmatrix} \boldsymbol{U} - \langle \boldsymbol{u} \rangle \\ \boldsymbol{\Omega} - \langle \boldsymbol{\omega} \rangle \\ \boldsymbol{0} \end{pmatrix} \\ + \left[\boldsymbol{R}^{\text{far}} - \boldsymbol{R}^{\text{far}}_{\text{2B}}\right] \begin{pmatrix} -\boldsymbol{e} + \boldsymbol{Q}_{\text{sq}} \\ \boldsymbol{0} \\ -\frac{3}{10}\beta(3\boldsymbol{e}\boldsymbol{e} - \boldsymbol{I}) \end{pmatrix} + \begin{pmatrix} \boldsymbol{F}^{\text{near}}_{\text{sq}} \\ \boldsymbol{G}^{\text{near}}_{\text{sq}} \\ \boldsymbol{S}^{\text{near}}_{\text{sq}} \end{pmatrix}, \end{aligned} \tag{2.24}$$

where $\boldsymbol{R}^{\text{far}}$ is the inverse of $\boldsymbol{M}^{\text{far}}$, $\boldsymbol{R}^{\text{far}}_{\text{2B}}$ the subtracted two-sphere far-field interaction resistance matrix, $\boldsymbol{R}^{\text{near}}_{\text{2B}}$ the exact two sphere resistance matrix from Ref. [127] and $\boldsymbol{F}^{\text{near}}_{\text{sq}}$, $\boldsymbol{G}^{\text{near}}_{\text{sq}}$ and $\boldsymbol{S}^{\text{near}}_{\text{sq}}$ are the force, torque and stresslet due to the interaction of two squirmers, which are taken from a precomputed database using lubrication theory [109]. The three terms on the right-hand side of Eq. (2.24) therefore constitute passive, far-field squirming and near-field squirming contributions respectively.

Finally, a very short range repulsive force is additionally included to model steric interactions and regularise the computational time step [110].

Chapter 3

Stokes flow due to point torques and sources in a spherical geometry

3.1 Introduction

Since George Gabriel Stokes first wrote down the low-Reynolds number flow equations that now bear his name [223], countless studies have been devoted to their mathematical properties and applications in fluid mechanics [90, 94, 127, 174, 176]. Perhaps most fundamentally, their Green's function, corresponding to the flow due to a point force in an unbounded fluid, has been known since 1896 [151]. It is today referred to as the Stokeslet, and has been applied and generalised in many different ways [94, 127].

One such extension is achieved through adding several cancelling point forces and taking the limit of zero separation in such a fashion that the product of their separation and their relative strengths remains finite. This process gives rise to higher-order faster decaying singularities such as force dipoles and quadrupoles, similar to charges in electrostatics but with an additional degree of complexity due to the vectorial nature of the Stokeslet. In particular, the force dipole singularity may be decomposed [10] into (i) a symmetric part, termed the stresslet, that corresponds to a symmetric hydrodynamic stress applied locally to the fluid, and (ii) an antisymmetric part, termed the rotlet, corresponding to a local hydrodynamic torque. These singularities also emerge naturally in the far-field asymptotic expansion of moving bodies in Stokes flow [94], and are useful for the modelling of suspensions of passive [90] and active [199, 200] particles and cells swimming in fluids [19, 26, 60, 135, 136, 144, 260]. Furthermore, these singularities form the basis of boundary integral methods that are among the most powerful computational tools for Stokes flows [188].

A different but desirable extension of the free-space Green's function adapts it to more complex geometries. In a landmark paper, Blake derived the singularity solution for a Stokeslet

in the presence of a plane rigid wall [22], and later extended it to higher-order singularities [23]. Since then, these have been applied extensively for their relevance in computational fluid mechanics [44, 188], and in the study of microorganisms near boundaries [216]. In a similar fashion, many other geometries have been explored, including fluid-fluid interfaces [3], the fluid outside [176, 207] and inside a rigid sphere [32, 159, 206], and viscous fluid confined between parallel plates [150, 212]. A concise account of the most important results and their derivations may be found in the textbook by Kim and Karrila [127]. More recently, a significant interest in regularised flow singularities and the corresponding image systems has also emerged [5, 45, 48], well suited e.g. for the efficient numerical simulation of slender fibres in viscous fluid [93].

Given a set of well-posed boundary conditions, the solution to the Stokes equations is unique [127]. However, in many cases multiple equivalent formulations exist of the same solution, each with their own advantages and disadvantages. For problems in a spherical geometry, Lamb's general solution [133] is a useful mathematical tool since it provides a complete set of eigenfunctions, however it is often cumbersome to use in numerical applications and lacks physical intuition. A similar problem arises for multipole expansions about the centre of the sphere, which are accurate for flows caused by disturbances far from the sphere, but become unwieldy when singularities near the sphere surface are considered [127]. A third option is given by Oseen's original solution [176], which is written as the free-space Stokeslet singularity plus an integral over the sphere surface that corrects for the no-slip boundary condition. Perhaps the most elegant and useful formulation, and motivated by the method of images, is written in terms of a distribution of hydrodynamic singularities. This form provides an intuitive physical interpretation, and since, unlike a multipole expansion, only singularities up to a finite order need to be calculated it is easy to achieve high numerical accuracy. Blake's solution for the Stokeslet near a wall is of this form, as are expressions for the Stokeslet near a spherical drop of arbitrary viscosity [72, 73].

Most of the results in the literature concerning the singularity representation were derived in work that focused on the dynamics of passive suspensions, and thus limited to only the kind of singularities appearing at leading order there. In contrast, for problems such as the rotation of flagellar filaments outside bacterial cell bodies [39], or the growth of bubbles near catalytic colloids [74], it is necessary to obtain the solution for point torques (e.g. rotation of flagellar filament) and sources (e.g. growth of bubble) outside a stationary sphere. Since there are presumably more situations in which these solutions would be useful, in this chapter we derive and summarise these results and their derivations so that they can be easily accessed and extended if desired.

The chapter is organised as follows. First we present our setup and notation in §3.2. By linearity of the Stokes equations, a general rotlet may be decomposed into an axisymmetric and

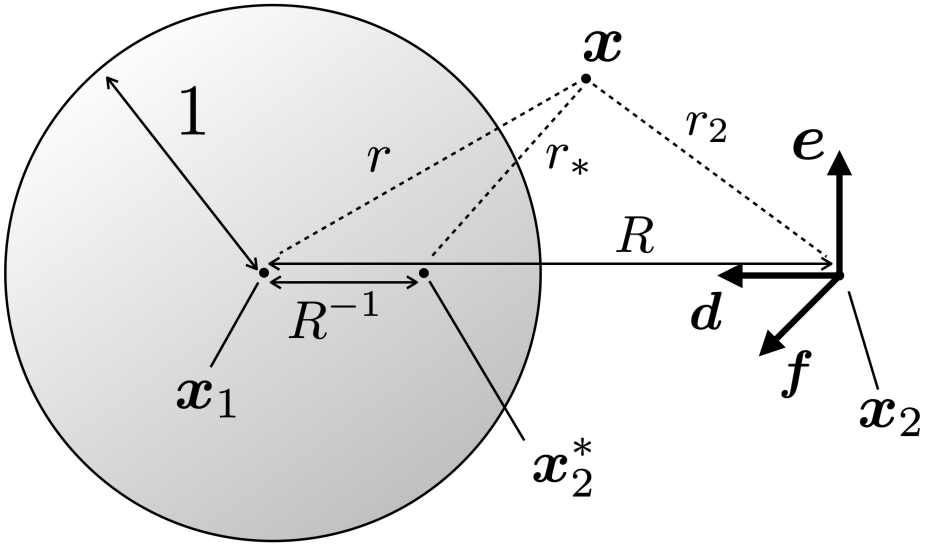

Figure 3.1 Illustration of the geometrical setup for flow singularities in a spherical geometry. A Stokes flow is induced by hydrodynamic singularities placed at $\boldsymbol{x}_2$, a distance R from the centre of a unit sphere positioned at $\boldsymbol{x}_1$. The mirror image point $\boldsymbol{x}_2^*$ is located a distance R^{-1} from $\boldsymbol{x}_1$ towards $\boldsymbol{x}_2$. The left-handed triad $\{\boldsymbol{d}, \boldsymbol{e}, \boldsymbol{f}\}$, and the lengths r, r_2 and r_* are defined in relation to $\boldsymbol{x}_1$, $\boldsymbol{x}_2$, $\boldsymbol{x}_2^*$ and a general point $\boldsymbol{x}$ as shown.

transverse component, which we then tackle in §3.3 and §3.4 respectively. Finally, the source is treated in §3.5. In each case, we begin with the known preliminary result listed in Ref. [127] and then derive the solutions, first in the case of a rigid sphere (no-slip boundary condition) and next in the case of a spherical bubble (no-shear boundary condition). We complement our results with numerically-obtained visualisations of the flow field in each case, and summarise our results in §3.6.

3.2 Geometry and setup

3.2.1 Geometry

The geometry of our problem is defined by a rigid sphere, or spherical bubble, centred at a point $\boldsymbol{x}_1$ (see sketch in Fig. 3.1). Whenever we refer to spherical coordinates $\{r, \theta, \phi\}$ in what follows, we define them with respect to the origin at $\boldsymbol{x}_1$. Since the radius of the sphere is the only extrinsic length scale in the problem, we choose to scale lengths such that the radius becomes unity. Without loss of generality, we can then consider a hydrodynamic singularity located at a point $\boldsymbol{x}_2$, where $\boldsymbol{x}_2 = \boldsymbol{x}_1 - R\boldsymbol{d}$, where $R > 1$ is the distance from the singularity to the sphere centre and $\boldsymbol{d}$ a unit vector pointing from $\boldsymbol{x}_2$ to $\boldsymbol{x}_1$. In order to maintain a notation that is

consistent with previous work [72, 73, 127] we extend this to a left-handed orthonormal triad $\{\boldsymbol{d}, \boldsymbol{e}, \boldsymbol{f}\}$. Furthermore, in what follows an important role will be played by the mirror image point $\boldsymbol{x}_2^*$, defined by $\boldsymbol{x}_2^* = \boldsymbol{x}_1 - R^{-1}\boldsymbol{d}$, and we will repeatedly refer to the distances defined by

$$r = |\boldsymbol{x} - \boldsymbol{x}_1|, \quad r_2 = |\boldsymbol{x} - \boldsymbol{x}_2|, \tag{3.1}$$

$$r_* = |\boldsymbol{x} - \boldsymbol{x}_2^*|, \quad \tilde{r}(\xi) = |\boldsymbol{x} + \xi\boldsymbol{d}|, \tag{3.2}$$

$$R = |\boldsymbol{x}_2 - \boldsymbol{x}_1|, \tag{3.3}$$

and the following shorthand,

$$D = \boldsymbol{d} \cdot \boldsymbol{\nabla} = -\frac{\partial}{\partial r}, \tag{3.4}$$

for a gradient in the radial direction.

3.2.2 Problem setup

We consider the incompressible Stokes equations

$$\boldsymbol{\nabla} p = \mu \nabla^2 \boldsymbol{u} + \boldsymbol{f}, \quad \boldsymbol{\nabla} \cdot \boldsymbol{u} = 0, \tag{3.5}$$

where $\boldsymbol{u}$ is the fluid velocity field, p is dynamic pressure, μ is dynamic viscosity and $\boldsymbol{f}$ a force density. In free space, the fundamental solution corresponds to a point force with $\boldsymbol{f}(\boldsymbol{x}) = \boldsymbol{F}\delta(\boldsymbol{x})$ and is given by

$$\boldsymbol{u}(\boldsymbol{x}) = \frac{\boldsymbol{F}}{8\pi\mu} \cdot \left(\frac{\boldsymbol{I}}{|\boldsymbol{x}|} + \frac{\boldsymbol{x}\boldsymbol{x}}{|\boldsymbol{x}|^3} \right) \equiv \boldsymbol{F} \cdot \boldsymbol{G}(\boldsymbol{x}), \quad p(\boldsymbol{x}) = \frac{\boldsymbol{F} \cdot \boldsymbol{x}}{4\pi|\boldsymbol{x}|^3}, \tag{3.6}$$

where $\boldsymbol{G}(\boldsymbol{x}) = (8\pi\mu|\boldsymbol{x}|^3)^{-1}(|\boldsymbol{x}|^2\boldsymbol{I} + \boldsymbol{x}\boldsymbol{x})$ is known as the Oseen tensor [127]. The solution in Eq. (3.6) is called the Stokeslet with strength $\boldsymbol{F}$.

The rotlet then emerges in the form of an antisymmetric force-dipole of the form $\frac{1}{2} g_a \varepsilon_{ajk} \nabla_k G_{ij}$ in index notation, where $\boldsymbol{g}$ is the rotlet strength and ε is the Levi-Civita tensor. The flow field may be written in vector form as

$$\boldsymbol{u}(\boldsymbol{x}) = -\frac{1}{8\pi\mu} \boldsymbol{g} \times \boldsymbol{\nabla} \frac{1}{|\boldsymbol{x}|} = \frac{1}{8\pi\mu} \frac{\boldsymbol{g} \times \boldsymbol{x}}{|\boldsymbol{x}|^3}, \quad p(\boldsymbol{x}) = 0. \tag{3.7}$$

Physically, a rotlet may be interpreted as the flow due to a point torque of strength $\boldsymbol{g}$ applied at the coordinate origin.

The solution for a point source cannot be directly obtained from the Green's function, since the latter is divergence-free while a point source is defined by the property that compressibility is locally singular. However, a simple mass conservation argument shows that a point source solution to Eq. 3.5 in free space is given by

$$\boldsymbol{u}(\boldsymbol{x}) = -\frac{Q}{4\pi}\boldsymbol{\nabla}\frac{1}{|\boldsymbol{x}|} = \frac{Q}{4\pi|\boldsymbol{x}|^3}\boldsymbol{x}, \quad p(\boldsymbol{x}) = 0, \tag{3.8}$$

where Q has the interpretation of volume flux (with $Q > 0$ for a source and $Q < 0$ for a sink respectively).

The goal of this chapter is to find the analogue of Eqs. (3.7) or (3.8) in the geometry described above. In the rigid-sphere case, we therefore seek the solution to Eq. (3.5) with boundary condition

$$\boldsymbol{u} = \boldsymbol{0} \qquad \text{at} \quad r = 1, \tag{3.9a}$$

$$\boldsymbol{u} \to \boldsymbol{0} \qquad \text{as} \quad r \to \infty. \tag{3.9b}$$

For a spherical bubble held in shape by surface tension γ (i.e. with vanishing Capillary number $\mathrm{Ca} = \mu U/\gamma$, where U is a characteristic scale for the flow velocity) the stress-free condition on the bubble surface leads to boundary conditions

$$\boldsymbol{n}\cdot\boldsymbol{u} = 0, \quad \boldsymbol{n}\times\boldsymbol{\sigma}\cdot\boldsymbol{n} = \boldsymbol{0} \qquad \text{at} \quad r = 1, \tag{3.10a}$$

$$\boldsymbol{u} \to \boldsymbol{0} \qquad \text{as} \quad r \to \infty, \tag{3.10b}$$

where $\boldsymbol{n} = \hat{\boldsymbol{r}}$ is defined as the unit normal to the sphere surface and $\boldsymbol{\sigma}$ is the hydrodynamic stress tensor, i.e. $\boldsymbol{\sigma} = -p\boldsymbol{I} + \mu\left(\boldsymbol{\nabla u} + (\boldsymbol{\nabla u})^T\right)$. Finally, we require that the solution diverges at $\boldsymbol{x}_2$ similarly to the divergence of $\boldsymbol{u}(\boldsymbol{x} - \boldsymbol{x}_2)$ in Eqs. (3.7) or (3.8), i.e. that the difference between the solution and the free-space singularity remains bounded.

3.2.3 Method of solution

Fundamentally, in each case the solution may be written as

$$\boldsymbol{u} = \boldsymbol{u}_0 + \boldsymbol{u}_*, \tag{3.11}$$

where $\boldsymbol{u}_0$ is the flow due to the free-space singularities as in Eqs. (3.7) or (3.8) and $\boldsymbol{u}_*$ is an image flow field that corrects for the boundary condition on the sphere surface and is therefore non-singular everywhere in the fluid domain. In previous work [72, 73] (see also the summary

in Ref. [127]), $\boldsymbol{u}_*$ was derived for the Stokeslet by writing $\boldsymbol{u}_0$ in terms of spherical harmonics about $\boldsymbol{x}_1$, expanding the image system $\boldsymbol{u}_*$ as a multipole series about $\boldsymbol{x}_1$ also written in terms of spherical harmonics, and matching five infinite families of coefficients. The singularity solution is then obtained from the multipole expansion by postulating the equivalence to a line integral of finite-order singularities from $\boldsymbol{x}_1$ to $\boldsymbol{x}_2^*$ and again matching coefficients through the exploitation of a number of integral identities.

For the force dipole singularity, the literature only provides the multipole expansions of the image flow for (i) $(\boldsymbol{e}\cdot\boldsymbol{\nabla})\boldsymbol{d}\cdot\boldsymbol{G}(\boldsymbol{x}-\boldsymbol{x}_2)$, which is the difference between two axisymmetric Stokeslets with the difference taken in a line orthogonal to the line of centres, (ii) the image flow for $(\boldsymbol{d}\cdot\boldsymbol{\nabla})\boldsymbol{e}\cdot\boldsymbol{G}(\boldsymbol{x}-\boldsymbol{x}_2)$, which is the difference between two transverse Stokeslets with the difference taken in a line away from the sphere centre, and (iii) the image flow for $(\boldsymbol{f}\cdot\boldsymbol{\nabla})\boldsymbol{e}\cdot\boldsymbol{G}(\boldsymbol{x}-\boldsymbol{x}_2)$, which is the difference between two transverse Stokeslets with the difference taken in a line orthogonal to the line of centres and the line from the sphere centre.

While the expressions for the singularity dipoles are equivalent up to a permutation of the vectors $\{\boldsymbol{d},\boldsymbol{e},\boldsymbol{f}\}$, the image flow depends on the direction in which gradients are taken, since the images all lie on the axis between $\boldsymbol{x}_1$ and $\boldsymbol{x}_2$, and perturbations in the $\boldsymbol{e}$-$\boldsymbol{f}$ plane change the direction of this axis. Despite the presence of some typographical errors in the derivations, we have verified the correctness of the relevant expressions given in Ref. [127] and take these as the starting point of our calculation for the rotlet. By linearity of the Stokes equations, a general rotlet may be decomposed into an axisymmetric (parallel to $\boldsymbol{d}$) and transverse (in the $\boldsymbol{e}-\boldsymbol{f}$ plane) component, so without loss of generality we tackle these separately in §3.3 and §3.4 respectively. For the source, we derive the solution from first principles in §3.5.

3.3 The axisymmetric rotlet

3.3.1 No-slip boundary condition (rigid sphere)

Derivation

From the summary in Ref. [127] we quote the image for the dipole $(\boldsymbol{f}\cdot\boldsymbol{\nabla})\boldsymbol{e}\cdot\boldsymbol{G}(\boldsymbol{x}-\boldsymbol{x}_2)$, which can be written in terms of a multipole expansion as

$$\begin{aligned}\boldsymbol{u}_* = &\sum_{n=0}^{\infty}\frac{D^n}{n!}(A_n+B_n\nabla^2)(\boldsymbol{f}\cdot\boldsymbol{\nabla})\boldsymbol{e}\cdot\boldsymbol{G}(\boldsymbol{x}-\boldsymbol{x}_1)\\ &+\sum_{n=0}^{\infty}\frac{D^n}{8\pi\mu n!}\left[C_n(\boldsymbol{e}\times\boldsymbol{f})+C_{n+1}(\boldsymbol{f}\cdot\boldsymbol{\nabla})(\boldsymbol{e}\times\boldsymbol{d})\right]\times\boldsymbol{\nabla}r^{-1},\end{aligned}\tag{3.12}$$

where

$$A_n = \frac{n(2n+5)}{2(n+3)}R^{-(n+3)} - \frac{(n+2)(2n+3)}{2(n+3)}R^{-(n+5)}, \tag{3.13a}$$

$$B_n = \frac{n}{4(n+3)}R^{-(n+3)} - \frac{n^2+5n+3}{2(n+3)(n+5)}R^{-(n+5)} + \frac{n+2}{4(n+5)}R^{-(n+7)}, \tag{3.13b}$$

$$C_n = \frac{2n+3}{n+3}R^{-(n+3)} - \frac{2n+3}{n+3}R^{-(n+5)}. \tag{3.13c}$$

In order to obtain from this the image field of an axisymmetric dipole, we need to anti-symmetrise this expression in the vectors $\boldsymbol{e}$ and $\boldsymbol{f}$. Defining $S_{jk} = (e_k f_j - e_j f_k)/2$ and noting that $\boldsymbol{e} \times \boldsymbol{f} = -\boldsymbol{d}$ we hence have the multipole expansion

$$[\boldsymbol{u}_*]_i = g\sum_{n=0}^{\infty}\frac{D^n}{n!}A_n S_{jk}\nabla_k G_{ij} + \frac{D^n}{8\pi\mu n!}\left[C_n d_a + C_{n+1}S_{jb}\nabla_b\varepsilon_{ajl}d_l\right]\varepsilon_{iak}\nabla_k r^{-1}, \tag{3.14}$$

for the image of an axisymmetric rotlet with $\boldsymbol{g} = g\boldsymbol{d}$. We note that the terms proportional to $\nabla^2\nabla_k G_{ij}$ have disappeared since they are symmetric in $\{i, j, k\}$. In addition we can exploit the identities $S_{jk}\nabla_k G_{ij} = 2S_{ik}\nabla_k r^{-1}$ and $2S_{jk} = d_a\varepsilon_{ajk}$ to simplify this result further and obtain an expression just in terms of derivatives of $\boldsymbol{\nabla} r^{-1}$ as

$$[\boldsymbol{u}_*]_i = g\sum_{n=0}^{\infty}\frac{D^n}{8\pi\mu n!}\left[(C_n - A_n)d_a + \frac{1}{2}C_{n+1}\varepsilon_{ajl}\varepsilon_{cjb}d_c d_l\nabla_b\right]\varepsilon_{iak}\nabla_k r^{-1}. \tag{3.15}$$

Noting that $\boldsymbol{d}\cdot\boldsymbol{d} = 1$ and $\boldsymbol{\nabla}\times\boldsymbol{\nabla} = \boldsymbol{0}$, this can be written more elegantly as

$$\boldsymbol{u}_* = \boldsymbol{g}\times\sum_{n=0}^{\infty}\frac{D^n}{8\pi\mu n!}\alpha_n\boldsymbol{\nabla} r^{-1} \tag{3.16}$$

where

$$\alpha_n = \frac{n+2}{2}C_n - A_n = R^{-n-3}. \tag{3.17}$$

The goal of this calculation is then to replace the infinite sum of higher order singularities at the point $\boldsymbol{x}_1$ in Eq. (3.16) by a line integral of lower order singularities between $\boldsymbol{x}_1$ and $\boldsymbol{x}_2^*$. Specifically, we seek a solution of the form

$$\boldsymbol{u}_* = \frac{\boldsymbol{g}}{8\pi\mu}\times\int_0^{R^{-1}} f(\xi)\boldsymbol{\nabla}\frac{1}{\tilde{r}}\,\mathrm{d}\xi, \tag{3.18}$$

where $\tilde{r} = |\boldsymbol{x} - \boldsymbol{\xi}|$ and $\boldsymbol{\xi} = -\xi \boldsymbol{d}$. Here the upper limit of the integrals is to be understood as $R^{-1} + \varepsilon$ where $\varepsilon > 0$ is infinitesimally small and f and g as identically zero for $\xi > R^{-1}$. As a consequence we have the identities

$$\int_0^{R^{-1}} \delta(\xi - R^{-1}) \xi^n \, \mathrm{d}\xi = R^{-n}, \tag{3.19}$$

$$\int_0^{R^{-1}} \delta'(\xi - R^{-1}) \xi^n \, \mathrm{d}\xi = -nR^{-(n-1)}, \tag{3.20}$$

$$\int_0^{R^{-1}} \xi^{k-1} \xi^n \, \mathrm{d}\xi = \frac{R^{-(n+k)}}{n+k}. \tag{3.21}$$

These are useful when combined with the Taylor series of the singularities about $\boldsymbol{x}_1$,

$$\boldsymbol{\nabla} \frac{1}{\tilde{r}} = \sum_{n=0}^{\infty} \xi^n \frac{D^n}{n!} \boldsymbol{\nabla} \frac{1}{r}, \tag{3.22}$$

because this gives

$$\alpha_n = \int_0^{R^{-1}} f(\xi) \xi^n \, \mathrm{d}\xi. \tag{3.23}$$

In this particular case, the relationship is straightforward and we have

$$f(\xi) = R^{-3} \delta(\xi - R^{-1}), \tag{3.24}$$

and so the flow is simply given by

$$\boldsymbol{u} = \frac{\boldsymbol{g}}{8\pi\mu} \times \left[-\boldsymbol{\nabla} \frac{1}{r_2} + R^{-3} \boldsymbol{\nabla} \frac{1}{r_*} \right], \tag{3.25}$$

where, as a reminder, the axisymmetric torque is defined by $\boldsymbol{g} = g\boldsymbol{d}$ and located at $\boldsymbol{x}_2$. It is straightforward to verify that this expression satisfies the boundary condition in Eq. (3.9).

Interpretation

Our results show that, similar to the case of a rigid wall [23], the image of the rotlet consists of just a single other rotlet, in this case with its strength modified by a factor of $-R^{-3}$. Since there is no Stokeslet response in the image, there is no net force exerted on the boundary in either case. However, the presence of a rotlet image response may be interpreted as due to a non-zero torque that needs to be applied to the sphere to remain stationary. Indeed, the torque exerted by

the rotlet on the sphere is given by

$$\boldsymbol{T}_{\text{rigid}}^{\text{rotlet, axisym}} = \alpha_0 \boldsymbol{g} = \frac{1}{R^3}\boldsymbol{g}. \tag{3.26}$$

An illustration of the flow field induced by the axisymmetric rotlet outside the sphere is shown in Fig. 3.2a. We consider a rotlet with $\boldsymbol{g} = \boldsymbol{d}$ with $R = 3/2$ and use colour to visualise the magnitude of the flow, with dark blue indicating weak and bright yellow indicating strong flow. The structure of the solution is reminiscent of the well known problem for the electrostatic potential due to a point charge outside a conducting sphere. In that case, the potential solves Laplace's equation, whose fundamental solution is proportional to $1/r_2$. This differs from the solution to the azimuthal component of the Stokes equations which is proportional to ρ/r_2^3. In both cases, however, the simplicity of the image system may be understood with the help of a geometric argument. Specifically, the image point $\boldsymbol{x}_2^*$ is defined in a way that the ratio r_*/r_2 is constant on the sphere surface, which may thus be interpreted as the surface of revolution of an Apollonian circle defined by $\boldsymbol{x}_2$ and $\boldsymbol{x}_2^*$. In the case of electrostatic charges, it is then immediate from this that the strength of the image charge may be chosen to meet an equipotential boundary condition on the sphere surface. In the case of the rotlet, this is only possible because ρ is the same for both the singularity and its image. However, we stress that the simple form of Eq. 3.25 is not to be expected *a priori* from the complexity of the image systems required to match the no-slip condition in many geometries. In fact, usually a free surface boundary condition leads to a simpler image system than a rigid boundary, though as we will show in §3.3.2 this is not the case here.

A further implication of our results is that the equivalent solution for an axisymmetric rotlet inside a sphere ($R < 1$) may also be expressed by a single image singularity. The flow obtained in that case is illustrated in Fig. 3.2b. The general case of an arbitrary rotlet inside a rigid spherical shell has been studied before using flow potentials [92, 98], although this simple formulation for the axisymmetric case had not been identified.

3.3.2 No tangential stress boundary condition (spherical bubble)

In order to derive the solution for an axisymmetric rotlet outside a bubble, we follow a similar procedure to the one presented in §3.3.1. The structure of the solution is the same, but due to the different boundary conditions on the sphere surface, Eq. (3.10), the values of the coefficients A_n, B_n and C_n are different. Using expressions for the multipole expansions for Stokeslets outside a bubble listed in Ref. [127], it is possible to show that the dipole $(\boldsymbol{f}\cdot\boldsymbol{\nabla})\boldsymbol{e}\cdot\boldsymbol{G}(\boldsymbol{x}-\boldsymbol{x}_2)$

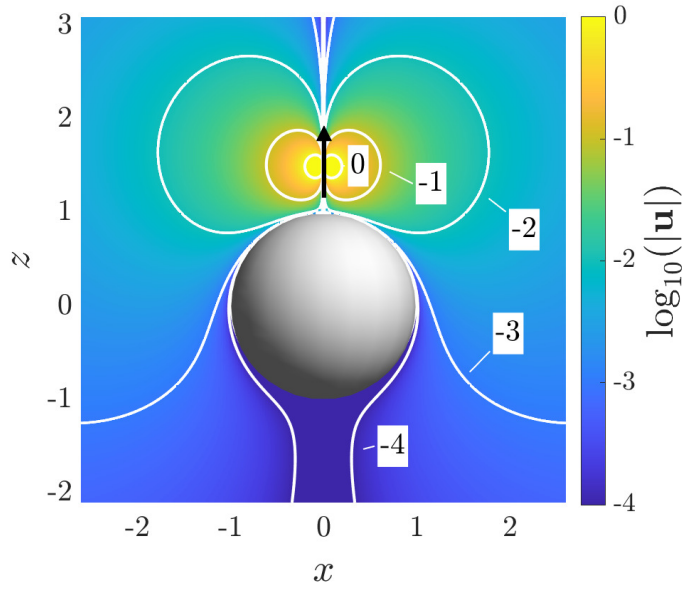

(a) Outside a rigid sphere

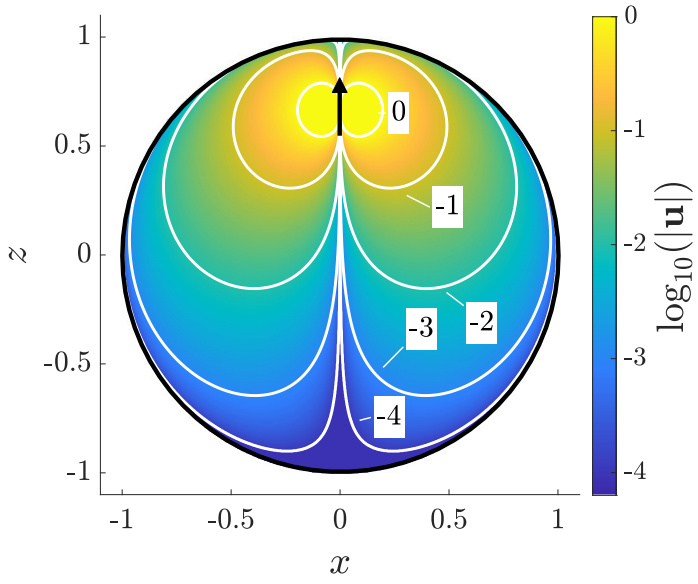

(b) Inside a spherical shell

Figure 3.2 Logarithmic magnitude of the flow due to an axisymmetric rotlet in a Cartesian coordinate system with a rigid unit sphere at its origin and $\boldsymbol{g} = \hat{\boldsymbol{z}}$. In (a) the rotlet is positioned outside the sphere at $\boldsymbol{x}_2 = \frac{3}{2}\hat{\boldsymbol{z}}$, while in (b) it is located inside the sphere at $\boldsymbol{x}_2 = \frac{2}{3}\hat{\boldsymbol{z}}$. At each point, the flow is directed azimuthally around the z-axis. Bright yellow indicates regions of strong flow and dark blue regions of weak flow, while white contours are labelled with the order of magnitude of the flow. Black arrows indicate the position and orientation of the rotlet.

has the image

$$\boldsymbol{u}_* = \sum_{n=0}^{\infty} \frac{D^n}{n!} A_n (\boldsymbol{f} \cdot \boldsymbol{\nabla}) \boldsymbol{e} \cdot \boldsymbol{G}(\boldsymbol{x} - \boldsymbol{x}_1), \tag{3.27}$$

where

$$A_n = \frac{n}{n+3} R^{-n-3}. \tag{3.28}$$

From this, it is straightforward to obtain

$$\alpha_n = -A_n = -R^{-3} R^{-n} + 3 \frac{R^{-(n+3)}}{n+3}, \tag{3.29}$$

and following the same replacement rules as before we have

$$f(\xi) = -R^{-3} \delta(\xi - R^{-1}) + 3\xi^2. \tag{3.30}$$

The flow field due to an axisymmetric rotlet $\boldsymbol{g} = g\boldsymbol{d}$ outside a spherical bubble is therefore given by

$$\boldsymbol{u} = \frac{\boldsymbol{g}}{8\pi\mu} \times \left[-\boldsymbol{\nabla} \frac{1}{r_2} - R^{-3} \boldsymbol{\nabla} \frac{1}{r_*} + \int_0^{R^{-1}} 3\xi^2 \boldsymbol{\nabla} \frac{1}{\tilde{r}} \, \mathrm{d}\xi \right], \tag{3.31}$$

corresponding to a point image rotlet and a line of image rotlets.

An illustration of the flow field obtained in this case is shown in Fig. 3.3. Surprisingly, its mathematical structure is more complex than in the case of a rigid boundary, which is unusual for boundary value problems in Stokes flow. Indeed, the much simpler form of the multipole expansion would suggest a simple image system, but this is not the case because of the substantial cancellation that occurs in the rigid case. The simplicity of the earlier result is a non-trivial consequence of the geometry, boundary condition and structure of the rotlet flow.

It may furthermore be verified that the bubble does not experience a torque due to the axisymmetric rotlet, as expected from the boundary condition of zero tangential stress, Eq. (3.10a). Indeed, the leading-order term in the multipole expansion, α_0, is equal to zero and so

$$\boldsymbol{T}_{\text{bubble}}^{\text{rotlet, axisym}} = \boldsymbol{0}, \tag{3.32}$$

as required.

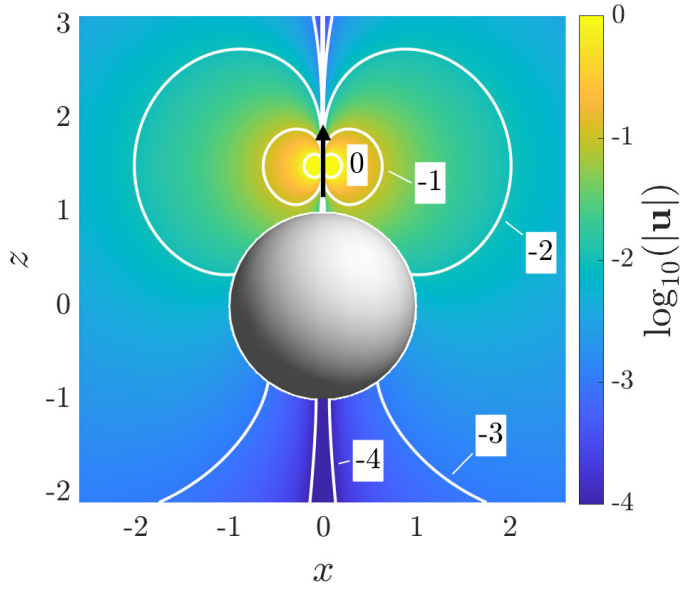

Figure 3.3 Logarithmic magnitude of the flow due to an axisymmetric rotlet in a Cartesian coordinate system outside a spherical bubble at its origin, $\boldsymbol{g} = \hat{\boldsymbol{z}}$ and $\boldsymbol{x}_2 = \frac{3}{2}\hat{\boldsymbol{z}}$. At each point the flow is directed azimuthally around the z-axis. Bright yellow indicates regions of strong flow and dark blue regions of weak flow, while white contours are labelled with the order of magnitude of the flow. A black arrow indicate the position and orientation of the rotlet.

3.4 The transverse rotlet

3.4.1 No-slip boundary condition (rigid sphere)

Derivation

As might be expected from the broken symmetry, the relevant expressions for the case of a transverse rotlet, i.e. one such that $\boldsymbol{g} \cdot \boldsymbol{d} = 0$, are more tedious. Once again we quote the image flow for the dipole $(\boldsymbol{e} \cdot \boldsymbol{\nabla})\boldsymbol{d} \cdot \boldsymbol{G}(\boldsymbol{x} - \boldsymbol{x}_2)$ from Ref. [127] as

$$\boldsymbol{u}_* = \sum_{n=0}^{\infty} \frac{D^n}{n!} \left[(\hat{A}_n + \hat{B}_n \nabla^2)\boldsymbol{e} \cdot \boldsymbol{G}(\boldsymbol{x} - \boldsymbol{x}_1) + \frac{\hat{C}_n}{8\pi\mu} \boldsymbol{f} \times \boldsymbol{\nabla} r^{-1} \right], \tag{3.33}$$

and for the dipole $(\boldsymbol{d} \cdot \boldsymbol{\nabla})\boldsymbol{e} \cdot \boldsymbol{G}(\boldsymbol{x} - \boldsymbol{x}_1)$ as

$$\boldsymbol{u}_* = \sum_{n=0}^{\infty} \frac{D^n}{n!} \left[(\tilde{A}_n + \tilde{B}_n \nabla^2)\boldsymbol{e} \cdot \boldsymbol{G}(\boldsymbol{x} - \boldsymbol{x}_2) + \frac{\tilde{C}_n}{8\pi\mu} \boldsymbol{f} \times \boldsymbol{\nabla} r^{-1} \right], \tag{3.34}$$

where the six families of coefficients are given by

$$\hat{A}_n = \frac{\left(2n^3+9n^2+10n+3\right)}{2(n+2)}R^{-(n+4)} - \frac{\left(2n^3+11n^2+14n+3\right)}{2(n+2)}R^{-(n+2)}, \tag{3.35a}$$

$$\tilde{A}_n = \frac{\left(2n^3+9n^2+10n+3\right)}{2(n+2)}R^{-(n+4)} - \frac{\left(2n^3+3n^2-2n-3\right)}{2(n+2)}R^{-(n+2)}, \tag{3.35b}$$

$$\hat{B}_n = -\frac{\left(n^2+6n+5\right)}{4(n+4)}R^{-(n+6)} + \frac{\left(n^3+8n^2+17n+7\right)}{2(n+2)(n+4)}R^{-(n+4)} - \frac{\left(n^2+4n+1\right)}{4(n+2)}R^{-(n+2)}, \tag{3.35c}$$

$$\tilde{B}_n = -\frac{\left(n^2+6n+5\right)}{4(n+4)}R^{-(n+6)} + \frac{\left(n^3+6n^2+8n-3\right)}{2(n+2)(n+4)}R^{-(n+4)} - \frac{\left(n^2-1\right)}{4(n+2)}R^{-(n+2)}, \tag{3.35d}$$

$$\hat{C}_n = \frac{\left(2n^2+11n+12\right)}{n+3}R^{-(n+5)} - \frac{\left(2n^2+13n+18\right)}{n+3}R^{-(n+3)}, \tag{3.35e}$$

$$\tilde{C}_n = \frac{\left(2n^2+11n+12\right)}{n+3}R^{-(n+5)} - \frac{\left(2n^2+7n+6\right)}{n+3}R^{-(n+3)}. \tag{3.35f}$$

For the antisymmetric dipole defined by $\frac{1}{2}g\left[(\boldsymbol{d}\cdot\boldsymbol{\nabla})\boldsymbol{e}-(\boldsymbol{e}\cdot\boldsymbol{\nabla})\boldsymbol{d}\right]\cdot\boldsymbol{G}$, corresponding to a rotlet with $\boldsymbol{g}=g\boldsymbol{f}$, we thus obtain that the image flow is given by

$$\boldsymbol{u}_* = g\sum_{n=0}^{\infty}\frac{D^n}{n!}\left[(\alpha_n+\beta_n\nabla^2)\boldsymbol{e}\cdot\boldsymbol{G}(\boldsymbol{x}-\boldsymbol{x}_1)+\frac{\gamma_n}{8\pi\mu}\boldsymbol{f}\times\boldsymbol{\nabla}r^{-1}\right], \tag{3.36}$$

where the coefficients simplify to

$$\alpha_n = \frac{1}{2}\left(\tilde{A}_n-\hat{A}_n\right) = 2R^{-3}nR^{-(n-1)} + \frac{3}{2}\frac{R^{-(n+2)}}{n+2}, \tag{3.37a}$$

$$\beta_n = \frac{1}{2}\left(\tilde{B}_n-\hat{B}_n\right) = -\frac{1}{2}\left(R^{-4}-R^{-2}\right)R^{-n} - \frac{3}{4}\frac{R^{-(n+2)}}{n+2} + \frac{3}{4}\frac{R^{-(n+4)}}{n+4}, \tag{3.37b}$$

$$\gamma_n = \frac{1}{2}\left(\tilde{C}_n-\hat{C}_n\right) = 3R^{-3}R^{-n} - 3\frac{R^{-(n+3)}}{n+3}. \tag{3.37c}$$

In analogy with the axisymmetric case, we next want to write the solution as

$$\boldsymbol{u}_* = g\int_0^{R^{-1}}(f(\xi)+g(\xi)\nabla^2)\boldsymbol{e}\cdot\boldsymbol{G}(\boldsymbol{x}-\boldsymbol{\xi})+\frac{h(\xi)}{8\pi\mu}\boldsymbol{f}\times\boldsymbol{\nabla}\tilde{r}^{-1}\,\mathrm{d}\xi, \tag{3.38}$$

which, in this case, requires that

$$\alpha_n = \int_0^{R^{-1}} f(\xi)\xi^n \,\mathrm{d}\xi, \tag{3.39a}$$

$$\beta_n = \int_0^{R^{-1}} g(\xi)\xi^n \,\mathrm{d}\xi, \tag{3.39b}$$

$$\gamma_n = \int_0^{R^{-1}} h(\xi)\xi^n \,\mathrm{d}\xi. \tag{3.39c}$$

Thus, using again the identities in Eqs. (3.19)-(3.21), we find that

$$f(\xi) = -2R^{-3}\delta'(\xi - R^{-1}) + \frac{3}{2}\xi, \tag{3.40a}$$

$$g(\xi) = -\frac{1}{2}\left(R^{-4} - R^{-2}\right)\delta(\xi - R^{-1}) - \frac{3}{4}(\xi - \xi^3), \tag{3.40b}$$

$$h(\xi) = 3R^{-3}\delta(\xi - R^{-1}) - 3\xi^2, \tag{3.40c}$$

and so

$$\begin{aligned}\boldsymbol{u}_* = g\Bigg(&2R^{-3}D\boldsymbol{e}\cdot\boldsymbol{G}(\boldsymbol{x}-\boldsymbol{x}_2^*) - \frac{1}{2}\left(R^{-4}-R^{-2}\right)\boldsymbol{e}\cdot\nabla^2\boldsymbol{G}(\boldsymbol{x}-\boldsymbol{x}_2^*) + \frac{3R^{-3}}{8\pi\mu}\boldsymbol{f}\times\boldsymbol{\nabla}r_*^{-1} \\ &+ \int_0^{R^{-1}}\left(\frac{3}{2}\xi - \frac{3}{4}(\xi-\xi^3)\nabla^2\right)\boldsymbol{e}\cdot\boldsymbol{G}(\boldsymbol{x}-\boldsymbol{\xi}) - \frac{3\xi^2}{8\pi\mu}\boldsymbol{f}\times\boldsymbol{\nabla}\tilde{r}^{-1}\,\mathrm{d}\xi\Bigg).\end{aligned} \tag{3.41}$$

Finally, we eliminate $\boldsymbol{e}$ by replacing it with $-\boldsymbol{f}\times\boldsymbol{d}$ to obtain an expression that is linear in the rotlet strength $\boldsymbol{g}$. For a general rotlet in the $\boldsymbol{e}$-$\boldsymbol{f}$ plane we can therefore write the flow field as

$$\begin{aligned}\boldsymbol{u} = &\frac{1}{8\pi\mu}\left[-\boldsymbol{g}\times\boldsymbol{\nabla}\frac{1}{r_2} + 3R^{-3}\boldsymbol{g}\times\boldsymbol{\nabla}\frac{1}{r_*}\right] \\ &+ (\boldsymbol{g}\times\boldsymbol{d})\cdot\left(\frac{1}{2}(R^{-4}-R^{-2})\nabla^2 - 2R^{-3}(\boldsymbol{d}\cdot\boldsymbol{\nabla})\right)\boldsymbol{G}(\boldsymbol{x}-\boldsymbol{x}_2^*) \\ &- (\boldsymbol{g}\times\boldsymbol{d})\cdot\int_0^{R^{-1}}\left(\frac{3}{2}\xi - \frac{3}{4}(\xi-\xi^3)\nabla^2\right)\boldsymbol{G}(\boldsymbol{x}-\boldsymbol{\xi})\,\mathrm{d}\xi \\ &- \frac{\boldsymbol{g}}{8\pi\mu}\times\int_0^{R^{-1}} 3\xi^2\boldsymbol{\nabla}\frac{1}{\tilde{r}}\,\mathrm{d}\xi.\end{aligned} \tag{3.42}$$

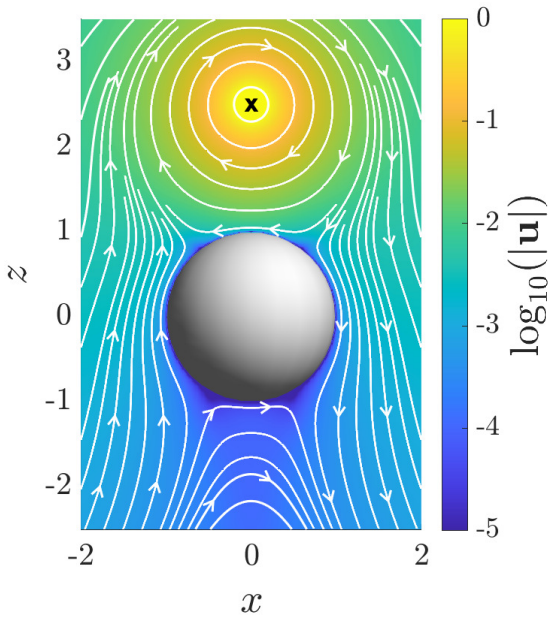

(a) $R = 2.5$

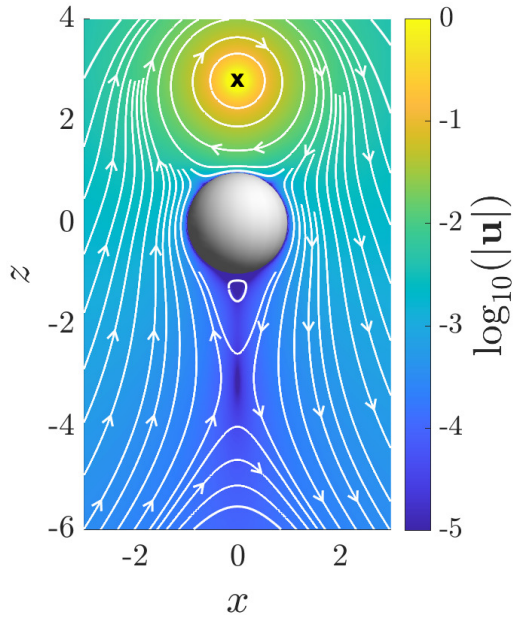

(b) $R = 2.8$

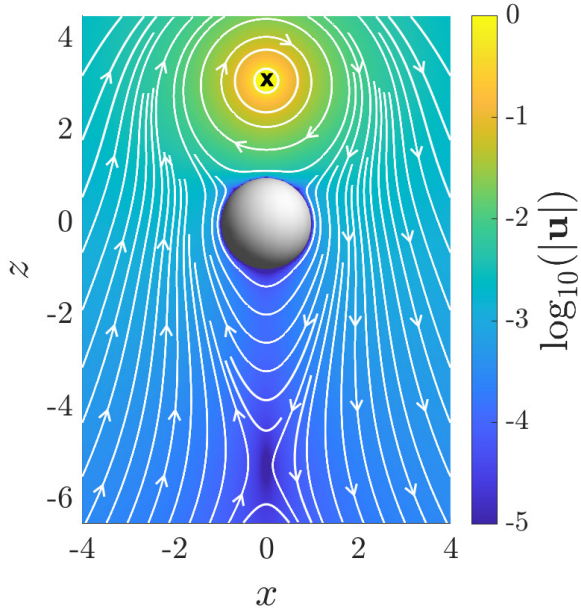

(c) $R = 3.1$

Figure 3.4 Flow field in the x-z plane due to a transverse rotlet with $\boldsymbol{g} = \hat{\boldsymbol{y}}$ located at $\boldsymbol{x}_2 = R\hat{\boldsymbol{z}}$ outside a rigid unit sphere centred at the origin. Streamlines are drawn in white and the logarithm of the flow magnitude is superposed in colour while black crosses indicate the position of the rotlet, pointing into the page. The flow undergoes two bifurcations as R increases, occurring at $R \approx 2.71$ and $R = 3$, between which a counter-rotating vortex appears on the far side of the sphere.

Interpretation

Evidently, the image system for the transverse rotlet is significantly more complicated than in the axisymmetric case. It is composed of three point singularities at $\boldsymbol{x}_2^*$, namely a rotlet, a source dipole and a stresslet, as well as a line of three different singularities from $\boldsymbol{x}_1$ to $\boldsymbol{x}_2^*$: Stokeslets, source dipoles and rotlets. However, the integrals are nowhere singular and therefore can be readily evaluated by standard numerical routines.

Three representative illustrations of the flow field are given in Fig. 3.4. In contrast to the axisymmetric case, we observe two bifurcation points of the flow field as R is varied, occuring at $R \approx 2.71$ and $R = 3$. Between these a counter-rotating vortex appears on the far side of the sphere, which is analysed in detail in Ref. [207] using a solution obtained with the use of flow potentials and sphere theorems. Interestingly, the far-field flow on the far side of the sphere is always in the direction opposite what is expected from a free rotlet. This is due to the Stokeslet response that appears in Eq. (3.42), which dominates over the original rotlet singularity due to its slower decay. Physically, this arises because a non-zero force needs to be exerted on the sphere in order to keep it stationary, and its slower decay dominates at long distances. The force and torque exerted by the rotlet on the sphere can be calculated from our solution. They are given by the coefficients α_0, α_1 and γ_0 in Eq. (3.37) as

$$\boldsymbol{F}_{\text{rigid}}^{\text{rotlet, transverse}} = \alpha_0 \boldsymbol{g} \times \boldsymbol{d} = \frac{3}{4R^2} \boldsymbol{g} \times \boldsymbol{d}, \tag{3.43}$$

$$\boldsymbol{T}_{\text{rigid}}^{\text{rotlet, transverse}} = (\gamma_0 - \alpha_1)\boldsymbol{g} = -\frac{1}{2R^3} \boldsymbol{g}, \tag{3.44}$$

both of which are consistent with the application of Faxén's law to a sphere in the background flow $\boldsymbol{u}_0$ [127].

3.4.2 No tangential stress boundary condition (spherical bubble)

In the case of a spherical bubble, we have a no-tangential-stress as well as a no-penetration boundary condition on the surface of the sphere, see Eq. (3.10). Using multipole expansions for the axisymmetric and transverse Stokeslet listed in Ref. [127], we obtain the image field for the dipole $(\boldsymbol{e} \cdot \boldsymbol{\nabla})\boldsymbol{d} \cdot \boldsymbol{G}(\boldsymbol{x} - \boldsymbol{x}_2)$ as

$$\boldsymbol{u}_* = \sum_{n=0}^{\infty} \frac{D^n}{n!} \left[\hat{A}_n \boldsymbol{e} \cdot \boldsymbol{G}(\boldsymbol{x} - \boldsymbol{x}_1) + \frac{\hat{C}_n}{8\pi\mu} \boldsymbol{f} \times \boldsymbol{\nabla} \frac{1}{r} \right], \tag{3.45}$$

and the image field for the dipole $(\boldsymbol{d}\cdot\boldsymbol{\nabla})\boldsymbol{e}\cdot\boldsymbol{G}(\boldsymbol{x}-\boldsymbol{x}_2)$ as

$$\boldsymbol{u}_* = \sum_{n=0}^{\infty}\frac{D^n}{n!}\tilde{A}_n\boldsymbol{e}\cdot\boldsymbol{G}(\boldsymbol{x}-\boldsymbol{x}_1), \tag{3.46}$$

where

$$\hat{A}_n = -\frac{n^2+4n+1}{n+2}R^{-n-2}, \tag{3.47a}$$
$$\hat{C}_n = -2R^{-n-3}, \tag{3.47b}$$
$$\tilde{A}_n = -\frac{n^2-1}{n+2}R^{-n-2}. \tag{3.47c}$$

In a familiar fashion we hence obtain the image for $\boldsymbol{g}=g\boldsymbol{f}$ as

$$\boldsymbol{u}_* = g\sum_{n=0}^{\infty}\frac{D^n}{n!}\left[\alpha_n\boldsymbol{e}\cdot\boldsymbol{G}(\boldsymbol{x}-\boldsymbol{x}_1)+\frac{\gamma_n}{8\pi\mu}\boldsymbol{f}\times\boldsymbol{\nabla}r^{-1}\right], \tag{3.48}$$

where

$$\alpha_n = \frac{1}{2}\left(\tilde{A}_n-\hat{A}_n\right) = 2R^{-2}R^{-n}-3\frac{R^{-(n+2)}}{n+2}, \tag{3.49a}$$
$$\gamma_n = -\frac{1}{2}\hat{C}_n = R^{-3}R^{-n}. \tag{3.49b}$$

Using the same replacement rules as in Eqs. (3.19)-(3.21), we can write the flow due to a transverse rotlet outside a bubble as

$$\begin{aligned}\boldsymbol{u} = \frac{1}{8\pi\mu}&\left[-\boldsymbol{g}\times\boldsymbol{\nabla}\frac{1}{r_2}+R^{-3}\boldsymbol{g}\times\boldsymbol{\nabla}\frac{1}{r_*}\right]-(\boldsymbol{g}\times\boldsymbol{d})\cdot 2R^{-2}\boldsymbol{G}(\boldsymbol{x}-\boldsymbol{x}_2^*)\\ &+(\boldsymbol{g}\times\boldsymbol{d})\cdot\int_0^{R^{-1}}3\xi\boldsymbol{G}\left(\boldsymbol{x}-\boldsymbol{\xi}\right)\,\mathrm{d}\xi,\end{aligned} \tag{3.50}$$

which may be interpreted as due to a point image rotlet, a point image Stokeslet and a line of Stokeslets.

An illustration of the flow is given in Fig. 3.5. In this case there is only a single bifurcation, which occurs as R increases to $R\approx 1.77$, where a saddle point appears on the far side of the bubble. Since the bubble surface cannot sustain any tangential stress, no counter-rotating vortex

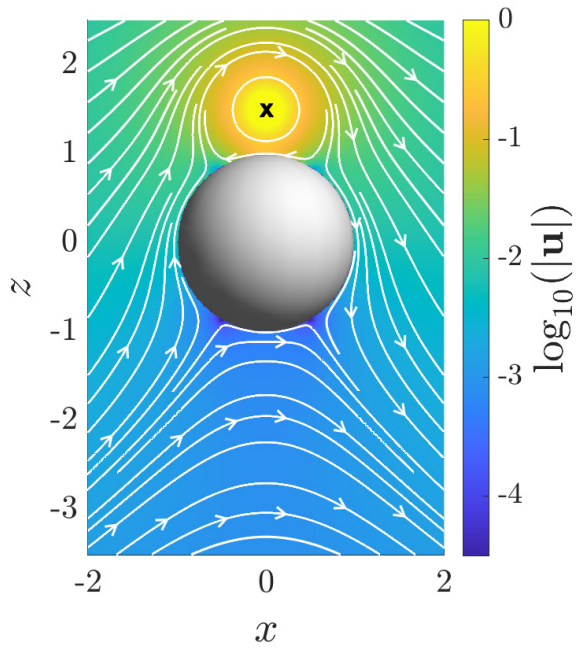

(a) $R = 1.5$

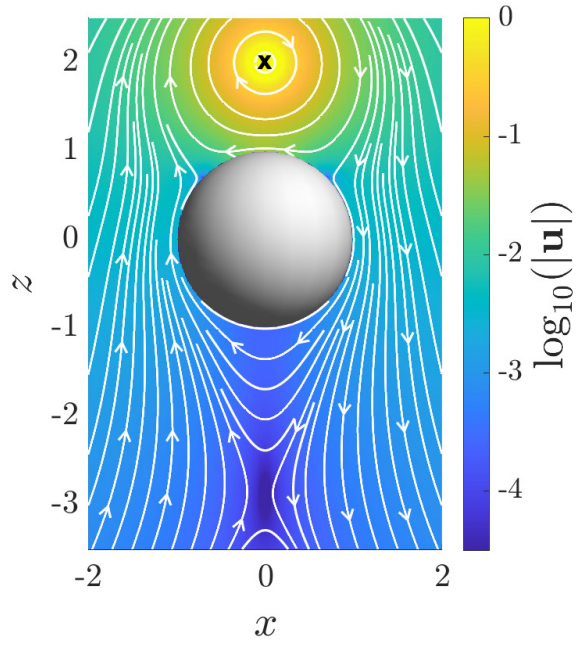

(b) $R = 2$

Figure 3.5 Flow field in the x-z plane due to a transverse rotlet with $\boldsymbol{g} = \hat{\boldsymbol{y}}$ located at $\boldsymbol{x}_2 = R\hat{\boldsymbol{z}}$ outside a spherical bubble at the origin. Streamlines are drawn in white and the logarithm of the flow magnitude is superposed in colour with black crosses indicating the position of the rotlet, pointing into the page. The flow undergoes one bifurcation at $R \approx 1.77$ as R increases where a saddle point appears on the far side of the sphere.

emerges. Using the coefficients from Eq. (3.49), the force and torque on the bubble are given by

$$\boldsymbol{F}_{\text{bubble}}^{\text{rotlet, transverse}} = \alpha_0 \boldsymbol{g} \times \boldsymbol{d} = \frac{1}{2R^2} \boldsymbol{g} \times \boldsymbol{d}, \tag{3.51}$$

$$\boldsymbol{T}_{\text{bubble}}^{\text{rotlet, transverse}} = (\gamma_0 - \alpha_1)\boldsymbol{g} = \boldsymbol{0}, \tag{3.52}$$

where the latter was expected to be zero due to the no-stress boundary condition. This result is consistent with the generalisation of Faxén's law to a spherical bubble [192].

3.5 The point source

3.5.1 The multipole expansion for a source

We now turn our attention to the problem involving a source (or sink). In this case there is no intermediate result that we can quote from the literature, and we need to start the derivation from first principles. The flow due to a free space point source of strength Q located at $\boldsymbol{x}_2$ is

$$\boldsymbol{u}_0 = -\frac{Q}{4\pi} \boldsymbol{\nabla} \frac{1}{r_2} = \frac{Q}{4\pi r_2^3} \boldsymbol{r}_2. \tag{3.53}$$

Since $1/r$ is the fundamental solution to Laplace's equation, we can write $\boldsymbol{u}_0$ as a series of spherical harmonics about $\boldsymbol{x}_1$. Specifically, since we have the identity

$$\frac{D^n}{n!} \frac{1}{r} = \frac{P_n(-\boldsymbol{d} \cdot \hat{\boldsymbol{r}})}{r^{n+1}}, \tag{3.54}$$

where P_n is the nth Legendre polynomial, we can write

$$\frac{1}{r_2} = \sum_{n=0}^{\infty} \frac{r^{2n+1}}{R^{n+1}} \frac{D^n}{n!} \frac{1}{r}, \tag{3.55}$$

and therefore

$$\begin{aligned} \boldsymbol{u}_0 &= -\frac{Q}{4\pi} \boldsymbol{\nabla} \frac{1}{r_2} = \frac{Q}{4\pi} \sum_{n=0}^{\infty} -\boldsymbol{\nabla} \left[\frac{r^{2n+1}}{R^{n+1}} \frac{D^n}{n!} \frac{1}{r} \right] \\ &= \frac{Q}{4\pi} \sum_{n=0}^{\infty} \frac{r^{2n-1}}{R^{n+1}} \left[-(2n+1)(\boldsymbol{x} - \boldsymbol{x}_1) - r^2 \boldsymbol{\nabla} \right] \frac{D^n}{n!} \frac{1}{r}. \end{aligned} \tag{3.56}$$

Furthermore, due to the axisymmetry of the flow field, the multipole expansion of the image field must take the form

$$\boldsymbol{u}_* = 2\mu Q \sum_{n=0}^{\infty} \frac{D^n}{n!} \left[A_n \boldsymbol{d} \cdot \boldsymbol{G}(\boldsymbol{x} - \boldsymbol{x}_1) + B_n \boldsymbol{d} \cdot \nabla^2 \boldsymbol{G}(\boldsymbol{x} - \boldsymbol{x}_1) \right]. \tag{3.57}$$

In analogy with the work in Ref. [72], it may then be shown that

$$\boldsymbol{u}_* = \frac{Q}{4\pi} \sum_{n=1}^{\infty} \left[-\frac{2(n+1)}{2n-1} A_{n-1} (\boldsymbol{x} - \boldsymbol{x}_1) + \left(\frac{(n-2)r^2}{2n-1} A_{n-1} - \frac{n}{2n+3} A_{n+1} - 2nB_{n-1} \right) \boldsymbol{\nabla} \right] \frac{D^n}{n!} \frac{1}{r}. \tag{3.58}$$

Since the $n = 0$ term in Eq. (3.59) is identically zero, we may write the total velocity $\boldsymbol{u} = \boldsymbol{u}_0 + \boldsymbol{u}_*$ as

$$\begin{aligned} \boldsymbol{u} = \frac{Q}{4\pi} \sum_{n=1}^{\infty} \Bigg[& \left(-\frac{2(n+1)}{2n-1} A_{n-1} - \frac{(2n+1)r^{2n-1}}{R^{n+1}} \right) (\boldsymbol{x} - \boldsymbol{x}_1) \\ & + \left(\frac{(n-2)r^2}{2n-1} A_{n-1} - \frac{n}{2n+3} A_{n+1} - 2nB_{n-1} - \frac{r^{2n+1}}{R^{n+1}} \right) \boldsymbol{\nabla} \Bigg] \frac{D^n}{n!} \frac{1}{r}. \end{aligned} \tag{3.59}$$

In order to make further progress, we now distinguish between the problems of a source outside a rigid (no-slip) sphere, and outside a spherical no-shear bubble.

3.5.2 No-slip boundary condition (rigid sphere)

In this case the boundary condition is given by Eq. (3.9). By inspection, the condition on the surface of the sphere is equivalent to the two conditions

$$-\frac{2(n+1)}{2n-1} A_{n-1} - (2n+1) R^{-n-1} = 0, \tag{3.60a}$$

$$\frac{n-2}{2n-1} A_{n-1} - \frac{n}{2n+3} A_{n+1} - 2nB_{n-1} - R^{-n-1} = 0, \tag{3.60b}$$

whose solutions are

$$A_n = -\frac{(2n+1)(2n+3)}{2(n+2)} R^{-n-2} = 2R^{-3} \left(-nR^{-(n-1)} \right) - \frac{3}{2} \frac{R^{-n-2}}{n+2}, \tag{3.61a}$$

$$B_n = \frac{2n+7}{4(n+4)} R^{-n-4} - \frac{2n+1}{4(n+2)} R^{-n-2} = \frac{1}{2} \left(R^{-4} - R^{-2} \right) R^{-n} + \frac{3}{4} \frac{R^{-n-2}}{n+2} - \frac{1}{4} \frac{R^{-n-4}}{n+4} \tag{3.61b}$$

We can now follow the same procedure as for the rotlet in §3.3.1 and convert this into a singularity solution of the form

$$\boldsymbol{u}_* = 2\mu Q \boldsymbol{d} \cdot \int_0^{R^{-1}} (f(\xi) + g(\xi)\nabla^2)\boldsymbol{G}(\boldsymbol{x} - \boldsymbol{\xi})\,\mathrm{d}\xi, \tag{3.62}$$

which yields

$$f(\xi) = 2R^{-3}\delta'(\xi - R^{-1}) - \frac{3}{2}\xi, \tag{3.63a}$$

$$g(\xi) = \frac{1}{2}\left(R^{-4} - R^{-2}\right)\delta(\xi - R^{-1}) + \frac{1}{4}\left(3\xi - \xi^3\right), \tag{3.63b}$$

and hence

$$\begin{aligned}\boldsymbol{u} = -\frac{Q}{4\pi}\boldsymbol{\nabla}\frac{1}{r_2} + 2\mu Q\boldsymbol{d}\cdot\Bigg[&-2R^{-3}(\boldsymbol{d}\cdot\boldsymbol{\nabla})\boldsymbol{G}\left(\boldsymbol{x} - \boldsymbol{x}_2^*\right) + \frac{1}{2}\left(R^{-4} - R^{-2}\right)\cdot\nabla^2\boldsymbol{G}\left(\boldsymbol{x} - \boldsymbol{x}_2^*\right) \\ &+ \int_0^{R^{-1}}\left(-\frac{3}{2}\xi + \frac{1}{4}\left(3\xi - \xi^3\right)\nabla^2\right)\boldsymbol{G}\left(\boldsymbol{x} - \boldsymbol{\xi}\right)\,\mathrm{d}\xi\Bigg].\end{aligned} \tag{3.64}$$

The image field for the source is therefore due to a point stresslet and point source dipole, as well as a line of Stokeslets and source dipoles. Note that, as expected from mass conservation across the sphere surface, it does not contain another source term. Furthermore, even though the axisymmetric source dipole only requires a finite number of images [72], this is not the case for a source.

Since a distribution of Stokeslets is present on the line between $\boldsymbol{x}_1$ and $\boldsymbol{x}_2$, the net force on the sphere due to the source is non-zero. That force is given by the zeroth term in the Stokeslet multipole expansion, A_0, which leads to

$$\boldsymbol{F}_{\text{rigid}}^{\text{source}} = -2\mu Q A_0 \boldsymbol{d} = \frac{3\mu Q}{2R^2}\boldsymbol{d}, \tag{3.65}$$

which once again is consistent with Faxén's law [127]. By axisymmetry, the torque on the sphere vanishes.

An illustration of the flow field is shown in Fig. 3.6. This time there are three qualitative bifurcations in the flow features as R is increased from 1. The first is a saddle-node bifurcation in the wake of the sphere at $R \approx 4.82$, which gives rise to a vortex ring. A further transcritical bifurcation at $R \approx 4.99$ changes the structure of the vortex, and it disappears again at $R \approx 5.81$ when a pitchfork bifurcation occurs on the surface of the sphere.

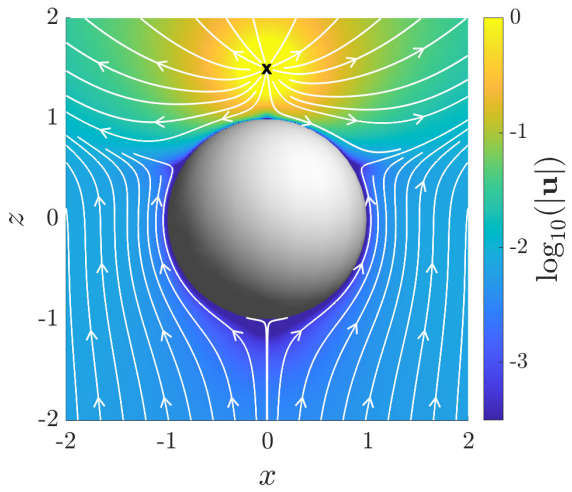

(a) $R = 1.5$

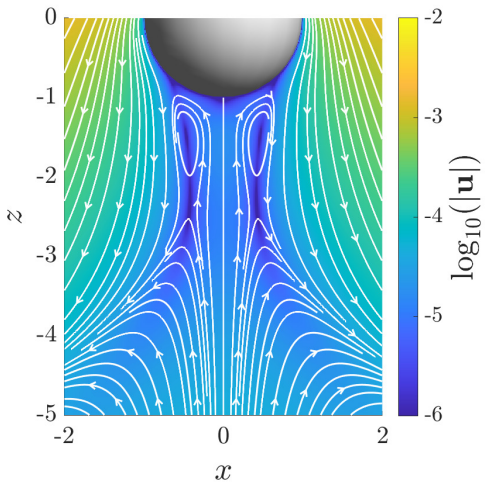

(b) $R = 4.9$

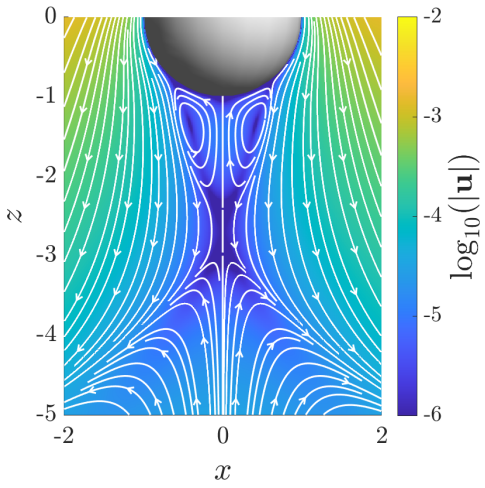

(c) $R = 5$

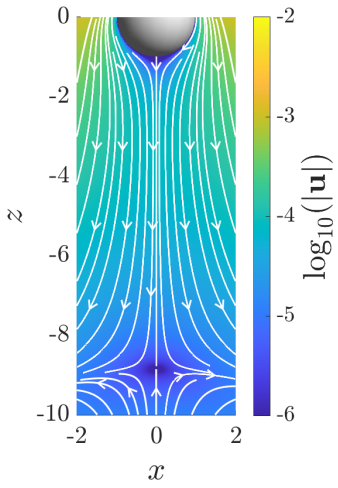

(d) $R = 5.85$

Figure 3.6 Flow field in the x-z plane due to a source with $Q = 1$ located at $\boldsymbol{x}_2 = R\hat{\boldsymbol{z}}$ outside a rigid sphere at the origin. Streamlines are drawn in white and the logarithm of the flow magnitude is superposed in colour. The black cross indicates the position of the source. The flow undergoes three bifurcations as R increases, at $R \approx 4.82$, $R \approx 4.99$ and $R \approx 5.81$, with a vortex ring appearing in the wake of the sphere at intermediate values of R.

3.5.3 No tangential stress boundary condition (spherical bubble)

In the case of a bubble we have a no-penetration velocity boundary condition, as well as the requirement of vanishing tangential stress on the sphere surface, Eq. (3.10). The condition that the normal velocity vanishes may be obtained by taking the $\hat{\boldsymbol{r}}$ component of Eq. (3.59). Noting from Eq. (3.54) that $D^n(r^{-1})/n! \sim r^{-n-1}$ we have the result

$$-\frac{n(n+1)}{2n-1}A_{n-1} + \frac{n(n+1)}{2n+3}A_{n+1} + 2n(n+1)B_{n-1} - nR^{-n-1} = 0. \tag{3.66}$$

For the tangential stress condition, we observe that since the flow is axisymmetric the boundary condition simply requires that the component $\sigma_{r\theta}$ of the stress tensor vanishes on the sphere surface. In spherical polar coordinates about $\boldsymbol{x}_1$ this stress component is given by

$$\sigma_{r\theta} = \mu\left[r\frac{\partial}{\partial r}\left(\frac{u_\theta}{r}\right) + \frac{1}{r}\frac{\partial u_r}{\partial \theta}\right], \tag{3.67}$$

but since u_r is zero at $r = 1$ for all values of θ, the no-stress boundary condition becomes just

$$\frac{\partial}{\partial r}\left(\frac{u_\theta}{r}\right)\bigg|_{r=1} = 0. \tag{3.68}$$

Defining the projection operator $\boldsymbol{\Pi} = \boldsymbol{I} - \hat{\boldsymbol{r}}\hat{\boldsymbol{r}}$, it is easy to see from Eq. (3.54) that $\boldsymbol{\Pi}\cdot\boldsymbol{\nabla}D^n(r^{-1})/n! \sim r^{-n-2}$ and thus Eq. (3.68) reduces to

$$-\frac{(n+1)(n-2)}{2n-1}A_{n-1} + \frac{n(n+3)}{2n+3}A_{n+1} + 2n(n+3)B_{n-1} - (n-2)R^{-n-1} = 0. \tag{3.69}$$

The system given by Eqs. (3.66) and (3.69) may then be solved to give

$$A_n = -2R^{-2}R^{-n} + 3\frac{R^{-(n+2)}}{n+2}, \tag{3.70a}$$

$$B_n = \frac{1}{2}\frac{R^{-(n+4)}}{n+4}, \tag{3.70b}$$

which lead to the flow field

$$\boldsymbol{u} = -\frac{Q}{4\pi}\boldsymbol{\nabla}\frac{1}{r_2} + 2\mu Q\boldsymbol{d}\cdot\left[-2R^{-2}\boldsymbol{G}\left(\boldsymbol{x}-\boldsymbol{x}_2^*\right) + \int_0^{R^{-1}}\left(3\xi + \frac{1}{2}\xi^3\nabla^2\right)\boldsymbol{G}\left(\boldsymbol{x}-\boldsymbol{\xi}\right)\,\mathrm{d}\xi\right]. \tag{3.71}$$

The image field for a point source outside a bubble may therefore be represented by a point Stokeslet, together with a line of Stokeslets and source dipoles. An illustration of this flow is shown in Fig. 3.7. Only one bifurcation of the flow field occurs, at $R = 1$. As in the case of the

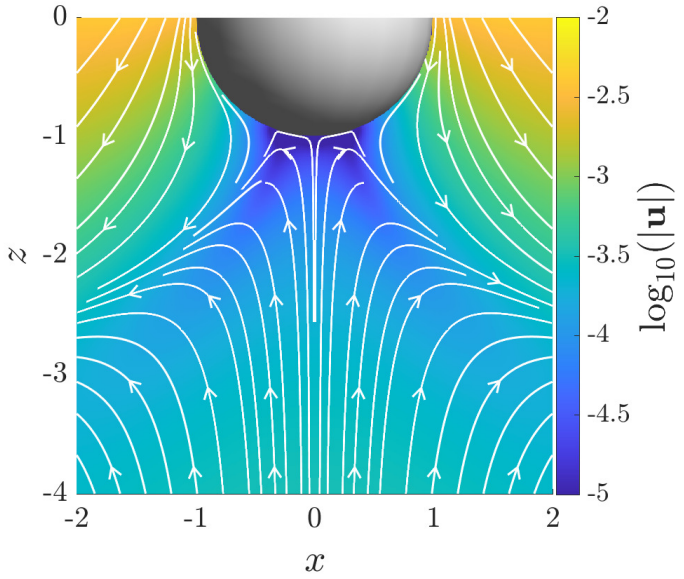

(a) $R = 2.9$

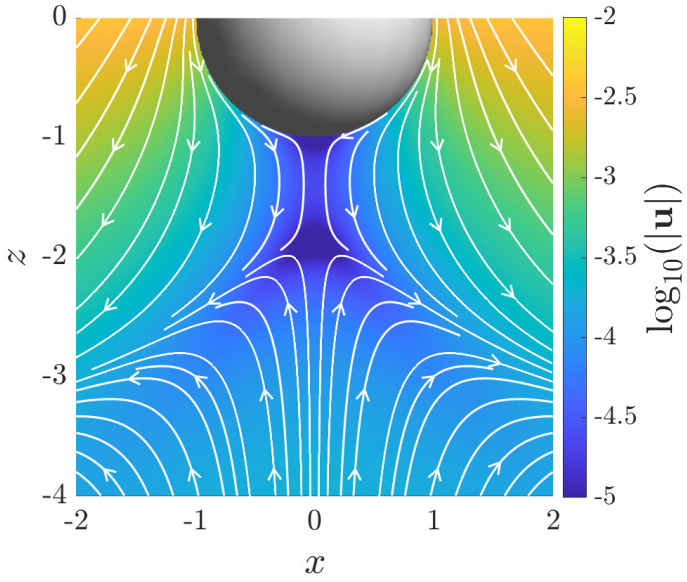

(b) $R = 3.1$

Figure 3.7 Flow field in the x-z plane due to a source with $Q = 1$ located at $\boldsymbol{x}_2 = R\hat{\boldsymbol{z}}$ outside a spherical bubble at the origin. Streamlines are drawn in white and the logarithm of the flow magnitude is superposed in colour. The flow undergoes one bifurcation at $R = 3$.

rotlet, the zero-shear condition on the bubble surface prevents the formation of a vortex in the bubble wake.

By considering the coefficient A_0, we obtain that the force on the bubble is

$$\boldsymbol{F}^{\text{source}}_{\text{bubble}} = \frac{\mu Q}{R^2}\boldsymbol{d} = \frac{1}{6}\boldsymbol{F}^{\text{source}}_{\text{rigid}}, \tag{3.72}$$

and its value is six times smaller than the force on a rigid sphere. The torque is zero again, as required for a bubble.

3.6 Discussion

In this chapter we derived physically-intuitive expressions for the flow due to an arbitrary point torque (rotlet, split into axisymmetric and transverse components) and a point source exterior to either a rigid sphere or a spherical bubble in Stokes flow. In the case of an axisymmetric rotlet outside a rigid sphere, the image flow may be interpreted as due to a single image torque, which can be explained using an argument involving Apollonian circles. The solution is therefore equally valid for an axisymmetric torque inside a spherical shell. Surprisingly, we find that the image field is much simpler in the rigid case than for a bubble, contrary to the other situations considered in this chapter and most known singularity solutions near plane surfaces [216]. In the transverse rotlet case, the image system is more complicated and involves multiple line integrals of singularities, yet the expression remains compact and easy to evaluate numerically. Two bifurcations occur in the flow field as the distance of the singularity to the sphere centre varies. In the case of a point source, the solution cannot be written in terms of a finite number of images for either a rigid or a stress-free (bubble) boundary condition.

In addition to classical applications for the hydrodynamic interactions between colloidal particles [90], our results could be useful for the theoretical modelling of biologically motivated hydrodynamic problems, such as the interaction of rotating bacterial flagella with the cell body [39, 69, 187]. Our results are easily implemented and calculated numerically, and particularly suited to modelling the interaction of any number of singularities in an object-oriented programming style. The result for an axisymmetric torque within a rigid spherical shell may find additional use in the modelling of flows transport within biological cells [98, 167]. Furthermore, closely separated singularities can be used to model dipoles, which appear in the flow signature of swimming bacteria [216] and artificial colloids [20]. A proof-of-concept illustration is shown in Fig. 3.8 in the case of two rotlet-dipoles near a rigid sphere (as relevant for the locomotion of helically flagellated bacteria) and a source-dipole (modelling a Janus

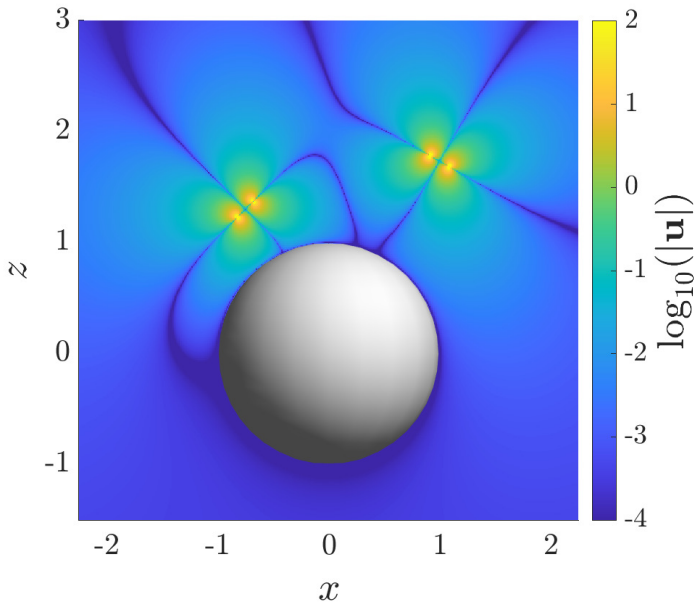

(a)

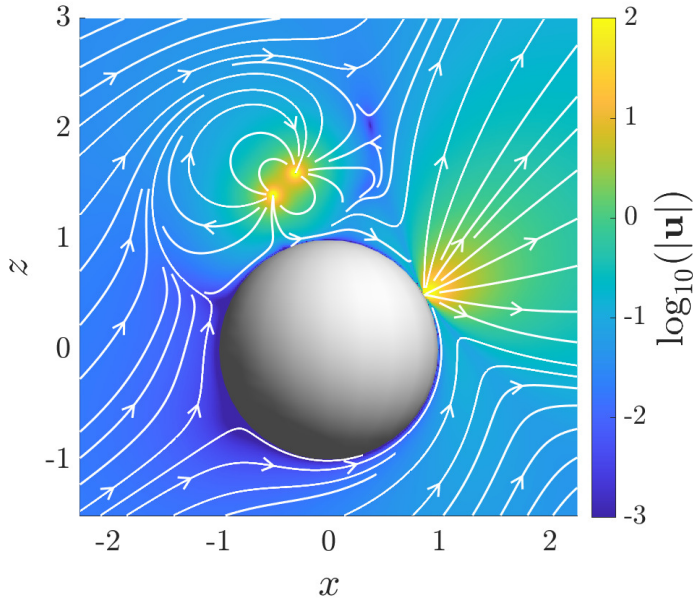

(b)

Figure 3.8 Illustration of two systems that can be modelled using a superposition of hydrodynamic singularities derived in this chapter (flow magnitudes shown on a logarithmic scale). (a) Interaction between two rotlet-dipoles near a rigid sphere, as relevant for the locomotion of helically flagellated bacteria. (b) A source-dipole microswimmer, modelling a self-diffusiophoretic Janus particle, near a rigid sphere emitting fluid at one location on its surface.

colloid swimming via self-diffusiophoresis) near a rigid sphere that also emits fluid at one location on its surface.

Recently, regularised hydrodynamic singularities [47, 266] have become a popular tool to carry out efficient numerical simulations of the dynamics slender filaments in Stokes flow [111, 162, 214] and great progress has been made in employing them to reduce numerical stiffness [46, 93]. Regularising a singularity in a non-trivial geometry also requires a modification of its image flow field in order to preserve the boundary condition, and doing this turns out to not be straightforward [5]. While this has been achieved for the Stokeslet [259], more work needs to be done to derive regularised versions of the rotlet and the source in a spherical geometry. We hope that the work outlined in this chapter will be useful for this purpose, too.

Chapter 4

Direct vs indirect hydrodynamic interactions in bacterial flagellar bundling

4.1 Introduction

Bacteria are present on Earth in great abundance in all kinds of environments, including on land [75, 87], in the ocean [8, 221] and inside living hosts [177]. Their study is not only important in order to understand many pathogenic diseases, but also serves as a model system for the locomotion of microorganisms and active particles in fluids [17, 135, 136] and their responses to environmental cues [14, 177]. Moreover, their collective dynamics provide one of the smallest model systems for the physics of active matter [157, 193].

The majority of swimming bacteria are powered by so-called flagella. Many bacteria such as the model organism *Escherichia coli* (*E. coli*) are peritrichous, meaning that they are driven by several flagella. These are distributed almost randomly over the cell body, with a slight bias due to the history of cell division [91]. Each flagellum consists of a long passive filament connected at its base to a specialised rotary molecular motor through a short flexible hook [17, 18, 236]. The flagellar filaments are slender helices, assembled from proteins that form a relatively rigid structure, while the hook is significantly more flexible and acts both as a mechanical link and as a torsional spring.

Although flagellar motors are actuated independently with no known biological coordination, it is observed experimentally that bacteria are able to perform a two-gait "run-and-tumble" motion to explore their fluid environment [15]. During a run event, the flagellar filaments co-rotate in a counter-clockwise (CCW) fashion and form a coherent helical bundle behind the cell, pushing it forward and leading to swimming. During a tumble event at least one of the motors switches to rotate clockwise (CW), leading to unbundling, i.e. dispersion of the filament assembly, and a random reorientation of the cell. After a short period, the reversed

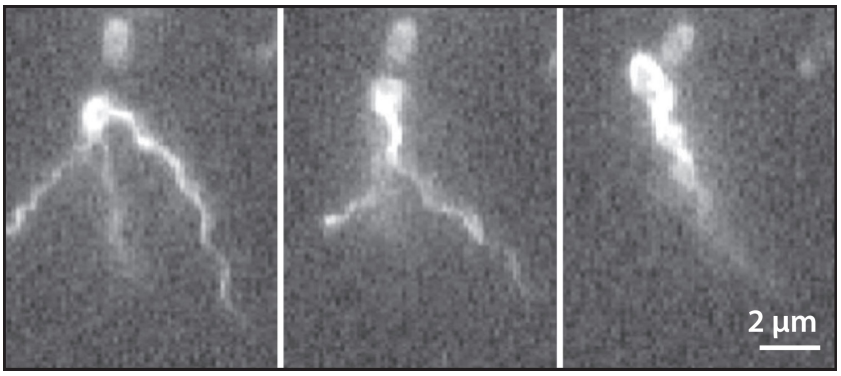

Figure 4.1 Snapshots of the bundling process occurring during the motion of *E. coli* bacteria wherein counter-clockwise rotating helical flagellar filaments arrange to form a bundle behind the cell body. Adapted from Turner, Ryu and Berg (2000) "Real-Time Imaging of Fluorescent Flagellar Filaments" *J. Bacteriol.*, **182**, 2793-2801, with permission [236].

motor switches back to CCW rotation, the bundle reforms and the process repeats [51, 236]. An illustration of the bundling process in *E. coli* experiments is shown in Fig. 4.1 [236].

Unlike the flagella of eukaryotic organisms such as the green alga *Chlamydomonas reinhardtii* [186], ciliates such as *Paramecium* [26], and spermatozoa [108], which are able to generate internal forces through the contraction of molecular motors within their flagella [26, 99, 148, 149], the flagellar filaments of bacteria are passive, and the rotation of the flagella motor is the exclusive source of dynamic forcing [18, 209]. Nevertheless, the dynamics of flagellated bacteria are a highly complex elastohydrodynamic problem [135]. The protein structure of the filaments allows for multiple different helical configurations, a phenomenon called polymorphism [33, 220], which may change depending on the dynamic load [50]. Moreover, because the flagellar filaments and especially the hook are flexible, and the interaction between these slender elastic structures, the cell body and the fluid lead to non-linearities that are difficult to compute [120].

Despite these challenges, the dynamics of bundling and unbundling have been the subject of numerous theoretical [123, 156, 196, 230], numerical [4, 65, 69, 79, 112, 114, 139, 146, 170, 194, 195, 255] and experimental [16, 17, 51, 122, 125, 153, 191, 236, 238] studies. Early studies examined the dynamics of filaments without taking into account the cell body [69, 79, 114, 123, 125, 146, 156, 195], or ignored elastic effects [194]. With advances in computational power and the sophistication of numerical methods [45, 46, 93], more recent work has been able to accurately simulate the swimming dynamics of multi-flagellated motile bacteria [4, 112, 170]. Some studies also focus on a particular aspect of the problem, such as flagellar polymorphism [139] or the geometrical constraints of entanglement [230].

In this chapter we address the early stages of bundle formation, and aim to understand fundamentally which hydrodynamic effects dominate in the process of flagellar filament assembly. Several different possible candidates have been proposed in the literature. For instance, it was shown numerically and experimentally that the co-rotation of two elastic helices orthogonal to an interface leads to wrapping and mutual attraction [123, 125], while the wrapping occurs also for rotating straight filaments in an unbounded fluid [156]. In both cases the effect is due to *direct* hydrodynamic interactions between the filaments.

Other models have focused on the role of the cell body. It was found theoretically [187] and numerically [4] that the motility of the cell body enables bundle formation through a "zipping" effect. The existence of an elastohydrodynamic instability due to a balance between fluid drag and hook elasticity has also been demonstrated [196]. The crucial difference between these examples and those above is that bundling here does not occur as a result of *direct* hydrodynamic interactions between the flagellar filaments, but rather *indirectly* through flows that are generated in the swimming frame due to rotation and translation of the cell body.

With this physical description in mind, we introduce a minimal hydrodynamic model of flagellar bundling in §4.2, which allows us to make precise the notion of direct vs indirect interactions. We then proceed to analyse the two hydrodynamic contributions in details, first for the flows due to flagellar thrust in §4.3, and then for the flows due to their rotation in §4.4. We then present a numerical elastohydrodynamic rod-and-spring model for the axis of flagellar filaments in §4.5 that allows us to analyse the dominant hydrodynamic contributions to the early bundling process for a model bacterium in detail. We conclude with a discussion of our results in §4.6.

4.2 Minimal model of flagellar bundling

In this section we introduce a minimal model for the advection of bacterial flagellar filaments by the flow fields created by their actuation and the swimming of the cell. While idealised in its structure, the simplicity of the model allows us to study its dynamics analytically and to gain a quantitative understanding of the hydrodynamic forces at play.

4.2.1 Hydrodynamics of flagellar propulsion

Due to the microscopic size of bacteria, the fluid dynamics of their locomotion in a Newtonian viscous fluid are accurately described by the incompressible Stokes equations [135, 189],

$$\mathbf{0} = -\boldsymbol{\nabla} p + \mu \nabla^2 \boldsymbol{u} + \boldsymbol{f}, \quad \boldsymbol{\nabla} \cdot \boldsymbol{u} = 0, \tag{4.1}$$

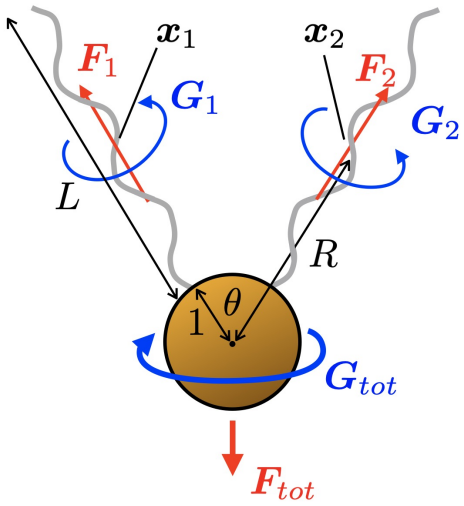

Figure 4.2 Minimal hydrodynamic model for flagellar bundling. The bacterium is modelled as a rigid sphere of unit radius, and equipped with two flagella. The flagellar filaments have axial length L and are separated by a solid angle θ at their base. Labelling the filaments by $i = \{1, 2\}$, each is modelled as a radial point force $\boldsymbol{F}_i$ and point torque $\boldsymbol{G}_i$ acting on the surrounding fluid and placed at $\boldsymbol{x}_i$, which is at a distance $R = L/2 + 1$ from the centre of the cell body at the coordinate origin. Since the swimming cell is force- and torque-free, the cell body exerts a counterforce and -torque on the fluid.

where $\boldsymbol{u}(\boldsymbol{x})$ is the flow velocity field, $p(\boldsymbol{x})$ the dynamic pressure, $\boldsymbol{f}(\boldsymbol{x})$ a body force density and μ the dynamic viscosity. Since the Stokes equations are linear, they allow for solution approaches using Green's functions (termed Stokeslets, corresponding physically to point forces), including the method of images and boundary integral methods [94, 127, 188]. The boundary condition on the (rigid) surface of the bacterium is "no-slip", i.e. the flow field matches the velocity of the cell body.

We consider the setup shown in Fig. 4.2. For simplicity, we assume that the bacterium has a spherical cell body, and is equipped with exactly two rigid helical flagellar filaments, labelled by $i = \{1, 2\}$, that point away radially from the centre of the cell body. The filaments are slender rigid left-handed helices, each rotating with the same angular velocity $\boldsymbol{\Omega}$ at its base in a counter-clockwise (CCW) fashion (when viewed from behind the cell looking towards it [17]). We non-dimensionalise all lengths so that the cell body has unit radius. The dimensionless axial length of each flagellar filament is denoted by L, and their points of attachment are separated by a solid angle θ ranging from 0 to 2π. We further assume that the organism is neutrally buoyant.

Fundamentally, for any rigid body immersed in Stokes flow there is a linear relationship between its translational and rotational velocities $\boldsymbol{U}$ and $\boldsymbol{\Omega}$, and the hydrodynamic force $\boldsymbol{F}$ and torque $\boldsymbol{G}$ that it exerts on the surrounding fluid [94]. The so-called resistance matrix instantaneously linking kinematic and dynamic quantities depends only on the fluid viscosity

and the geometry (shape and size) of the body. Moreover, for a chiral body it includes terms that couple translation and rotation.

Consequently, the rotation of each flagellar filaments results in both a force and a torque exerted onto the surrounding fluid [190]. In the case where $\boldsymbol{U}_i = \mathbf{0}$ and $\boldsymbol{\Omega}_i$ aligned with the axis of the helix i, these can be easily evaluated using the resistive-force theory of slender filaments as [53, 136]

$$\boldsymbol{F}_i = \xi_\perp (1 - \tilde{\xi}) \sin\Psi \cos\Psi \rho \Lambda \boldsymbol{\Omega}_i, \tag{4.2}$$

$$\boldsymbol{G}_i = \xi_\perp (\cos^2\Psi + \tilde{\xi} \sin^2\Psi) \rho^2 \Lambda \boldsymbol{\Omega}_i, \tag{4.3}$$

where ρ is the radius of the flagellar helix, P the helix pitch, $\Psi = \tan^{-1}(2\pi\rho/P)$ the helix pitch angle, $\Lambda = L \sec\Psi$ is the arc-length of the flagellar helix, and $\tilde{\xi} = \xi_{||}/\xi_\perp$ the ratio of the drag coefficients given by [145]

$$\xi_{||} = \frac{2\pi\mu}{\ln\left(1.13\rho \sec\left(\Psi\right)/d\right)}, \quad \xi_\perp = \frac{4\pi\mu}{1/2 + \ln\left(1.13\rho \sec\left(\Psi\right)/d\right)}, \tag{4.4}$$

which also depend weakly on the filament thickness d. Typically, $d \ll \rho$ and so $\tilde{\xi} \approx 0.5$ [51, 53]. We note that resistive-force theory is only the leading-order approximation for the hydrodynamic forces in the slenderness of the filaments. More accurate theories such as slender-body theory [143], or such accounting for elasticity [120] give more accurate though significantly more complicated estimates for $\boldsymbol{F}_i$ and $\boldsymbol{G}_i$. However, as we show in §4.3.3, their absolute values do not actually matter when comparing direct and indirect interactions since they both scale linearly with the kinematic quantities.

4.2.2 Modelling flagellar filaments by flow singularities

The main idea behind our minimal model is to abstract away the geometric shape of the flagellar filaments by replacing them with their averaged hydrodynamic signatures. Specifically, the effect of each filament on the fluid can be represented by a point force (Stokeslet) and a point torque (rotlet) singularities, located a distance $R = L/2 + 1$ away from the centre of the cell body and with strengths calculated according to Eqs. 4.2 and 4.3 respectively. This step is motivated by the well-known multipole expansion for the motion of a rigid body in Stokes flow [127]. For each helical filament, we may write the flow disturbance due to its motion as a series in powers of $1/r$, where r is the distance from a point in the fluid to the centrepoint of the filament. The leading order $O(1/r)$ term is equivalent to a point force at the centre of the body, with magnitude equal to the total force it exerts on the surrounding fluid. The next higher order, $O(1/r^2)$, corresponds to a force dipole, which may be split into symmetric and antisymmetric

parts. The antisymmetric part may be interpreted as a point torque, equal to the total torque exerted by the body, while the symmetric part may be calculated as an integral of the stress distribution over its surface [10].

It is known that for a model organism such as *E. coli* the filaments rotate with a period on the order of 10 ms, which is much shorter than the time scale of bundle formation, which is around 500 ms [51, 236]. We therefore assume that the force $\boldsymbol{F}_i$, torque $\boldsymbol{G}_i$ and symmetric force dipole that are exerted by flagellum i can be averaged over one period of flagellar rotation and are all oriented approximately in the radial direction. In that case, the force and symmetric force dipole both give rise to an axisymmetric flow field, while the torque decouples and gives an azimuthal flow. We may then discount the symmetric force dipole as it is less dominant at long distances than the flow induced by the force, but we retain the torque as it is the leading-order contribution in the azimuthal direction. This approach allows us therefore to model the leading-order flows in both the polar and azimuthal directions.

Furthermore, the physics of Stokes flow require that the total hydrodynamic force and torque exerted by the swimmer on the fluid vanish [189], so in the absence of body forces such as gravity, a force $\boldsymbol{F}_{\text{tot}}$ and torque $\boldsymbol{G}_{\text{tot}}$ are also exerted by the cell body on the fluid to maintain dynamic equilibrium. However, as we will show in §4.3.2 and is a subtle point, these do not balance the flagellar thrust and torque exactly, since the flows generated by the actuation of the filaments induce additional stresses and drag on the cell body.

4.2.3 Direct vs indirect interactions

With these prerequisites it is now possible to define the main terminology used in our study. Labelling the positions of the singularities by $\boldsymbol{x}_i$, we define the *direct* hydrodynamic interaction as the magnitude of the flow induced instantaneously at $\boldsymbol{x}_2$ (resp. $\boldsymbol{x}_1$) by the singularities located at $\boldsymbol{x}_1$ (resp. $\boldsymbol{x}_2$). Since both flagellar filaments are rotated at the same angular velocity $|\boldsymbol{\Omega}|$, we have $|\boldsymbol{F}_1| = |\boldsymbol{F}_2|$ and likewise for the torques, so the magnitude of the direct hydrodynamic interaction is symmetric in the label i used to measure the magnitude of the flow. In contrast, we define the *indirect* interaction as the magnitude of the flow induced instantaneously at $\boldsymbol{x}_2$ (resp. $\boldsymbol{x}_1$) by the rigid-body motion of the cell body induced by the hydrodynamic forcing at $\boldsymbol{x}_1$ (resp. $\boldsymbol{x}_2$), i.e. the flow induced by the motion of the cell as measured in the co-moving body frame.

In order to illustrate these definitions intuitively, we can describe two thought experiments highlighting each kind of hydrodynamic interaction separately. For direct interactions consider a bacterium that is held stationary, e.g. by means of a micro-pipette. In this case the direct hydrodynamic interactions between its flagella are unaffected; both still create forces and torques which move the fluid and thus move the neighbouring flagellum. However, since the

cell does not move no flow is created by the motion of the cell body, and therefore there are no indirect interactions at play. In contrast, to understand indirect interactions imagine that the flagella are shielded from another by a vane-like structure, such as the one featured by the choanoflagellate *Diaphanoeca grandis* [171]. In that case there are no direct interactions since a hydrodynamic forcing contained within one vane does not affect the flow in another; however, as the cell swims the flows induced by the swimming motion advect and rotate the flagella, so indirect interactions are still present.

These two definitions allow us to characterise a wide range of different hydrodynamic effects, including that considered in past work. By considering direct interactions, we take into account both the geometric configuration of the flagella relative to one another, as well as any boundary effects due to the no-slip condition on the cell body. This captures both wall-induced attraction [219] in the case of the Stokeslet, and wrapping [156] in the case of the rotlet. Meanwhile, indirect interactions capture global flows such as rotation-induced wrapping [187] or zipping [4] and translation-induced contraction [196].

Furthermore, since all Stokes flows are linear in the force and torque, for any given geometrical setup the ratio of direct to indirect advection is in fact independent of the magnitude of the hydrodynamic forcing, and depends only on the geometric configuration of the flagellar filaments. In the context of our model, this reduces to the two parameters R (distance to centre of cell body) and θ (angle between the two flagellar filaments), allowing us to analyse the parameter space comprehensively. In §4.3 we carry out the analysis for the force and consider the torque in §4.4.

4.3 Advection induced by flagellar thrust

4.3.1 Direct polar advection between flagella

We first analyse the direct flow due to flagellar thrust. To this end we consider a radial point force $\boldsymbol{F}_1$ located at $\boldsymbol{x}_1$ and analyse the flow that it generates at location $\boldsymbol{x}_2$. For convenience we define Cartesian coordinates so that the cell body is located at the origin and the force $\boldsymbol{F}_1$ is aligned with the z-axis. The solution to the Stokes equations Eq. (4.1) for a radial point force outside a rigid sphere, originally due to Oseen, may be written in a compact fashion as [127]

$$\boldsymbol{u}(\boldsymbol{x}) = \boldsymbol{F}_1 \cdot \left\{ \boldsymbol{\mathcal{G}}(\boldsymbol{x} - \boldsymbol{x}_1) + \alpha \boldsymbol{\mathcal{G}}(\boldsymbol{x} - \boldsymbol{x}_1^*) + \beta(\boldsymbol{e} \cdot \nabla)\boldsymbol{\mathcal{G}}(\boldsymbol{x} - \boldsymbol{x}_1^*) + \gamma \nabla^2 \boldsymbol{\mathcal{G}}(\boldsymbol{x} - \boldsymbol{x}_1^*) \right\}, \quad (4.5)$$

where we define

$$\boldsymbol{e} = \boldsymbol{x}_1/R, \tag{4.6}$$

$$\boldsymbol{x}_1^* = \boldsymbol{e}/R = \boldsymbol{x}_1/R^2, \tag{4.7}$$

$$\boldsymbol{F}_1 = F\boldsymbol{e}, \tag{4.8}$$

$$\alpha = -\frac{3}{2}R^{-1} + \frac{1}{2}R^{-3}, \tag{4.9}$$

$$\beta = R^{-2} - R^{-4}, \tag{4.10}$$

$$\gamma = -\frac{1}{4}R^{-1}\left(1 - R^{-2}\right)^2, \tag{4.11}$$

$$\boldsymbol{\mathcal{G}}(\boldsymbol{x}) = \frac{1}{8\pi\mu}\left(\frac{\boldsymbol{I}}{|\boldsymbol{x}|} + \frac{\boldsymbol{x}\boldsymbol{x}}{|\boldsymbol{x}|^3}\right). \tag{4.12}$$

Here $\boldsymbol{\mathcal{G}}$ is the Oseen tensor and the point $\boldsymbol{x}_1^*$ is the mirror image of $\boldsymbol{x}_1$ inside the cell body. In Eq. (4.5), the quantity $\boldsymbol{F}_1 \cdot \boldsymbol{\mathcal{G}}$ is the flow due to a point force of strength $\boldsymbol{F}_1$ in an unbounded fluid. By taking gradients of $\boldsymbol{\mathcal{G}}$, it is then possible to describe the flow due to force dipoles, quadrupoles and so on. This allows us to interpret the solution in Eq. (4.5) physically in terms of image singularities. The term with coefficient α corresponds to an image force, the β term corresponds to a collinear force dipole and the γ term is a source dipole (or degenerate force quadrupole). These coefficients are functions of R and ensure that the no-slip boundary condition,

$$\boldsymbol{u}(\boldsymbol{x}) = \boldsymbol{0}, \quad \text{if } |\boldsymbol{x}| = 1, \tag{4.13}$$

is satisfied at all points on the spherical body. The solution is structurally identical to the image system for a force near a plane wall [127], albeit with different values for the coefficients. Importantly, the sign of α is negative since $R > 1$, and $|\alpha| < 1$. Physically this means that an opposite but not equal force needs to be exerted on the cell body to keep it stationary. Balancing this force with drag will give rise to the indirect advection discussed in §4.3.2.

We illustrate the flow induced by such a radial force in the case $R = 2$ in Fig. 4.3a. The effect of the cell body is a distortion of the streamlines leading to advection predominantly in the polar θ-direction. Since we are interested in the advection of an inextensible flagellum of the same length, we focus therefore on the polar component of the flow. We write $\boldsymbol{x}_2 = R(\sin\theta, 0, \cos\theta)$ and define $\boldsymbol{r} = \boldsymbol{x}_2 - \boldsymbol{x}_1$, and $r = |\boldsymbol{r}|$ as the distance to the singularity. In a similar fashion we use $\boldsymbol{r}^* = \boldsymbol{x}_2 - \boldsymbol{x}_1^*$ and $r^* = |\boldsymbol{x}_2 - \boldsymbol{x}_1^*|$ to describe the distance to the image point. Both r and r^*

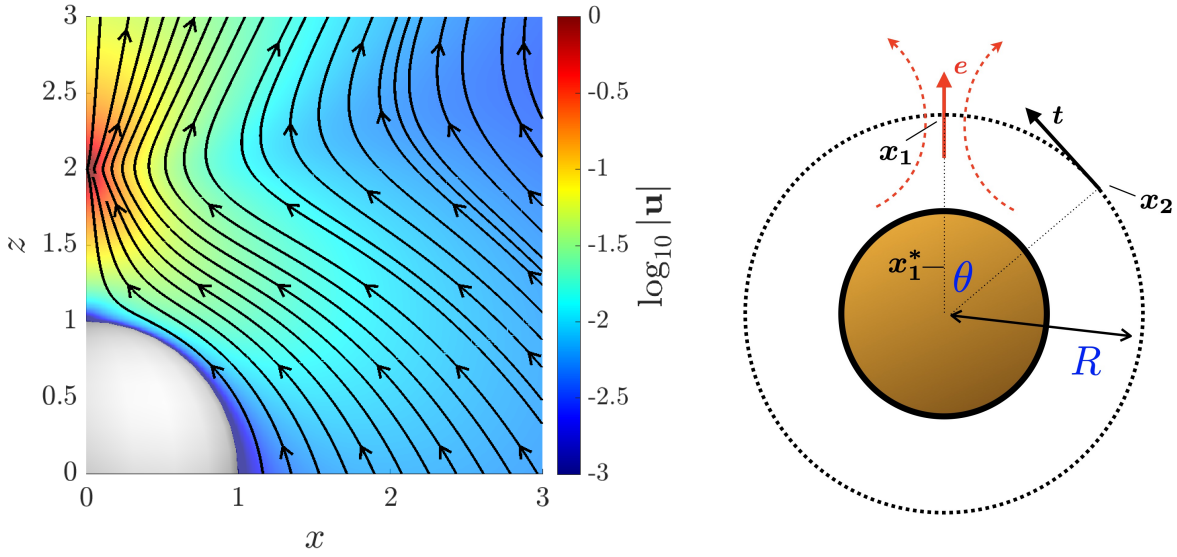

(a) (b)

Figure 4.3 (a) Illustration of the flow due to a radial point force with $R = 2$ and $\boldsymbol{F} = \hat{\boldsymbol{z}}$ in a Cartesian coordinate system with the cell body centred at the origin in the bottom-left corner. Colours quantify iso-magnitudes of the flow and black streamlines are superimposed. The force induces a flow that advects fluid around the cell body towards the singularity. (b) Sketch of the relevant geometric quantities to calculate the direct polar advection induced at $\boldsymbol{x}_2$ by a point force at $\boldsymbol{x}_1$ (see text for notation).

may be written in terms of R and θ as

$$r = 2R \sin\frac{\theta}{2}, \quad r^* = \sqrt{\left(R - R^{-1}\right)^2 + 4\sin^2\frac{\theta}{2}}. \tag{4.14}$$

Finally we define the vector $\boldsymbol{t} = (-\cos\theta, 0, \sin\theta)$. An illustrative sketch is provided in Fig. 4.3b.

The flow component of interest for direct interactions, which we call u_F^{dir}, is then given by

$$\begin{aligned} u_F^{\text{dir}} &\equiv \boldsymbol{t} \cdot \boldsymbol{u}(\boldsymbol{x}_2) \\ &= \frac{F}{8\pi\mu} \cdot \left\{ \boldsymbol{e} \cdot \boldsymbol{\mathcal{G}}(\boldsymbol{r}) \cdot \boldsymbol{t} + \alpha \boldsymbol{e} \cdot \boldsymbol{\mathcal{G}}(\boldsymbol{r}^*) \cdot \boldsymbol{t} + \beta \boldsymbol{e} \cdot (\boldsymbol{e} \cdot \nabla)\boldsymbol{\mathcal{G}}(\boldsymbol{r}^*) \cdot \boldsymbol{t} + \gamma \boldsymbol{e} \cdot \nabla^2 \boldsymbol{\mathcal{G}}(\boldsymbol{r}^*) \cdot \boldsymbol{t} \right\} \\ &= \frac{3F}{16\pi\mu} \left[\frac{1}{r} - \frac{1}{R}\frac{1}{r^*} - \frac{\left(R^2-1\right)^2}{2R^3}\frac{1}{r^{*3}} + \frac{\left(R^2+1\right)\left(R^2-1\right)^3}{2R^5}\frac{1}{r^{*5}} \right] \sin\theta. \end{aligned} \tag{4.15}$$

The term in brackets is a complicated function of R and θ but strictly positive for $R > 1$ and $0 < \theta < \pi$, i.e. for every possible geometric configuration. The generation of thrust by each

flagellar filament is therefore sufficient to facilitate the polar advection of neighbouring filaments from direct hydrodynamic interactions, eventually leading to the formation of a bundle.

4.3.2 Cell kinematics and indirect polar advection between flagella

We now consider the flow induced in the cell body frame due to its swimming motion. In order to find the translation velocity $\boldsymbol{U}$ we exploit the fact that the swimmer as a whole is force-free [189]. Neglecting the viscous drag on the flagellar filaments, we have the classical Stokes flow result $\boldsymbol{U} = \boldsymbol{F}_{\text{tot}}/6\pi\mu$ [127] where the total force $\boldsymbol{F}_{\text{tot}}$ that the cell body exerts on the fluid is given by

$$\boldsymbol{F}_{\text{tot}} = -\sum_i (1+\alpha)\boldsymbol{F}_i. \tag{4.16}$$

The factor $(1+\alpha)$ arises because the thrust that the flagellar filaments exert is already partially balanced by the hydrodynamic image system described in§4.3.1. Physically, the fact that $\alpha \neq 0$ may be attributed to the flagellar filament-induced flow that entrains the cell body towards the flagellum, thus increasing drag in the direction of motion.

For $\boldsymbol{x}_1$ and $\boldsymbol{x}_2$ as defined in §4.3.1 the total force in Eq. (4.16) evaluates to

$$\boldsymbol{F}_{\text{tot}} = 2F(1+\alpha)\cos\frac{\theta}{2}\left(-\sin\frac{\theta}{2}, 0, -\cos\frac{\theta}{2}\right), \tag{4.17}$$

from which it follows that the swimming speed is

$$|\boldsymbol{U}| = \frac{2F}{6\pi\mu}\left(1 - \frac{3}{2}R^{-1} + \frac{1}{2}R^{-3}\right)\cos\frac{\theta}{2}. \tag{4.18}$$

The flow field in the body frame is then given by the classical expression for the flow around a translating rigid sphere, which is [125]

$$\begin{aligned}\boldsymbol{u}(\boldsymbol{x}) &= \frac{\boldsymbol{F}_{\text{tot}}}{8\pi\mu}\cdot\left\{\mathcal{G}(\boldsymbol{x}) + \frac{1}{6}\nabla^2\mathcal{G}(\boldsymbol{x})\right\} - \frac{\boldsymbol{F}_{\text{tot}}}{6\pi\mu} \\ &= \frac{\boldsymbol{F}_{\text{tot}}}{8\pi\mu}\left(R^{-1} + \frac{1}{3}R^{-3} - \frac{4}{3}\right) + \frac{\boldsymbol{F}_{\text{tot}}\cdot\boldsymbol{x}\boldsymbol{x}}{8\pi\mu}\left(R^{-3} - R^{-5}\right).\end{aligned} \tag{4.19}$$

From this it is straightforward to find the indirect advective polar component, u_F^{ind}, which is given by

$$u_F^{\text{ind}} \equiv \boldsymbol{t}\cdot\boldsymbol{u}(\boldsymbol{x}_2) = \frac{F}{6\pi\mu}\left(1 - \frac{9}{4}R^{-1} + \frac{9}{8}R^{-2} + \frac{1}{4}R^{-3} - \frac{1}{8}R^{-6}\right)\sin\theta. \tag{4.20}$$

Notably, unlike the direct advection from Eq. (4.15), the indirect flow is simply proportional to $\sin\theta$. It is also strictly positive in the entire parameter range, and thus it also always contributes to bundling.

4.3.3 Direct vs indirect interactions

From Eqs. (4.15) and (4.20) we see that both direct and indirect advection always facilitate bundling between two flagellar filaments, since the induced lateral velocity is positive in both cases. The fundamental question is therefore under which condition one type of hydrodynamic interaction dominates the other. To this end we consider their ratio, which is given by

$$\frac{u_F^{\mathrm{dir}}}{u_F^{\mathrm{ind}}} = \frac{9}{8}\frac{r^{-1} - (Rr^*)^{-1} - \frac{1}{2}\left(R^2-1\right)^2 (Rr^*)^{-3} + \frac{1}{2}\left(R^2+1\right)\left(R^2-1\right)^3 (Rr^*)^{-5}}{1 - \frac{9}{4}R^{-1} + \frac{9}{8}R^{-2} + \frac{1}{4}R^{-3} - \frac{1}{8}R^{-6}}. \tag{4.21}$$

Since both u_F^{dir} and u_F^{ind} are linear in F, this ratio is independent of the flagellar forcing and hence only a function of the geometric parameters R and θ. Physically, this means that the relative contribution to bundling is independent of the (identical) rotation rate of the filaments. Only the absolute magnitude of the advection and hence the time scale on which bundling takes place depend (linearly) on the strength of the actuation, as expected for Stokes flow [94].

In order to compare u_F^{dir} to u_F^{ind}, we display the ratio $u_F^{\mathrm{dir}}/u_F^{\mathrm{ind}}$ graphically in Fig. 4.4 using a logarithmic scale. The diagram is to be interpreted as follows: one flagellar filament is located on the vertical axis, with a flow singularity at its midpoint, at a distance R from the origin; the colour of a point in the plane then indicates the ratio of direct to indirect advection that would be experienced by the midpoint of the second flagellar filament (i.e. a flow singularity) located at that position. Points on the vertical axis therefore correspond to two flow singularities on top of each other, while points on the horizontal axis correspond to filaments at right angles, $\theta = \pi/2$.

The thick red solid line in in Fig. 4.4 indicates the contour on which direct and indirect effects balance exactly, i.e. $u_F^{\mathrm{dir}}/u_F^{\mathrm{ind}} = 1$. From Eq. (4.21) we deduce that this line behaves asymptotically as

$$R\sin\theta \to \frac{9}{8}, \quad \text{as } R \to \infty, \tag{4.22}$$

creating a closed wake-like region surrounding the vertical axis inside of which direct interactions dominate. This observation may be rationalised physically. The indirect interactions are proportional to $\sin\theta$, so when the two filaments are nearly aligned then the flow generated by translation of the cell body only has a small component in the polar direction that brings them closer together. In contrast, direct hydrodynamic interactions grow when the filament-filament

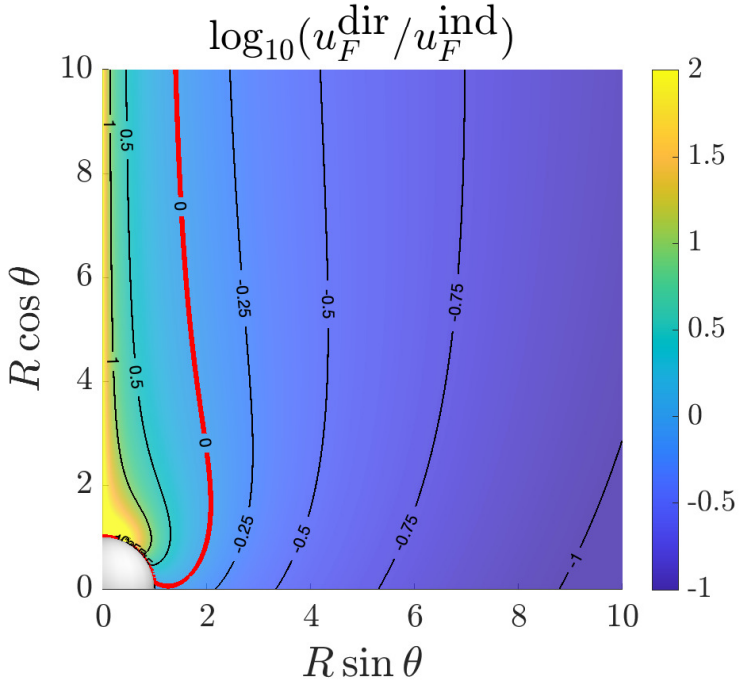

Figure 4.4 Contour plot of the ratio of direct to indirect polar advection, $u_F^{\mathrm{dir}}/u_F^{\mathrm{ind}}$, as induced by flagellar thrust. The magnitude is displayed using a logarithmic scale. The thick red line indicates the boundary where direct and indirect interactions exactly balance ($u_F^{\mathrm{dir}}/u_F^{\mathrm{ind}} = 1$). At close separation and for short filaments direct interactions dominate, while for large separation and long filaments the balance is reversed.

separation decreases; this is true in the singular representation used here and is also true for real finite-sized filaments. Direct effects dominate therefore at close separation between the filaments, while passive effects dominate at wide separations. Thinking in terms of a dynamic bundling process, we therefore obtain that indirect effects dominate at early stages, and are then surpassed by the direct interactions when the separation between the filaments decreases and they enter each other's 'wake'.

Another important conclusion obtained from Fig. 4.4 is that indirect effects are more important for large R, i.e. for long flagellar filaments relative to the cell body. Indeed, for a fixed value of R, we see that a larger proportion of the θ-range is indirect-dominated. Furthermore, as $R \to \infty$ with the separation angle θ fixed, the direct advection decays to zero, while the indirect component tends to a finite value, $\frac{1}{2}\sin\frac{\theta}{2}|\boldsymbol{U}|$, because the filaments are moving in the body frame of the cell, whose swimming speed asymptotes to a finite value. The converse is true in the limit of short filaments, i.e. $R \to 1$, where direct interactions always dominate. This is because the swimming speed disappears, $|\boldsymbol{U}| \to 0$, as $R \to 1$, due to the backwards drag that short flagella exert on the cell body (i.e. $\alpha \to -1$ in Eq. 4.16).

4.4 Advection induced by flagellar rotation

In section §4.3 we analysed the effect of flagellar thrust on bundling by modelling individual filament as radial Stokeslets. Here we conduct a similar analysis for the flow induced by flagellar rotation and therefore focus on the flows created by rotlets, i.e. point torques. While thrust generates both direct and indirect polar flows that act to reduce the separation between flagellar filaments, we show here that the flows created by rotation only have components in the azimuthal direction, and therefore lead only to relative rotation but not, on their own, to a relative change in the separation between the filaments.

The expression for a radial rotlet located outside a rigid sphere was recently derived in Ref. [38]. The flow field can be written as

$$\boldsymbol{u}(\boldsymbol{x}) = \boldsymbol{G}_1 \times \left[\mathcal{R}(\boldsymbol{x} - \boldsymbol{x}_1) + \delta\mathcal{R}(\boldsymbol{x} - \boldsymbol{x}_1^*)\right], \tag{4.23}$$

$$\boldsymbol{G}_1 = G\boldsymbol{e}, \tag{4.24}$$

$$\delta = -R^{-3}, \tag{4.25}$$

$$\mathcal{R}(\boldsymbol{x}) = -\frac{1}{8\pi\mu}\boldsymbol{\nabla}\frac{1}{|\boldsymbol{x}|}, \tag{4.26}$$

and the image system may be interpreted as simply due to a single rotlet located at the mirror image point $\boldsymbol{x}_1^*$. As claimed, the only non-zero component of $\boldsymbol{u}$ is in the azimuthal ϕ-direction, decoupling it therefore from advection due to thrust. This direct component, which we denote by u_G^{dir}, is given by

$$u_G^{\mathrm{dir}} \equiv \hat{\boldsymbol{\phi}} \cdot \boldsymbol{u}(\boldsymbol{x}_2) = \frac{GR}{8\pi\mu}\left[\frac{1}{r^3} - \frac{1}{(Rr^*)^3}\right]\sin\theta, \tag{4.27}$$

where $\hat{\boldsymbol{\phi}} = (0, 1, 0)$.

In order to compute the indirect interactions, we need to calculate the torque $\boldsymbol{G}_{\mathrm{tot}}$ exerted by the cell body on the fluid. In analogy with Eq. (4.16) it is

$$\begin{aligned}\boldsymbol{G}_{\mathrm{tot}} &= -\sum_i (1+\delta)\boldsymbol{G}_i \\ &= 2G(1+\delta)\cos\frac{\theta}{2}\left(-\sin\frac{\theta}{2}, 0, -\cos\frac{\theta}{2}\right),\end{aligned} \tag{4.28}$$

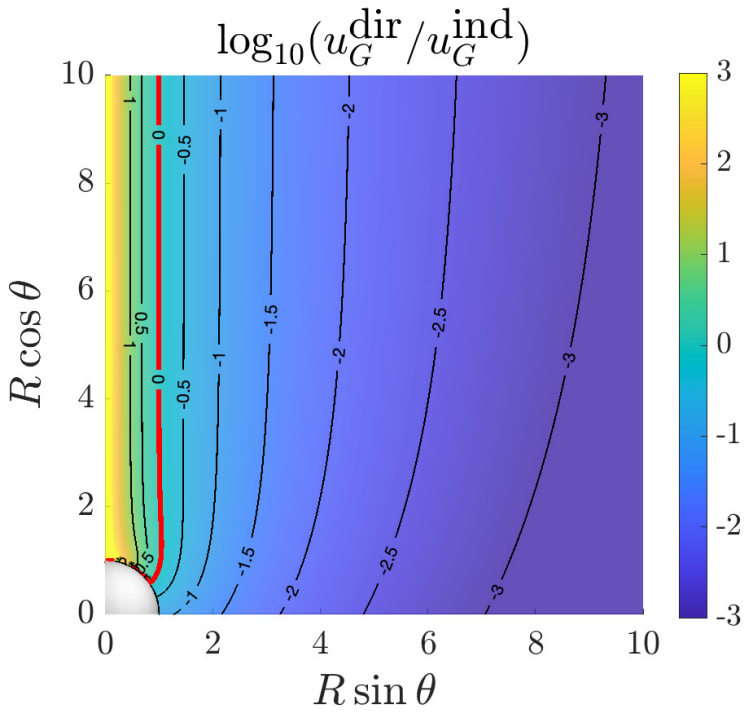

Figure 4.5 Contour plot of the ratio between direct and indirect azimuthal advection, $u_G^{\mathrm{dir}}/u_G^{\mathrm{ind}}$, due to flagellar rotation (logarithmic scale). The thick red contour indicates the boundary where direct and indirect interactions exactly balance. As for the thrust, direct rotation dominate at close separation of the filaments, while indirect rotation dominates for large separation.

and $-1 < \delta < 0$ for $R > 1$. Neglecting the viscous drag on the filaments, the rotation rate of the cell body is then found to have magnitude

$$|\boldsymbol{\Omega}| = \frac{G}{4\pi\mu}\left(1 - R^{-3}\right)\cos\frac{\theta}{2}, \tag{4.29}$$

where we used the well-known value for the rotational drag on a unit sphere, $\boldsymbol{G} = -8\pi\mu\boldsymbol{\Omega}$ [127]. The indirect swirling flow experienced in the body frame is then found from the classical formula for the flow due to a rotating rigid sphere,

$$\boldsymbol{u}(\boldsymbol{x}) = \frac{\boldsymbol{G}_{\mathrm{tot}}}{8\pi\mu} \times \{\boldsymbol{\mathcal{R}}(\boldsymbol{x}) - \boldsymbol{x}\}, \tag{4.30}$$

which again only has an azimuthal component,

$$u_G^{\mathrm{ind}} \equiv \hat{\boldsymbol{\phi}} \cdot \boldsymbol{u}(\boldsymbol{x}) = \frac{GR}{8\pi\mu}\left(1 - R^{-3}\right)^2 \sin\theta. \tag{4.31}$$

Hence the ratio between direct (Eq. 4.27) and indirect (Eq. 4.31) rotational advection is given by

$$\frac{u_G^{\mathrm{dir}}}{u_G^{\mathrm{ind}}} = \frac{r^{-3} - (Rr^*)^{-3}}{\left(1 - R^{-3}\right)^2}. \tag{4.32}$$

In Fig. 4.5 we illustrate this ratio as we did for the thrust in §4.3.3 (Fig. 4.4). The result is very similar in its general shape and features to, but there are a couple of notable differences. The region of direct dominance is smaller, with Eq. (4.32) implying that

$$R \sin\theta \to 1, \quad \text{as } R \to \infty, \tag{4.33}$$

and we also note a smaller bulge of the dividing contour for small values of the flagellar length R. This is for two reasons. The first is that the direct rotational interactions decay faster, since the rotlet decays as $1/r^2$ while the Stokeslet (which is absent here) decays as $1/r$. The second is that hydrodynamic interactions with the cell body are less significant, and therefore for short filaments, i.e. small values of R, the indirect interactions are stronger. Another difference is that, in the case of rotation, the dominance of indirect advection is generally stronger in magnitude (compare scales for the colour scheme in Figs. 4.4 and 4.5). This is again due to the faster spatial decay of the rotlet flow.

We note that the close separation between singularities and cell body is modelled accurately even in the limit $R \to$. The theory breaks down if the singularities (i.e. the filaments) are very close to another, this is not the case here.

4.5 Dynamic elastohydrodynamic model

4.5.1 Motivation

While the minimal model allows us to calculate and compare hydrodynamic interactions exactly, it can only do so under very simplified modelling assumptions. In particular, it does not take into account the fact that flagellar filaments are flexible and tethered at their base to a fixed location on the cell body. It is also limited by the assumption that the filaments point radially outward, and only applies instantaneously. In order to address these shortcomings, we complement our theory with a numerical elastohydrodynamic model and use it to simulate the bundling dynamics of the helical axes of two inextensible flexible flagellar filaments.

Numerous sophisticated computational models have been proposed to tackle the bundling of bacterial flagella [4, 69, 118]. These numerical approaches usually employ variants of the

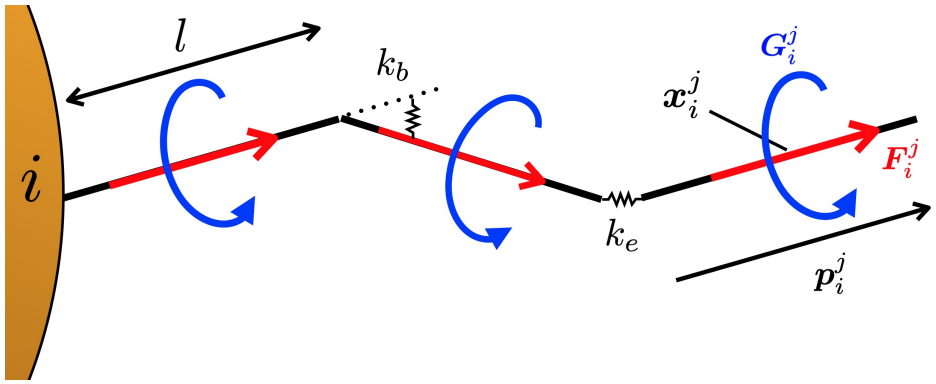

Figure 4.6 Sketch of the computational model. The helical axis of each flagellar filament, labelled by i, is divided into straight rod segments labelled by j, each of length l, orientation $\boldsymbol{p}_i^j$ (unit vectors), and centred at $\boldsymbol{x}_i^j$. A force $\boldsymbol{F}_i^j$ and torque $\boldsymbol{G}_i^j$, each parallel to $\boldsymbol{p}_i^j$, act on the fluid at location $\boldsymbol{x}_i^j$. Segments are connected by extensional springs of stiffness k_e and torsional springs of stiffness k_b.

boundary element method and slender-body theory, resolving the structure of the flagellar helix exactly and obtaining accurate approximations to cellular dynamics. However, by calculating flow velocities using such realistic computational method, some of the physical origin of the induced flows can be difficult to grasp. Here, instead of attempting to model the details of the flagellar filament geometry, we follow an approach similar to past work on the rheology and dynamics of fibres and polymers, which models each flagellum as a rod-spring chain [49, 79, 114, 116, 195, 205, 255]. Specifically, we propose a rod-spring singularity model that describes the dynamics of the *helical axis* of each flagellar filament. After summarising the model setup in §4.5.2, we use it in §4.5.3 to quantify the individual contributions of direct and indirect hydrodynamic interactions during the dynamic bundling process.

4.5.2 Computational modelling

An illustration of our computational model is shown in Fig. 4.6. We divide the helical axis of the ith flagellar filament into N straight segments that we label by $j = 1, \ldots, N$. We call the outward pointing unit tangent vector to each segment $\boldsymbol{p}_i^j$. At the centre point of each segment $\boldsymbol{x}_i^j$ we place a point force $\boldsymbol{F}_i^j$ and a point torque $\boldsymbol{G}_i^j$ that are both parallel to, and pointing in the same direction as, $\boldsymbol{p}_i^j$ and have magnitudes $|\boldsymbol{F}_i^j| = |\boldsymbol{F}_i|/N$ and $|\boldsymbol{G}_i^j| = |\boldsymbol{G}_i|/N$ respectively. The first segment is tethered to a point on the cell body, and the segments are linked by extensional and torsional springs of stiffness k_e and k_b, respectively. Since the axial length of each filament is L, each segment has length $l = L/N$. The cell body has unit radius as in the minimal model. In contrast however, we now allow the forces and torques to have an arbitrary orientation, since

$\boldsymbol{p}_i^j$ need not point in the radial direction at all times. For our numerical calculations we use the analytical expressions for the corresponding image systems and flows that are available in Ref. [127] for the Stokeslet and in Ref. [38] for the rotlet.

For each filament (omitting the index i for clarity) the set of $2N$ vectors $\{\boldsymbol{x}^j, \boldsymbol{p}^j\}$ is subject to the evolution equations

$$\dot{\boldsymbol{x}}^j = \sum_{n=1}^{N} \boldsymbol{u}_k^{\mathrm{dir},n}\left(\boldsymbol{x}^j\right) + \boldsymbol{u}^{\mathrm{ind}}\left(\boldsymbol{x}^j\right) + \mathbb{A}^{-1,j} \cdot \left(\boldsymbol{f}_{\mathrm{ex}}^{j+1} - \boldsymbol{f}_{\mathrm{ex}}^{j} + \boldsymbol{f}_{\mathrm{ster}}^{j}\right), \tag{4.34}$$

$$\dot{\boldsymbol{p}}^j = \boldsymbol{\omega}^j \times \boldsymbol{p}^j, \tag{4.35}$$

where

$$\boldsymbol{\omega}^j = \mathbb{C}^{-1,j} \cdot \left[\frac{l}{2}\boldsymbol{p}^j \times \left(\boldsymbol{f}_{\mathrm{ex}}^{j+1} + \boldsymbol{f}_{\mathrm{ex}}^{j}\right) + h^j \boldsymbol{p}^j \times \boldsymbol{f}_{\mathrm{ster}}^{j} + \boldsymbol{g}_{\mathrm{bend}}^{j+1} - \boldsymbol{g}_{\mathrm{bend}}^{j}\right]. \tag{4.36}$$

The first term on the right-hand side of Eq. (4.34) describes advection due to direct hydrodynamic interactions. Here $k \neq i$ labels the second filament, so that direct interactions with the individual forces and torques from the other filament are included, but self-interactions are neglected.

The second term on the right-hand side of Eq. (4.34) describes advection due to indirect interactions. These are found by first solving for the swimming kinematics of the cell body (as we did for the minimal model) and then applying the classical solution for flow due to a translating and rotating rigid sphere [127]. For this, we again need to find the total hydrodynamic force $\boldsymbol{F}_{\mathrm{tot}}$ and torque $\boldsymbol{G}_{\mathrm{tot}}$ exerted by the cell body onto the fluid. Using expressions from Refs. [38, 127] for the hydrodynamic interactions with the cell body these become

$$\boldsymbol{F}_{\mathrm{tot}} = \sum_{i,j}\left[\left(\frac{3}{4R_i^j} + \frac{1}{4{R_i^j}^3} - 1\right)\boldsymbol{F}_i^j + \left(\frac{3}{4R_i^j} - \frac{3}{4{R_i^j}^3}\right)\boldsymbol{F}_i^j \cdot \hat{\boldsymbol{r}}_i^j \hat{\boldsymbol{r}}_i^j - \frac{3}{4{R_i^j}^2}\boldsymbol{G}_i^j \times \hat{\boldsymbol{r}}_i^j\right], \tag{4.37}$$

$$\boldsymbol{G}_{\mathrm{tot}} = \sum_{i,j}\left[\left(-\frac{1}{2{R_i^j}^3} - 1\right)\boldsymbol{G}_i^j + \frac{3}{2{R_i^j}^3}\boldsymbol{G}_i^j \cdot \hat{\boldsymbol{r}}_i^j \hat{\boldsymbol{r}}_i^j + \left(R_i^j - \frac{1}{{R_i^j}^2}\right)\boldsymbol{F}_i^j \times \hat{\boldsymbol{r}}_i^j\right], \tag{4.38}$$

where $\boldsymbol{x}_i^j = R_i^j \hat{\boldsymbol{r}}_i^j$.

The remaining terms in Eqs. (4.34) and (4.36) describe dynamic forces due to extension, steric interactions and bending. The tensors $\mathbb{A}^{-1,j}$ and $\mathbb{C}^{-1,j}$ are hydrodynamic motility tensors for the segments, which are approximated by the corresponding expressions for prolate ellipsoids [127] with a short semi-axis length equal to r (the filament radius) and the long semi-axis length equal to $l/2$ (the segment length). The long axis is parallel to $\boldsymbol{p}^j$ by definition, which introduces the explicit dependence on j.

The extensional restoring force exerted on the $(j-1)$th segment by the hinge linking it to the jth segment, $\boldsymbol{f}^j_{\text{ex}}$, is given by

$$\boldsymbol{f}^j_{\text{ex}} = k_e \left[\boldsymbol{x}^j - \boldsymbol{x}^{j-1} - \frac{l}{2}\left(\boldsymbol{p}^j + \boldsymbol{p}^{j-1}\right)\right], \tag{4.39}$$

where k_e is the strength of a Hookean elastic spring. Since real flagella are almost inextensible, we choose k_e sufficiently large to suppress any significant extension of the filament.

Steric interactions are often included in elastohydrodynamic models to avoid the overlapping of physical filaments. In our case they serve the additional purpose of maintaining a minimum distance between individual singularities. Since the singularities are located on the helical axis of the flagellar filaments, we use these steric interactions to prevent an approach of less than ρ, the radius of the flagellar helix (i.e. the radius of the cylinder on which the helix is coiled). Specifically, we choose

$$\boldsymbol{f}^j_{\text{ster,i}} = k_s \exp\left(-20\frac{|\boldsymbol{d}^j_{ik}| - \rho}{\rho}\right)\frac{\boldsymbol{d}^j_{ik}}{|\boldsymbol{d}^j_{ik}|}, \tag{4.40}$$

where k_s is the strength of the interaction, and

$$\boldsymbol{d}^j_{ik} = \boldsymbol{x}^j_i + h^j_i \boldsymbol{p}^j_i - \boldsymbol{x}^j_k + h^j_k \boldsymbol{p}^j_k, \tag{4.41}$$

and

$$h^j_i = \frac{\left(\boldsymbol{x}^j_k - \boldsymbol{x}^j_i\right)\cdot\left(\boldsymbol{I} - \boldsymbol{p}^j_k\boldsymbol{p}^j_k\right)\cdot\boldsymbol{p}^j_i}{1-\left(\boldsymbol{p}^j_i\cdot\boldsymbol{p}^j_k\right)^2}, \quad h^j_k = \frac{\left(\boldsymbol{x}^j_i - \boldsymbol{x}^j_k\right)\cdot\left(\boldsymbol{I} - \boldsymbol{p}^j_i\boldsymbol{p}^j_i\right)\cdot\boldsymbol{p}^j_k}{1-\left(\boldsymbol{p}^j_i\cdot\boldsymbol{p}^j_k\right)^2}, \tag{4.42}$$

are the distances from the midpoint of the $\{i,j\}$-th and $\{k,j\}$-th segment, respectively, where the steric forces act. Since the segments have a finite length l, the force is set to zero if $|h^j_i| > l/2$ or $|h^j_k| > l/2$. By symmetry of the dynamics, only N different interactions are possible and need to be calculated.

Finally, the bending torque exerted on the $(j-1)$th segment by the hinge connecting to the jth segment, $\boldsymbol{g}^j_{\text{bend}}$, is included as

$$\boldsymbol{g}^j_{\text{bend}} = k_b \boldsymbol{p}^{j-1} \times \boldsymbol{p}^j, \tag{4.43}$$

Parameter	Symbol	Value	Source
Fluid viscosity	μ	1.00 mPa s	[96]
Cell body radius		1 µm	[51], see text.
Bending stiffness	EI	3.5 pN µm^2	[51]
Helix radius	ρ	0.2 µm	[51]
Helix pitch	P	2.22 µm	[51]
Filament thickness	d	12 nm	[51]
Filament rotation rate	$\lvert\boldsymbol{\Omega}_i\rvert$	697 s^{-1}	[51]
Thrust per length	$\lvert\boldsymbol{F}_i\rvert/L$	89.9 fN µm^{-1}	Eq. (4.2)
Torque per length	$\lvert\boldsymbol{G}_i\rvert/L$	87.0 fN	Eq. (4.3)
# of segments per length	N/L	2 µm^{-1}	N/A
Steric force constant	k_s	400 pN	N/A
Extensional spring constant	k_e	100 pN µm^{-1}	N/A
Flagellar axial length	L	4, 6, 8 µm	[51], see text.
Base separation angle	θ	$\pi/8, \pi/4, 3\pi/8, \pi/2$	N/A

Table 4.1 Experimentally-obtained physical parameters for our computational elastohydrodynamic model as applicable to the swimming of *E. coli*. We assume that the motor rotation rate $|\boldsymbol{\Omega}_i|$, rather than the motor torque $|\boldsymbol{G}_i|$, is held constant in order to compare filaments of different lengths l.

where k_b is a torsional spring, related to the bending modulus of the filament, EI, as $k_b = EI/l$. At the base where the more flexible hook is located, we choose $k_{b,\text{hook}} = k_b/20$ in agreement with Ref. [114].

Two physical contributions are absent from Eq. (4.36), namely vorticity and torsion. Vorticity influences the rotation of filament segments but neglecting it is justified by the stiffness and inextensibility of the filament, since the strengths of the extensional and torsional springs k_e and k_b are sufficiently large to dominate the dynamics. The torsion term is neglected following the scaling argument presented in Ref. [187], which shows that torsion is insignificant compared to extension and bending.

4.5.3 Numerically simulated filament dynamics

Our computational model has a large number of parameters, so we take representative values for many of them from the experimental literature. We focus on the model bacterium *E. coli*, and summarise these values in Table 4.1. We note that there exists considerable spread in the bending moduli of flagellar filaments across species [120, 124], as well as specifically for *E. coli* in the flagellar length [237] and estimates for the motor torque [52]. Nevertheless,

these representative values are sufficient to gain an understanding of the general dynamics of bundling.

We also make the simplifying assumption that the cell body is spherical. In reality, *E. coli* resembles a prolate ellipsoid [51], and here we choose the sphere radius to be comparable to the cell's long semi-axis. This assumption allows us to include hydrodynamic interactions analytically with no need for a mesh and the use of boundary element or similar methods. We also restrict our attention to two flagella in order to focus on the simplest possible setup where hydrodynamic interactions can be measured; real *E. coli* features between two and five flagella [185].

We simulate the cell and flagella dynamics for axial lengths $L = 4, 6, 8\,\mu\text{m}$ and base separation angles $\theta = \pi/8, \pi/4, 3\pi/8, \pi/2$. An axial length $L = 6.0\,\mu\text{m}$ corresponds to a filament length of $\Lambda \approx 6.9\,\mu\text{m}$, close to the average for *E. coli* [51]. The values $L = 4\,\mu\text{m}$ and $8\,\mu\text{m}$ correspond to short and long flagella respectively.

First, in order to gain a general understanding of the bundling process we analyse the dynamics for $L = 6\,\mu\text{m}$ and $\theta = \pi/2$ in detail, before considering their variation for different values of L and θ. The filament axes are initialised as pointing straight radially outwards. In Fig. 4.7 we plot snapshots of the resulting bundling dynamics, as viewed in the laboratory frame (see also the Supplementary Material [1] for movies showing the dynamics in both the body frame and the laboratory frame). As the cell body rotates, the orientation of the axis segments remains nearly fixed in space, but due to cell body rotation they are being pulled at the base. After half a revolution, the filaments are sufficiently close for direct hydrodynamic interactions to have an effect. Over the course of another revolution of the cell body the axes of the filaments then slowly wrap around each other to form a bundle. The entire process takes about 0.3 s, a result which is consistent with experimental observations [17, 51].

We compute the ratio of direct to indirect advection at various points along the filament axis, and show the results in Fig. 4.8. Here each line, labelled by j, corresponds to one segment on the filament axis, with $j = 1$ referring to the one linked to cell body, and $j = 12$ referring to the free end of the flagellum. The quantities u^{dir} and u^{ind} are computed by projecting the corresponding velocity vector at $\boldsymbol{x}_i^j$ into the plane perpendicular to $\boldsymbol{p}_i^j$ and calculating the norm of that projection. In this analysis we combine force- and torque-induced advection into one quantity; a study where forces and torques are computed separately yields a picture that is qualitatively similar to the one shown in Fig. 4.8.

We then observe in Fig. 4.8 that during the bundling process indirect interactions dominate everywhere along the filaments at early stages, consistent with the prediction from the minimal model. Moreover, the dominance is stronger at the outer ends, again consistent with our theoretical results. As the bundling process progresses, direct interactions become gradually

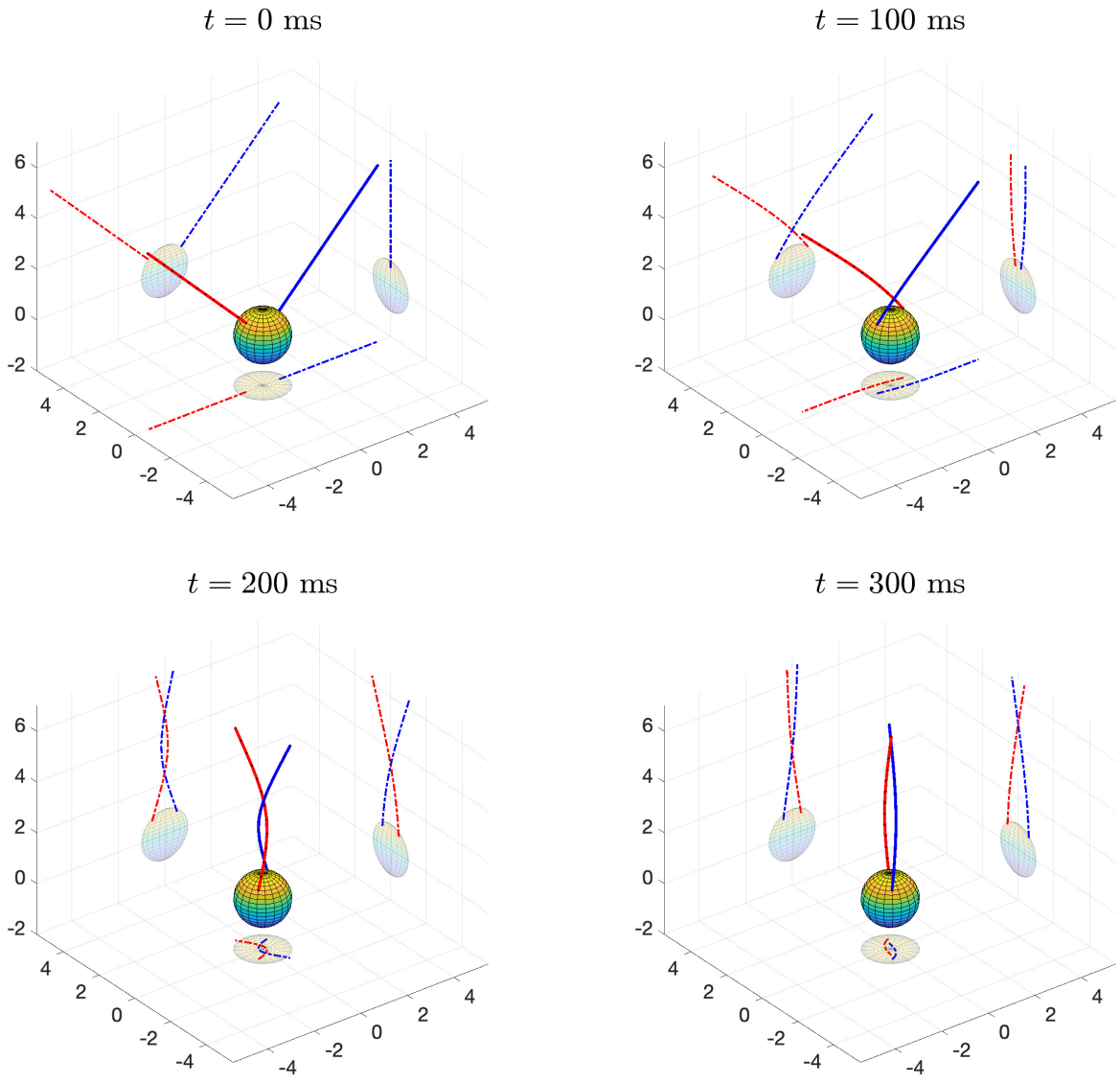

Figure 4.7 Snapshots of the bundling dynamics for $L = 6\,\mu\text{m}$ and $\theta = \pi/2$ viewed in the laboratory frame. The axes of the helical filaments are plotted in red and blue respectively with black dots representing hinges between segments. Shadows are drawn in dashed lines on three orthogonal planes to aid visualisation.

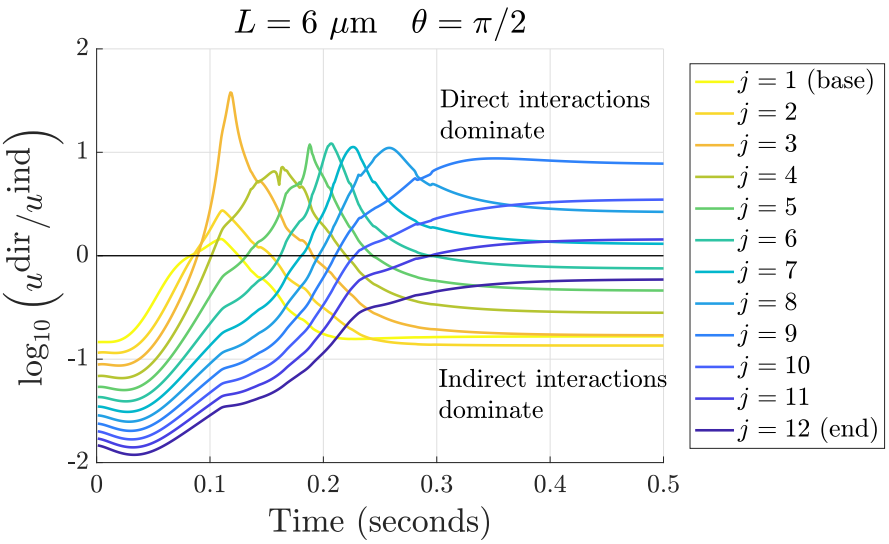

Figure 4.8 Ratio of direct and indirect interactions along the filament axis during the bundling process, obtained using the computational elastohydrodynamic model for filaments of axis length $L = 6\,\mu\text{m}$ and base separation angle $\theta = \pi/2$ with $N = 12$ segments. Log-ratios for all segments from the base ($j = 1$, yellow) to the end of the flagellum ($j = 12$, blue) are shown.

more important. Interestingly, they peak in each case, first at the base and then with delay further along the filament. For $j \geq 10$ the balance shift is monotonic, and along the entire filament the ratio plateaus once the bundle is formed. Surprisingly, the ratio is not monotonic along the filament in this final state. The dominance of direct effects is strongest for $j = 9$, three quarters along the filament, while at the base and at the free end the balance is even shifted again in favour of indirect contributions. At the base this is due to the tether preventing a close approach. On the other hand, the ends of the filaments are the furthest away from the cell body centre and hence subject to the strongest indirect flows. The stiffness of the filaments is another contributing factor to this effect, since the absence of a bending moment at the free end requires the filaments to be straight there, as can also be seen in Fig. 4.7.

Having analysed one case in detail, we now ask how the bundling dynamics depend on the geometric parameters. To this end we illustrate in Fig. 4.9 results for different values of the filament axial length L and the angle between the motors θ. For clarity we only plot three lines in each case, representing the base, middle and end of the flagellum respectively (the specific values of the element j plotted are listed in the caption of Fig. 4.9).

At close separation, $\theta = \pi/8$, the dynamics are very similar for different filament lengths. In each case the shift from indirect to direct interactions is nearly monotonic, and occurs first at the base, then in the centre and finally at the end. In the case of long flagella however, we observe that in the final state direct interactions are strongest close to the centre points of the

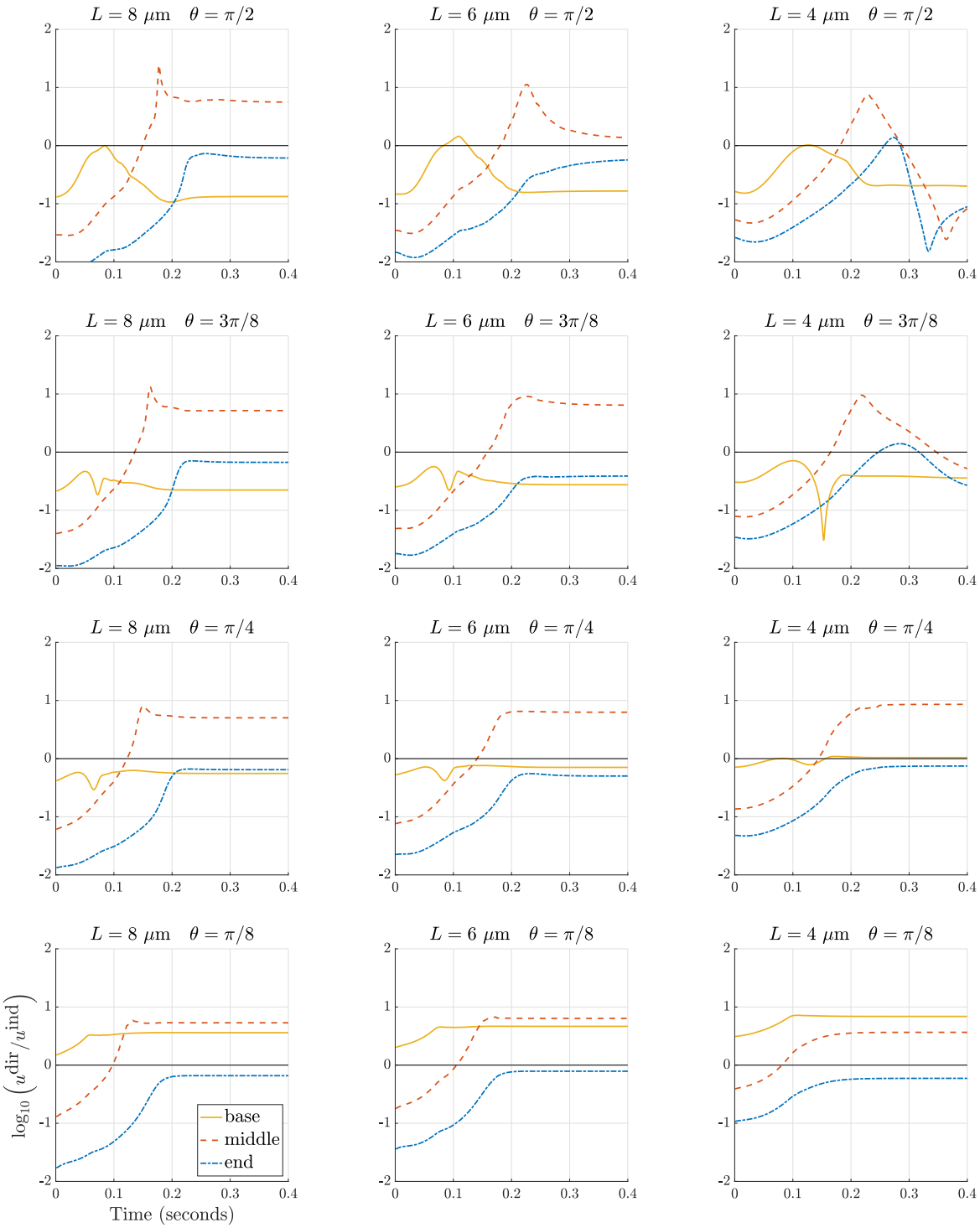

Figure 4.9 Computed bundling dynamics for filament axial lengths $L = 4$, 6 and 8 µm (with $N = 8$, 12, 16 respectively) and $\theta = \pi/8$, $\pi/4$, $3\pi/8$ and $\pi/2$. Lines are drawn for three representative values of j at the base of the flagellar filament (yellow), middle (red, dashed) and end (blue, dash-dotted), which are $j = \{1, 5, 8\}$, $\{1, 7, 12\}$ and $\{1, 9, 16\}$ for $L = 4$, 6, 8 µm respectively.

filament. This effect is significantly more pronounced when the filaments are more widely separated at their base. This is due to the stiffness of the filaments, which makes it harder to align their free ends if they are bundled at an angle.

For short filaments, $L = 4\,\mu\text{m}$, we note that a bundle fails to form if $\theta \geq 3\pi/8$. As shown in the Supplementary Material [1], the filament axes touch after half a revolution of the cell body but instead of wrapping they slide past each other until they reach an aligned steady state. During this sliding process the separation between them increases, which explains the non-monotonic behaviour of the advection ratio.

4.6 Discussion

In this chapter we defined the notion of direct and indirect advection of bacterial flagellar filaments, and used it to classify the fundamental flows contributing to the bundling process. In addition we derived a computational elastohydrodynamic model that corroborates our predictions and leads to new ones.

First, we saw that the generation of thrust by flagella is sufficient to initiate bundling through hydrodynamic interactions. This follows from the fact that both the direct and indirect interactions, computed in Eq. (4.15) and Eq. (4.20) respectively, lead to non-zero advection towards a bundle in the entire geometric parameter range. Secondly, for both thrust- and rotation-induced flows indirect advection always dominates for long filaments and at wide separation, i.e. during the early stages of the bundling process. The shape of the boundary between direct- and indirect-dominated regions suggests a 'wake' that a flagellar filament is generating behind the cell body with a width on the order of the cell body diameter. In other words, indirect interactions dominate unless the filaments are in each other's wake. Thirdly, in terms of the dynamic bundling process, the relative contribution of direct and indirect effects was seen to depend on the length of the flagellum, with active contributions being more important the shorter the flagellar filaments are.

Fourthly, the rotation of the flagella only generates flows in the azimuthal direction and thus does not facilitate bundling purely through hydrodynamic effects. However, as evidenced by our computational model, they do play a role in conjunction with other physical constraints, such as tethering. This was already known for direct hydrodynamic interactions [125, 156], and here we demonstrate that it holds true for indirectly generated flows as well. Finally, from the computational model we see that the shift in balance between direct and indirect effects is non-monotonic during the bundling process, with a peak in direct dominance, and furthermore that different sections of the flagella are affected by these changes to different extents.

Naturally, by reducing the system to two geometric parameters we made a number of simplifying assumptions. In reality, cells are slightly denser than water (for *E. coli* $\rho \approx 1.08\ \mathrm{g\,ml^{-1}}$ [129] while for water $\rho \approx 1.00\ \mathrm{g\,ml^{-1}}$), also their cell body is normally better approximated by a prolate spheroid and they feature more than two flagella [17]. Furthermore, we restricted our attention to two flagella, while *E. coli* features between two and five [185]. A particularly interesting direction to explore with this framework would be the dynamics of more than two flagella, since in that case much of the symmetry of this problem is lost, which could lead to more complex dynamics. In addition, our model might lead to a better understanding of the unbundling process, which triggers the 'tumble' gait of multi-flagellated bacteria. When a peritrichous bacterium reverses the direction of one flagellar motor to clockwise rotation, the torque exerted by that flagellum is reversed. However, the total torque, and hence the strength of the indirect advection, is weakened but not cancelled due to continuing counter-clockwise rotation of the remaining flagella, thus acting to keep the bundle together at the end. These indirect effects may therefore provide the physical mechanism for the apparent 'pulled out' motion of the clockwise rotating flagellum observed at the base of the flagellar bundle [51].

Chapter 5

Stochastic dynamics of dissolving active particles

5.1 Introduction

In recent years, scientists from a wide variety of different fields have given considerable attention to the subject of synthetic microswimmers. This focus in research is no coincidence, as such colloids show great promise in biomedical and engineering applications [168, 250, 253]. The design of autonomous swimmers in particular has received significant theoretical and experimental attention [66, 164]. In an effort to exploit the peculiarities of the associated low-Reynolds number hydrodynamics [189], many different propulsion mechanisms have been invented. These include self-phoretic propulsion, such as chemophoresis [24, 86, 161, 249] and electrophoresis [62, 163, 179], as well as ultrasound propulsion [74, 166, 252], bubble propulsion [82, 251] and magnetic propulsion [80, 264].

Despite this remarkable progress, common experimental designs still need to be improved in order to be suitable for sensitive applications, such as non-invasive medicine. Next to potential toxicity of swimmer components or their fuel [78], the question of waste disposal remains largely open. This can be a serious problem, since artificial micron sized particles in the blood stream have the potential to cause clogging [9, 70, 204] and may thus pose a significant health risk [70, 169]. It is therefore essential to develop designs for microswimmers that degrade after fulfilling their purpose.

Very recently, novel experimental designs have begun to address these issues. Examples of such colloids include non-toxic magnesium-based bubble propelled swimmers [42] suitable for aqueous environments, as well as other kinds of inorganic compositions driven by reactions in either acidic or alkaline environments [41]. More designs have been proposed using organic compounds that may be 3D-printed [254] or that self-assemble into nanomotors [235].

These experimental advances raise new theoretical questions. While the dynamics of classical non-dissolving colloids have been studied extensively, the time-evolution of colloid size modifies its stochastic behaviour, and new quantities characterising its physics emerge. The purpose of this chapter is therefore to provide theoretical answers to two fundamental questions. First, we examine which material and environmental parameters determine the lifetime of a dissolving spherical microswimmer. Second, we study the influence of dissolution on the stochastic behaviour of both passive and self-propelled colloids. Here, a new dimensionless quantity arises which splits microswimmers into two categories: those that are subject to sufficient amounts of thermal noise during their lifetime to evolve diffusively, and those that exhibit near-ballistic trajectories that may be exploited for delivery applications. We show that both scenarios may enter for realistic values of the material and environmental parameters. Knowledge of these and their scaling relations is thus essential for the application-specific engineering of degradable microswimmer designs.

The structure of this chapter is as follows. We begin by presenting two theoretical models for the dissolution process in §5.2, one suitable for designs in which the dissolution process is not driven by a reaction with a fuel in the solvent (such as dissolution by hydrogen bonding), and one for swimmers whose matrix is decomposed by means of a reaction (chemical or enzymatic). For further analysis the latter case is considered in the two limits of slow and fast reaction, the former corresponding to a fixed material flux boundary condition. In all these models we find expressions for the time dependence of the swimmer size, as well as their total lifetime in terms of the essential physical parameters. We present the necessary modification to classical Brownian motion in §5.3, and derive expressions for the passive mean squared displacement of not self-propelling colloids. Based on this, we next derive corresponding expressions for active motion in §5.4 and validate our results numerically. Finally we discuss the implications of our research on future studies in §5.5.

5.2 Dissolution models

Inspired by recent experimental realisations, we propose two models for the dissolution of a spherical colloid based on different possibilities for the boundary conditions at its surface. Specifically, we distinguish between the case in which dissolution occurs through binding colloid material to fluid molecules (for example, the case of ionic dissolution in water), which we call non-reacting, and the case of dissolution through a chemical or enzymatic reaction that consumes a fuel. In the latter scenario we distinguish further between the limits of slow and fast reaction, and discuss their physical implications.

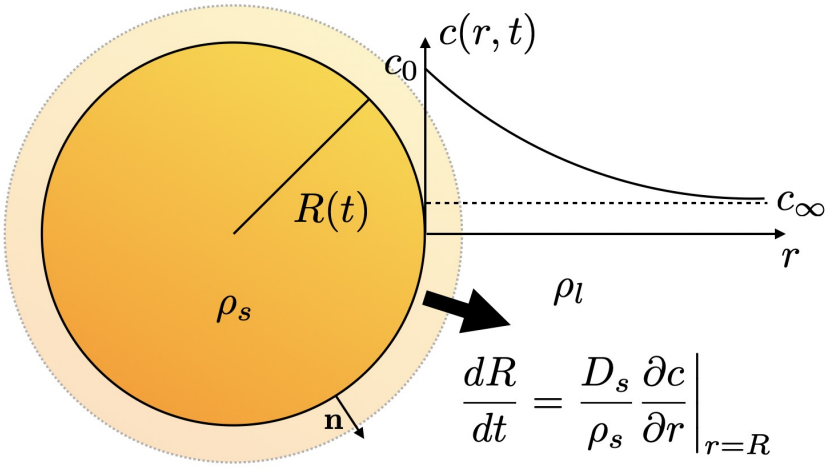

Figure 5.1 Schematic presentation of non-reacting dissolution dynamics. The matrix of the swimmer consists of a substance that dissolves by bonding to the fluid (thus acting as a solvent). Near the boundary, solute is present at a saturation concentration c_0 and subject to advective-diffusive transport in the bulk. Dissolution is facilitated through an osmotic imbalance generated by a normal concentration gradient at the swimmer surface.

As a preamble, we note that, unlike geophysical melting processes [258], there is no phase transition affecting the solvent in the dissolution processes considered in this chapter. This means the Stefan boundary condition does not apply and the dynamics we derived is different from e.g. the dissolution of ice crystals in water. While the general dynamics of diffusive dissolution have been considered in the geophysical literature [265], there has to the best of our knowledge been no study that derived the asymptotic solutions we compute below. This is likely due to the dominance of convection-driven processes on relevant geophysical scales that require different modelling [121].

5.2.1 Non-reacting swimmer

In our first model, we assume that the colloidal particle is composed of a material that dissolves in the surrounding fluid through bonding of solute colloid material to fluid molecules, as illustrated schematically in Fig. 5.1. We consider this an appropriate model for non-reacting dissolution processes, such as dissolution of many organic compounds as well as ionic salts in water. In order to keep the mathematics simple we make the simplifying assumption that only one species of solute is dissolved into the bulk. This allows us to define the (mass) concentration, $c(\boldsymbol{r}, t)$, of solute defined as the mass of solute dissolved in a unit volume of solvent, with $c = c_\infty \geq 0$ far away from the colloid. We note that this differs from the definition of molar concentration common in chemistry by a factor equal to the molar mass of the solute. We make

this choice in order to avoid clutter that would arise from the application of mass conservation below.

In this model and the following we assume the absence of any background flow that would disturb the distribution of solute or reactant in the bulk fluid. This assumption is of course violated for self-propelled particles moving relative to a background fluid. However, we can use a scaling argument to show that this does not affect our leading-order results. Since typical propulsion velocities U are expected to be on the order of a few microns per second, initial colloid radii R_0 on the scale of microns [66] and for many ions in water at room temperature the solute diffusivity is approximately $D_s \sim 10^{-9}$ m^2/s [96], the Péclet number quantifying the relative important of advection to diffusion for the solute is $\mathrm{Pe}_{\mathrm{sol}} = R_0 U/D_s \sim 10^{-4} - 10^{-3}$. This indicates that advection of solute can be safely neglected. This remains true even when the Péclet number associated with motion of the colloid, $\mathrm{Pe}_{\mathrm{col}} = R_0 U/D$ is large, since the particle is several orders of magnitude larger than a solvent molecule and therefore has a much smaller diffusivity. The same result applies to phoretic slip flows, which are typically of the same strength as the propulsion velocity. In the context of dissolution dynamics, the flows arising from propulsion can therefore be neglected in the transport processes of solute and reactant.

We further assume that the swimmer has a homogeneous mass density, ρ_s, and the fluid solvent a constant density, ρ_l. In general the density of the solvent depends weakly on the amount of solute dissolved [96]. However, we will soon develop an asymptotic analysis based on the assumption that the solubility is weak and therefore can neglect this effect. Finally, we assume also that the swimmer remains spherical at all times, and that that the dissolution dynamics is independent of any self-propulsion mechanism or background flow. Both these assumptions will be justified *a posteriori* in section §5.2.1. A brief discussion of the case of a partially dissolving swimmer is included our discussion §5.5.

Mathematical model

We consider a spherically symmetric colloid or radius $R(t)$ with initial condition $R(0) = R_0 > 0$. Near the boundary, there is a chemical equilibrium between solute attached to the swimmer surface and solute present in the fluid. In this case the dissolution process is driven by removal (through diffusion) of solute from a boundary layer into the bulk and subsequent replenishment from the swimmer surface (Fig. 5.1). We model this effect by imposing the boundary condition

$$c(R(t), t) = c_0 > c_\infty, \quad t \geq 0, \tag{5.1}$$

where c_0 is the saturation concentration of solute in the solvent. This condition assumes that the boundary layer is negligibly thin and that the surface reaches chemical equilibrium

instantaneously, which may be justified by noting that time scales of interest will be much larger than the molecular collision time, $\tau_{MC} \approx 10^{-13}$ s [96]. The other condition we impose is the requirement that the solute is initially distributed homogeneously in the bulk, i.e.

$$c(r, 0) = c_\infty, \quad r > R_0. \tag{5.2}$$

Conservation of solute at the boundary gives

$$4\pi R^2 \rho_s \frac{dR}{dt} = -(\text{solute flux into the fluid}) = -\left(-D_s 4\pi R^2 \frac{\partial c}{\partial r}\bigg|_{r=R}\right), \tag{5.3}$$

and therefore

$$\frac{dR}{dt} = \frac{D_s}{\rho_s} \frac{\partial c}{\partial r}\bigg|_{r=R}, \tag{5.4}$$

where D_s is the diffusivity of solute in the solvent.

Furthermore, in the case of unequal densities we also get a non-zero fluid flux at the boundary since by mass conservation there is equality

$$-\dot{R}\rho_s = (-\dot{R} + \boldsymbol{u} \cdot \hat{\boldsymbol{r}})\rho_l \tag{5.5}$$

and thus

$$\boldsymbol{u} \cdot \hat{\boldsymbol{r}} = \dot{R} \frac{\rho_l - \rho_s}{\rho_l}, \tag{5.6}$$

where $\hat{\boldsymbol{r}}$ denotes a unit vector in the outward radial direction.

For a self-propelled microscopic colloid in water, the Reynolds number, defined as the ratio of colloid radius times velocity divided by kinematic viscosity, is typically $\ll 1$ [12]. Therefore the fluid dynamics obey the incompressible Stokes equations,

$$\mu \nabla^2 \boldsymbol{u} = \nabla p, \quad \nabla \cdot \boldsymbol{u} = 0, \tag{5.7}$$

where μ is dynamic viscosity and p is the pressure field. Solving these with the boundary condition given in Eq. (5.6) at $r = R$ leads to the flow of a point source

$$\boldsymbol{u} = \dot{R} \frac{\rho_l - \rho_s}{\rho_l} \frac{R^2}{r^2} \hat{\boldsymbol{r}}. \tag{5.8}$$

The transport equation for $c(r, t)$ is the standard advection-diffusion equation

$$\frac{\partial c}{\partial t} + \nabla \cdot (c\boldsymbol{u}) = D_s \nabla^2 c. \tag{5.9}$$

Using the result of Eq. (5.8) together with incompressibility and assuming radial symmetry of the solute concentration, this becomes

$$\frac{\partial c}{\partial t} + \frac{\rho_l - \rho_s}{\rho_l}\frac{D_s}{\rho_s}\frac{R^2}{r^2}\frac{\partial c}{\partial r}\bigg|_{r=R}\frac{\partial c}{\partial r} = D_s\left(\frac{\partial^2 c}{\partial r^2} + \frac{2}{r}\frac{\partial c}{\partial r}\right), \tag{5.10}$$

Next we non-dimensionalise this transport equation using the scalings

$$c^* = \frac{c - c_\infty}{c_0 - c_\infty},\ R^* = \frac{R}{R_0},\ r^* = \frac{r}{R_0},\ t^* = \frac{D_s t}{R_0^2}. \tag{5.11}$$

Substituting in Eq. (5.10) and dropping stars in what follows for notational convenience, we obtain the colloid dynamics as solution to

$$\frac{dR}{dt} = \alpha_1 \frac{\partial c}{\partial r}\bigg|_{r=R} \tag{5.12}$$

with c solution to

$$\frac{\partial c}{\partial t} + \frac{R^2}{r^2}(\alpha_1 - \beta_1)\frac{\partial c}{\partial r}\bigg|_{r=R}\frac{\partial c}{\partial r} = \left(\frac{\partial^2 c}{\partial r^2} + \frac{2}{r}\frac{\partial c}{\partial r}\right), \tag{5.13}$$

with dimensionless boundary conditions

$$c(R(t), t) = 1,\ t \geq 0, \quad \text{and} \quad c(r, 0) = 0,\ r > 1, \tag{5.14}$$

where we have defined the two dimensionless parameters

$$\alpha_1 = \frac{c_0 - c_\infty}{\rho_s}, \quad \beta_1 = \frac{c_0 - c_\infty}{\rho_l}. \tag{5.15}$$

We note that despite a negligibly small solute Péclet number, it was necessary to include an advective term due to volume conservation, whose relative strength is given by $(\alpha_1 - \beta_1)$. It is therefore independent of the Péclet number and the fact that it is small at leading order will be only a consequence of the weak solubility assumption. Only when there is no density mismatch between colloid and fluid is this term identically zero. Furthermore, the swimmer radius remains constant when the solvent is saturated with solute, as may be expected intuitively.

Asymptotic solution

In order to make analytical progress, we make the assumptions that

$$\alpha_1 \ll 1, \quad \beta_1 \ll 1, \tag{5.16}$$

which corresponds to a low-solubility limit for the colloid material. We can then develop an asymptotic expansion to solve for c and R. Here we will only calculate the leading-order solution, but our setup allows for calculations to arbitrarily high orders. We proceed by a rescaling of our spatial coordinate as

$$x = \frac{r}{R}, \quad y(x,t) = xc(x,t), \tag{5.17}$$

so that our system becomes

$$R^2\frac{\partial y}{\partial t} + R\dot{R}y + (\alpha_1 - \beta_1)\left(\frac{1}{x^2}\frac{\partial y}{\partial x} - \frac{y}{x^3}\right)\left(\left.\frac{\partial y}{\partial x}\right|_{x=1} - 1\right) = \frac{\partial^2 y}{\partial x^2} \tag{5.18}$$

and

$$R^2 = 1 + 2\alpha_1\left(\int_0^t \left.\frac{\partial y}{\partial x}\right|_{x=1} dt' - t\right) \tag{5.19}$$

with boundary conditions

$$y(1,t) = 1, \quad y(x,0) = 0. \tag{5.20}$$

The solution may be written as

$$y(x,t;\alpha_1,\beta_1) = y_0(x,t) + \alpha_1 y_\alpha(x,t) + \beta_1 y_\beta(x,t) + o(\alpha_1,\beta_1). \tag{5.21}$$

The problem for y_0 reduces to the one-dimensional heat equation with Dirichlet boundary conditions and its solution is well known to be

$$y_0(x,t) = \operatorname{erfc}\left(\frac{x-1}{2\sqrt{t}}\right), \tag{5.22}$$

whence to leading order

$$R^2 = 1 - 2\alpha_1\left(t + 2\sqrt{\frac{t}{\pi}}\right), \tag{5.23}$$

or, after reinserting dimensions, we obtain our desired result

$$R(t) = R_0\sqrt{1 - 2\alpha_1\left(\frac{t}{t_s} + \frac{2}{\sqrt{\pi}}\sqrt{\frac{t}{t_s}}\right)}. \tag{5.24}$$

where $t_s = R_0^2/D_s$ is the diffusive time scale for the solute. An illustration of this decay, along with a comparison to the reacting model is presented in Fig. 5.3. Denoting by T_d the finite time at which the particle disappears, and taking into account the order of terms we neglect, we can

deduce that

$$T_d = \frac{t_s}{2\alpha_1}\left(1 - \sqrt{\frac{8}{\pi}}\sqrt{\alpha_1} + O(\alpha_1, \beta_1)\right). \tag{5.25}$$

Therefore at leading order, the lifetime of the colloid scales inversely proportional with the solubility and diffusivity of its material, but quadratically with the initial colloid radius R_0. However, the correction from the next-to-leading order term remains significant for $\alpha_1 \gtrsim 10^{-3}$ due to its slow square-root like decay.

Physical interpretation

The aim of this section is to provide some physical interpretation for Eq. (5.24). For many ions in water at room temperature, the diffusivity is approximately $D_s \sim 10^{-9}\,\mathrm{m^2\,s^{-1}}$ [96]. In the case of an initially micron-sized colloid this gives

$$t_s \sim 10^{-3}\,\mathrm{s}. \tag{5.26}$$

The other (previously unknown) time scale in the problem is the swimmer lifetime T_d. There is a separation of scales that is to leading order inversely proportional to α_1. In the specific example of $CaCO_3$ with $\alpha_1 \approx 10^{-6}$ [96], we obtain

$$T_d \sim 10^3\,\mathrm{s} \sim 10\,\mathrm{min}, \tag{5.27}$$

which is a conceivably desirable lifetime for a microswimmer.

The separation of scales has further consequences for the decay rate. For $t \ll t_s$ we have $R^2 \sim 1 - 4\sqrt{t\alpha_1^2/t_s\pi}$, while for $t \gg t_s$ we obtain the behaviour $R^2 \sim 1 - 2\alpha_1 t/t_s$. Therefore the particle size satisfies $R \sim \sqrt{1 - 2\alpha_1 t/t_s}$ except for a short, transient period on the order of t_s. This feature may be explained physically. Initially, the discontinuity in concentration at $r = R$ causes a large concentration gradient and fast dissolution but on the (fast) scale of solute diffusion the system relaxes to equilibrium in a boundary layer of thickness $\sim \sqrt{D_s t_s}$, which is on the order of the colloid size, R_0. From this point onwards the colloid is surrounded by a cloud of solute in equilibrium and the process becomes quasi-static. At leading order, the dissolution dynamics therefore reduce to steady diffusion. This also justifies our assumption of that the colloid remains spherical, since the diffusive boundary layer smooths out any surface inhomogeneities.

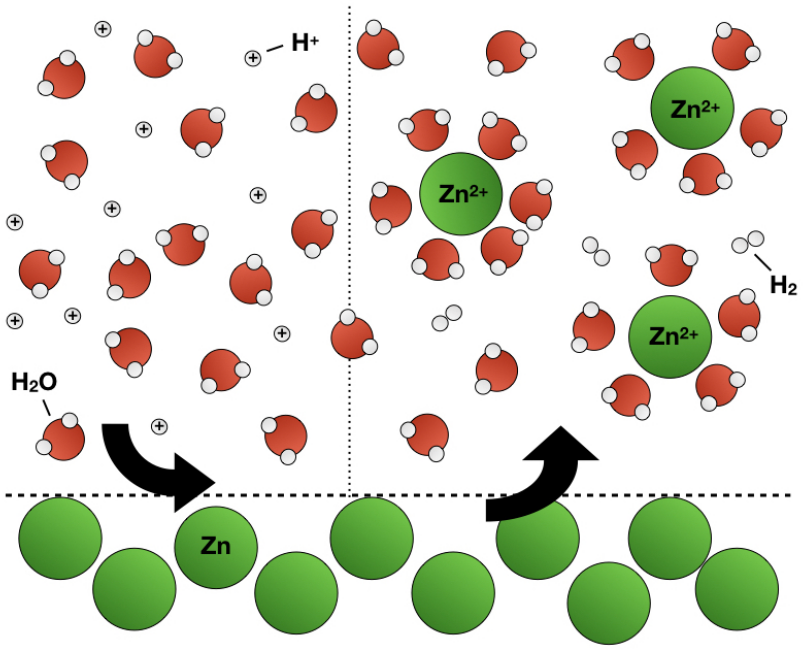

Figure 5.2 Schematic presentation of the molecular dynamics near the boundary of a reacting colloid. In this example, motivated by experiments in Ref. [41], zinc is dissolved in acid forming zinc-ions and molecular hydrogen according to $\mathrm{Zn} + 2\,\mathrm{H}^+ \longrightarrow \mathrm{H}_2 + \mathrm{Zn}^{2+}$. If $\mathrm{Da} = 0$, i.e. infinitely much H^+ is present to sustain the reaction, the dissolution rate is constant. If $\mathrm{Da} > 0$, the reaction rate will depend on the amount of fuel present but not on the amount of reaction product.

As an aside, we note while the dissolution process of microbubbles is driven by capillary pressures [160], the $R \sim \sqrt{1-t}$ behaviour also emerges in the absence of surface tension, essentially also due to the dominance of diffusive effects.

Finally, we point out that α_1 and β_1 depend only on the material that the swimmer is composed of (and its abundance in the bulk fluid). Unsurprisingly, only materials that are considered insoluble on the macroscale yield appreciable microswimmer lifetimes. Hence, together with fine tuning of the initial radius R_0, full control of the dissolution dynamics can be achieved through the microswimmer design.

5.2.2 Dissolution through reaction

Artificial microswimmers are rarely composed solely of chemically inert materials. Indeed, autophoretic swimmers often consume a fuel in the solvent, like in the widely studied case of catalytic platinum swimmers splitting hydrogen peroxide ($\mathrm{H_2O_2}$) into water and oxygen [164]. A sketch of the process is illustrated in Fig. 5.2 in the specific case of zinc dissolving in acid as

realised experimentally by Chen et. al. [41]. An analogous picture may be imagined for the case of biodegradation by enzymes.

A degradable autophoretic colloid might therefore consist of a reactant that will then dissolve into the fluid. To this end, let us consider a fixed reaction-rate boundary condition. It will be important to distinguish between the concentration of fuel $c_f(\boldsymbol{r}, t)$ and concentration of swimmer substrate $c_s(\boldsymbol{r}, t)$. For example, in the case of zinc, the fuel concentration might be provided by H^+-ions in acid, which relates their concentration directly to the pH-value of the solvent, while the concentration of substrate influences the dissolution rate through mass conservation. Notation-wise, we will use the subscript f to refer below to the fuel and the subscript s to the substrate.

Mathematical model

The mathematical development is similar to the non-reacting swimmer, with an important change to the boundary conditions. Indeed, unlike Eq. (5.4) where the concentration at the boundary was fixed, the boundary conditions for the fields c_s and c_f are now given by

$$-D_s \boldsymbol{n} \cdot \nabla c_s|_R = k_s c_f, \quad -D_f \boldsymbol{n} \cdot \nabla c_f|_R = -k_f c_f, \tag{5.28}$$

where k_s and k_f are the constant reaction rates for solute and fuel respectively and D_f the diffusivity of fuel in the solution. Mass conservation for the colloidal particle leads to

$$\frac{dR}{dt} = -\frac{k_s c_f(R)}{\rho_s}. \tag{5.29}$$

Furthermore, we once again have conservation of fluid volume giving rise to a source flow

$$\boldsymbol{u} = \dot{R}(1 - \rho_s/\rho_l)\frac{R^2}{r^2}\hat{\boldsymbol{r}}. \tag{5.30}$$

Similar to what was done in §5.2.1, we assume that the Péclet numbers associated with the solute and the fuel dynamics are small, so that only volume conservation gives rise to advective flows. We can then write the advection-diffusion equation for c_f as

$$\frac{\partial c_f}{\partial t} - (1 - \rho_s/\rho_l)\frac{k_s c_f(R)}{\rho_s}\frac{R^2}{r^2}\frac{\partial c_f}{\partial r} = D_f\left(\frac{\partial^2 c_f}{\partial r^2} + \frac{2}{r}\frac{\partial c_f}{\partial r}\right). \tag{5.31}$$

We introduce non-dimensionalised variables as

$$c_f^* = \frac{c_f}{c_{f,\infty}}, \quad R^* = \frac{R}{R_0}, \quad r^* = \frac{r}{R_0}, \quad t^* = \frac{D_f t}{R_0^2}, \tag{5.32}$$

where $c_{f,\infty}$ is the mass concentration of fuel in the bulk. We can substitute these into Eqs. (5.29) and (5.31), and dropping stars immediately we find

$$\frac{\partial c_f}{\partial t} - \mathrm{Da}(\alpha_2 - \beta_2) c_f(R) \frac{R^2}{r^2} \frac{\partial c}{\partial r} = \frac{\partial^2 c}{\partial r^2} + \frac{2}{r} \frac{\partial c}{\partial r}, \tag{5.33}$$

$$\frac{dR}{dt} = -\mathrm{Da}\alpha_2 c_f(R), \tag{5.34}$$

with the boundary conditions

$$\begin{aligned} &c_f \to 1, && r \to \infty, \\ &\frac{\partial c_f}{\partial r} = \mathrm{Da} c_f, && r = 1, \\ &c_f(r, 0) = 1, && r > 1, \\ &R(0) = 1, \end{aligned} \tag{5.35}$$

where we have defined the three dimensionless numbers

$$\mathrm{Da} = \frac{R_0 k_f}{D_f}, \quad \alpha_2 = \frac{c_{f,\infty} k_s}{\rho_s k_f}, \quad \beta_2 = \alpha_2 \frac{\rho_s}{\rho_l}. \tag{5.36}$$

Here Da is a Damköhler number for the fuel, indicating the ratio between reactive and diffusive fluxes, while α_2 and β_2 may be interpreted as dimensionless ratios comparing the mass of fuel consumed against the mass of solute shed in the reaction.

Upon rescaling our coordinates according to

$$x = \frac{r}{R}, \quad y(x, t) = c_f x, \tag{5.37}$$

our system becomes

$$R^2 \frac{\partial y}{\partial t} + R\dot{R} y - \mathrm{Da}(\alpha_2 - \beta_2) R \left(\frac{1}{x^2} \frac{\partial y}{\partial x} - \frac{y}{x^3} \right) y(1, t) = \frac{\partial^2 y}{\partial x^2}, \tag{5.38}$$

and

$$R = 1 - \mathrm{Da}\alpha_2 \int_0^t y(1, t') dt', \tag{5.39}$$

with

$$y(x,0) = 1, \quad \frac{\partial y}{\partial x}(1,t) = \mathrm{Da}\, y(1,t). \tag{5.40}$$

From here, we can again proceed by means of an asymptotic expansion.

Asymptotic expansion

We next assume $\alpha_2 \mathrm{Da}$, $\beta_2 \mathrm{Da} \ll 1$ and write the solution as a power expansion

$$y(x,t;\alpha_2,\beta_2;\mathrm{Da}) = y_0(x,t;\mathrm{Da}) + \alpha_2 y_\alpha(x,t;\mathrm{Da}) + \beta_2 y_\beta(x,t;\mathrm{Da}) + \text{h.o.t.} \tag{5.41}$$

The boundary condition in Eq. (5.40) consitutes a Robin problem and can be solved by considering the quantity $\phi = y - \mathrm{Da}^{-1}\partial y/\partial x$ subject to Cauchy conditions [34]. The solution for y_0 is

$$y_0(x,t;\mathrm{Da}) = \mathrm{erf}\left(\frac{x-1}{2\sqrt{t}}\right) + e^{\mathrm{Da}(x-1)+\mathrm{Da}^2 t}\mathrm{erfc}\left(\frac{x-1}{2\sqrt{t}} + \mathrm{Da}\sqrt{t}\right). \tag{5.42}$$

It follows that

$$y_0(1,t;\mathrm{Da}) = e^{\mathrm{Da}^2 t}\mathrm{erfc}\left(\mathrm{Da}\sqrt{t}\right), \tag{5.43}$$

and hence to leading order in α_2,

$$R(t) = 1 - 2\alpha_2\sqrt{\frac{t}{\pi}} - \frac{\alpha_2}{\mathrm{Da}}\left[e^{\mathrm{Da}^2 t}\mathrm{erfc}\left(\mathrm{Da}\sqrt{t}\right) - 1\right]. \tag{5.44}$$

Upon reinserting dimensions we finally arrive at

$$R(t) = R_0\left\{1 - \alpha_2\frac{2}{\sqrt{\pi}}\sqrt{\frac{t}{t_f}} - \frac{\alpha_2}{\mathrm{Da}}\left[e^{\mathrm{Da}^2 t/t_f}\,\mathrm{erfc}\left(\mathrm{Da}\sqrt{\frac{t}{t_f}}\right) - 1\right]\right\}. \tag{5.45}$$

where $t_f = R_0^2/D_f$ is the diffusive time scale for the fuel.

Slow reaction limit (fixed solute flux)

Inspired by a study of boundary conditions in the context of finite Péclet-number propulsion in Ref. [161], we may consider separately the limits $\mathrm{Da} \to 0$ and $\mathrm{Da} \to \infty$. Each of these limits will lead to a different model that we will consider in the remainder of this chapter.

For small Damköhler number, we find

$$R(t) = R_0\left[1 - \frac{\alpha_2 \mathrm{Da}}{t_f}t + \mathcal{O}\left(\mathrm{Da}^2\left(\frac{t}{t_f}\right)^{3/2}\right)\right], \qquad \mathrm{Da} \to 0, \quad \frac{t}{t_f} \lesssim \mathrm{Da}^{-2}. \tag{5.46}$$

When Da = 0, no reaction takes place and the radius of the colloid remains constant. At next to leading order we have linear decay, so the lifetime T_d is

$$T_d = \frac{t_f}{\alpha_2}\mathrm{Da}^{-1} = \frac{R_0\rho_s}{c_{f,\infty}k_s} \quad (\mathrm{Da} \to 0), \tag{5.47}$$

which is consistent with the asymptotic expansion to this order. Thus we arrive at a model for the dissolution with a constant solute flux. We note the different scaling compared to the non-reacting model where the lifetime scaled as $T_d \sim R_0^2$. This is indicative of the absence of diffusion in this limit. We note that the model can be recovered from simply applying mass conservation to a flux boundary condition of the form

$$-D_s\frac{\partial c}{\partial r}\bigg|_{r=R(t)} = c_{f,\infty}k_s, \tag{5.48}$$

which shows that the flux is equal to $c_{f,\infty}k_s$ in the limit $\mathrm{Da} \to 0$.

Fast reaction limit

Conversely, as $\mathrm{Da} \to \infty$ (still with $\alpha_2\mathrm{Da} \ll 1$), we find that

$$R(t) = R_0\left\{1 - \frac{2\alpha_2}{\sqrt{\pi}}\sqrt{\frac{t}{t_f}} + O\left(\mathrm{Da}^{-1}\right)\right\}, \qquad \mathrm{Da} \to \infty, \quad \frac{t}{t_f} \gtrsim \mathrm{Da}^{-2}. \tag{5.49}$$

In this limit the reaction is infinitely fast, so the boundary condition on the fuel effectively reduces to instantaneous depletion, $c_f(R,t) = 0$, and the dissolution rate is controlled by the diffusive flux of fuel from the bulk. Correspondingly the lifetime T_d in dimensional units is

$$T_d = \frac{\pi}{4\alpha_2^2}\frac{R_0^2}{D_f} \quad (\mathrm{Da} \to \infty, \alpha_2\mathrm{Da} \ll 1), \tag{5.50}$$

a result which is again consistent with the expansion. Apart from the introduction of reaction rates, this result is qualitatively different from the non-reacting swimmer insofar as the lifetime depends on the square of swimmer density and reactant concentration at infinity, rather than being inversely proportional to solubility. We remark that in the case of H^+-ions, the concentration c_f is directly related to the pH value of the solvent, which establishes an experimentally accessible relationship between the pH and swimmer dissolution dynamics.

In Fig. 5.3 we illustrate the different decay behaviour for our three models: (i) Non-reacting (red solid line, with $t_d/T_d = 0.01$); (ii) Slow reaction (green dashed line); and (iii) Fast reaction (blue dash-dotted line). We note for the non-reacting model the decay rate increases with time,

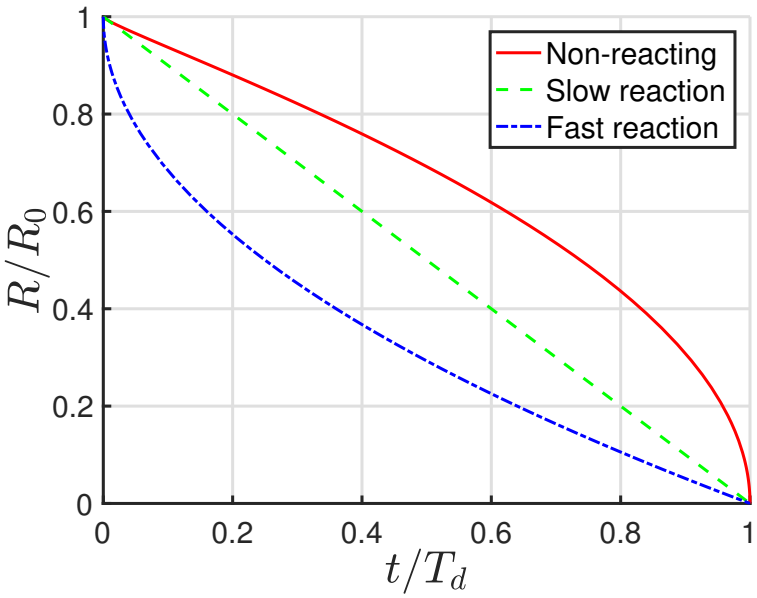

Figure 5.3 Comparison of the decay dynamics between the three models: decay of the dimensionless colloid radius as a function of dimensionless time. (i) Non-reacting (red solid line; $t_d/T_d = 0.01$); (ii) Slow reaction (green dashed line); (iii) Fast reaction (blue dash-dotted line).

whereas it is constant for the slowly reacting, and decreasing for the fast reacting model. In the following two sections, we will explore the important consequences this has for the stochastic behaviour of dissolving microswimmers.

5.3 Passive dynamics of dissolving colloids

After developing a non-reacting, a slow-reaction and a fast-reaction model for the dissolution of a spherical colloid, we now ask what effect this reduction in size has on its fluctuating trajectory. As will be shown, the mean squared displacement of a stochastic self-propelled particle is given by the sum of the contributions from translational noise and active motion. This allows us to split the analysis into the case of a passive colloid with no intrinsic propulsion mechanism but with translational noise and an active colloid with rotational but no translational diffusion. We treat the former case in this section and consider the motion of self-propelled particles in §5.4.

5.3.1 Mathematical model

The change in the dynamics of colloidal particles arises through the time dependence of the translational diffusion coefficient, which is given by the Stokes-Einstein relation [63]

$$D(t) = \frac{k_B T}{6\pi\mu R(t)} \equiv D_0 \frac{R_0}{R(t)}, \tag{5.51}$$

where k_B is Boltzmann's constant, T is absolute temperature and $D_0 \equiv D(0) = k_B T/6\pi\mu R_0$. In analogy with classical Brownian motion, we consider the following overdamped Langevin equation for the position of the passive colloidal particle, $\boldsymbol{r}(t)$,

$$d\boldsymbol{r} = \sqrt{2D(t)}d\boldsymbol{W}. \tag{5.52}$$

Classically, $\boldsymbol{W}(t)$ is white noise with the properties that

$$\langle d\boldsymbol{W}\rangle = \boldsymbol{0}, \quad \langle dW_i(t)dW_j(t')\rangle = \delta_{ij}\delta(t-t')dt, \tag{5.53}$$

with brackets denoting ensemble averages. The right-hand side of Eq. (5.52) therefore varies on two different time scales: the rate of change of D and the time scale of the molecular chaos τ_{MC} that gives rise to noise. Typically, $\tau_{MC} = O(10^{-13}\,\mathrm{s})$ [96]. The mathematical assumption of δ-correlated noise only holds true if τ_{MC} is very small compared to the time scale of diffusion, which holds true for microscopic colloids. However, since the rate of change of D diverges as the swimmer size tends to zero, this model is expected break down at the very end of the swimmer lifetime. In the case of the non-reacting model this singularity is integrable and poses no problem, whereas for the reacting model we will also include a physical discussion of the breakdown.

For an active self-propelled particle at velocity $\boldsymbol{U}(t)$, the right-hand side of the Langevin equation Eq. (5.52) includes an additional term $\boldsymbol{U}(t)dt$, which is deterministic in the sense that it is uncorrelated with translational white noise (even if $\boldsymbol{U}(t)$ is subject to rotational noise). A straightforward integration using the properties in Eq. (5.53) then shows that the total mean squared displacement is given by the sum of active and passive contributions,

$$\langle r^2\rangle_{tot} = \langle r^2\rangle_a + \langle r^2\rangle_p, \tag{5.54}$$

as claimed.

The stochastic dynamics in Eq. (5.52) give rise to a Fokker-Planck equation for the probability for the position of the particle, $P(\boldsymbol{r}, t)$, as

$$\frac{\partial P}{\partial t} = D(t)\nabla^2 P, \tag{5.55}$$

since the separation of time scales between molecular colliosn and particle diffusion is satisfied. We can solve this by a rescaling of time, introducing $\tau(t)$ such that

$$\tau = \int_0^t D(s)ds = D_0 \int_0^t \frac{R_0}{R(s)} ds, \tag{5.56}$$

which yields

$$\frac{\partial \tilde{P}}{\partial \tau} = \nabla^2 \tilde{P}. \tag{5.57}$$

where $\tilde{P}(\boldsymbol{r}, \tau) = P(\boldsymbol{r}, t)$. In three spatial dimensions this equation has a well known Gaussian solution corresponding to the initial condition of a particle located at the origin,

$$\tilde{P}(\boldsymbol{r}, \tau) = \tilde{P}(r = |\boldsymbol{r}|, \tau) = \frac{1}{(4\pi\tau)^{3/2}} \exp\left(-\frac{r^2}{4\tau}\right). \tag{5.58}$$

The first two moments are well known to be $\langle \boldsymbol{r} \rangle = 0$ and $\langle r^2 \rangle = 6\tau$. The total passive mean squared displacement of the particle in its lifetime, $\langle r^2 \rangle_p \equiv \langle r^2 \rangle(T_d)$, is therefore given by the integral

$$\langle r^2 \rangle_p = 6D_0 \int_0^{T_d} \frac{R_0}{R(t)} dt. \tag{5.59}$$

Note that since $R \leq R_0$, the integral has value larger than T_d. Therefore dissolution always enhances passive diffusion. All that remains to be done is to calculate the integral for each of our three models.

5.3.2 Total root mean squared displacement

In the following we consider the solutions to Eq. (5.59). Bearing in mind the order of terms we neglected in the derivation of Eq. (5.24), we can integrate Eq. (5.59) directly to obtain the following result for the non-reacting model

$$\langle r^2 \rangle_p = 6D_0 \times \frac{t_s}{\alpha_1} \left(1 - \sqrt{\frac{\pi}{2}}\sqrt{\alpha_1} + O(\alpha_1, \beta_1)\right), \quad \text{(non-reacting)}. \tag{5.60}$$

Comparing with Eq. (5.25) we can see that at leading order in α_1, dissolution enhances the total mean squared displacement by a factor of two. Through the scaling of t_s with R_0 we

also find that $\langle r^2 \rangle_p \sim R_0$. This may be tested easily in experiments without affecting the other parameters. Perhaps surprisingly, this also means that in contrast to fixed-size swimmers, the importance of passive Brownian effects increases with swimmer size, since the smaller diffusivity is overcompensated for by the longer life span. The scaling with α_1 can be explained the same way, as a colloid with small α_1 decays slower, lives longer and therefore travels further.

For the slow reaction model we can use Eq. (5.46) in the integration of Eq. (5.59) to find

$$\langle r^2 \rangle(t) = 6D_0 \times T_d \log\left(\frac{R_0}{R(t)}\right), \quad \text{(slow reaction)}. \tag{5.61}$$

This expression diverges logarithmically as $t \to T_d$. This should not be taken as indicative of superdiffusion, but can be resolved by the breakdown of the Stokes-Einstein relation below a certain colloid size. Past experiments suggest this happens for colloids smaller than a few nanometres in diameter [141]. Compared to an initial colloid size on the scale of a few microns, this corresponds to 2 to 4 orders of magnitude. Since the divergence of the mean squared displacement is logarithmic, this will give a total mean squared displacement that is greater than that of a non-dissolving colloid by a factor of $O(1) - O(10)$. Furthermore, since $D_0 T_d$ is independent of R_0 for this model, the contribution of passive Brownian motion only depends weakly on the initial colloid size. This is in contrast with the other models, and indicative of the absence of diffusion.

Finally, using Eq. (5.49) in Eq. (5.59) we obtain for the fast reaction limit the result

$$\langle r^2 \rangle(t) = 6D_0 \times 2T_d \left(\log\left(\frac{R_0}{R(t)}\right) + \frac{R(t)}{R_0} - 1\right), \quad \text{(fast reaction)}. \tag{5.62}$$

where again we have a logarithmic divergence as $t \to T_d$. Using previous definitions we find that as in the non-reacting model $\langle r^2 \rangle_p \sim R_0$ (+ logarithmic corrections) and also that $\langle r^2 \rangle_p \sim \alpha_2^{-2}$. The passive mean squared displacement therefore depends rather sensitively on the availability of fuel for the reaction.

5.4 Active motion of dissolving colloids

After examining the dynamics of passive particles, we now turn to the effect of dissolution on self-propelled microswimmers. For the case of active particles subject to rotational diffusion with coefficient D_r, it is well known that self-propulsion at velocity U gives rise to an effective enhanced translational diffusivity [86]

$$D_{\text{eff}} = D + \frac{U^2}{6D_r}, \tag{5.63}$$

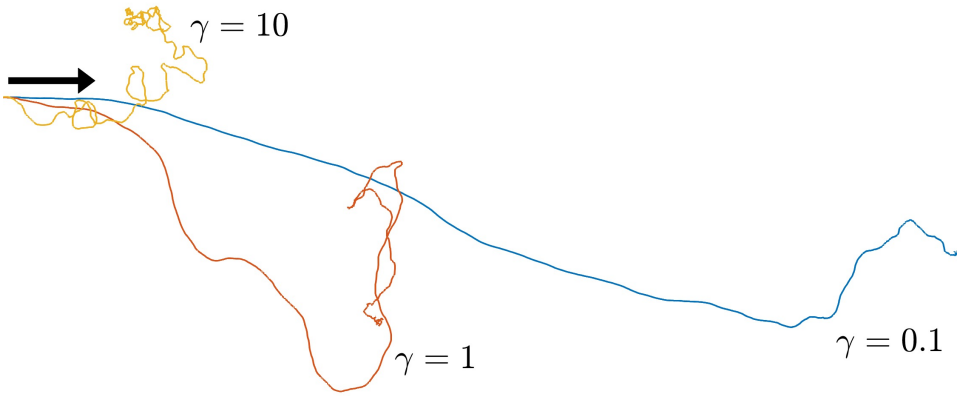

Figure 5.4 2D-projections of sample trajectories for different values of γ. The colloids initially swim from left to right (see arrow) and dissolve according to the non-reacting model with the same length scales and lifetimes.

for times much longer than D_r^{-1}, the time scale of rotational diffusion (i.e. in the limit $tD_r \gg 1$). On scales much shorter than this the motion is instead ballistic, i.e. $\langle r^2 \rangle \sim U^2 t^2$.

In this new scenario however, an additional scale is introduced through the swimmer lifetime, T_d. It is therefore vital to consider the dimensionless quantity

$$\gamma := D_{r,0} T_d, \tag{5.64}$$

where we define $D_{r,0} = k_B T / 8\pi\mu R_0^3$. If $\gamma \lesssim 1$, then the particle disappears before exhibiting macroscopically diffusive behaviour. Conversely, if $\gamma \gtrsim 1$ we expect trajectories that are qualitatively similar to that of a classically diffusive colloid at long time scales. The qualitative role of γ is illustrated in Fig. 5.4 where we observe three trajectories becoming more curly as time progresses, since diffusivity increases as the swimmer dissolves. However, only colloids with large values of γ (here, $\gamma = 10$) exist long enough for this effect to become significant, giving rise to a macroscopically 'diffusive' trajectory. Conversely, for small γ (here, $\gamma = 0.1$) trajectories appear macroscopically 'ballistic'. Depending on the application, it may be desirable to design swimmers that belong to either of these two regimes. In water at room temperature we have $D_{r,0}^{-1} \approx 6\,(R_0/\mu\text{m})^3$ s [96], so depending on the initial colloid size the threshold lifetime ranges from seconds to hours. Therefore both regimes are conceivable for applications and thus relevant to study. We proceed with the development of our theoretical framework to derive expressions for the active mean squared displacement and present analytical solutions for each model both as $\gamma \to 0$ and as $\gamma \to \infty$. We then validate our theoretical results against numerical simulations of the associated Langevin dynamics.

5.4.1 Mathematical model

In the rest of this section we assume that the colloid is subject to Langevin dynamics as

$$d\boldsymbol{r} = U\boldsymbol{e}dt, \tag{5.65}$$

$$d\boldsymbol{e} = -2D_r(t)\boldsymbol{e}dt + \sqrt{2D_r(t)}\boldsymbol{\Pi}(\boldsymbol{e}) \cdot d\boldsymbol{W}, \tag{5.66}$$

to be understood in the Itô formulation of stochastic calculus, as to allow for an explicit numerical scheme. Here U is the particle self-propulsion speed, $\boldsymbol{e}$ the unit vector along the direction of propulsion and $\Pi_{ij} = \delta_{ij} - e_i e_j$. As is the case for a wide range of phoretic swimmers [164], we assume the velocity U to be independent of the swimmer size. Moreover, we set $D = 0$ to isolate the effect of active diffusion, which generally exceeds that of (regularised) passive diffusion discussed previously. Since both contribute independently however, they may simply be added together if the total mean squared displacement is desired. We also neglect the details of the propulsion mechanism and possible interactions with our dissolution models.

As in the classical case, the $\boldsymbol{e}$-dynamics decouple from the $\boldsymbol{r}$-dynamics. With the same assumptions regarding the separation of time scales as in the passive case, $\boldsymbol{e}(\theta, \phi)$ is therefore subject to the Fokker-Planck equation

$$\frac{\partial}{\partial t}P(\theta, \phi, t) = D_r(t)\nabla^2_{\text{ang}}P, \tag{5.67}$$

where ∇^2_{ang} denotes the angular part of the Laplacian operator. By introducing a rescaled time $\tau_r(t)$ as

$$\tau_r = \int_0^t D_r(s)ds = D_{r,0}\int_0^t \left(\frac{R_0}{R(s)}\right)^3 ds, \tag{5.68}$$

this may be used to show that $\langle \boldsymbol{e}(t) \cdot \boldsymbol{e}(0)\rangle = \exp(-2\tau_r)$. Therefore we have the following expression for the total active mean squared displacement,

$$\langle r^2\rangle_a = 2U^2 \int_0^{T_d} dt' \int_0^{t'} dt'' \exp\left\{-2\left[\tau_r(t') - \tau_r(t'')\right]\right\}. \tag{5.69}$$

Substituting values for our models and rescaling variables, this gives the following general expressions.

$$\langle r^2\rangle_a = U^2T_d^2\int_0^\infty dx'\int_0^{x'} dx''\frac{2e^{-2\gamma(x'-x'')}}{(1+x'/2)^3(1+x''/2)^3}, \qquad \text{(non-reacting)} \qquad (5.70)$$

$$\langle r^2\rangle_a = U^2T_d^2\int_0^\infty dx'\int_0^{x'} dx''\frac{2e^{-2\gamma(x'-x'')}}{(1+2x')^{3/2}(1+2x'')^{3/2}}, \qquad \text{(slow reaction)} \qquad (5.71)$$

$$\langle r^2\rangle_a = U^2T_d^2\int_0^\infty dx'\int_0^{x'} dx''\frac{2e^{-2\gamma(x'-x'')}}{(1+\sqrt{x'})^3(1+\sqrt{x''})^3}. \qquad \text{(fast reaction)} \qquad (5.72)$$

Unfortunately, while these are exact results, we cannot evaluate these integrals analytically for arbitrary values of γ. However, we can derive asymptotic solutions in both the diffusive and ballistic limits, as we now show.

Diffusive limit ($\gamma \to \infty$)

In the diffusive limit, $\gamma \gg 1$, we can use Watson's lemma to develop an asymptotic expansion, with details given in §5.A.1. In the case of a non-reacting swimmer, we find

$$\langle r^2\rangle_a \sim \frac{2}{5}\frac{U^2T_d}{D_{r,0}}\left[1-\frac{5}{8\gamma}+\ldots\right], \quad \gamma\to\infty \quad \text{(non-reacting)}. \qquad (5.73)$$

As expected, the behaviour is diffusive and the leading-order scaling is

$$\langle r^2\rangle_a \sim \frac{U^2\mu\rho_s R_0^5}{k_BTD_s(c_0-c_\infty)}, \quad \gamma\to\infty \quad \text{(non-reacting)}. \qquad (5.74)$$

We notice the appearance of the $2/5$ factor in Eq. (5.73), indicating that the enhancement of the diffusivity through active motion is reduced dramatically, to just 40% of that of a comparable classical colloid. Furthermore, the active mean squared displacement scales as $\sim R_0^5$, making the range of the swimmer extremely sensitive to its initial size. This scaling breaks down for very large swimmers, since it is necessary that $\gamma \sim R_0^{-1}$ is sufficiently large for this expansion to remain valid.

For the slowly reacting swimmer we find in a similar fashion that

$$\langle r^2\rangle_a \sim \frac{1}{4}\frac{U^2T_d}{D_{r,0}}\left[1-\frac{1}{\gamma}+\ldots\right], \quad \gamma\to\infty \quad \text{(slow reaction)}. \qquad (5.75)$$

with the leading-order scaling

$$\langle r^2 \rangle_a \sim \frac{U^2 \mu \rho_s R_0^4}{k_B T c_{f,\infty} k_s}, \quad \gamma \to \infty \quad \text{(slow reaction)}. \tag{5.76}$$

We see that the diffusivity in Eq. (5.75) is reduced even further, to 25% that of a classical colloid. Finally for the fast reacting swimmer we obtain

$$\langle r^2 \rangle_a \sim \frac{1}{10} \frac{U^2 T_d}{D_{r,0}} \left[1 - \frac{5}{2\gamma} + \dots \right], \quad \gamma \to \infty \quad \text{(fast reaction)}, \tag{5.77}$$

and the leading-order scaling

$$\langle r^2 \rangle_a \sim \frac{U^2 \mu \rho_s^2 k_f^2 R_0^5}{k_B T D_f c_{f,\infty}^2 k_s^2}, \quad \gamma \to \infty \quad \text{(fast reaction)}. \tag{5.78}$$

This third dissolution model gives the strongest reduction of the active mean squared displacement in the diffusive regime, to just 10% that of a classical colloid.

The strong reduction in mean squared displacement across all three models suggests that it is impractical to rely on active diffusion to transport dissolving microswimmers. Instead designs may be aimed at exploiting the ballistic regime ($\gamma \ll 1$) or making use of external flows and geometries to direct swimmers.

Ballistic limit ($\gamma \to 0$)

The asymptotic expansions in the ballistic limit are more complicated, and rely on carefully splitting the integration range to tame divergences. With all details shown in the §5.A.2, we obtain the following leading-order results:

$$\langle r^2 \rangle_a = U^2 T_d^2 \left(1 - \frac{16}{3}\gamma + O(\gamma^{3/2}) \right), \quad \text{(non-reacting)} \tag{5.79}$$

$$\langle r^2 \rangle_a = U^2 T_d^2 \left(1 - 2\sqrt{\pi}\sqrt{\gamma} + O(\gamma \log \gamma) \right), \quad \text{(slow reaction)} \tag{5.80}$$

$$\langle r^2 \rangle_a = U^2 T_d^2 \left(1 - 4\sqrt{2\pi}\sqrt{\gamma} + O(\gamma \log \gamma) \right). \quad \text{(fast reaction)} \tag{5.81}$$

Once again, we observe the same hierarchy among the three models, with the non-reacting swimmer exhibiting the smallest decrease in range compared to a classical colloid, in contrast with a fast reacting swimmer with the same lifetime T_d. We note that in this limit not only the coefficient but also the leading-order scaling varies between the models.

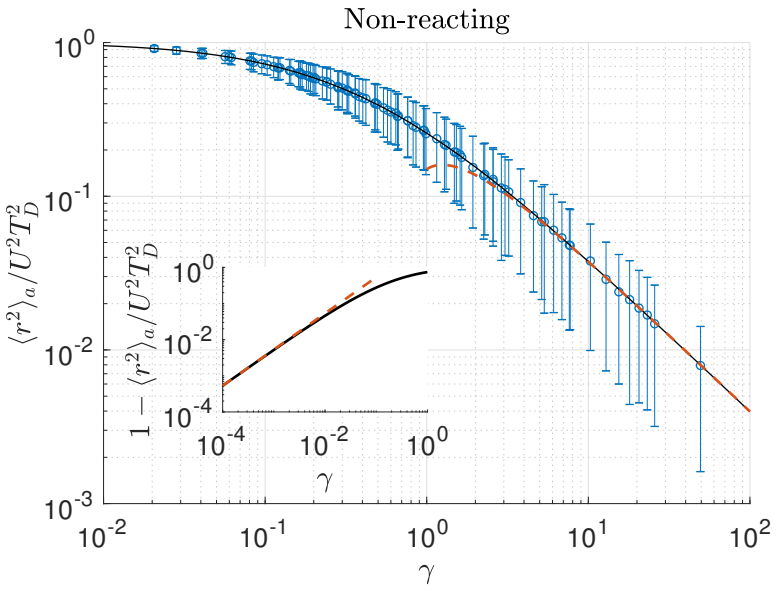

Figure 5.5 Normalised active mean squared displacement as a function of γ for the non-reacting model. The solid black line corresponds to direct numerical integration of Eq. (5.70), while the dashed orange line is our theoretical prediction in Eq. (5.73) for the large γ limit. Each scatter point represents the mean and one standard deviation obtained from 10^3 Brownian dynamics simulations of the associated Langevin equations. Inset: the small γ behaviour, comparing Eq. (5.70) (solid black) with the asymptotic solution Eq. (5.79) (dashed orange).

We find therefore that in both the ballistic and diffusive limit there exists a hierarchy among the three models. The mean squared displacement for a given value of γ is always largest for the non-reacting swimmer, followed by the slowly reacting and finally the fast reacting colloid. This may be explained by considering the decay behaviour in Fig. 5.3. Since the decay rate of the non-reacting swimmer is accelerating, it is only significantly smaller than its original size for a comparatively short proportion of its total lifetime. Since rotational diffusion is strongest for particles of small radius, this means that it is comparatively weakly affected by the enhancement in rotational diffusion. In contrast, colloids decaying according to the other two models experience strong rotational diffusion for a significantly longer proportion of their lifetime, leading to less directed motion and smaller overall displacement. In Fig. 5.8 and 5.9 we illustrate this further using results from our numerical simulations.

5.4.2 Computational results

Validation of the method

In order to test our theoretical approach, we perform direct numerical integrations of our integral expressions for the active mean squared displacement in Eqs. (5.70)-(5.72). We compare

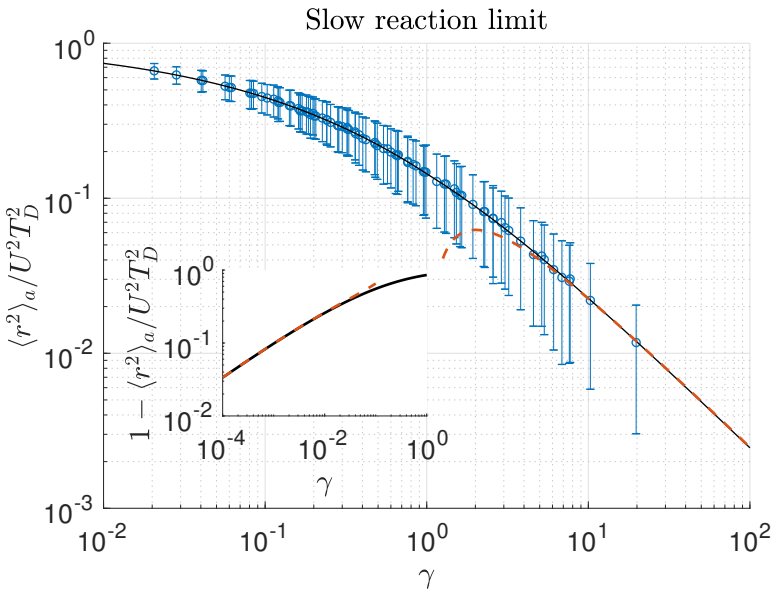

Figure 5.6 Normalised active mean squared displacement against γ for the slow reaction limit of the reacting model. The solid black line corresponds to direct numerical integration of Eq. (5.71), the dashed orange lines to the theoretical predictions of Eq. (5.75) and Eq. (5.80), and the scatter points to Brownian dynamics simulations in analogy with Fig. 5.5.

these with Brownian dynamics simulations performed by integrating the associated Langevin equations, and with our analytical predictions for the asymptotic behaviour. The results are shown in Figs. 5.5, 5.6 and 5.7 for the non-reacting, slowly reacting and fast reacting models respectively. Since the large γ limit corresponds to strong rotational diffusion and long lifetimes, the Brownian dynamics simulations require very small time steps and very long run times. Depending on the model, such simulations therefore become prohibitively expensive even for moderate values of γ. Since rotational diffusion is strongest for small colloids, this effect is most pronounced for the fast reacting swimmer whose rate of dissolution is decreasing since this swimmer spends the longest proportion of its lifetime in this regime. Conversely, the non-reacting swimmer is the least expensive to simulate.

As can be seen in Fig. 5.5, we obtain excellent agreement between the Langevin dynamics and the predicted mean-squared displacement for a wide range of γ values. In the diffusive limit ($\gamma \gg 1$), the next-to leading order asymptotics agree extremely well with the exact result down to $\gamma = O(1)$ on a log-log scale. In the ballistic limit, divergences begin to appear at $\gamma = O(10^{-1})$. Similar conclusions hold for the slowly reacting swimmer, as shown in Fig. 5.6. In the case of the fast reacting swimmer, shown in Fig. 5.7, the active mean squared displacement is a less smooth function of γ, leading to a stronger divergence from the asymptotic expressions.

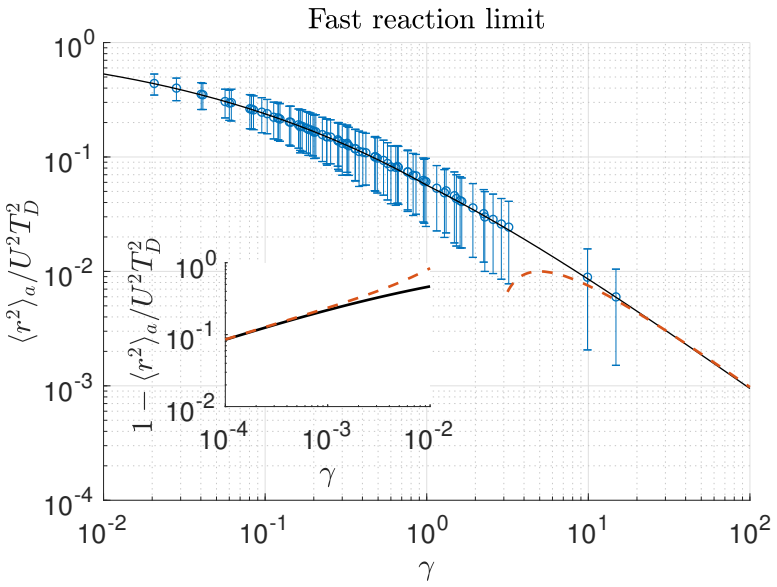

Figure 5.7 Normalised active mean squared displacement against γ for the fast reaction limit of the reacting model. The solid black line corresponds to direct numerical integration of Eq. (5.72), the dashed orange lines to the theoretical predictions of Eq. (5.77) and Eq. (5.81), and the scatter points to Brownian dynamics simulations in analogy with Fig. 5.5.

Distribution of spread

From these Brownian dynamics simulations we can deduce further information regarding the spread of particle trajectories. As predicted in §5.4.1, a hierarchy between the models is revealed that applies for a wide range of values of γ, covering both the ballistic and the diffusive regime. This is illustrated in Fig. 5.8, where we show histograms of root-mean-square displacement distributions. For equal values of γ, the non-reacting model consistently produces the largest displacement. The distribution is strongly peaked for small γ (ballistic), but spreads as γ shifts to larger values. This may be attributed to the general shift towards diffusion. Contrastingly however, the distribution of the fast-reacting colloids is spread rather widely even in the ballistic regime and in fact peaked much more strongly in the diffusive regime than both the non-reacting and the slowly reacting particles, whose distribution lies between the two others. This is indicative of fast-reacting dissolution fostering diffusive behaviour independent of the parameter γ.

In order to further illustrate this point, we examine the lateral spread of colloid trajectories in the weakly ballistic regime. In Fig. 5.9, we plot the final positions of colloids with identical initial orientations, including non-dissolving particles for comparison. A clear stratification between the models is visible with non-dissolving colloids being closely confined to a spherical cap on the one extreme, and fast reacting colloids in a near-spherical diffusive cloud close to

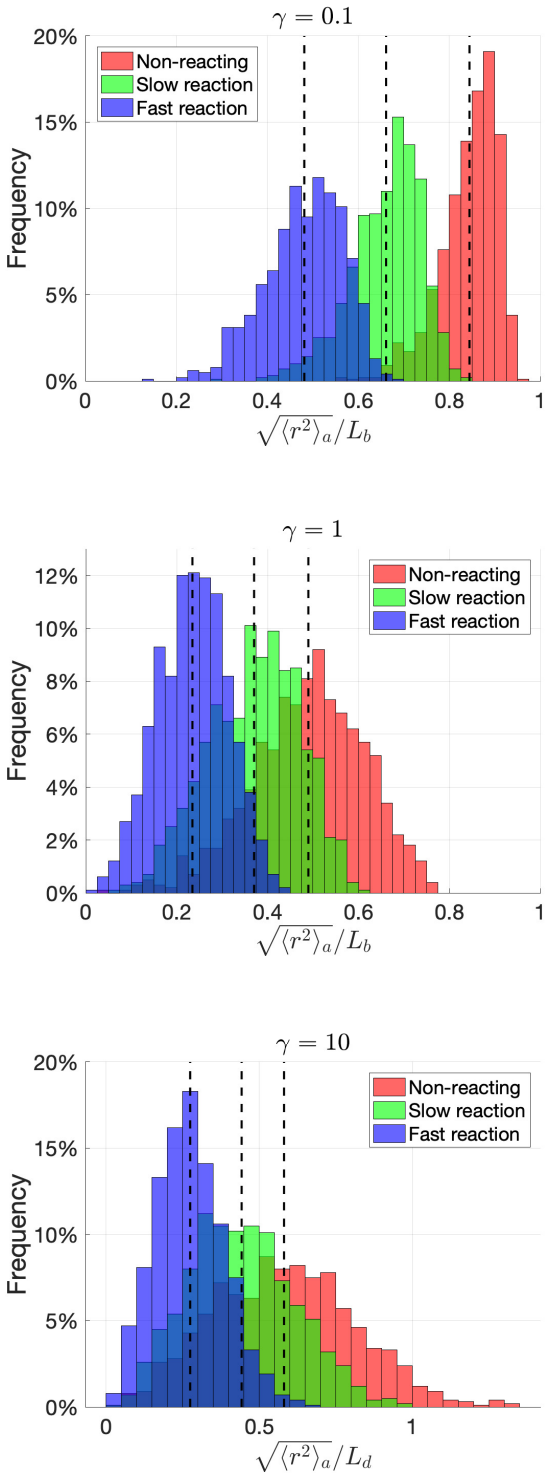

Figure 5.8 Histograms illustrating the distribution of the root mean squared displacement from the initial position for different values of γ, scaled by the ballistic length scale $L_b = UT_d$ for $\gamma = 0.1$ and $\gamma = 1$, and the diffusive length scale $L_d = L_b/\sqrt{\gamma}$ for $\gamma = 10$. Each histogram is generated from 10^3 Brownian dynamics simulations. Dashed lines indicate sample means.

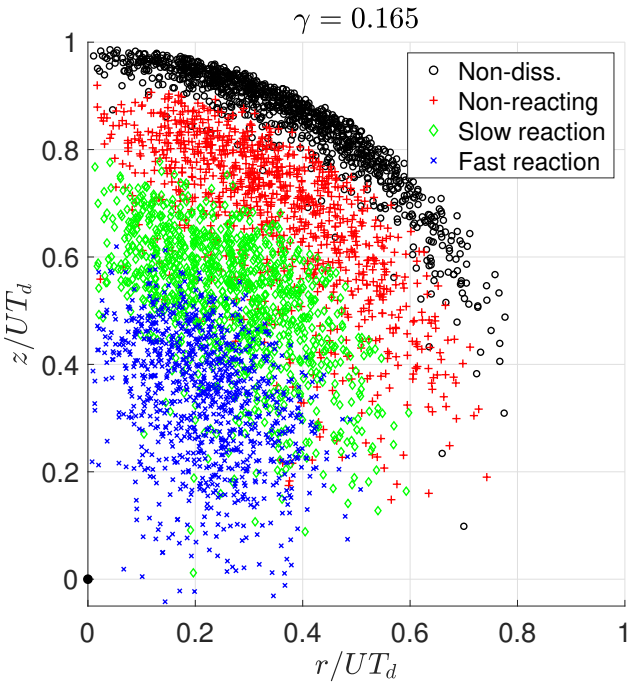

Figure 5.9 Cloud scatter plot of lateral displacement, $r_\perp = \sqrt{x^2 + y^2}$, vs. vertical displacement, z, of 10^3 Brownian dynamics simulations in the weakly ballistic regime for our three models compared to the non-dissolving case. All simulations are started at the coordinate origin (filled circle) with initial orientation vertically upwards in Cartesian coordinates (x, y, z). Symbols indicate positions of the colloids at time of disappearance. The non-dissolving data points are generated by initialising a simulation with a given rotational diffusivity D_r and terminating after a time T such that $TD_r = \gamma$. Lengths are scaled by the ballistic length scale UT_d.

the origin. These also exhibit the smallest absolute lateral spread, while the classical colloids are the most spread out. However, the average angular spread is similar between the models.

5.5 Discussion

In this chapter we presented two fundamental models for the dissolution and stochastic dynamics of self-propelled artificial microswimmers. Inspired by recent experimental realisations, we sough to identify the swimmer decay rates and their influence on translational and rotational diffusivity, and in turn analysed both theoretically and numerically how changes in these modify the distribution of swimmer trajectories. We identified a new dimensionless parameter, γ defined as the product of lifetime and initial rotational diffusivity, that classifies colloids with finite lifetime into 'ballistic' and 'diffusive' types independent of the dissolution process, and studied the differences between our dissolution models in three distinct limits for various

values of this parameter. We found that for a given value of γ, particles dissolving in the absence of a reaction behave the most ballistically, whereas colloids reacting at high Damköhler number, defined as the ratio of fuel reactivity and diffusive replenishment, behave the most diffusively. We found that this is due to increasing and decreasing dissolution rates respectively for the different models. Furthermore we derived asymptotic expressions of their mean squared displacement for both small and large values of γ, and performed extensive Brownian dynamics simulations to validate our theoretical results and derive more information about the distribution of spread.

Under experimental conditions, Damköhler numbers larger than about 10 are often very difficult to realise, due to limited control of diffusivities and reaction rates. However, this does not really constrain the applicability of our fast-reacting model, since we only require $t_f/\mathrm{Da}^2 \ll T_d$ for the expansion to be valid on the scale of dissolution dynamics. Since typically $t_f \ll T_d$ anyway, we find that even Damköhler numbers of order unity are sufficient for this limit. On the other hand, this argument implies that very small Damköhler numbers are required in the slow-reaction asymptotic limit, a situation which might not be realisable experimentally. Note however that we include also the general expression of the decay for arbitrary Damköhler number in Eq. (5.45), for which computations similar to the ones provided in §5.4.2 may be performed.

Despite this, not all our models can apply to all kinds of microswimmer designs. Specifically, the non-reacting model might be at odds with phoretic self-propulsion. Therefore this model only describes colloids that propel through different mechanisms, such as magnetic swimmers. Furthermore, our statistical results only hold true for microswimmers that are fully degradable. A Janus colloid with, e.g., degradable and inert halves is not going to exhibit divergent diffusivity since the relevant length scale is bounded. Instead such a swimmer would show a decrease in velocity, which if known can be dealt with in a manner similar to our theoretical approach. In this case, however, the changing geometry of the swimmer would likely have to be solved for numerically.

Another important problem that remains to be investigated is the influence of directed motion, such as chemotaxis. Breaking the isotropy of orientational dynamics prevents an analytical investigation similar to the one carried out in this chapter since it relies on the result that the directional correlation of a particle decays exponentially. However, we can still address the issue directly in at least one special case. It was shown recently in Ref. [229] that artificial colloids perform chemotaxis by adjusting their trajectory by means of rotation, translation in the direction to a chemical gradient, and translation at an angle, each with a coefficient of strength that can be calculated from the surface activity and mobility of the colloid. In the case of uniform surface activity, the only coefficient that is non-zero is the one giving rise to translation

in the direction of a chemical gradient. In particular, the rotational dynamics remain unaffected. In that case, the swimmer trajectories behave therefore just like we describe in this chapter, plus a constant velocity displacing the colloid in the direction of the chemical gradient. Furthermore numerical work will be required to address the full interplay between chemotaxis behaviour and dissolution dynamics.

Before degradable designs may be employed in real-world applications, it will be furthermore necessary to examine the effects of collective dissolution. Since our models are sensitive to the background distribution of fuel and/or solute, the influence of other nearby colloids on their dissolution will be noticeable. It is conceivable that, in analogy with bubbles [160], different decay patterns and complex stochastic behaviour emerges. Similar effects may also be triggered by confinement and also warrant further investigation.

5.A Details of the asymptotics for active MSD

5.A.1 Diffusive limit ($\gamma \to \infty$)

The general expression for the active mean squared displacement is

$$\langle r^2 \rangle_a = 2U^2 \int_0^{T_d} dt' \int_0^{t'} dt'' \exp\left\{-2\left[\tau_r(t') - \tau_r(t'')\right]\right\}. \tag{5.82}$$

In the case of the non-reacting swimmer we have $R \approx R_0\sqrt{1 - t/T_d}$, and thus

$$\tau_r = D_{r,0}T_d \int_0^{t/T_d} \frac{dt'}{(1-t')^{3/2}} = 2\gamma\left(\frac{1}{\sqrt{1-t/T_d}} - 1\right). \tag{5.83}$$

We can use this to change integration variables in Eq. (5.82) by setting $x = \tau_r/\gamma$ and obtain

$$\langle r^2 \rangle_a = 2U^2T_d^2 \int_0^{\infty} dx' \int_0^{x'} dx'' \frac{e^{-2\gamma(x'-x'')}}{(1+x'/2)^3(1+x''/2)^3}. \tag{5.84}$$

This transformation can be interpreted as mathematically equivalent to the motion of a non-dissolving colloid with constant rotational diffusivity and algebraically decaying velocity. We switch variables again to

$$\begin{aligned} y' &= x', \\ y'' &= x' - x''. \end{aligned} \tag{5.85}$$

and obtain

$$\langle r^2\rangle_a = 2U^2T_d^2\int_0^\infty dy'\int_0^{y'} dy'' e^{-2\gamma y''}\left(1+\frac{y'}{2}\right)^{-3}\left(1+\frac{y'-y''}{2}\right)^{-3}. \tag{5.86}$$

It is then possible to write the y''-integral in terms of auxiliary Gamma functions. These may be expanded in the limit $\gamma\to\infty$ to give

$$\langle r^2\rangle_a = U^2T_d^2\int_0^\infty dy'\left[\frac{64}{\gamma(2+y')^6}+\frac{96}{\gamma^2(2+y')^7}-\frac{8e^{-2\gamma y'}}{\gamma(2+y')^3}+O(\gamma^{-3})\right]. \tag{5.87}$$

The first two terms can be evaluated directly, while the last one may be expanded using Watson's lemma. We find that

$$\langle r^2\rangle_a = U^2T_d^2\left(\frac{2}{5\gamma}-\frac{1}{4\gamma^2}+O\left(\gamma^{-3}\right)\right), \tag{5.88}$$

which is the same as Eq. (5.73).

The case of a slowly reacting swimmer can be solved in a very similar fashion. This time we have

$$x = \frac{1}{2}\left(\frac{1}{(1-t/T_d)^2}-1\right). \tag{5.89}$$

It follows that the active part of the mean squared displacement may be written as

$$\langle r^2\rangle_a = 2U^2T_d^2\int_0^\infty dx'\int_0^{x'} dx''\frac{e^{-2\gamma(x'-x'')}}{(1+2x')^{3/2}(1+2x'')^{3/2}}. \tag{5.90}$$

Developing an asymptotic expansion as before we get

$$\begin{aligned}\langle r^2\rangle_a &= U^2T_d^2\int_0^\infty dy'\left[\frac{1}{\gamma(1+2y')^3}+\frac{3}{2\gamma^2(1+2y')^4}-\frac{e^{-2\gamma y'}}{\gamma(1+2y')^{3/2}}+O(\gamma^{-3})\right]\\ &= U^2T_d^2\left(\frac{1}{4\gamma}-\frac{1}{4\gamma^2}+O\left(\gamma^{-3}\right)\right),\end{aligned} \tag{5.91}$$

which is Eq. (5.75).

Finally, for the fast reacting swimmer we have

$$x = \frac{t/T_d}{(1-\sqrt{t/T_d})^2}, \tag{5.92}$$

from which we can derive that

$$\langle r^2\rangle_a = 2U^2T_d^2\int_0^\infty dx'\int_0^{x'} dx''\frac{e^{-2\gamma(x'-x'')}}{(1+\sqrt{x'})^3(1+\sqrt{x''})^3}. \tag{5.93}$$

In this case it is easier to interchange the integrals as $\int_0^\infty dx' \int_0^{x'} dx'' = \int_0^\infty dy'' \int_{y''}^\infty dy'$ and perform the y'-integral first. The resulting expression produced by Wolfram Mathematica 11 contains 1692 terms, but may again be expanded and simplified significantly upon the application of Watson's lemma, giving

$$\begin{aligned}\langle r^2\rangle_a &= U^2T_d^2\int_0^\infty dy'' e^{-2\gamma y''}\left(\frac{1}{5}-y''+O\left(y''^{3/2}\right)\right)\\ &= U^2T_d^2\left(\frac{1}{10\gamma}-\frac{1}{4\gamma^2}+O\left(\gamma^{-5/2}\right)\right),\end{aligned} \tag{5.94}$$

as claimed in Eq. (5.77).

5.A.2 Ballistic limit ($\gamma \to 0$)

First, the non-reacting swimmer. We have

$$\langle r^2\rangle_a = 2U^2T_d^2\int_0^\infty dx\int_0^x dy\frac{e^{-2\gamma(x-y)}}{(1+x/2)^3(1+y/2)^3}, \tag{5.95}$$

and are interested in the limit $\gamma \to 0$. We set $U^2T_d^2 = 1$ to keep the notation clean. Since the denominator decays rapidly enough at ∞ we can Taylor expand the exponential to pick up the two leading-order contributions to the integral.

$$\begin{aligned}\langle r^2\rangle_a &= \int_0^\infty dx\int_0^x dy\frac{2-4\gamma(x-y)+\ldots}{(1+x/2)^3(1+y/2)^3}\\ &= 1-\frac{16}{3}\gamma+o(\gamma),\end{aligned} \tag{5.96}$$

which is Eq. (5.79).

For the slowly reacting swimmer we have

$$\langle r^2\rangle_a = 2\int_0^\infty dx\int_0^x dy\frac{e^{-2\gamma(x-y)}}{(1+2x)^{3/2}(1+2y)^{3/2}}. \tag{5.97}$$

Because of the slower decay, it is necessary to divide and conquer from the start. We set $z = x - y$ and note that $\int_0^\infty dx \int_0^x dy = \int_0^\infty dz \int_z^\infty dx$. Upon performing the inner integral we have

$$\langle r^2\rangle_a = \int_0^\infty dz\frac{e^{-2\gamma z}}{1+\sqrt{1+2z}+z(2+\sqrt{1+2z})}. \tag{5.98}$$

We define δ such that $1 \ll \delta \ll \gamma^{-1}$ and split the integral into

$$I_1 = \int_0^\delta dz \frac{e^{-2\gamma z}}{1+\sqrt{1+2z}+z(2+\sqrt{1+2z})}, \tag{5.99}$$

$$I_2 = \int_\delta^\infty dz \frac{e^{-2\gamma z}}{1+\sqrt{1+2z}+z(2+\sqrt{1+2z})}. \tag{5.100}$$

Upon expanding the exponential in I_1 and taking $\delta \to \infty$ we have

$$I_1 = 1 + (2 - 2\log 2)\gamma + O(\gamma^2) + \text{terms depending on } \delta. \tag{5.101}$$

Meanwhile, we rescale $z \to \gamma z$ in I_2 and expand the denominator for small γ.

$$I_2 = \int_{\gamma\delta}^\infty dz e^{-2z} \left(\frac{\gamma^{1/2}}{\sqrt{2}z^{3/2}} - \frac{\gamma}{z^2} + \dots \right). \tag{5.102}$$

Performing the integral and taking the limit $\delta \to 0$ we arrive at

$$I_2 = -2\sqrt{\pi}\gamma^{1/2} - 2\gamma\log\gamma + (2 - 2\gamma_e - 2\log 2)\,\gamma + o(\gamma) + \text{terms depending on } \delta, \tag{5.103}$$

where γ_e is the Euler-Mascheroni constant. Since δ is arbitrary, the divergent terms in both integrals must cancel. In summary, we have for the slowly reacting swimmer that

$$\langle r^2 \rangle_a = 1 - 2\sqrt{\pi}\gamma^{1/2} - 2\gamma\log\gamma + (4 - 2\gamma_e - 4\log 2)\,\gamma + o(\gamma), \tag{5.104}$$

which is Eq. (5.80).

Finally, for the fast reacting swimmer we have

$$\langle r^2 \rangle_a = 2\int_0^\infty dx \int_0^x dy \frac{e^{-2\gamma(x-y)}}{(1+\sqrt{x})^3(1+\sqrt{y})^3}. \tag{5.105}$$

This time there is no closed-form expression for the inner integral, forcing us to split both integrals in two domains. We define δ as before and write

$$\langle r^2 \rangle_a = \underbrace{\left[\int_0^\delta dx \int_0^x dy}_{I_1} + \underbrace{\int_\delta^\infty dx \int_0^x dy\right]}_{I_2} \frac{2e^{-2\gamma(x-y)}}{(1+\sqrt{x})^3(1+\sqrt{y})^3}. \tag{5.106}$$

The first part, I_1, is straightforward to do once the exponential is expanded and yields

$$I_1 = 1 - \frac{296}{3}\gamma + O(\gamma^2) + \text{terms depending on } \delta. \tag{5.107}$$

To perform I_2 we write

$$I_2 = \int_\delta^\infty dx \frac{2e^{-2\gamma x}}{(1+\sqrt{x})^3} \underbrace{\int_0^x dy \frac{e^{2\gamma y}}{(1+\sqrt{y})^3}}_{J(x)}, \tag{5.108}$$

and split the range of $J(x)$ again with the goal to obtain an expansion valid for small γ. Defining δ_1, J_1 and J_2 in a similar fashion, we find

$$J_1 = 1 + 10\gamma + O(\gamma^2) + \text{terms depending on } \delta_1, \tag{5.109}$$

whereas for J_2 we have

$$\begin{aligned} J_2 = {} & \frac{3e^{2\gamma x}}{x} - \frac{2e^{2\gamma x}}{\sqrt{x}} + 2\sqrt{2\pi}\gamma^{1/2}\mathrm{Erfi}\left(\sqrt{2\gamma x}\right) \\ & - 6\gamma \mathrm{Ei}\left(2\gamma x\right) + 2\gamma \log\gamma + \gamma\left(6\gamma_e - 6 + 6\log 2\right) \\ & + o(\gamma) + \text{terms depending on } \delta_1, \end{aligned} \tag{5.110}$$

where $\mathrm{Erfi}(z) = \mathrm{Erf}(iz)/i$ and $\mathrm{Ei}(z) = -\int_{-z}^\infty e^{-t}/t\, dt$. Combining these allows us to write

$$I_2 = \int_{\gamma\delta}^\infty dz \left[\frac{2\gamma^{1/2}e^{-2z}}{z^{3/2}} - \frac{\gamma}{z^2}\left(6e^{-2z} + 4 - 4\sqrt{2\pi z}\mathrm{Erfi}\left(\sqrt{2z}\right)\right) + o(\gamma)\right]. \tag{5.111}$$

Expanding as before and combining with I_1 we ultimately find that

$$\langle r^2\rangle_a = 1 - 4\sqrt{2\pi}\gamma^{1/2} - 28\gamma\log\gamma - \gamma\left(\frac{164}{3} + 28\gamma_e + 60\log 2\right) + o(\gamma), \tag{5.112}$$

corresponding to Eq. (5.81) in the main part of the chapter.

Chapter 6

Irreversible hydrodynamic trapping by surface rollers

6.1 Introduction

One of the first practical skills acquired by babies is the catching and moving of small items. The fluid world provides a similar challenge and the entrapment and manipulation of small objects has long been of great technological interest in micro- and nanofluidics. A wide range of physical mechanics may be exploited to achieve these tasks, giving rise to optical [88], magnetic [56], electrostatic [128], or hydrodynamic forces [208]. In recent years, synthetic swimmers actuated by external fields, chemical fuels or bacteria have been attracting attention and been employed successfully for the transport of cargo towards biomedical applications [6, 76, 117, 234].

In what is perhaps the simplest configuration suitable for the manipulation of objects in a fluid at small scales, rotating nanowires have been shown to be capable of trapping and transporting small particles within hydrodynamic vortices, as shown in Fig. 6.1a [154, 183, 268]. These magnetic nanowires are made of nickel and located near a flat surface. When the rotational axis of the magnetic field is parallel to that interface, asymmetric viscous drag near the wall converts rotation of the wire into a translation force in the direction parallel to the surface [210, 233]. When the nanowire then rotates near a non-magnetic body (in this particular case the bacterium *Escherichia coli*), the body can be trapped and transported by the resulting vortical flow.

Similar results have also been reported using magnetic particles rotating along an axis slightly tilted from the perpendicular direction, as shown in Fig. 6.1b [262]. Related hydrodynamic bound phenomena have been demonstrated using a pair of magnetically driven rollers [58, 158]. In general, when a body rotates and translates simultaneously, a vortical flow field of finite size

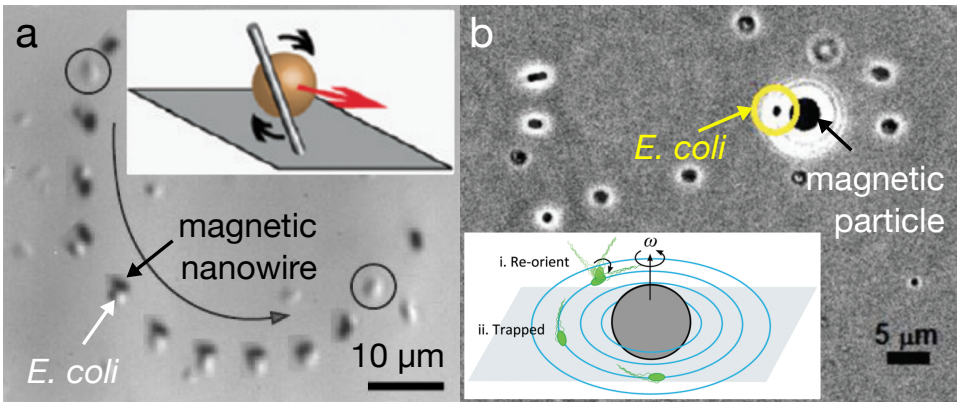

Figure 6.1 (a) A rotating magnetic nanowire traps and transports *Escherichia coli* (*E. coli*). Rotating axis is parallel to the bottom surface. Adapted from Ref. [183] with permission. Copyright (2012) American Chemical Society. (b) A rotating magnetic microparticle traps and transports *E. coli*. Rotating axis is slightly tilted (15°) from the normal direction to the bottom surface. Adapted from Ref. [262] with permission from the Royal Society of Chemistry.

appears around the body. Both fluid and particles in this region are transported together with a moving roller, as was previously shown for a rod simultaneously rotating and translating in an unbounded fluid [267]. However the onset of trapping demonstrated experimentally has so far remained elusive and both the physical mechanism behind the trapping and the optimal trapping conditions have yet to be identified.

At relatively high Reynolds number, inertial forces have been exploited to focus or trap particles in microfluidic channels [7, 59, 243]. However, in the low Reynolds number limit that is relevant for small particles, inertial terms become negligible and the fluid motion is quasi-steady. Specifically, the fluid velocity, $\boldsymbol{u}$, satisfies the incompressible Stokes equations [94]

$$\boldsymbol{\nabla} p = \mu \nabla^2 \boldsymbol{u}, \quad \boldsymbol{\nabla} \cdot \boldsymbol{u} = 0, \tag{6.1}$$

where p and μ are the dynamic pressure and viscosity of the fluid, respectively. Since these equations have no explicit time dependence, no time-irreversible motion and thus no focusing and entrapment is possible unless irreversible forces are introduced through the boundary conditions.

In this chapter we demonstrate that the mechanism of hydrodynamic trapping by a surface roller is due to the steric interaction of cargo particles with the solid boundary. Specifically, when the cargo is advected by the flow created by the roller and also sufficiently large, the steric interactions with the bounding surface allow it to migrate across streamlines into the steady flow vortex and it remains trapped there. We begin by investigating the mechanism numerically using a model roller and finite-element simulations that we describe in §6.2. Our results

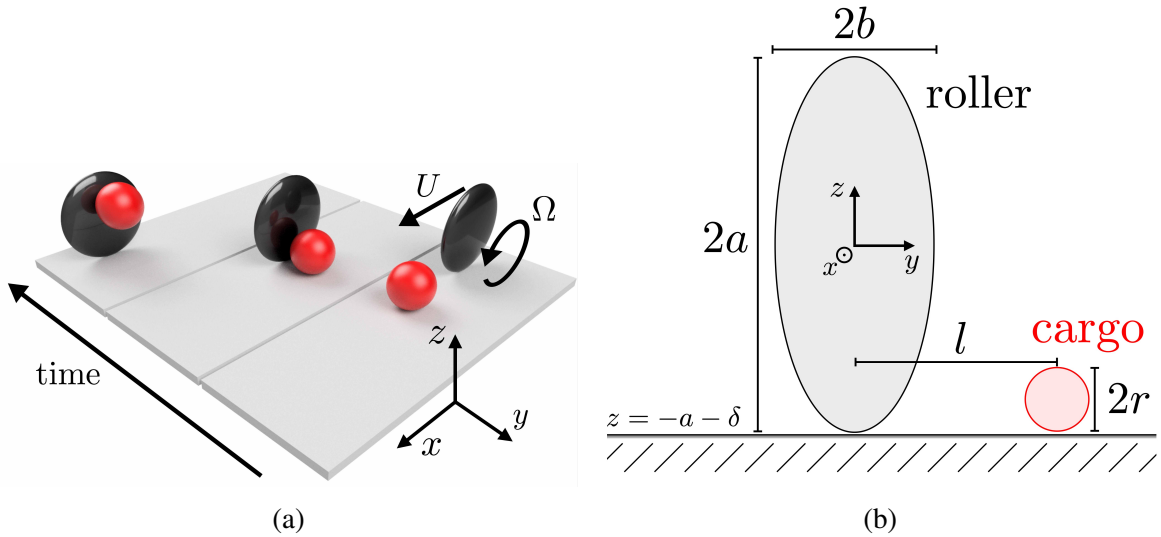

(a) (b)

Figure 6.2 (a): Schematic illustration of irreversible trapping by a surface roller illustrating the trapping of a passive spherical particle (cargo, red) by the rotating ellipsoidal particle (roller, black) due to steric repulsion from the bottom wall. (b): Sketch of the initial geometry projected in the y-z plane, illustrating relevant length scales.

are summarised in §6.3, where we present a phase diagram that indicates which parameter configurations lead to trapping and which do not. Furthermore, we illustrate the process of cargo migration and investigate the case of pure translation and no rolling. In §6.4 we present two theoretical models focusing on different aspects of our setup and explaining different features of the phase diagram, as well as the physical mechanism of cargo trapping. The chapter concludes with a discussion in section §6.5 where we show in particular that trapping is analogous to deterministic lateral displacement (DLD), a technique widely used in microfluidics [54, 104, 126, 152] and recently demonstrated to function down to nanometer scales [261].

6.2 Computational model

6.2.1 Setup

The geometrical setup of our model problem is illustrated in Fig. 6.2. We consider Stokes flow as described by Eq. (6.1) (i.e. we assume the Reynolds number to be much smaller than unity) in a semi-infinite domain described by Cartesian coordinates (x, y, z). The roller is modelled as an oblate spheroid with semi-major axes of length a in the x- and z-directions and semi-minor axis of length $b \leq a$ in the y-direction, centred at $(0, 0, 0)$ in a frame where it is stationary (illustrated in black in the figure). A rigid boundary is placed at $z = -a - \delta$, where $\delta \ll a$ is the

width of the gap between the roller and the domain boundary, which is non-zero due to the presence of a lubrication film in creeping flow. The roller translates with a velocity $\boldsymbol{U} = U\hat{\boldsymbol{x}}$, rotates at a rate $\boldsymbol{\Omega} = \Omega\hat{\boldsymbol{y}}$, is force-free and subject to a fixed external torque of the form $\boldsymbol{G} = G\hat{\boldsymbol{y}}$. The cargo particle, illustrated in red, is assumed spherical with radius r, force- and torque-free and initially placed far ahead of the roller with its centre at height $z = r$ and displaced sideways by a distance l in the y-direction. We note that l refers to the initial value of this displacement, which changes when the roller passes the cargo. Finally, we assume that the no-slip boundary condition holds on both the wall and the roller and hence that the fluid velocity matches the velocity of the boundary.

6.2.2 The finite-element routine

Since a full dynamic simulation of the roller and the cargo in this geometry is prohibitively expensive, we approximate the dynamics by calculating the flow due to the roller alone and determine the trajectories of the cargo under the assumption that it is sufficiently small not to create a significant disturbance to the velocity field. This approximation is exact in the case of a vanishingly small cargo particle and approximately correct for small values of r/a.

In Stokes flow, the hydrodynamic force $\boldsymbol{F}$ and torque $\boldsymbol{G}$ acting on the roller are related to its translational velocity $\boldsymbol{U}$ and angular velocity $\boldsymbol{\Omega}$ by an instantaneous linear relation of the form

$$\begin{pmatrix} \boldsymbol{F} \\ \boldsymbol{G} \end{pmatrix} = -\begin{pmatrix} \boldsymbol{A} & \boldsymbol{B} \\ \boldsymbol{C} & \boldsymbol{D} \end{pmatrix} \cdot \begin{pmatrix} \boldsymbol{U} \\ \boldsymbol{\Omega} \end{pmatrix}, \tag{6.2}$$

where $\boldsymbol{A}$, $\boldsymbol{B}$, $\boldsymbol{C} = \boldsymbol{B}^T$ and $\boldsymbol{D}$ are positive definite matrices that depend on the instantaneous position and orientation of the spheroid. Their combination is called the resistance tensor [94]. For a spheroid with the orientation described above, classical symmetry arguments allow one to deduce that the components of the resistance tensor associated with translation in the x-direction and rotation about the y-axis decouple from the others and only give rise to forces in the x-direction and torques in the y-direction (in other words, the resistance tensor is block-diagonal). In particular, there can be no motion in the z-direction and consequently the associated components of the resistance tensor are constant in time.

In order to determine the values of the resistance tensor, we use a finite-element routine (COMSOL Multiphysics version 4.4) and compute the flow field $\boldsymbol{u}(\boldsymbol{x})$ due to an ellipsoid in this geometry with prescribed translational velocity and zero orientational velocity, and vice versa. In both cases, we compute the hydrodynamic force and torque on the ellipsoid according to

$$\boldsymbol{F} = \iint \boldsymbol{\sigma} \cdot \boldsymbol{n}\, \mathrm{d}S, \quad \boldsymbol{G} = \iint \boldsymbol{x} \times \boldsymbol{\sigma} \cdot \boldsymbol{n}\, \mathrm{d}S, \tag{6.3}$$

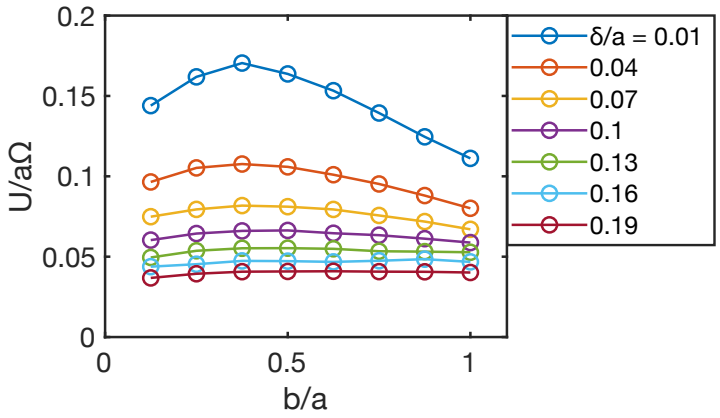

Figure 6.3 Computed rotation-translation coupling rate, $U/a\Omega$, for an ellipsoid subject to a constant torque, $G\hat{\boldsymbol{y}}$, as a function of its aspect ratio, b/a, for a range of dimensionless gap widths, δ/a (see notation in Fig. 6.2).

where $\boldsymbol{\sigma} = -p\boldsymbol{I} + \mu\left(\boldsymbol{\nabla u} + (\boldsymbol{\nabla u})^T\right)$ is the hydrodynamic stress tensor, $\boldsymbol{n}$ the unit outward normal to the roller surface, $\boldsymbol{x}$ the position vector and the integral is taken over the surface of the ellipsoid. Exploiting linearity, this allows us to invert (the relevant part of) the resistance tensor and thus find the translational velocity $\boldsymbol{U} = U\hat{\boldsymbol{x}}$ and orientational velocity $\boldsymbol{\Omega} = \Omega\hat{\boldsymbol{y}}$ for a given value of the applied torque, G, the roller aspect ratio, b/a, and the relative gap width, δ/a.

In order to validate our code we compare the hereby obtained values for the ratio of U and Ω to values in the literature derived theoretically using bipolar coordinates [57, 173] and find good quantitative agreement (see Fig. 6.4). From dimensional analysis we may deduce that we can write the coupling rate as $U/a\Omega = \gamma(\delta/a, b/a)$ where γ is a dimensionless function of two dimensionless variables. This is illustrated in Fig. 6.3, where we see that the coupling rate depends only weakly on the precise value of the parameters unless δ/a becomes very small. This is in agreement with lubrication theory, which predicts a divergence as $\delta \to 0$ [83]. In a similar fashion, we expect the flow field and trapping dynamics to be robust against variations of the parameter δ, as long as $\delta/a \gtrsim 0.04$. In what follows, we shall therefore limit our computational analysis to the case $\delta/a = 0.04$.

6.2.3 Simulating cargo trajectories

Next we consider the trajectory of a force- and torque-free spherical cargo particle in the flow field created by the roller. Faxén's first law states that the velocity, $\boldsymbol{V}$, of a force-free spherical

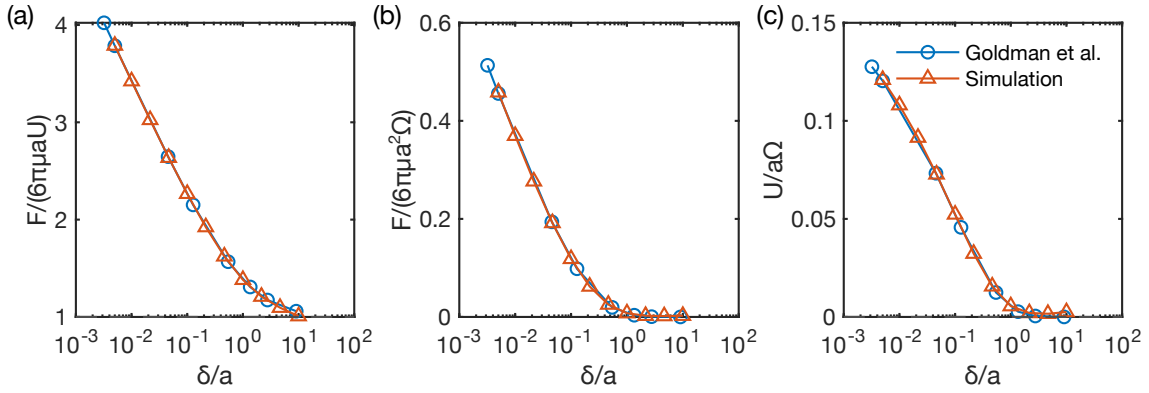

Figure 6.4 Comparison of our numerical method with the results by Goldman et al. for $a/b = 1$ [83]. (a) Normalised force on a translating sphere, (b) normalised force on a rotating sphere, and (c) force-free rotation-translation coupling rate as a function of the dimensionless gap width δ/a. The mesh was refined until the deviation from Goldman et al.'s data fell below 1% at the gap width $\delta/a = 0.005004$.

body with radius r in an unbounded Stokes flow $\boldsymbol{u}(\boldsymbol{x})$ is given by [127]

$$\boldsymbol{V} = \left(1 + \frac{r^2}{6}\nabla^2\right)\boldsymbol{u}(\boldsymbol{x}). \tag{6.4}$$

We note that this formula is only exact in an unbounded geometry, while near a wall that there are corrections of $O(r^2/d^2)$ where d is the distance between the centre of the cargo and the closest boundary. Furthermore, the relative size of the Laplacian term is $O(r^2/L^2)$, where L is the typical length scale of variations in the flow velocity. We make a simplifying assumption here and neglect both these terms, so that $\boldsymbol{V} = \boldsymbol{u}(\boldsymbol{x})$ and therefore approximate cargo trajectories may be obtained by integrating streamlines of the flow created by the roller. Mathematically this corresponds to the limit $r^2 \ll d^2$ and $r^2 \ll L^2$.

A crucial ingredient for the lateral migration of particles is taking into account the steric interactions between the lower boundary and the roller. With the aim to remove the velocity component normal to the boundary and thus model steric repulsion with no friction, we integrate trajectories according to

$$\frac{d\boldsymbol{x}}{dt} = \begin{cases} (\mathbf{1} - \boldsymbol{n}\boldsymbol{n}) \cdot \boldsymbol{u}(\boldsymbol{x}) & \text{if cargo is in contact with boundary,} \\ \boldsymbol{u}(\boldsymbol{x}) & \text{if not,} \end{cases} \tag{6.5}$$

where $\boldsymbol{n}(\boldsymbol{x})$ is a unit normal vector at the point of contact for any position $\boldsymbol{x}(t)$ of the cargo centre such that the cargo touches a boundary (which is permitted to be either the wall or the roller). In appendix §6.A we examine the accuracy of this model by comparing it with

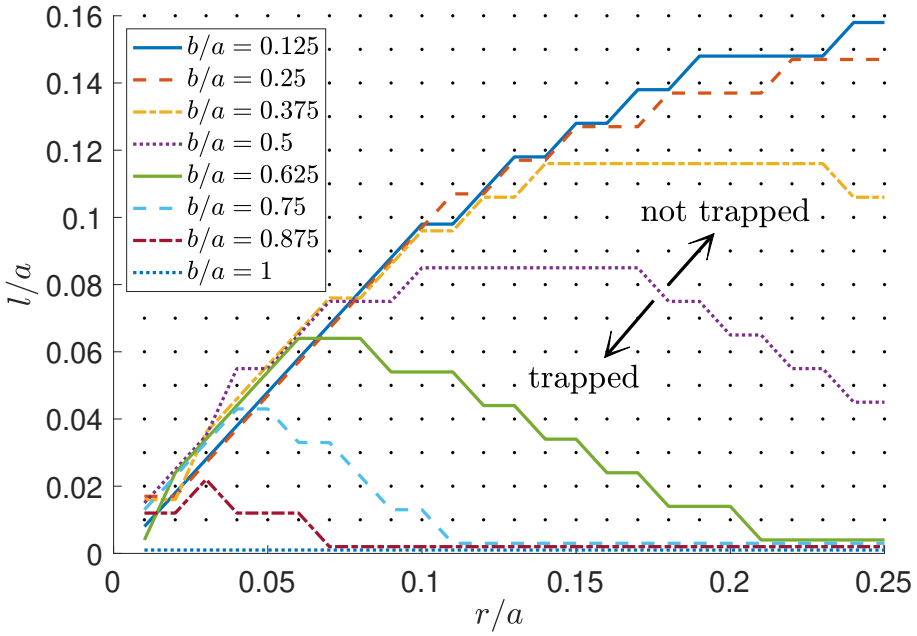

Figure 6.5 Phase diagram for entrapment of cargo particles by rollers with different aspect ratios, b/a. Each black dot corresponds to a numerically simulated parameter configuration of relative cargo size r/a and initial lateral displacement l/a. For configurations above a given curve no trapping occurred, while for parameters below the curve the cargo particle was trapped in a periodic trajectory in the frame of the roller.

detailed finite-element simulations at judiciously chosen values of the model parameters, and demonstrate its relevance for the modelling of our problem.

In the computations we initialise the cargo centre at position $(3a, l, -a + r)$ in the frame where the roller is stationary and centred at $(0, 0, 0)$ and solve for the cargo trajectory, $\boldsymbol{x}(t)$, for various values of the roller aspect ratio b/a, the relative cargo size r/a and the initial lateral displacement l/a. To this end, we use a forward-Euler scheme with a time-step sufficiently small for the results to be robust to variations in step size by a factor of two. We note that since the flow is linear in G, the value of the applied torque has no influence on the geometry of particle trajectories and it only determines the overall magnitude of the flow field.

6.3 Computational results

6.3.1 Phase diagram for cargo entrapment

In our simulations we probe the parameter space of r/a between 0.01 and 0.25 and l/a between 0.01 and 0.30 in increments of 0.01 for eight different values of the aspect ratio b/a between

0.125 and 1 in increments of 0.125. Our computational results are summarised in the phase diagram shown in Fig. 6.5. Each black dot corresponds to a single simulation and the coloured lines indicate the boundary between configurations for which trapping of the cargo by the roller vortex is observed (below) and not observed (above). Here entrapment is defined as the convergence of the cargo to a periodic orbit in the frame where the roller is stationary. Since no entrapment occurs for $l/a \geq 0.16$ we omit this range in the diagram for clarity. Furthermore, we observe that steric interactions generally occur only between the cargo and the lower wall, but never between cargo and roller. For all values in our examined parameter range, the flow induced by the roller advects the cargo sufficiently far to the side to prevent this situation.

We draw four main conclusions from the data summarised in Fig. 6.5. First, and most obviously, the range of cargo sizes (r/a) and initial lateral displacements (l/a) that lead to entrapment decreases as the aspect ratio is varied from a very flat ellipsoid ($b/a = 0.125$) to a sphere ($b/a = 1$). In fact, in the case of a sphere no trapping is observed at all. These results suggest that a narrow aspect ratio is conducive to trapping. Secondly, the dependence on the initial cargo position, l/a, is monotonic for every configuration of the other parameters, with a well-defined threshold above which no trapping occurs. This result makes intuitive sense, since a cargo particle placed very far to the side of the roller will experience little to no deflection, while particles in the path of the roller experience the strongest flows. Thirdly, and perhaps most importantly, we observe that the dependence of the trapping threshold on cargo size r/a is not monotonic. Instead, a well-defined range of values exists for each configuration of lateral placement l/a and roller aspect ratio b/a in which trapping occurs. Therefore this provides a constraint on what type of cargo a given roller can trap and transport at all, since only cargo of the right size will be pushed from its unbounded trajectories into a region of closed streamlines. Finally, we see in Fig. 6.5 that the slope of the separatrices for small values of l/a and r/a are all approximately one, regardless of the roller aspect ratio. This suggests that in order to be trapped, a cargo particles must not lie entirely on one side of the plane of symmetry of the roller.

6.3.2 Illustration of cargo migration

In order to shed more light on the entrapment mechanism, we illustrate in Fig. 6.6 three exemplary parameter configurations. We choose the values $b/a = 0.5$ and $l/a = 0.07$, which can be seen in Fig. 6.5 (and as reproduced in Fig. 6.6d) to feature different behaviour for three different ranges of r/a, for which we select the values $r/a = 0.05$, 0.10 and 0.25. An examination of the trajectories reveals that a cargo particle that is too small squeezes through below a region of closed streamlines next to the roller (Fig. 6.6a), while cargo that is too large is instead lifted up to trajectories around the same region (Fig. 6.6c). For a particle of intermediate

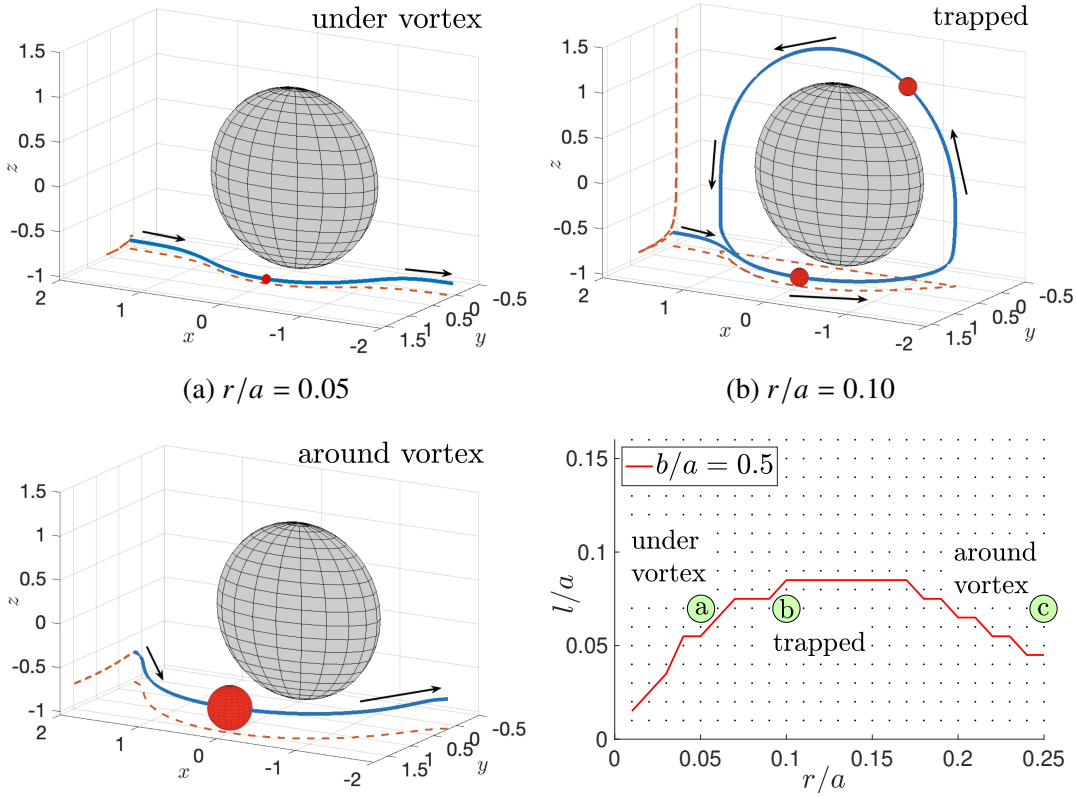

(a) $r/a = 0.05$ (b) $r/a = 0.10$

(c) $r/a = 0.25$ (d)

Figure 6.6 Numerical illustration of trapping for a roller (grey) of aspect ratio $b/a = 0.5$ and spherical cargo (red) of initial lateral displacement $l/a = 0.07$ and of three different sizes r/a. The thick blue line show the cargo trajectory in the frame where the roller is stationary, with the dashed red lines indicating shadows on planes perpendicular to the x- and z-axes added for clarity. The roller travels in the positive x-direction. Arrows indicate the direction of the cargo trajectories and axes are scaled by a. (a): Small cargo particles are squeezed through under a region of closed streamlines; (b): Medium-sized particles are pushed into a vortex of closed streamlines through steric interactions with the bottom wall and are therefore trapped; (c): Large particles are confined to unbounded trajectories around the vortex; (d): Location of (a)-(c) in the phase diagram in Fig. 6.5.

size (Fig. 6.6b), we observe a trajectory that is not fore-aft symmetric, as the cargo is pushed into a vortex of closed streamlines by steric interactions with the bottom wall.

6.3.3 Pure translation does not lead to trapping

In a similar fashion to the case of a roller that is subject to a constant torque, we also examined the case of a purely translating spheroid with $\Omega = 0$ and $U \neq 0$. Such a scenario is somewhat artificial, since it requires a finely tuned ratio of non-zero force and torque, but is nonetheless instructive to examine because it exhibits strikingly different behaviour. We considered the cases of a sphere ($b/a = 1$) and a very flat spheroid ($b/a = 0.125$) for the range $l/a = 0.01 - 0.30$ and $r/a = 0.01 - 0.25$ in steps of 0.01 each and integrate streamlines numerically in the same fashion as above. In this case, we find that for no parameter value in this range the cargo particle is trapped, instead it always passes the spheroid on a nearly unperturbed trajectory. From this we can hence conclude that the rotation of the spheroid is essential for entrapment and bounded transport of cargo particles.

6.4 Theoretical models

The phase diagram in Fig. 6.5 was obtained by simulating the trajectories of cargo particles numerically. Since the geometry of the problem is rather complex, we propose two different theoretical models that each focus on a different feature of the numerical observations. First, we consider the flow induced by a rotating and translating disc in an unbounded fluid (neglecting the influence of the wall), in order to explain why trapping is more pronounced for flat rollers and why there is an upper limit to the size of cargo that may be trapped. We then propose a two-dimensional singularity model, to explain the physical mechanism of trapping and why no trapping is observed for a purely translating spheroid.

6.4.1 Vortex flow surrounding a translating and rotating rigid disc

The first important feature of the phase diagram is the prominence of trapping for rollers with a narrow aspect ratio. In order to elucidate this further, we begin by considering the extreme case of a rolling disc, i.e. we consider the limit $b = 0$, and in order to make analytical progress, we ignore the presence of the wall. We consider a frame in which the disc is stationary but rotating with angular velocity $\mathbf{\Omega} = \Omega\hat{\boldsymbol{y}}$, and scale lengths by the disc radius, a. Since the no-slip condition is applied on the disc's surface, very near to it (that is for $|y|$ small) the fluid is approximately in solid body rotation. In terms of cylindrical polar coordinates (ρ, θ, y) with $\rho^2 = x^2 + z^2$ and $\tan\theta = x/z$ we show in appendix §6.B that the streamfunction for a rotating

rigid disc in a quiescent infinite fluid is of the form $\boldsymbol{\psi} = \psi(\rho; y)\hat{\boldsymbol{y}}$ where

$$\psi = \frac{\Omega}{\pi}\left[-3\frac{y^2}{\lambda} + \lambda + \left(\frac{y^2}{\lambda^2} + 1 + 3y^2 - \lambda^2\right)\cot^{-1}\lambda\right], \tag{6.6}$$

and

$$\lambda = \left\{\frac{1}{2}\left(\rho^2 + y^2 - 1\right) + \frac{1}{2}\left[\left(\rho^2 + y^2 - 1\right)^2 + 4y^2\right]^{1/2}\right\}^{1/2}. \tag{6.7}$$

To model our simulations, we still need to add translation in the plane perpendicular to the axis of rotation. To this end we define the non-dimensional coupling rate between translation and rotation as $\gamma = U/a\Omega$. As illustrated in Fig. 6.3, the translation is slow and typically $\gamma \approx 0.1 \ll 1$. In order to describe the flow topology and identify regions of closed streamlines, we would like to use the streamfunction formalism for the more complicated problem of coupled translation and rotation as well, since it is easy to identify the value of ψ at stationary points, where $\boldsymbol{\nabla}\psi = \mathbf{0}$, and then trace the contours that separate topologically distinct regions of the flow. However, as is evident from the numerics also, there is a new out-of-plane component of the flow in the y-direction as soon as translation is considered.

In order to circumvent this issue, we exploit the fact that γ is small and simply add a background flow of magnitude $-U\hat{\boldsymbol{x}}$. This effectively amounts to neglecting the correction to the streamfunction due to the no-slip condition on the disc surface. It is easily seen that the magnitude of the discrepancy on the boundary is uniformly equal to γ and thus, by linearity of Stokes flow, the global error in $\boldsymbol{u}$ incurred is also linear in γ.

After rescaling and removing an apparent divergence at $\lambda = 0$ by substituting ρ for y we then find that the approximated translation-rotation streamfunction is hence given by

$$\psi(x, z; y, \gamma) = \frac{1}{\pi}\left(\frac{3\lambda}{1+\lambda^2}\rho^2 - 2\lambda + \left(2 + 2\lambda^2 - \frac{1+3\lambda^2}{1+\lambda^2}\rho^2\right)\cot^{-1}\lambda\right) + \gamma z. \tag{6.8}$$

This streamfunction now allows us to identify a region of closed streamlines semi-analytically. We find numerically that for small values of $|y|$ there exist two stagnation points which are located at $x = 0$ and z positive. As $|y|$ increases, these vanish through a saddle-node bifurcation. By identifying contours of ψ equal to the value at the saddle, we can then determine the size and shape of the vortex. For the representative value of $\gamma = 0.1$ this is illustrated in Fig. 6.7 by means of two cross-sections in the planes $x = 0$ and $y = 0$. We see two topologically distinct regions, separated by the thick red line that corresponds to intersection of the streamlines that pass through the line of saddle points with the plane $x = 0$ (Fig. 6.7a). Inside this region, streamlines are closed and encircle the lines of centre points (dashed line), while outside the streamlines are unbounded and extend to infinity in the x-direction (Fig. 6.7b). The discrepancy between the

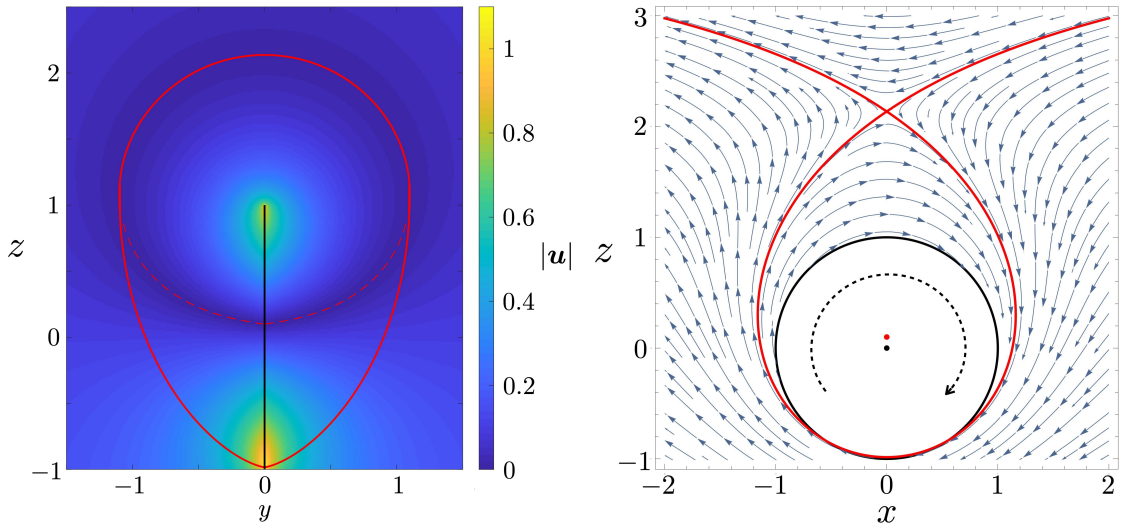

(a) y-z plane (b) x-z plane

Figure 6.7 Illustration of the vortex surrounding a rotating and translating disc for $\gamma = 0.1$ with lengths scaled by the disc radius a. (a) Front view (y-z plane): The thick red line indicates the vortex boundary, with saddle points constituting the top half, while the dashed red line indicates two lines of centre stagnation points. (b) Side view (x-z plane): The separatrix streamline is indicated in red, as is the centre stagnation point. The geometrical centre of the roller is indicated in black for comparison. The discrepancy between the points gives an indication of the magnitude of the error in this model.

centre of the disc and the centre stagnation point of the flow is due to the approximation we made earlier and is equal to γ.

While it is expected that the presence of the wall will also alter the general topology of the flow field, the model illustrates that the flat geometry leads to the fluid in the region $\{\rho < 1, |y| \ll 1\}$ moving in nearly solid-body rotation. As seen in Fig. 6.6, this still holds true for the vortex in the presence of the wall, except very close to the boundary, where this is a small distortion in the y-direction. This provides a constraint on the size of cargo particles that may be trapped at all, since cargo particles exceeding the size of the vortex width cannot be trapped in it by volume exclusion. Likewise, a particle placed too far to the side of the roller will simply circumvent the vortex and not get trapped either. This explains why no trapping is observed in the phase diagram in Fig. 6.5 for large values of l/a and r/a.

When the aspect ratio instead approximates that of a sphere, volume exclusion is more significant. Furthermore, due to the increased curvature of the ellipsoid, the effective solid body rotation is also less pronounced. Both of these factors contribute to the observation that trapping is less pronounced for near-spherical rollers.

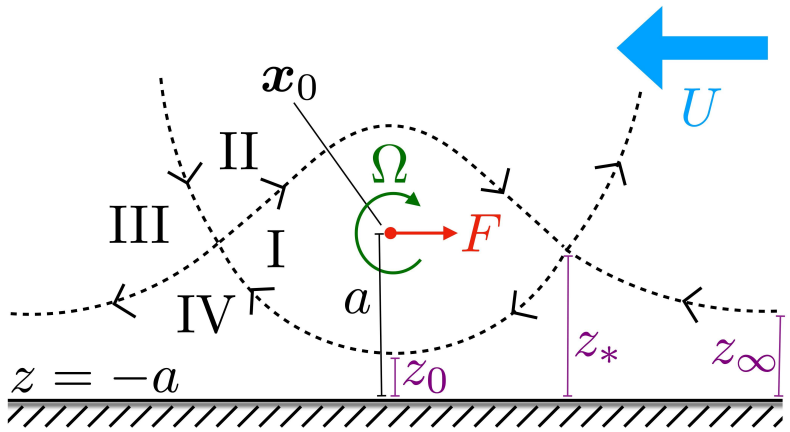

Figure 6.8 Sketch of the 2D model geometry. Dashed black lines correspond to separatrix streamlines dividing the flow into four topologically distinct regions I-IV described in §6.4.2. For a force-free roller model, $F = 0$.

6.4.2 Physical mechanism of trapping by the squeezing of streamlines

As seen in Fig. 6.6, the fluid on either side of the roller is nearly in solid body rotation except very close to the boundary, where this is a distortion in the y-direction. In order to derive a model for the trapping mechanism we can exploit this nearly two-dimensional nature of the flow to find a 2D streamfunction, $\psi(x, z)$ whose contours approximate the flow field close to the side of the roller. Fundamentally, the flow is composed of two different components, namely one due to the roller rotation and one due to the translation. We choose to model the rotation by means of a point (line) vortex of strength $\Omega\hat{\boldsymbol{y}}$ placed at $\boldsymbol{x}_0 = \boldsymbol{0}$ above a rigid, flat no-slip surface that we place at $z = -a$. In order to model translation we add a background flow of magnitude $-U\hat{\boldsymbol{x}}$ and keep the ratio $\gamma = U/a\Omega$ as a parameter. For some additional generality we furthermore include a force per unit length of strength $F\hat{\boldsymbol{x}}$, which we set to zero for the case of a force-free roller. A sketch of the setup is shown in Fig. 6.8.

The flow due to a point line vortex next to a rigid wall differs from that of a line vortex in infinite space due to a correction that is necessary to satisfy the no-slip condition on the boundary. The method of images provides a way to interpret this correction as equivalent to the influence of image singularities located in a hypothetical fluid on the other side of the boundary. In the case of a line vortex, these are a line vortex, a symmetric force dipole and a source-doublet placed at the mirror image point of the singularity [23], just as in the case of a three-dimensional rotlet singularity. Similarly, the image of the force is given by another force, a symmetric force dipole and a source dipole. We define the streamfunction, ψ, such that $\boldsymbol{u} = (\partial\psi/\partial z, -\partial\psi/\partial x)$ and streamlines are lines of constant ψ. As described in detail in

appendix §6.C , the streamfunction is given by

$$\psi = (\eta z - 1)\log\frac{R}{r} + \frac{2(1+\eta)(z+1)(z+2)}{R^2} - \gamma(z+1), \tag{6.9}$$

where lengths have been scaled with a, $r^2 = z^2+x^2$, $R^2 = (z+2)^2+x^2$ and the two dimensionless parameters γ and η are defined as

$$\gamma = \frac{U}{\Omega a}, \quad \eta = \frac{F}{8\pi\mu\Omega a}. \tag{6.10}$$

A force-free roller then corresponds to the case $\eta = 0$. As is illustrated in Fig. 6.8, the flow is divided into four topologically distinct regions for non-zero values of γ, namely (I) a vortex of closed streamlines around the singularities, (II) a counter-rotating vortex vertically above the singularities, (III) streamlines passing around the roller above and (IV) streamlines passing below. Streamlines in regions (I) and (II) are closed, while streamlines in (III) and (IV) are unbounded. The origin of these regions may be understood in terms of the actual three-dimensional geometry around the roller, in which the stagnation points in the centres of regions (I) and (II) are linked up by a vortex ring in the y-z plane while regions (III) and (IV) are linked by streamlines circumventing the roller by bending out of the x-z plane.

The four regions are divided by a single separatrix streamline $\psi = \psi_0$ with two stagnation points fore and aft to the roller. In the degenerate case $\gamma = 0$ (no translation) these stagnation points collapse onto the wall. If $\eta = 0$ and $\gamma \geq 3/8$ they coalesce in a pitchfork bifurcation into a single saddle point vertically above the singularity and region (II) disappears.

For non-zero η, the position of these stagnation points is the solution to a transcendental equation. However, by means of a Taylor expansion it may be shown that for small γ their height z_* above the surface and the value of ψ_0 are given by

$$z_* = \frac{2(1+\eta)}{(1+2\eta)^2}\gamma + O(\gamma^2), \quad \psi_0 = -\frac{1+\eta}{(1+2\eta)^2}\gamma^2 + O(\gamma^3). \tag{6.11}$$

With this, we can trace the height of the separatrix to its value centrally below the roller z_0 and far away z_∞, which are found to be

$$z_0 = \frac{1}{2+4\eta}\gamma + O(\gamma^2), \; z_\infty = \frac{1+\eta}{(1+2\eta)^2}\gamma + O(\gamma^2). \tag{6.12}$$

We see that their ratio obeys

$$\frac{z_0}{z_\infty} = \frac{1+2\eta}{2+2\eta} \leq 1. \tag{6.13}$$

Therefore we have shown theoretically that the separatrix streamline is squeezed for any finite value of η, i.e. any flow with a rotational component regardless of any forcing. As $\eta \to \infty$ and there is only a force and no rotation, no squeezing of the streamlines occurs.

In order to understand the consequences of this consider a cargo particle of radius $r \lesssim z_\infty$ resting in the path of the roller at a height less than z_∞ from the wall. The particle will be advected by the flow, first towards the stagnation point, and then below the roller. If $r \lesssim z_0$ the particle will survive the squeezing and will escape on the other side of the roller, to be advected away. In contrast, if $r \gtrsim z_0$ the steric repulsion between the cargo particle and the wall means that the cargo will not survive the squeezing. Instead, it will experience a time-irreversible migration across the separatrix streamline into the vortex surrounding the flow singularities. Since the streamlines in this vortex are closed, such a particle will then remain trapped forever thereafter. This is the physical mechanism for trapping of cargo particles, and similar to the irreversibility phenomenon observed in sheared suspensions [184].

We note that z_0/z_∞ is minimised for $\eta = 0$, that is a force-free roller. Furthermore, since the squeezing requires $z_0/z_\infty < 1$, it is not sufficient to have $\eta = \infty$, i.e. pure translation. Therefore rotation of the roller is a necessary ingredient for squeezing, even though it is not for the flow topology (see illustration in Fig. 6.9b). This agrees with our numerical observations, where no trapping occurs for a purely translating ellipsoid and any choice of parameters.

6.5 Discussion

In this chapter we showed that the onset of hydrodynamic trapping by a surface roller near a wall is due to the physical contact of a passive finite-sized particle to the bottom wall, which breaks the time reversibility of the system. The flow field around a rotating and translating rigid body features a vortex of closed streamlines, in which particles can be trapped. However, the migration from unbounded streamlines into the vortex in the absence of gravity is only possible due to steric repulsion. While the actual three-dimensional flow field is rather complex, a simple two-dimensional singularity model allowed us to explain why rotation is the essential factor that contributes to trapping. A passive particle with a radius larger than the height of the deflected streamline experiences a steric repulsion from the bottom wall and translates into a vortex.

The trapping mechanism proposed here is analogous to the deterministic lateral displacement commonly used in micro-and nanofluidic separation systems [54, 104, 126, 152, 261]. In a typical deterministic lateral displacement (DLD) device, particle trajectories are controlled by the steric interaction between particles and pillar arrays, as shown schematically in Fig. 6.10. Here small particles are approximately advected with the flow, but large particles collide with the array and migrate across streamlines. As a consequence, differently sized particles can

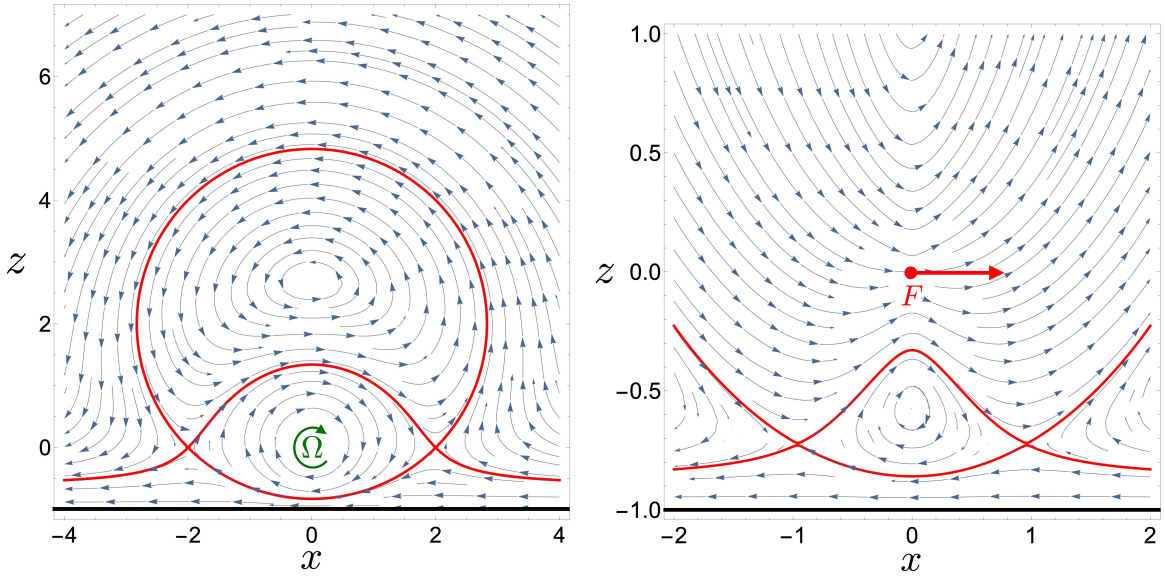

(a) $\eta = 0$, $\gamma = 0.25$ (b) ψ/η for $\eta \to \infty$ and $\gamma/\eta = 0.5$

Figure 6.9 Illustration of the squeezing of streamlines in the two-dimensional singularity model, with parameter values chosen to emphasise important features of the flow field. (a): In the presence of a rotation, the separatrix streamline (bold, red) is squeezed below the singularity. (b): For a translating force with no rotation there is still a region of closed streamlines but no squeezing occurs.

be sorted by their size. Similarly, in our model only particles that are sufficiently large to experience steric interactions with the bottom wall but small enough to fit into the vortex can be selectively trapped inside of it.

In our approach to modelling this problem we made a few important assumptions. First, we assumed for computational feasibility that a finite-sized particle follows the streamlines of an isolated roller near a wall. In reality there are corrections due to the distortion of the flow field in the presence of the particle, and by Faxén's law also the fact that finite-sized particles do not exactly follow streamlines. Detailed numerical calculations at judiciously chosen values of the parameters are reproduced in the appendix §6.A. They support the accuracy of our model and show that it is able to capture the key feature that enables DLD-like trapping in the entire parameter range considered in this chapter. Nevertheless, due to lubrication forces the velocity of approach to the boundary is modified, and a more detailed analysis might be necessary to obtain certainty for a particular parameter configuration. In an experimental system, further deviations may be induced by the effects of thermal noise when the roller and cargo particles are sufficiently small.

Secondly, in order to remain analytically tractable our minimal theoretical models contain many simplifications of the real problem. Indeed, our numerics show that the three-dimensional

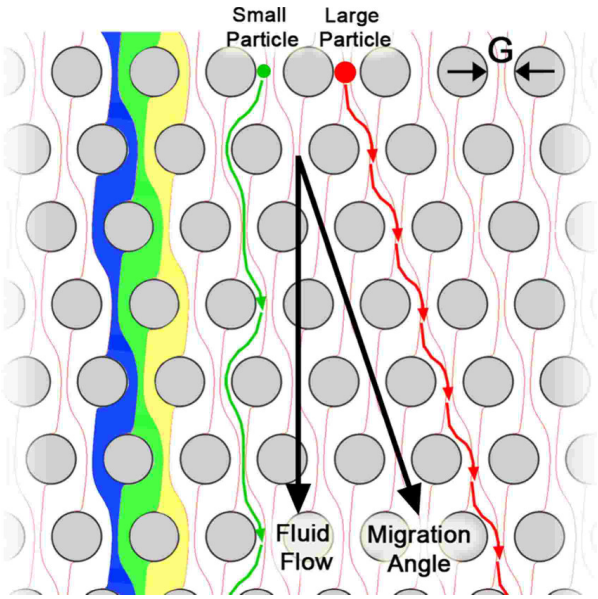

Figure 6.10 Schematic illustration of deterministic lateral displacement (DLD). While small particles (green) approximately follow the flow streamlines, large particles (red) divert their trajectories due to steric interactions with a micro-pillar array. Reprinted from Ref. [106], with the permission of AIP Publishing.

nature of the geometry and the no-slip condition on the roller surface generate a velocity field that is more complex than either of the theoretical models predict. However, for a range of parameters the essential aspects flow topology are revealed to be similar to the 2D case, with regions containing closed vortical structures present at the sides of the roller and squeezed streamlines beneath.

Finally, we assumed that the passive particles are neutrally buoyant to eliminate the effect of gravity for simplification. In a typical experiment, the trapped objects are polystyrene particles or biological cells, which are slightly heavier than the surrounding fluid (water). In this case, the sedimentation of passive particles can be another irreversible force and induce trapping. However, this gravity-induced time-irreversibility becomes less significant in the case of a rapidly rotating roller, while the squeezing of streamlines and the thereby induced lateral migration is always present.

6.A Analysis of the flow disturbance due to finite cargo size

In this chapter we employ a simplified, minimal approach to calculate the trajectory of the cargo particle in the flow created by the roller. Specifically, we calculate the flow field in the absence of any cargo particle using a finite-element routine, and then assume that the cargo simply

	b/a	r/a	l/a (see text)	Trapped?	Cargo location	Δ^2	β
(a)	0.5	0.05	0.07	No	Centre of squeezing	0.1300	0.14°
(b)	0.5	0.10	0.07	Yes	Centre of squeezing	0.1203	0.03°
(c)	0.5	0.10	0.07	Yes	Halfway up vortex	0.0033	0.16°
(d)	0.5	0.25	0.07	No	Centre of squeezing	0.0179	0.10°
(e)	0.125	0.25	0.15	Yes	Centre of squeezing	0.0818	0.04°
(f)	0.125	0.25	0.15	Yes	Halfway up vortex	0.0033	0.67°

Table 6.1 Parameter configurations for the verification of our methodology (left of double line) and two measures for the accuracy of the computed cargo velocity (right of double line).

follows the streamlines of this flow (except when altered by steric interactions). We employ this methodology since dynamic simulations in this geometry require computation times on the order of weeks to months for each individual data point, which is prohibitively expensive. However, it is of course still necessary to quantify the error incurred by this simplification.

In order to assert the accuracy of our analysis, we calculate the flow field in the presence of a force- and torque-free cargo particle at six judiciously chosen positions and parameter configurations using the same finite-element routine with the remaining boundary conditions unchanged. These parameter configurations are listed on the left side of Table 6.1. Here, (a) to (d) are chosen to match the data points analysed in detail in Fig. 6.6, while (e) and (f) represent an extreme point in the top right of the phase diagram of Fig. 6.5, where we expect our analysis to be least accurate. We assume in each case that the cargo follows streamlines according to our minimal model up to the location where we calculate the flow field exactly. The value of l/a is therefore to be understood as an identifier of the minimal model configuration that informs a particular cargo location, rather than a direct input to the numerical procedure.

As illustrated in Fig. 6.11, the nature of the streamline through the cargo centre is the same as in the simplified case presented in the main text in all cases considered. Furthermore, the qualitative disturbance of the flow topology due to the presence of the cargo is very small, even for a comparatively large particle with $r/a = 0.25$ as shown in Fig. 6.11 (d) to (f). In the cases where the cargo is located at the centre of squeezing there is no visible deformation, while in the cases where the cargo is transported upward in the vortex there is a slight bending of the streamlines immediately in contact with the particle. This is due to a rigid-body rotation that the cargo experiences due to a non-zero vorticity of the flow. Crucially, the topology of the vortex remains intact. Even in the extreme case (f) the cargo particle is located well inside the vortex, with streamlines that escape to infinity separated from the cargo surface by more one cargo radius. However, as is illustrated in case (d), the picture is less clear at the centre of squeezing, where a slight upward dislocation of the cargo might lead to trapping. This threshold may conceivably be crossed even just due to thermal noise. The boundaries of our phase diagram

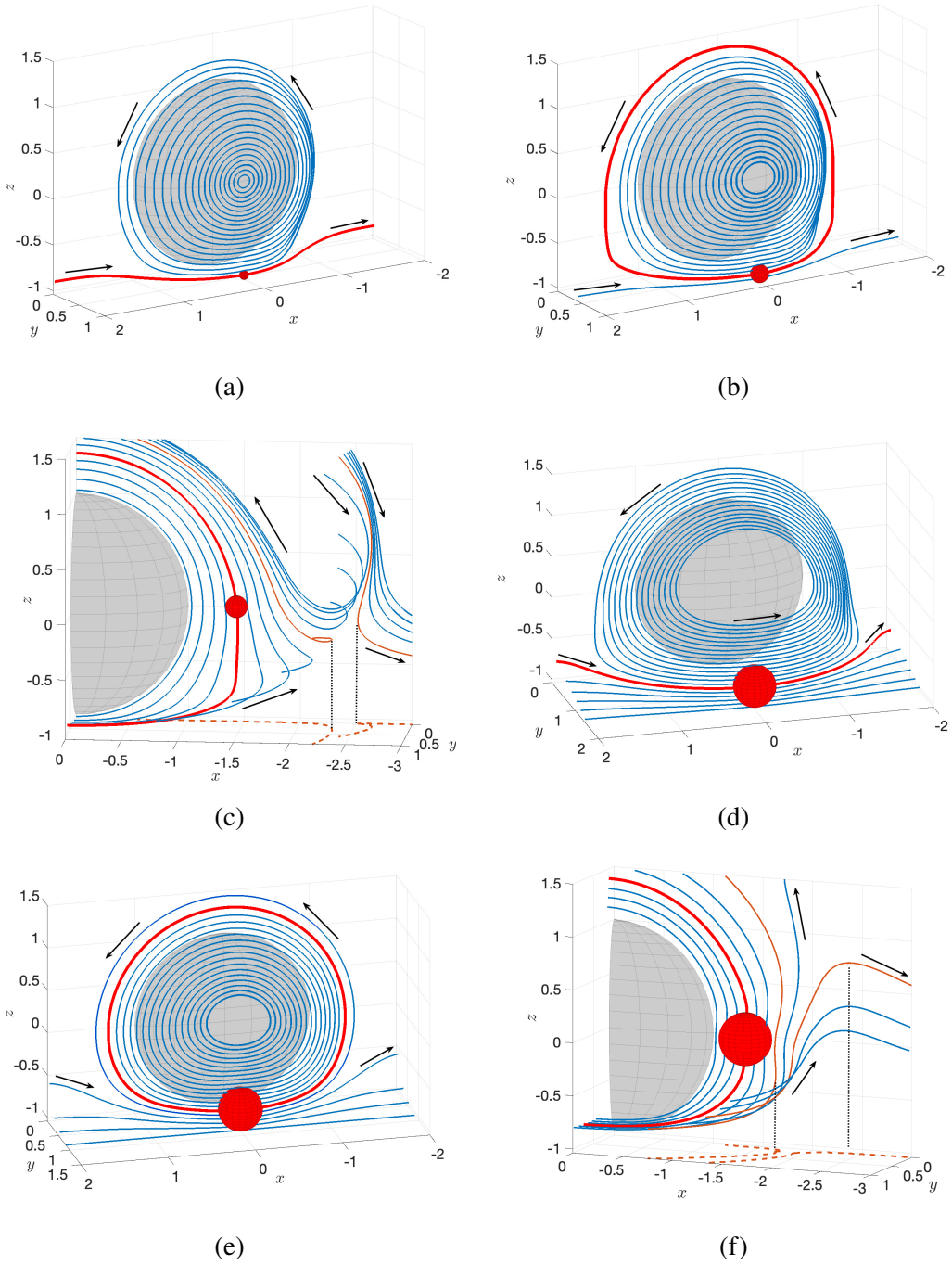

Figure 6.11 Illustration of numerically obtained streamlines for each of the parameter configurations listed in Table 6.1. The streamline through the cargo centre is highlighted in bold red, black arrows give an indication of flow direction. In (c) and (f) the shadows of certain (orange) streamlines are drawn in dashed orange to help visualise the flow topology.

may therefore be slightly blurred in a real system. Nevertheless, these results provide strong evidence that our methodology classifies particle trajectories accurately.

To provide further quantitative evidence for the accuracy of the methodology, we compute the velocity of the cargo particle $\boldsymbol{u}_c$ in the cases (a) to (f) and compare it with the flow velocity $\boldsymbol{u}(\boldsymbol{x}_c)$ at the position of the cargo centre $\boldsymbol{x}_c$ calculated in the absence of the particle. Since the velocities are vectors, we compare both the normalised squared difference in magnitude $\Delta^2 = |\boldsymbol{u}_c - \boldsymbol{u}(\boldsymbol{x}_c)|^2/|\boldsymbol{u}_c|^2$, and the angle $\beta = \cos^{-1}(\boldsymbol{u}_c \cdot \boldsymbol{u}(\boldsymbol{x}_c)/|\boldsymbol{u}_c||\boldsymbol{u}(\boldsymbol{x}_c)|)$ between the velocity vectors. These results are summarised on the right side of Table 6.1. In all cases, the difference in direction is vanishingly small and amounts to less than 1°. The difference in magnitude is larger, especially when the cargo is located at the centre of squeezing. This is due to friction forces that could be calculated using lubrication theory. These are most significant in the cases (a) and (b) when the cargo is squeezed below the vortex while still passing close to the side of the roller, and smaller when the particle is deflected further to the side in the cases (d) and (e) and especially when it is located further away from rigid boundaries as in cases (c) and (f). Overall however the error remains small, and supports the modelling approach in the main text.

6.B Derivation of the streamfunction for a rotating rigid disc

The first important feature of the phase diagram is the prominence of trapping for rollers with a narrow aspect ratio. In order to elucidate this further, we begin by considering the extreme case of a rolling disc, i.e. we consider the limit $b = 0$, and in order to make analytical progress, we ignore the presence of the wall. We consider a frame in which the disc is stationary but rotating with angular velocity $\boldsymbol{\Omega} = \Omega\hat{\boldsymbol{y}}$, and scale lengths by the disc radius, a. Since the no-slip condition is applied on the disc's surface, very near to it (that is for $|y|$ small) the fluid is approximately in solid body rotation. In terms of cylindrical polar coordinates (ρ, θ, y) with $\rho^2 = x^2 + z^2$ and $\tan\theta = x/z$ we therefore seek a solution to the Stokes equations with boundary condition

$$\boldsymbol{u} = \Omega\rho\boldsymbol{e}_\theta, \quad y = 0, \rho < 1, \tag{6.14}$$

and flow decaying to zero at infinity. For convenience, we introduce oblate spheroidal coordinates (λ, ξ, θ) defined by

$$y = \lambda\xi, \tag{6.15}$$

$$\rho^2 = (\lambda^2 + 1)(1 - \xi^2), \tag{6.16}$$

$$\theta = \theta. \tag{6.17}$$

Note that λ and θ are dimensionless, while ξ has units of length. Surfaces of constant λ are oblate spheroids that are defined by the relation

$$\frac{\rho^2}{1+\lambda^2} + \frac{y^2}{\lambda^2} = 1. \tag{6.18}$$

In particular, the degenerate case $\lambda = 0$ corresponds to a disc of radius 1. Casting the problem in these coordinates therefore lends itself to a particularly convenient form of the boundary condition Eq. (6.14), namely

$$\boldsymbol{u} = \Omega\rho\boldsymbol{e}_\theta, \quad \lambda = 0. \tag{6.19}$$

where $\rho(\lambda, \xi)$ is defined implicitly. It can be shown [228] that the solution is a purely azimuthal flow given

$$\boldsymbol{u} = u_\theta(\rho, \lambda)\boldsymbol{e}_\theta, \quad u_\theta = \Omega\rho \times \frac{2}{\pi}\left(\cot^{-1}\lambda - \frac{\lambda}{1+\lambda^2}\right), \tag{6.20}$$

which we can evaulate by using the relation

$$\lambda = \left\{\frac{1}{2}\left(\rho^2 + y^2 - 1\right) + \frac{1}{2}\left[\left(\rho^2 + y^2 - 1\right)^2 + 4y^2\right]^{1/2}\right\}^{1/2}. \tag{6.21}$$

Since the flow is purely azimuthal in the x-z plane, and therefore two-dimensional (2D) incompressible, we can define a streamfunction of the form $\boldsymbol{\psi} = \psi(\rho; y)\hat{\boldsymbol{y}}$ that recovers this flow field if we treat y as a parameter that labels different 'slices' of the fluid. Since $u_\theta = -\partial\psi/\partial\rho$ we have

$$\psi = \frac{2\Omega}{\pi}\int\left(\frac{\lambda}{1+\lambda^2} - \cot^{-1}\lambda\right)\rho\,\mathrm{d}\rho, \tag{6.22}$$

We note that Eq. (6.18) implies $\rho d\rho/d\lambda = \lambda + y^2/\lambda^3$ and so we can integrate Eq. (6.22) exactly to find

$$\psi = \frac{\Omega}{\pi}\left[-3\frac{y^2}{\lambda} + \lambda + \left(\frac{y^2}{\lambda^2} + 1 + 3y^2 - \lambda^2\right)\cot^{-1}\lambda\right], \tag{6.23}$$

where we choose the constant of integration such that $\psi \to 0$ as $\lambda \to \infty$. This is the streamfunction for a rotating rigid disc in a quiescent infinite fluid.

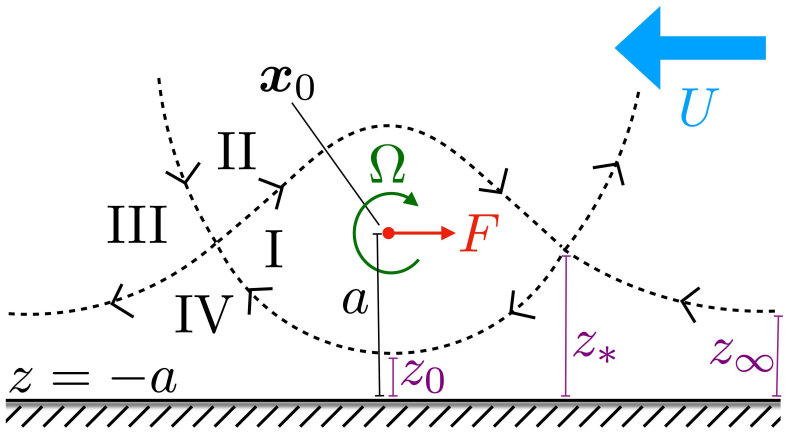

Figure 6.12 Sketch of the 2D singularity model geometry with the separatrix streamline and stagnation points.

6.C Details of the 2D singularity model

6.C.1 Derivation

Here we give some additional details for the 2D singularity model presented in §6.4.2. For convenience we repeat the sketch from Fig. 6.8 in Fig. 6.12.

The Oseen tensor for 2D Stokes flow in the x-z plane is given by[188]

$$\boldsymbol{j}(\boldsymbol{x};\boldsymbol{x}_0) = -\log r\boldsymbol{I} + \frac{\boldsymbol{r}\boldsymbol{r}}{r^2}, \tag{6.24}$$

where $\boldsymbol{r} = \boldsymbol{x} - \boldsymbol{x}_0$ and $r = |\boldsymbol{r}|$. Some relevant derivatives are given by

$$\partial_k j_{ij} = \frac{-r_k\delta_{ij} + r_j\delta_{ik} + r_i\delta_{jk}}{r^2} - 2\frac{r_i r_j r_k}{r^4}, \qquad \text{(force dipole)} \tag{6.25}$$

$$\nabla^2 j_{ij} = 2\frac{\delta_{ij}}{r^2} - 4\frac{r_i r_j}{r^4}. \qquad \text{(source dipole)} \tag{6.26}$$

We consider the flow due to point singularities located at $\boldsymbol{x}_0 = (0,0)$ in the presence of a rigid wall at $z = -a$ with normal $\boldsymbol{n} = (0,1)$. The flow due to a point force per unit length $\boldsymbol{F}$ is given in this geometry by

$$\boldsymbol{u}^f = \frac{\boldsymbol{F}}{8\pi\mu}\cdot\left(\boldsymbol{j} - \boldsymbol{j}^* - 2a\boldsymbol{D}\cdot\boldsymbol{\nabla}(\boldsymbol{j}^*\cdot\boldsymbol{n}) + a^2\boldsymbol{D}\cdot\nabla^2\boldsymbol{j}^*\right), \tag{6.27}$$

where $\boldsymbol{D} = \boldsymbol{I} - 2\boldsymbol{n}\boldsymbol{n}$ and $\boldsymbol{j}^* = \boldsymbol{j}(\boldsymbol{x}; \boldsymbol{D}\cdot\boldsymbol{x}_0)$. This has exactly the same structure as a point force in 3D flow [23], and by linearity the same holds true for any higher order singularities. For a force parallel to the wall in the positive x-direction the expression in Eq. (6.27) evaluates to

$$\boldsymbol{u}^f = \frac{F}{8\pi\mu}\begin{pmatrix} -\log r + \log R + \frac{x^2}{r^2} - \frac{x^2}{R^2} - \frac{2a(z+a)}{R^2} + \frac{4ax^2(z+a)}{R^4} \\ \frac{xz}{r^2} - \frac{xz}{R^2} + \frac{4ax(z+a)(z+2a)}{R^4} \end{pmatrix}, \tag{6.28}$$

where $r^2 = x^2 + z^2$, and $R^2 = x^2 + (z+2a)^2$. 2D Stokes flow is incompressible and thus admits a streamfunction ψ such that $\boldsymbol{u} = (\psi_z, -\psi_x)$. For the force parallel to the wall we then have

$$\psi^f = \frac{F}{8\pi\mu}\left(z\log\frac{R}{r} + \frac{2a(z+a)(z+2a)}{R^2}\right). \tag{6.29}$$

For the flow due to a point vortex in the $x-z$ plane we consider the addition of a hypothetical y-axis with $\boldsymbol{\Omega} = (0, a\Omega, 0)$ oriented along that axis. With this setup $\Omega > 0$ corresponds to a clockwise rotation in the $x-z$ plane and thus rolling in the positive x-direction. The flow is given by

$$\boldsymbol{u}^r = -\frac{1}{2}(\boldsymbol{\Omega}\times\boldsymbol{\nabla})\cdot\boldsymbol{j} + \frac{1}{2}(\boldsymbol{\Omega}\times\boldsymbol{\nabla})\cdot\boldsymbol{j}^* - (\boldsymbol{n}\times\boldsymbol{\Omega}\,\boldsymbol{n} + \boldsymbol{n}\,\boldsymbol{n}\times\boldsymbol{\Omega}) : \boldsymbol{\nabla}\boldsymbol{j}^* + h(\boldsymbol{n}\times\boldsymbol{\Omega})\cdot\nabla^2\boldsymbol{j}^*. \tag{6.30}$$

This evaluates to the following flow in the x-z plane:

$$\boldsymbol{u}^r = \Omega a\begin{pmatrix} \frac{z}{r^2} - \frac{z}{R^2} + \frac{4x^2(z+a)}{R^4} \\ -\frac{x}{r^2} + \frac{x}{R^2} + \frac{4x(z+a)(z+2a)}{R^4} \end{pmatrix}. \tag{6.31}$$

The corresponding streamfunction is

$$\psi^r = \Omega a\left(-\log\frac{R}{r} + \frac{2(z+a)(z+2a)}{R^2}\right), \tag{6.32}$$

which is actually quite similar to ψ^f since similar image singularities are required for this solution. Finally we note that the streamfunction for a constant background flow in the negative x-direction $\boldsymbol{u}^b = (-U, 0)$ is

$$\psi^b = -U(z+a). \tag{6.33}$$

Most of these results have been derived previously, e.g. in [115]. All streamfunctions are defined so that they satisfy $\psi = 0$ on the wall.

We scale lengths by $a = 1$ from this point onwards and furthermore introduce the parameters $\eta = F/8\pi\mu a\Omega$ and $\gamma = U/a\Omega$ denoting the relative strength of the various terms. The combined

and rescaled streamfunction is then

$$\psi = (\eta z - 1)\log\frac{R}{r} + \frac{2(1+\eta)(z+1)(z+2)}{R^2} - \gamma(z+1), \tag{6.34}$$

as claimed in the main text. In the following, we analyse the stagnation points and topology of the streamlines in the two cases $\eta = 0$ (force-free) and $\eta > 0$ (with force).

6.C.2 No force, $\eta = 0$

Let us first consider the case of a force-free roller, i.e. $\eta = 0$. Our first goal is to find the stagnation points of the flow. Upon differentiating ψ with respect to x we find that the vertical velocity is zero when $z = -1$, $x = 0$ or when the condition

$$x^2 + z^2 = 4 \tag{6.35}$$

is satisfied. Differentiating ψ with respect to z and substituting for x we can determine the position of the stagnation points exactly and find that

$$\boldsymbol{\nabla}\psi = \mathbf{0} \quad \text{if} \quad (x,z) = \left(\pm\frac{\sqrt{3-8\gamma}}{1-2\gamma}, \frac{4\gamma-1}{1-2\gamma}\right), \quad 0 \le \gamma < \frac{3}{8}, \tag{6.36}$$

$$\text{or} \quad (x,z) = (0,z'), \tag{6.37}$$

where z' is solution to

$$\frac{4(1+z')}{z'(2+z')^2} = \gamma. \tag{6.38}$$

For $0 < \gamma < 3/8$ the first two constitute saddle points fore and aft the roller, while the third corresponds to a centre vertically above the singularity. When $\gamma = 0$, the centre disappears and the saddle points collapse onto the wall. When γ passes through $3/8$ then these coalesce in a pitchfork bifurcation and only one saddle remains. Since we observe $\gamma \approx 0.1$ in our numerical simulations, we discard this case and obtain a flow field with four topologically distinct regions as discussed in the main text.

The value of the streamfunction at the stagnation points is

$$\psi_0 = \gamma + \frac{1}{2}\log(1-2\gamma) = -\gamma^2 - \frac{4}{3}\gamma^3 + O(\gamma^4), \tag{6.39}$$

so that the streamline passing through the stagnation point satisfies $\psi = \psi_0$. We compare the height of this streamline centrally below the singularity (z_0), at the stagnation point (z_*) and far

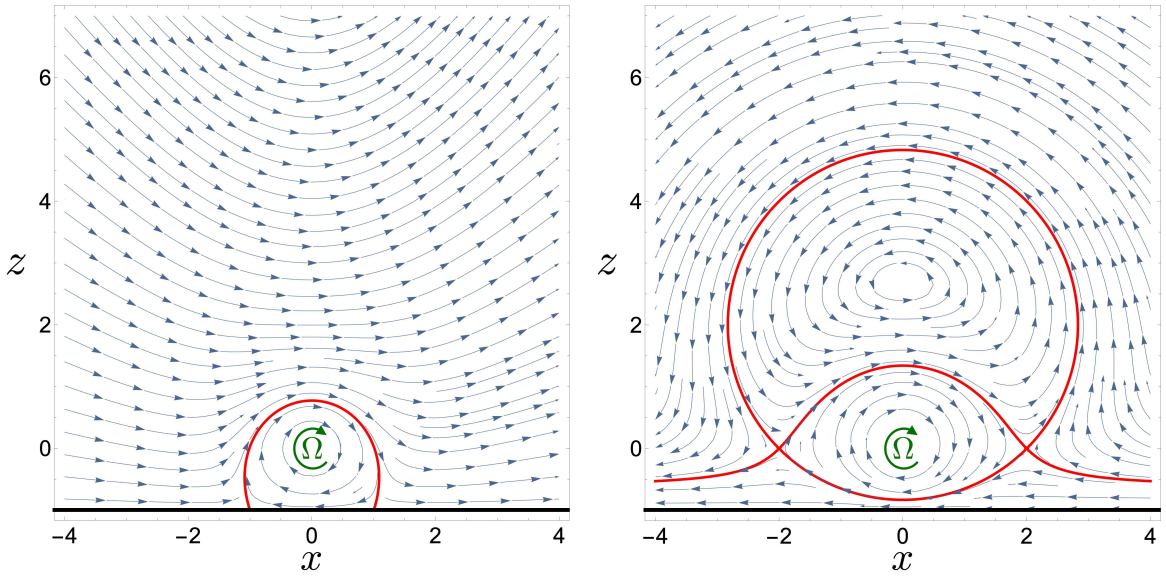

(a) $\gamma = 0$ (b) $\gamma = 0.25$

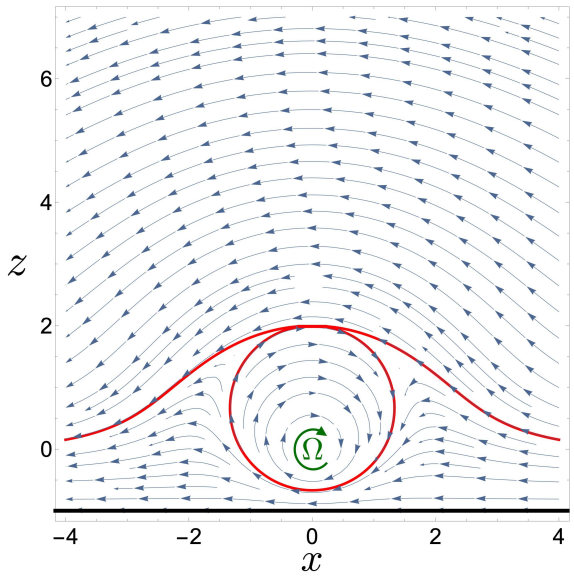

(c) $\gamma = 3/8$

Figure 6.13 Streamlines for $\eta = 0$ ((no force). The separatrix streamline is indicated in bold red. For $\gamma > 0$ we see that it is squeezed below the singularity.

away (z_∞) to understand whether squeezing occurs. As $x \to \infty$ we have

$$\psi = -\gamma(z+1) + 2\frac{(z+1)^2}{x^2} + O(x^{-4}), \quad \Rightarrow \quad z_\infty = -1 - \frac{1}{2\gamma}\log(1-2\gamma)\,. \tag{6.40}$$

At leading order in γ we therefore have $z_\infty = \gamma$. Meanwhile, z_0 satisfies

$$\gamma + \frac{1}{2}\log(1-2\gamma) = \log\frac{1-z_0}{1+z_0} + \frac{2z_0}{1+z_0} - \gamma z_0. \tag{6.41}$$

Due to the presence of the logarithm, this equation does not have an analytic solution. However, we may expand for small z_0 and γ and find

$$-\gamma^2 - \frac{4}{3}\gamma^3 + \cdots = -\gamma z_0 - 2z_0^2 + \frac{4}{3}z_0^3 + \ldots \tag{6.42}$$

Thus $z_0 \sim \gamma$ at leading order and we can solve a quadratic to find $z_0 = \gamma/2 + O(\gamma^2)$. In summary we have to leading order that

$$z_0 = \frac{1}{2}\gamma, \quad z_* = 2\gamma, \quad z_\infty = \gamma, \quad \psi_0 = -\gamma^2. \tag{6.43}$$

Thus the streamline coming in from infinity first goes up to twice its original height at the stagnation point before being squeezed down to half its original height below the singularity. As discussed in the main text, this squeezing of streamlines gives rise to irreversible trapping of cargo particles. An illustration is given in Figure 6.13.

6.C.3 With force, $\eta > 0$

In the case that the force is non-zero we have a more complicated streamfunction. The condition for no vertical flow ($\psi_x = 0$) becomes

$$x^2 + \left(z + \frac{2\eta}{1+2\eta}\right)^2 = 4\left(\frac{1+\eta}{1+2\eta}\right)^2. \tag{6.44}$$

Using this we find that the condition for no lateral velocity ($\psi_z = 0$) becomes

$$-\gamma + \frac{(1+2\eta)(z+1)}{2(z+2)} + \frac{\eta}{2}\log\left(\frac{(1+\eta)(z+2)}{1-\eta z}\right) = 0. \tag{6.45}$$

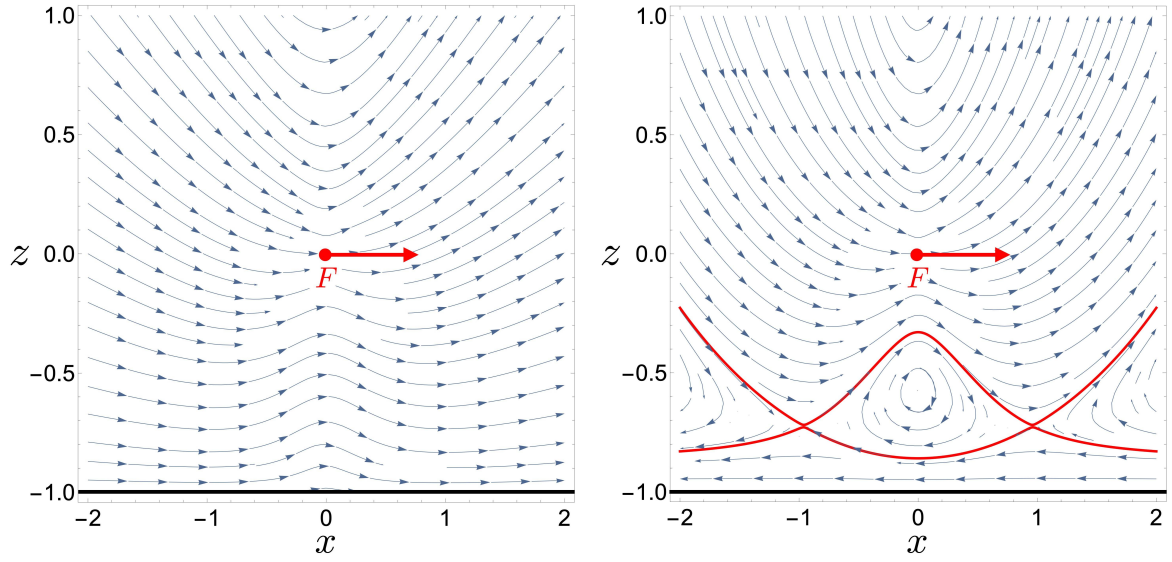

(a) $\gamma/\eta = 0$ (b) $\gamma/\eta = 0.5$

Figure 6.14 Streamlines for a force with no rotation (ψ/η for $\eta \to \infty$ and γ/η finite). The separatrix streamline is indicated in bold red. No squeezing occurs, yet a region of closed streamlines exists below the singularity.

This is now a transcendental equation for z with no analytical solution. To make progress, we expand this for small γ and find that

$$z_* = \frac{2(1+\eta)}{(1+2\eta)^2}\gamma + O(\gamma^2), \quad \psi_0 = -\frac{1+\eta}{(1+2\eta)^2}\gamma^2 + O(\gamma^3). \tag{6.46}$$

For as $x \to \infty$ we have

$$\psi = -\gamma(z+1) + \frac{(2+4\eta)(z+1)^2}{x^2} + O(x^{-4}), \tag{6.47}$$

so that $z_\infty = (1+\eta)\gamma/(1+2\eta)^2 + O(\gamma^2)$. For z_0 we find

$$-\frac{1+\eta}{(1+2\eta)^2}\gamma^2 + O(\gamma^3) = -\gamma z_0 - 2z_0^2 + \frac{4(1+\eta)}{3}z_0^3 + O(z_0^4) \tag{6.48}$$

so that to leading order $z_0 = \gamma/2(1+2\eta)$. In summary,

$$z_0 = \frac{1}{2+4\eta}\gamma, \quad z_* = \frac{2(1+\eta)}{(1+2\eta)^2}\gamma, \quad z_\infty = \frac{1+\eta}{(1+2\eta)^2}\gamma, \quad \psi_0 = -\frac{1+\eta}{(1+2\eta)^2}\gamma^2, \tag{6.49}$$

as quoted in the main text. As expected, we recover our previous results if we set $\eta = 0$. We also have

$$\frac{z_0}{z_\infty} = \frac{1+2\eta}{2+2\eta} \leq 1 \tag{6.50}$$

for $\eta \geq 0$, therefore squeezing always occurs in the presence of a force. However, the relative extent to which streamlines are squeezed is maximised for a force-free roller. Notably, in the limit $\eta \to \infty$ with γ/η finite, corresponding to a purely translating roller with no rotation we have

$$z_0 = \frac{1}{4\eta}\gamma, \quad z_* = \frac{1}{2\eta}\gamma, \quad z_\infty = \frac{1}{4\eta}\gamma, \quad \psi_0 = -\frac{1}{4\eta}\gamma^2, \tag{6.51}$$

indicating that no squeezing occurs. This shows that according to our model rotation is an essential ingredient for entrapment. An illustration is given in Figure 6.14.

Chapter 7

Summary

In this dissertation we have analysed a range of problems related to the propulsion, navigation and control of many different kinds of microswimmers.

In chapter 2 we used extensive numerical simulations to compute the trajectories of spherical squirmers through BCC lattices for a broad range of both the squirming parameter, β, and the lattice packing density, ϕ. We found a rich array of different qualitative behaviours, ranging from straight trajectories over weakly diffusive random walks to instant entrapment by the lattice.

We further demonstrated that much of this behaviour can be explained, at least qualitatively, using a combination of relatively simple hydrodynamic near-field and far-field arguments for the squirmer and its interactions with individual spheres in the lattice. Specifically, pullers tend to be stabilised and pushers destabilised on trajectories far from lattice elements. Close to lattice spheres, near-field and far-field hydrodynamic effects compete. There is a clear threshold in the squirming strength for entrapment, indicating that strong pushers are trapped, whereas weak pushers and pullers navigate through the lattice more or less unhindered. This may then result either in a trajectory resembling a weak random walk or, if too constrained by the lattice packing density, again a straight path. For a given squirming strength, there appears to be a clear threshold in packing density above which all trajectories are straight regardless of initial conditions.

In the parameter range for which the swimmer performs a random walk, it would be interesting to quantify the effective diffusive motion of the active particles. However, because reorientation events occur very infrequently, it is currently too computationally expensive to quantify it accurately from our simulations. A recent study has investigated this for a random Lorentz gas [165], and future work with more powerful numerical algorithms may shed more light on this issue taking hydrodynamics into account. Similarly, the effects of lattice geometry warrant further investigation: while test runs that we performed for a cubic lattice

reveal the same generic behaviour of squirmers in the far field, the question to what extent the stuck-to-orbiting and unbounded-to-trapped transitions depend on the lattice geometry remains to be answered. Recently, simulations using Lattice-Boltzmann methods have revealed a rich behaviour of squirmer dynamics near flat and curved surfaces, which add to the complexity of the dynamics [130, 131]. The phenomenology of straight pusher trajectories and deflected puller trajectories is also reminiscent of the stability behaviour of suspensions of such model microswimmers, where pushers generically interact chaotically while pushers tend to form stable or isotropic structures [200–202].

Future studies could address how additional properties of the squirmer can affect the dynamics, for example potential phoretic effects. In a setup with a chemically-patterned lattice, a passive particle may propel through phoretic interactions, or in the case of a weakly charged lattice a charged swimmer may be affected through electromagnetic effects. Practical applications in which our results may be put into use include the design of porous filters for swimmers of different types and strengths.

In chapter 3 we derived physically intuitive expressions for the flow due to an arbitrary point torque (rotlet, split into axisymmetric and transverse components) and a point source exterior to a rigid sphere and a spherical bubble in Stokes flow. In the case of an axisymmetric rotlet outside a rigid sphere, the image flow may be interpreted as due to a single image torque, which can be explained using an argument involving Apollonian circles. The solution is therefore equally valid for an axisymmetric torque inside a spherical shell. Surprisingly, we find that the image field is much simpler in the rigid case than for a bubble, contrary to the other cases considered in this chapter and most known singularity solutions near plane surfaces [216]. In the transverse rotlet case, the image system is more complicated and involves multiple line integrals of singularities, yet the expression remains compact and easy to evaluate numerically. Two bifurcations of the flow field occur as the distance of the singularity to the sphere centre is varied. In the case of a point source, the solution cannot be written in terms of a finite number of images for either a rigid or a stress-free (bubble) boundary condition.

In additional to classical applications for the hydrodynamic interactions between colloidal particles [90], our results could be useful for the theoretical modelling of biologically motivated hydrodynamic problems, such as the interaction of rotating bacterial flagella with the cell body [39, 69, 187]. Our results are easily implemented and calculated numerically, and particularly suited to modelling the interaction of any number of singularities in an object-oriented programming style. The result for an axisymmetric torque within a rigid spherical shell may find additional use in the modelling of flows transport within biological cells [98, 167].

Recently, regularised hydrodynamic singularities [47, 266] have become a popular tool to carry out efficient numerical simulations of the dynamics slender filaments in Stokes flow [111, 162, 214] and great progress has been made in employing them to reduce numerical stiffness [46, 93]. Regularising a singularity in a non-trivial geometry also requires a modification of its image flow field in order to preserve the boundary condition, and doing this turns out to not be straightforward [5]. While this has been achieved for the Stokeslet [259], more work needs to be done to derive regularised versions of the rotlet and the source in a spherical geometry. We hope that the work outlined in this chapter will be useful for this purpose, too.

In chapter 4 we have defined the notion of direct and indirect advection of bacterial flagellar filaments, and used it to classify the flows contributing to the bundling process. In addition we derived a numerical elastohydrodynamic model that corroborates our predictions and leads to new ones.

The first conclusion is that the generation of thrust by flagella is sufficient to initiate bundling through hydrodynamic interactions. This follows from the fact that both the direct and indirect interactions in Eq. (4.15) and Eq. (4.20) respectively lead to non-zero advection towards a bundle in the entire geometric parameter range.

The second conclusion is that for both thrust- and rotation-induced flows indirect advection dominates for long filaments and at wide separation, i.e. during the early stages of the bundling process. The shape of the boundary between direct- and indirect-dominated regions suggests a 'wake' that a flagellar filament is generating behind the cell body with a width on the order of the cell body diameter. Therefore another way to think of this result is to say that indirect interactions dominate unless the filaments are in each other's wake.

The third conclusion is that in terms of the dynamic bundling process, the relative contribution of direct and indirect effects depends on the length of the flagellum, with active contributions being more important the shorter the flagellar filaments are. This is because a larger part of the θ-parameter range is direct-dominated for small R, as discussed in §4.3.3.

The fourth conclusion is that the rotation of the flagella only generates flows in the azimuthal direction and thus does not facilitate bundling purely through hydrodynamic effects. However, evidenced by our numerical model, they do play a role in conjunction with other physical constraints, such as tethering. This was already known for direct hydrodynamic interactions [125, 156], here we demonstrate that it holds true for indirectly generated flows as well.

From the numerical model we make the further conclusion, that the shift in balance between direct and indirect effects is non-monotonic during the bundling process, with a peak in direct dominance, and furthermore that different sections of the flagella are affected by these changes to different extents.

Naturally, by reducing the system to two geometric parameters we make a number of simplifying assumptions. In reality, cells are slightly denser than water (for *E. coli* $\rho \approx 1.08\text{g ml}^{-1}$ [129] while for water $\rho \approx 1.00\text{g ml}^{-1}$), also their cell body is normally not spherical and they feature more than two flagella [17]. Furthermore, we restrict our attention to two flagella, while *E. coli* features between two and five [185].

An interesting direction to explore with this framework would be the dynamics of more than two flagella. If more than two flagella are present much of the symmetry of this problem is lost, which could potentially lead to more interesting behaviours. In addition, this model might lead to a better understanding of the unbundling process, that triggers the 'tumble' gait. When a peritrichous bacterium reverses the direction of one flagellar motor to clockwise rotation, the torque exerted by that flagellum is reversed. However, the total torque and hence the strength of the indirect advection is weakened but not negated due to continued counter-clockwise rotation of the remaining flagella, thus acting to keep the bundle together at the end. This may therefore be the physical explanation why the clockwise rotating flagellum appears to be 'pulled out' at the base of the bundle in experimental observations [51].

In chapter 5 we presented two fundamental models for the dissolution and stochastic dynamics of self-propelled artificial microswimmers. Inspired by recent experimental realisations, we sough to identify the swimmer decay rates and their influence on translational and rotational diffusivity, and in turn analysed both theoretically and numerically how changes in these modify the distribution of swimmer trajectories. We identified a new dimensionless parameter, γ defined as the product of lifetime and initial rotational diffusivity, that classifies colloids with finite lifetime into 'ballistic' and 'diffusive' types independent of the dissolution process, and studied the differences between our dissolution models in three distinct limits for various values of this parameter. We found that for a given value of γ, particles dissolving in the absence of a reaction behave the most ballistically, whereas colloids reacting at high Damköhler number, defined as the ratio of fuel reactivity and diffusive replenishment, behave the most diffusively. We found that this is due to increasing and decreasing dissolution rates respectively for the different models. Furthermore we derived asymptotic expressions of their mean squared displacement for both small and large values of γ, and performed extensive Brownian dynamics simulations to validate our theoretical results and derive more information about the distribution of spread.

Not all our models can apply to all kinds of microswimmer designs. Specifically, the non-reacting model might be at odds with phoretic self-propulsion. Therefore this model only describes colloids that propel through different mechanisms, such as magnetic swimmers. Furthermore, our statistical results only hold true for microswimmers that are fully degradable. A Janus colloid with, e.g., degradable and inert halves is not going to exhibit divergent diffusivity

since the relevant length scale is bounded. Instead such a swimmer would show a decrease in velocity, which if known can be dealt with in a manner similar to our theoretical approach. In this case, however, the changing geometry of the swimmer would likely have to be solved for numerically.

Another important problem that remains to be investigated is the influence of directed motion, such as chemotaxis. Breaking the isotropy of orientational dynamics prevents an analytical investigation similar to the one carried out in this chapter since it relies on the result that the directional correlation of a particle decays exponentially. However, we can still address the issue directly in at least one special case. It was shown recently in Ref. [229] that artificial colloids perform chemotaxis by adjusting their trajectory by means of rotation, translation in the direction to a chemical gradient, and translation at an angle, each with a coefficient of strength that can be calculated from the surface activity and mobility of the colloid. In the case of uniform surface activity, the only coefficient that is non-zero is the one giving rise to translation in the direction of a chemical gradient. In particular, the rotational dynamics remain unaffected. In that case, the swimmer trajectories behave therefore just like we describe in this chapter, plus a constant velocity displacing the colloid in the direction of the chemical gradient. Furthermore numerical work will be required to address the full interplay between chemotaxis behaviour and dissolution dynamics.

Before degradable designs may be employed in real-world applications, it will be furthermore necessary to examine the effects of collective dissolution. Since our models are sensitive to the background distribution of fuel and/or solute, the influence of other nearby colloids on their dissolution will be noticeable. It is conceivable that, in analogy with bubbles [160], different decay patterns and complex stochastic behaviour emerges. Similar effects may also be triggered by confinement and also warrant further investigation.

Finally, in chapter 6 we showed that the onset of hydrodynamic trapping by a surface roller near a wall is due to the physical contact of a passive finite-sized particle to the bottom wall, which breaks the time reversibility of the system. The flow field around a rotating and translating rigid body features a vortex of closed streamlines, in which particles can be trapped. However, the migration from unbounded streamlines into the vortex in the absence of gravity is only possible due to steric repulsion. While the actual three-dimensional flow field is rather complex, a simple two-dimensional singularity model allowed us to explain why rotation is the essential factor that contributes to trapping. A passive particle with a radius larger than the height of the deflected streamline experiences a steric repulsion from the bottom wall and translates into a vortex.

The trapping mechanism proposed here is analogous to the deterministic lateral displacement commonly used in micro-and nanofluidic separation systems [54, 104, 126, 152, 261]. In a

typical deterministic lateral displacement (DLD) device, particle trajectories are controlled by the steric interaction between particles and pillar arrays. Here small particles are approximately advected with the flow, but large particles collide with the array and migrate across streamlines. As a consequence, differently sized particles can be sorted by their size. Similarly, in our model only particles that are sufficiently large to experience steric interactions with the bottom wall but small enough to fit into the vortex can be selectively trapped inside of it.

In our approach to modelling this problem we made a few important assumptions. First, we assumed for computational feasibility that a finite-sized particle follows the streamlines of an isolated roller near a wall. In reality there are corrections due to the distortion of the flow field in the presence of the particle, and by Faxén's law also the fact that finite-sized particles do not exactly follow streamlines. Detailed numerical calculations at judiciously chosen values of the parameters support the accuracy of our model and show that it is able to capture the key feature that enables DLD-like trapping in the entire parameter range considered in this chapter. Nevertheless, due to lubrication forces the velocity of approach to the boundary is modified, and a more detailed analysis might be necessary to obtain certainty for a particular parameter configuration. In an experimental system, further deviations may be induced by the effects of thermal noise when the roller and cargo particles are sufficiently small.

Secondly, in order to remain analytically tractable our minimal theoretical models contain many simplifications of the real problem. Indeed, our numerics show that the three-dimensional nature of the geometry and the no-slip condition on the roller surface generate a velocity field that is more complex than either of the theoretical models predict. However, for a range of parameters the essential aspects flow topology are revealed to be similar to the 2D case, with regions containing closed vortical structures present at the sides of the roller and squeezed streamlines beneath.

Finally, we assumed that the passive particles are neutrally buoyant to eliminate the effect of gravity for simplification. In a typical experiment, the trapped objects are polystyrene particles or biological cells, which are slightly heavier than the surrounding fluid (water). In this case, the sedimentation of passive particles can be another irreversible force and induce trapping. However, this gravity-induced time-irreversibility becomes less significant in the case of a rapidly rotating roller, while the squeezing of streamlines and the thereby induced lateral migration is always present.

References

[1] see online Supplementary Material.

[2] L. K. Abdelmohsen et al., 'Micro-and nano-motors for biomedical applications', *Journal of Materials Chemistry B* **2**, 2395–2408 (2014).

[3] K. Aderogba and J. Blake, 'Action of a force near the planar surface between two semi-infinite immiscible liquids at very low Reynolds numbers', *Bulletin of the Australian Mathematical Society* **18**, 345–356 (1978).

[4] T. C. Adhyapak and H. Stark, 'Zipping and entanglement in flagellar bundle of E. coli: role of motile cell body', *Physical Review E* **92**, 052701 (2015).

[5] J. Ainley et al., 'The method of images for regularized Stokeslets', *Journal of Computational Physics* **227**, 4600–4616 (2008).

[6] Y. Alapan et al., 'Soft erythrocyte-based bacterial microswimmers for cargo delivery', *Sci. Robot.* **3**, eaar4423 (2018).

[7] H. Amini, W. Lee and D. Di Carlo, 'Inertial microfluidic physics', *Lab Chip* **14**, 2739 (2014).

[8] F. Azam et al., 'The ecological role of water-column microbes in the sea', *Marine ecology progress series*, 257–263 (1983).

[9] C. Bächer, L. Schrack and S. Gekle, 'Clustering of microscopic particles in constricted blood flow', *Physical Review Fluids* **2**, 013102 (2017).

[10] G. Batchelor, 'The stress system in a suspension of force-free particles', *Journal of fluid mechanics* **41**, 545–570 (1970).

[11] G. Batchelor, 'An introduction to fluid dynamics' (Cambridge university press, 2000).

[12] C. Bechinger et al., 'Active particles in complex and crowded environments', *Reviews of Modern Physics* **88**, 045006 (2016).

[13] C. Beenakker, 'Ewald sum of the Rotne–Prager tensor', *The Journal of chemical physics* **85**, 1581–1582 (1986).

[14] H. C. Berg, 'Chemotaxis in bacteria', *Annual review of biophysics and bioengineering* **4**, 119–136 (1975).

[15] H. C. Berg, 'Random walks in biology' (Princeton University Press, 1993).

[16] H. C. Berg, 'The rotary motor of bacterial flagella', *Annual review of biochemistry* **72** (2003).

[17] H. C. Berg, 'E. coli in Motion' (Springer Science & Business Media, 2008).

[18] H. C. Berg and R. A. Anderson, 'Bacteria swim by rotating their flagellar filaments', *Nature* **245**, 380–382 (1973).

[19] A. P. Berke et al., 'Hydrodynamic attraction of swimming microorganisms by surfaces', *Physical Review Letters* **101**, 038102 (2008).

[20] T. Bickel, A. Majee and A. Würger, 'Flow pattern in the vicinity of self-propelling hot Janus particles', *Physical Review E* **88**, 012301 (2013).

[21] J. Blake, 'A spherical envelope approach to ciliary propulsion', *Journal of Fluid Mechanics* **46**, 199–208 (1971).

[22] J. Blake, 'A note on the image system for a Stokeslet in a no-slip boundary', in Mathematical proceedings of the cambridge philosophical society, Vol. 70 (Cambridge University Press, 1971), pp. 303–310.

[23] J. Blake and A. Chwang, 'Fundamental singularities of viscous flow', *Journal of Engineering Mathematics* **8**, 23–29 (1974).

[24] J. F. Brady, 'Particle motion driven by solute gradients with application to autonomous motion: continuum and colloidal perspectives', *Journal of Fluid Mechanics* **667**, 216–259 (2011).

[25] J. F. Brady and G. Bossis, 'Stokesian dynamics', *Annual review of fluid mechanics* **20**, 111–157 (1988).

[26] D. Bray, 'Cell Movements' (Garland Publishing, New York, NY, 2000).

[27] C. Brennen and H. Winet, 'Fluid mechanics of propulsion by cilia and flagella', *Annual Review of Fluid Mechanics* **9**, 339–398 (1977).

[28] A. Bricard et al., 'Emergence of macroscopic directed motion in populations of motile colloids', *Nature* **503**, 95–98 (2013).

[29] A. T. Brown et al., 'Swimming in a crystal', *Soft Matter* **12**, 131–140 (2016).

[30] R. Brown, 'Xxvii. a brief account of microscopical observations made in the months of june, july and august 1827, on the particles contained in the pollen of plants; and on the general existence of active molecules in organic and inorganic bodies', *Philosophical Magazine Series 2* **4**, 161–173 (1828).

[31] D. R. Brumley et al., 'Metachronal waves in the flagellar beating of Volvox and their hydrodynamic origin', *Journal of the Royal Society Interface* **12**, 20141358 (2015).

[32] S. Butler, 'A note on Stokes's stream function for motion with a spherical boundary', in Mathematical proceedings of the cambridge philosophical society, Vol. 49 (Cambridge University Press, 1953), pp. 169–174.

[33] C. Calladine, 'Change of waveform in bacterial flagella: the role of mechanics at the molecular level', *Journal of molecular biology* **118**, 457–479 (1978).

[34] H. Carslaw and J. Jaeger, 'Heat conduction in solids', *Oxford University Press, Oxford*, 75 (1959).

[35] J. K. Carson et al., 'Low pore connectivity increases bacterial diversity in soil', *Appl. Environ. Microbiol.* **76**, 3936–3942 (2010).

[36] A. Chamolly, T. Ishikawa and E. Lauga, 'Active particles in periodic lattices', *New Journal of Physics* **19**, 115001 (2017).

[37] A. Chamolly and E. Lauga, 'Stochastic dynamics of dissolving active particles', *The European Physical Journal E* **42**, 88 (2019).

[38] A. Chamolly and E. Lauga, 'Stokes flow due to point torques and sources in a spherical geometry', *Physical Review Fluids* **5**, 074202 (2020).

[39] A. Chamolly and E. Lauga, 'Direct vs indirect hydrodynamic interactions during bundle formation of bacterial flagella', submitted.

[40] A. Chamolly, E. Lauga and S. Tottori, 'Irreversible hydrodynamic trapping by surface rollers', *Soft Matter* **16**, 2611–2620 (2020).

[41] C. Chen et al., 'Transient micromotors that disappear when no longer needed', *ACS Nano* (2016).

[42] C. Chen et al., 'Magnesium-based micromotors: water-powered propulsion, multifunctionality, and biomedical and environmental applications', *Small*, 1704252 (2018).

[43] S. L. Chown et al., 'The changing form of antarctic biodiversity', *Nature* **522**, 431–438 (2015).

[44] A. T. Chwang and T. Y.-T. Wu, 'Hydromechanics of low-reynolds-number flow. part 2. singularity method for Stokes flows', *Journal of Fluid Mechanics* **67**, 787–815 (1975).

[45] R. Cortez, 'The method of regularized Stokeslets', *SIAM Journal on Scientific Computing* **23**, 1204–1225 (2001).

[46] R. Cortez, 'Regularized Stokeslet segments', *Journal of Computational Physics* **375**, 783–796 (2018).

[47] R. Cortez, L. Fauci and A. Medovikov, 'The method of regularized Stokeslets in three dimensions: analysis, validation, and application to helical swimming', *Physics of Fluids* **17**, 031504 (2005).

[48] R. Cortez and D. Varela, 'A general system of images for regularized Stokeslets and other elements near a plane wall', *Journal of Computational Physics* **285**, 41–54 (2015).

[49] C. Cruz, F. Chinesta and G. Regnier, 'Review on the Brownian dynamics simulation of bead-rod-spring models encountered in computational rheology', *Archives of Computational Methods in Engineering* **19**, 227–259 (2012).

[50] N. C. Darnton and H. C. Berg, 'Force-extension measurements on bacterial flagella: triggering polymorphic transformations', *Biophysical journal* **92**, 2230–2236 (2007).

[51] N. C. Darnton et al., 'On torque and tumbling in swimming Escherichia coli', *Journal of bacteriology* **189**, 1756–1764 (2007).

[52] D. Das and E. Lauga, 'Computing the motor torque of Escherichia coli', *Soft matter* **14**, 5955–5967 (2018).

[53] J. Dauparas, D. Das and E. Lauga, 'Helical micropumps near surfaces', *Biomicrofluidics* **12**, 014108 (2018).

[54] J. A. Davis et al., 'Deterministic hydrodynamics: taking blood apart', *Proc. Natl. Acad. Sci. U.S.A* **103**, 14779 (2006).

[55] H. De Maleprade et al., 'Motility and phototaxis of Gonium, the simplest differentiated colonial alga', *Physical Review E* **101**, 022416 (2020).

[56] I. De Vlaminck and C. Dekker, 'Recent advances in magnetic tweezers', *Annu. Rev. Biophys.* **41**, 453 (2012).

[57] W. Dean and M. O'Neill, 'A slow motion of viscous liquid caused by the rotation of a solid sphere', *Mathematika* **10**, 13–24 (1963).

[58] B. Delmotte, 'Hydrodynamically bound states of a pair of microrollers: a dynamical system insight.' *Phys. Rev. Fluids* **4**, 044302 (2019).

[59] D. Di Carlo, 'Inertial microfluidics', *Lab Chip* **9**, 3038 (2009).

[60] K. Drescher et al., 'Fluid dynamics and noise in bacterial cell–cell and cell–surface scattering', *Proceedings of the National Academy of Sciences* **108**, 10940–10945 (2011).

[61] R. Dreyfus et al., 'Microscopic artificial swimmers', *Nature* **437**, 862–865 (2005).

[62] S. Ebbens et al., 'Electrokinetic effects in catalytic platinum-insulator Janus swimmers', *EPL (Europhysics Letters)* **106**, 58003 (2014).

[63] A. Einstein, 'On the motion of small particles suspended in liquids at rest required by the molecular-kinetic theory of heat', *Annalen der physik* **17**, 549–560 (1905).

[64] A. Einstein, 'A new determination of molecular dimensions', *Ann. Phys* **19**, 289–306 (1906).

[65] T. Eisenstecken, J. Hu and R. G. Winkler, 'Bacterial swarmer cells in confinement: a mesoscale hydrodynamic simulation study', *Soft matter* **12**, 8316–8326 (2016).

[66] J. Elgeti, R. G. Winkler and G. Gompper, 'Physics of microswimmers - single particle motion and collective behavior: a review', *Reports on progress in physics* **78**, 056601 (2015).

[67] L. J. Fauci and A. McDonald, 'Sperm motility in the presence of boundaries', *Bulletin of mathematical biology* **57**, 679–699 (1995).

[68] R. P. Feynman, 'There's plenty of room at the bottom', *California Institute of Technology, Engineering and Science magazine* (1960).

[69] H. Flores et al., 'A study of bacterial flagellar bundling', *Bulletin of mathematical biology* **67**, 137–168 (2005).

[70] A. L. Fogelson and K. B. Neeves, 'Fluid mechanics of blood clot formation', *Annual review of fluid mechanics* **47**, 377–403 (2015).

[71] P. D. Frymier et al., 'Three-dimensional tracking of motile bacteria near a solid planar surface', *Proceedings of the National Academy of Sciences* **92**, 6195–6199 (1995).

[72] Y. O. Fuentes, S. Kim and D. J. Jeffrey, 'Mobility functions for two unequal viscous drops in Stokes flow. i. axisymmetric motions', *The Physics of fluids* **31**, 2445–2455 (1988).

[73] Y. O. Fuentes, S. Kim and D. J. Jeffrey, 'Mobility functions for two unequal viscous drops in Stokes flow. ii. asymmetric motions', *Physics of Fluids A: Fluid Dynamics* **1**, 61–76 (1989).

[74] G. Gallino et al., 'Physics of bubble-propelled microrockets', *Advanced Functional Materials*, 1800686 (2018).

[75] J. Gans, M. Wolinsky and J. Dunbar, 'Computational improvements reveal great bacterial diversity and high metal toxicity in soil', *Science* **309**, 1387–1390 (2005).

[76] W. Gao et al., 'Cargo-towing fuel-free magnetic nanoswimmers for targeted drug delivery', *Small* **8**, 460 (2012).

[77] W. Gao and J. Wang, 'The environmental impact of micro/nanomachines: a review', *Acs Nano* **8**, 3170–3180 (2014).

[78] W. Gao et al., 'Artificial micromotors in the mouse's stomach: a step toward in vivo use of synthetic motors', *ACS nano* **9**, 117–123 (2015).

[79] Y. Gebremichael, G. S. Ayton and G. A. Voth, 'Mesoscopic modeling of bacterial flagellar microhydrodynamics', *Biophysical journal* **91**, 3640–3652 (2006).

[80] A. Ghosh and P. Fischer, 'Controlled propulsion of artificial magnetic nanostructured propellers', *Nano letters* **9**, 2243–2245 (2009).

[81] D. Giacché, T. Ishikawa and T. Yamaguchi, 'Hydrodynamic entrapment of bacteria swimming near a solid surface', *Physical Review E* **82**, 056309 (2010).

[82] J. G. Gibbs and Y.-P. Zhao, 'Autonomously motile catalytic nanomotors by bubble propulsion', *Applied Physics Letters* **94**, 163104 (2009).

[83] A. Goldman, R. Cox and H. Brenner, 'Slow viscous motion of a sphere parallel to a plane wall—II Couette flow', *Chemical engineering science* **22**, 653–660 (1967).

[84] A. J. Goldman, R. G. Cox and H. Brenner, 'Slow viscous motion of a sphere parallel to a plane wall—I motion through a quiescent fluid', *Chemical engineering science* **22**, 637–651 (1967).

[85] R. E. Goldstein, 'Green algae as model organisms for biological fluid dynamics', *Annual review of fluid mechanics* **47**, 343–375 (2015).

[86] R. Golestanian, T. Liverpool and A. Ajdari, 'Designing phoretic micro-and nano-swimmers', *New Journal of Physics* **9**, 126 (2007).

[87] A. A. Gorbushina and W. J. Broughton, 'Microbiology of the atmosphere-rock interface: how biological interactions and physical stresses modulate a sophisticated microbial ecosystem', *Annual review of microbiology* **63**, 431–450 (2009).

[88] D. G. Grier, 'A revolution in optical manipulation', *Nature* **424**, 810 (2003).

[89] J. S. Guasto, R. Rusconi and R. Stocker, 'Fluid mechanics of planktonic microorganisms', *Annual Review of Fluid Mechanics* **44**, 373–400 (2012).

[90] E. Guazzelli and J. F. Morris, 'A physical introduction to suspension dynamics', Vol. 45 (Cambridge University Press, 2011).

[91] S. B. Guttenplan, S. Shaw and D. B. Kearns, 'The cell biology of peritrichous flagella in Bacillus subtilis', *Molecular microbiology* **87**, 211–229 (2013).

[92] W. Hackborn, M. O'Neill and K. Ranger, 'The structure of an asymmetric Stokes flow', *The Quarterly Journal of Mechanics and Applied Mathematics* **39**, 1–14 (1986).

[93] A. L. Hall-McNair et al., 'Efficient implementation of elastohydrodynamics via integral operators', *Physical Review Fluids* **4**, 113101 (2019).

[94] J. Happel and H. Brenner, 'Low Reynolds number hydrodynamics: with special applications to particulate media', Vol. 1 (Springer Science & Business Media, 2012).

[95] J. Hassink et al., 'Relationships between habitable pore space, soil biota and mineralization rates in grassland soils', *Soil Biology and Biochemistry* **25**, 47–55 (1993).

[96] W. M. Haynes, 'CRC handbook of chemistry and physics' (CRC press, 2014).

[97] P. Hegemann and B. Bruck, 'Light-induced stop response in Chlamydomonas reinhardtii: occurrence and adaptation phenomena', *Cell motility and the cytoskeleton* **14**, 501–515 (1989).

[98] Y. Hernández-Pereira et al., 'On the necessary conditions for non-equivalent solutions of the rotlet-induced Stokes flow in a sphere: towards a minimal model for fluid flow in the Kupffer's vesicle', *Mathematics* **8**, 1 (2020).

[99] A. Hilfinger, A. K. Chattopadhyay and F. Jülicher, 'Nonlinear dynamics of cilia and flagella', *Physical Review E* **79**, 051918 (2009).

[100] N. Hill and D.-P. Häder, 'A biased random walk model for the trajectories of swimming micro-organisms', *Journal of Theoretical Biology* **186**, 503–526 (1997).

[101] R. Hooke, 'Micrographia (1665)', Vol. 20 (AppLife, 2014).

[102] A. Hosoi and D. I. Goldman, 'Beneath our feet: strategies for locomotion in granular media', *Annual Review of Fluid Mechanics* **47**, 431–453 (2015).

[103] J. Hu et al., 'Fabrication, properties and applications of Janus particles', *Chemical Society Reviews* **41**, 4356–4378 (2012).

[104] L. R. Huang et al., 'Continuous particle separation through deterministic lateral displacement', *Science* **304**, 987–990 (2004).

[105] J. Ingen-Housz, 'Remarks on the use of the microscope' (na, 1784).

[106] D. W. Inglis, 'Efficient microfluidic particle separation arrays', *Applied Physics Letters* **94**, 013510 (2009).

[107] J. L. Ingraham and C. A. Ingraham, 'Introduction to microbiology' (Wadsworth Publishing Company, 1995).

[108] S. Ishijima, S. Oshio and H. Mohri, 'Flagellar movement of human spermatozoa', *Gamete research* **13**, 185–197 (1986).

[109] T. Ishikawa, M. Simmonds and T. Pedley, 'Hydrodynamic interaction of two swimming model micro-organisms', *J. Fluid Mech.* **568**, 119–160 (2006).

[110] T. Ishikawa, J. Locsei and T. Pedley, 'Development of coherent structures in concentrated suspensions of swimming model micro-organisms', *Journal of Fluid Mechanics* **615**, 401–431 (2008).

[111] K. Ishimoto and E. A. Gaffney, 'An elastohydrodynamical simulation study of filament and spermatozoan swimming driven by internal couples', *IMA Journal of Applied Mathematics* **83**, 655–679 (2018).

[112] K. Ishimoto and E. Lauga, 'The N-flagella problem: elastohydrodynamic motility transition of multi-flagellated bacteria', *Proceedings of the Royal Society A* **475**, 20180690 (2019).

[113] Z. Izri et al., 'Self-propulsion of pure water droplets by spontaneous marangoni-stress-driven motion', *Physical review letters* **113**, 248302 (2014).

[114] P. Janssen and M. Graham, 'Coexistence of tight and loose bundled states in a model of bacterial flagellar dynamics', *Physical Review E* **84**, 011910 (2011).

[115] D. Jeffrey and Y. Onishi, 'The slow motion of a cylinder next to a plane wall', *Quart. J. Mech. Appl. Math.* **34**, 129 (1981).

[116] R. M. Jendrejack, J. J. de Pablo and M. D. Graham, 'Stochastic simulations of DNA in flow: dynamics and the effects of hydrodynamic interactions', *The Journal of chemical physics* **116**, 7752–7759 (2002).

[117] D. Kagan et al., 'Functionalized micromachines for selective and rapid isolation of nucleic acid targets from complex samples', *Nano Lett.* **11**, 2083 (2011).

[118] P. Kanehl and T. Ishikawa, 'Fluid mechanics of swimming bacteria with multiple flagella', *Physical Review E* **89**, 042704 (2014).

[119] V. Kantsler et al., 'Ciliary contact interactions dominate surface scattering of swimming eukaryotes', *Proceedings of the National Academy of Sciences* **110**, 1187–1192 (2013).

[120] P. Katsamba and E. Lauga, 'Propulsion by stiff elastic filaments in viscous fluids', *Physical Review E* **99**, 053107 (2019).

[121] R. C. Kerr, 'Convective crystal dissolution', *Contributions to Mineralogy and Petrology* **121**, 237–246 (1995).

[122] M. J. Kim et al., 'Particle image velocimetry experiments on a macro-scale model for bacterial flagellar bundling', *Experiments in fluids* **37**, 782–788 (2004).

[123] M. Kim and T. R. Powers, 'Hydrodynamic interactions between rotating helices', *Physical review E* **69**, 061910 (2004).

[124] M. Kim and T. R. Powers, 'Deformation of a helical filament by flow and electric or magnetic fields', *Physical Review E* **71**, 021914 (2005).

[125] M. Kim et al., 'A macroscopic scale model of bacterial flagellar bundling', *Proceedings of the National Academy of Sciences* **100**, 15481–15485 (2003).

[126] S. C. Kim et al., 'Broken flow symmetry explains the dynamics of small particles in deterministic lateral displacement arrays', *Proc. Natl. Acad. Sci. U.S.A.* **114**, E5034 (2017).

[127] S. Kim and S. J. Karrila, 'Microhydrodynamics: principles and selected applications' (Courier Corporation, 2013).

[128] M. Krishnan et al., 'Geometry-induced electrostatic trapping of nanometric objects in a fluid', *Nature* **467**, 692 (2010).

[129] H. Kubitschek, W. Baldwin and R. Graetzer, 'Buoyant density constancy during the cell cycle of Escherichia coli', *Journal of bacteriology* **155**, 1027–1032 (1983).

[130] M. Kuron et al., 'A lattice boltzmann model for squirmers', *The Journal of chemical physics* **150**, 144110 (2019).

[131] M. Kuron et al., 'Hydrodynamic mobility reversal of squirmers near flat and curved surfaces', *Soft matter* **15**, 5908–5920 (2019).

[132] K. Kyoya et al., 'Shape matters: near-field fluid mechanics dominate the collective motions of ellipsoidal squirmers', *Physical Review E* **92**, 063027 (2015).

[133] H. Lamb, 'Hydrodynamics' (Cambridge university press, 1993).

[134] P. Langevin, 'Sur la théorie du mouvement brownien', *CR Acad. Sci. Paris* **146**, 530 (1908).

[135] E. Lauga, 'Bacterial hydrodynamics', *Annual Review of Fluid Mechanics* **48**, 105–130 (2016).

[136] E. Lauga and T. R. Powers, 'The hydrodynamics of swimming microorganisms', *Reports on Progress in Physics* **72**, 096601 (2009).

[137] E. Lauga et al., 'Swimming in circles: motion of bacteria near solid boundaries', *Biophysical journal* **90**, 400–412 (2006).

[138] V. Lebedev and D. Laikov, 'A quadrature formula for the sphere of the 131st algebraic order of accuracy', in Doklady. mathematics, Vol. 59 no. 3 (MAIK Nauka/Interperiodica, 1999), pp. 477–481.

[139] W. Lee et al., 'Bacterial flagellar bundling and unbundling via polymorphic transformations', *Physical Review E* **98**, 052405 (2018).

[140] A. V. Leeuwenhoek, 'Observations, communicated to the publisher by Mr. Antony van Leewenhoeck, in a dutch letter of the 9th Octob. 1676, here English'd: concerning little animals by him observed in rain-well-sea-and snow water; as also in water wherein pepper had lain infused', *Philosophical Transactions of the Royal Society of London* **12**, 821–831 (1677).

[141] Z. Li, 'Critical particle size where the Stokes-Einstein relation breaks down', *Physical Review E* **80**, 061204 (2009).

[142] J. Lighthill, 'On the squirming motion of nearly spherical deformable bodies through liquids at very small Reynolds numbers', *Communications on Pure and Applied Mathematics* **5**, 109–118 (1952).

[143] J. Lighthill, 'Helical distributions of Stokeslets', *J. Eng. Math.* **30**, 35–78 (1996).

[144] J. Lighthill, 'Mathematical biofluiddynamics' (SIAM, 1975).

[145] J. Lighthill, 'Flagellar hydrodynamics', *SIAM review* **18**, 161–230 (1976).

[146] S. Lim and C. S. Peskin, 'Fluid-mechanical interaction of flexible bacterial flagella by the immersed boundary method', *Physical Review E* **85**, 036307 (2012).

[147] Z. Lin, J.-L. Thiffeault and S. Childress, 'Stirring by squirmers', *Journal of Fluid Mechanics* **669**, 167–177 (2011).

[148] C. B. Lindemann, 'A "geometric clutch" hypothesis to explain oscillations of the axoneme of cilia and flagella', *Journal of theoretical biology* **168**, 175–189 (1994).

[149] C. B. Lindemann, 'A model of flagellar and ciliary functioning which uses the forces transverse to the axoneme as the regulator of dynein activation', *Cell motility and the cytoskeleton* **29**, 141–154 (1994).

[150] N. Liron and S. Mochon, 'Stokes flow for a Stokeslet between two parallel flat plates', *Journal of Engineering Mathematics* **10**, 287–303 (1976).

[151] H. Lorentz, 'A general theorem concerning the motion of a viscous fluid and a few consequences derived from it', *Zittingsverlag Akad. Wet. Amsterdam* **5**, 168–175 (1896).

[152] K. Loutherback et al., 'Deterministic microfluidic ratchet', *Physical review letters* **102**, 045301 (2009).

[153] R. M. Macnab, 'Bacterial flagella rotating in bundles: a study in helical geometry', *Proceedings of the National Academy of Sciences* **74**, 221–225 (1977).

[154] L. O. Mair et al., 'Magnetic microkayaks: propulsion of microrods precessing near a surface by kilohertz frequency, rotating magnetic fields', *Nanoscale* **9**, 3375 (2017).

[155] T. Majmudar et al., 'Experiments and theory of undulatory locomotion in a simple structured medium', *Journal of the Royal Society Interface* **9**, 1809–1823 (2012).

[156] Y. Man, L. Koens and E. Lauga, 'Hydrodynamic interactions between nearby slender filaments', *EPL (Europhysics Letters)* **116**, 24002 (2016).

[157] M. C. Marchetti et al., 'Hydrodynamics of soft active matter', *Reviews of Modern Physics* **85**, 1143 (2013).

[158] F. Martinez-Pedrero et al., 'Emergent hydrodynamic bound states between magnetically powered micropropellers', *Science advances* **4**, eaap9379 (2018).

[159] C. Maul and S. Kim, 'Image systems for a Stokeslet inside a rigid spherical container', *Physics of Fluids* **6**, 2221–2223 (1994).

[160] S. Michelin, E. Guérin and E. Lauga, 'Collective dissolution of microbubbles', *Physical Review Fluids* **3**, 043601 (2018).

[161] S. Michelin and E. Lauga, 'Phoretic self-propulsion at finite Péclet numbers', *Journal of Fluid Mechanics* **747**, 572–604 (2014).

[162] T. D. Montenegro-Johnson, L. Koens and E. Lauga, 'Microscale flow dynamics of ribbons and sheets', *Soft matter* **13**, 546–553 (2017).

[163] J. L. Moran and J. D. Posner, 'Electrokinetic locomotion due to reaction-induced charge auto-electrophoresis', *Journal of Fluid Mechanics* **680**, 31–66 (2011).

[164] J. L. Moran and J. D. Posner, 'Phoretic self-propulsion', *Annual Review of Fluid Mechanics* **49**, 511–540 (2017).

[165] A. Morin et al., 'Distortion and destruction of colloidal flocks in disordered environments', *Nature Physics* **13**, 63–67 (2017).

[166] F. Mou et al., 'Single-component TiO2 tubular microengines with motion controlled by light-induced bubbles', *Small* **11**, 2564–2570 (2015).

[167] D. Needleman and M. Shelley, 'The stormy fluid dynamics of the living cell', *Physics Today* **72**, 32–38 (2019).

[168] B. J. Nelson, I. K. Kaliakatsos and J. J. Abbott, 'Microrobots for minimally invasive medicine', *Annual review of biomedical engineering* **12**, 55–85 (2010).

[169] W. S. Nesbitt et al., 'A shear gradient–dependent platelet aggregation mechanism drives thrombus formation', *Nature medicine* **15**, 665 (2009).

[170] F. T. Nguyen and M. D. Graham, 'Impacts of multiflagellarity on stability and speed of bacterial locomotion', *Physical Review E* **98**, 042419 (2018).

[171] L. T. Nielsen et al., 'Hydrodynamics of microbial filter feeding', *Proceedings of the National Academy of Sciences* **114**, 9373–9378 (2017).

[172] F. Nietzsche, 'Also sprach Zarathustra: ein Buch für alle und keinen' (Goldmann Verlag, 2010).

[173] M. E. O'Neill, 'A slow motion of viscous liquid caused by a slowly moving solid sphere', *Mathematika* **11**, 67–74 (1964).

[174] H. Ockendon and J. R. Ockendon, 'Viscous flow', Vol. 13 (Cambridge University Press, 1995).

[175] D. Or et al., 'Physical constraints affecting bacterial habitats and activity in unsaturated porous media–a review', *Advances in Water Resources* **30**, 1505–1527 (2007).

[176] C. W. Oseen, 'Neuere Methoden und Ergebnisse in der Hydrodynamik', *Leipzig: Akademische Verlagsgesellschaft mb H.* (1927).

[177] K. M. Ottemann and J. F. Miller, 'Roles for motility in bacterial–host interactions', *Molecular microbiology* **24**, 1109–1117 (1997).

[178] D. Patra et al., 'Intelligent, self-powered, drug delivery systems', *Nanoscale* **5**, 1273–1283 (2013).

[179] W. F. Paxton et al., 'Catalytically induced electrokinetics for motors and micropumps', *Journal of the American Chemical Society* **128**, 14881–14888 (2006).

[180] T. Pedley, D. R. Brumley and R. E. Goldstein, 'Squirmers with swirl: a model for Volvox swimming', *Journal of fluid mechanics* **798**, 165–186 (2016).

[181] T. Pedley, 'Spherical squirmers: models for swimming micro-organisms', *IMA Journal of Applied Mathematics* **81**, 488–521 (2016).

[182] T. Pedley and J. O. Kessler, 'Hydrodynamic phenomena in suspensions of swimming microorganisms', *Annual Review of Fluid Mechanics* **24**, 313–358 (1992).

[183] T. Petit et al., 'Selective trapping and manipulation of microscale objects using mobile microvortices', *Nano Lett.* **12**, 156 (2012).

[184] D. J. Pine et al., 'Chaos and threshold for irreversibility in sheared suspensions', *Nature* **438**, 997–1000 (2005).

[185] L. Ping, 'The asymmetric flagellar distribution and motility of Escherichia coli', *Journal of molecular biology* **397**, 906–916 (2010).

[186] M. Polin et al., 'Chlamydomonas swims with two "gears" in a eukaryotic version of run-and-tumble locomotion', *Science* **325**, 487–490 (2009).

[187] T. R. Powers, 'Role of body rotation in bacterial flagellar bundling', *Physical Review E* **65**, 040903 (2002).

[188] C. Pozrikidis et al., 'Boundary integral and singularity methods for linearized viscous flow' (Cambridge University Press, 1992).

[189] E. M. Purcell, 'Life at low Reynolds number', *American journal of physics* **45**, 3–11 (1977).

[190] E. M. Purcell, 'The efficiency of propulsion by a rotating flagellum', *Proceedings of the National Academy of Sciences* **94**, 11307–11311 (1997).

[191] Z. Qu et al., 'Changes in the flagellar bundling time account for variations in swimming behavior of flagellated bacteria in viscous media', *Proceedings of the National Academy of Sciences* **115**, 1707–1712 (2018).

[192] J. Rallison, 'Note on the Faxén relations for a particle in Stokes flow', *Journal of Fluid Mechanics* **88**, 529–533 (1978).

[193] S. Ramaswamy, 'The mechanics and statistics of active matter', *Annu. Rev. Condens. Matter Phys.* **1**, 323–345 (2010).

[194] M. Reichert and H. Stark, 'Synchronization of rotating helices by hydrodynamic interactions', *The European Physical Journal E* **17**, 493–500 (2005).

[195] S. Y. Reigh, R. G. Winkler and G. Gompper, 'Synchronization and bundling of anchored bacterial flagella', *Soft Matter* **8**, 4363–4372 (2012).

[196] E. E. Riley, D. Das and E. Lauga, 'Swimming of peritrichous bacteria is enabled by an elastohydrodynamic instability', *Scientific reports* **8**, 1–7 (2018).

[197] Rothschild, 'Non-random distribution of bull spermatozoa in a drop of sperm suspension', *Nature* **198**, 1221 (1963).

[198] U. Rüffer and W. Nultsch, 'High-speed cinematographic analysis of the movement of Chlamydomonas', *Cell Motility* **5**, 251–263 (1985).

[199] D. Saintillan, 'Rheology of active fluids', *Annual Review of Fluid Mechanics* **50**, 563–592 (2018).

[200] D. Saintillan and M. J. Shelley, 'Instabilities, pattern formation, and mixing in active suspensions', *Physics of Fluids* **20**, 123304 (2008).

[201] D. Saintillan and M. J. Shelley, 'Emergence of coherent structures and large-scale flows in motile suspensions', *Journal of the Royal Society Interface* **9**, 571–585 (2012).

[202] D. Saintillan and M. J. Shelley, 'Active suspensions and their nonlinear models', *Comptes Rendus Physique* **14**, 497–517 (2013).

[203] S. Sanchez et al., 'Superfast motion of catalytic microjet engines at physiological temperature', *Journal of the American Chemical Society* **133**, 14860–14863 (2011).

[204] A. Sauret et al., 'Growth of clogs in parallel microchannels', *Physical Review Fluids* **3**, 104301 (2018).

[205] C. F. Schmid, L. H. Switzer and D. J. Klingenberg, 'Simulations of fiber flocculation: effects of fiber properties and interfiber friction', *Journal of Rheology* **44**, 781–809 (2000).

[206] R. Shail, 'A note on some asymmetric Stokes flows within a sphere', *The Quarterly Journal of Mechanics and Applied Mathematics* **40**, 223–233 (1987).

[207] R. Shail and S. Onslow, 'Some Stokes flows exterior to a spherical boundary', *Mathematika* **35**, 233–246 (1988).

[208] A. Shenoy, C. V. Rao and C. M. Schroeder, 'Stokes trap for multiplexed particle manipulation and assembly using fluidics', *Proc. Natl. Acad. Sci. U.S.A* **113**, 3976 (2016).

[209] M. Silverman and M. Simon, 'Flagellar rotation and the mechanism of bacterial motility', *Nature* **249**, 73–74 (1974).

[210] C. E. Sing et al., 'Controlled surface-induced flows from the motion of self-assembled colloidal walkers', *Proc. Natl. Acad. Sci. U.S.A* **107**, 535 (2010).

[211] O. Sipos et al., 'Hydrodynamic trapping of swimming bacteria by convex walls', *Physical review letters* **114**, 258104 (2015).

[212] V. Skultéty and A. Morozov, 'A note on forces exerted by a Stokeslet on confining boundaries', *Journal of Fluid Mechanics* **882** (202).

[213] M. A. Sleigh, 'The biology of cilia and flagella: international series of monographs on pure and applied biology: zoology', Vol. 12 (Elsevier, 2016).

[214] D. J. Smith, 'A boundary element regularized Stokeslet method applied to cilia-and flagella-driven flow', *Proceedings of the Royal Society A: Mathematical, Physical and Engineering Sciences* **465**, 3605–3626 (2009).

[215] D. Smith et al., 'Human sperm accumulation near surfaces: a simulation study', *Journal of Fluid Mechanics* **621**, 289–320 (2009).

[216] S. E. Spagnolie and E. Lauga, 'Hydrodynamics of self-propulsion near a boundary: predictions and accuracy of far-field approximations', *Journal of Fluid Mechanics* **700**, 105–147 (2012).

[217] S. E. Spagnolie et al., 'Geometric capture and escape of a microswimmer colliding with an obstacle', *Soft Matter* **11**, 3396–3411 (2015).

[218] S. E. Spagnolie et al., 'Microorganism billiards', *Physica D: Nonlinear Phenomena* **341**, 33–44 (2017).

[219] T. M. Squires and M. P. Brenner, 'Like-charge attraction and hydrodynamic interaction', *Physical review letters* **85**, 4976 (2000).

[220] S. V. Srigiriraju and T. R. Powers, 'Model for polymorphic transitions in bacterial flagella', *Physical Review E* **73**, 011902 (2006).

[221] J. T. Staley and J. J. Gosink, 'Poles apart: biodiversity and biogeography of sea ice bacteria', *Annual reviews in Microbiology* **53**, 189–215 (1999).

[222] G. G. Stokes, 'On the friction of fluids in motion and the equilibrium and motion of elastic solids' (JW Parker, Pitt Press, 1846).

[223] G. G. Stokes, 'On the effect of the internal friction of fluids on the motion of pendulums', Vol. 9 (Pitt Press Cambridge, 1851).

[224] R. Strauss, 'Also sprach Zarathustra! Tondichtung (frei nach Friedr. Nietzsche) für grosses Orchester op. 30.' (Joseph Aibl, Munich, 1896).

[225] A. D. Stroock et al., 'Chaotic mixer for microchannels', *Science* **295**, 647–651 (2002).

[226] D. Takagi et al., 'Dispersion of self-propelled rods undergoing fluctuation-driven flips', *Physical review letters* **110**, 038301 (2013).

[227] D. Takagi et al., 'Hydrodynamic capture of microswimmers into sphere-bound orbits', *Soft Matter* **10**, 1784–1789 (2014).

[228] J. Tanzosh and H. Stone, 'A general approach for analyzing the arbitrary motion of a circular disk in a Stokes flow', *Chemical engineering communications* **148**, 333–346 (1996).

[229] M. Tătulea-Codrean and E. Lauga, 'Artificial chemotaxis of phoretic swimmers: instantaneous and long-time behaviour', *Journal of Fluid Mechanics* **856**, 921–957 (2018).

[230] M. Tătulea-Codrean and E. Lauga, 'Geometrical constraints on the tangling of bacterial flagellar filaments', *Scientific Reports* **10**, 1–10 (2020).

[231] G. I. Taylor, 'Analysis of the swimming of microscopic organisms', *Proceedings of the Royal Society of London. Series A. Mathematical and Physical Sciences* **209**, 447–461 (1951).

[232] S. Thutupalli, R. Seemann and S. Herminghaus, 'Swarming behavior of simple model squirmers', *New Journal of Physics* **13**, 073021 (2011).

[233] P. Tierno et al., 'Controlled swimming in confined fluids of magnetically actuated colloidal rotors', *Physical review letters* **101**, 218304 (2008).

[234] S. Tottori et al., 'Magnetic helical micromachines: fabrication, controlled swimming, and cargo transport', *Adv. Mater.* **24**, 811 (2012).

[235] Y. Tu et al., 'Biodegradable hybrid stomatocyte nanomotors for drug delivery', *ACS nano* **11**, 1957–1963 (2017).

[236] L. Turner, W. S. Ryu and H. C. Berg, 'Real-time imaging of fluorescent flagellar filaments', *Journal of bacteriology* **182**, 2793–2801 (2000).

[237] L. Turner, A. S. Stern and H. C. Berg, 'Growth of flagellar filaments of Escherichia coli is independent of filament length', *Journal of bacteriology* **194**, 2437–2442 (2012).

[238] L. Turner et al., 'Visualization of flagella during bacterial swarming', *Journal of bacteriology* **192**, 3259–3267 (2010).

[239] A. Van Helden, S. Dupré and R. van Gent, 'The origins of the telescope', Vol. 12 (Amsterdam University Press, 2010).

[240] M. T. Varro, 'Rerum rusticarum libri tres' (Teubner, 1889).

[241] T. Vicsek et al., 'Novel type of phase transition in a system of self-driven particles', *Physical review letters* **75**, 1226 (1995).

[242] M. A.-S. Vigeant et al., 'Reversible and irreversible adhesion of motile Escherichia coli cells analyzed by total internal reflection aqueous fluorescence microscopy', *Appl. Environ. Microbiol.* **68**, 2794–2801 (2002).

[243] D. Vigolo, S. Radl and H. A. Stone, 'Unexpected trapping of particles at a T junction', *Proc. Natl. Acad. Sci. U.S.A* **111**, 4770 (2014).

[244] V. Vladimirov et al., 'Measurement of cell velocity distributions in populations of motile algae', *Journal of experimental biology* **207**, 1203–1216 (2004).

[245] G. Volpe et al., 'Microswimmers in patterned environments', *Soft Matter* **7**, 8810–8815 (2011).

[246] M. Von Smoluchowski, 'Zur kinetischen theorie der brownschen molekularbewegung und der suspensionen', *Annalen der physik* **326**, 756–780 (1906).

[247] M. Vos et al., 'Micro-scale determinants of bacterial diversity in soil', *FEMS microbiology reviews* **37**, 936–954 (2013).

[248] D. H. Wall, U. N. Nielsen and J. Six, 'Soil biodiversity and human health', *Nature* **528**, 69–76 (2015).

[249] A. Walther and A. H. Muller, 'Janus particles: synthesis, self-assembly, physical properties, and applications', *Chemical reviews* **113**, 5194–5261 (2013).

[250] J. Wang and W. Gao, 'Nano/microscale motors: biomedical opportunities and challenges', *ACS nano* **6**, 5745–5751 (2012).

[251] S. Wang and N. Wu, 'Selecting the swimming mechanisms of colloidal particles: bubble propulsion versus self-diffusiophoresis', *Langmuir* **30**, 3477–3486 (2014).

[252] W. Wang et al., 'Autonomous motion of metallic microrods propelled by ultrasound', *ACS nano* **6**, 6122–6132 (2012).

[253] W. Wang et al., 'Small power: autonomous nano-and micromotors propelled by self-generated gradients', *Nano Today* **8**, 531–554 (2013).

[254] X. Wang et al., '3d printed enzymatically biodegradable soft helical microswimmers', *Advanced Functional Materials*, 1804107 (2018).

[255] N. Watari and R. G. Larson, 'The hydrodynamics of a run-and-tumble bacterium propelled by polymorphic helical flagella', *Biophysical journal* **98**, 12–17 (2010).

[256] H. Winet, G. Bernstein and J. Head, 'Observations on the response of human spermatozoa to gravity, boundaries and fluid shear', *Reproduction* **70**, 511–523 (1984).

[257] H. Wioland et al., 'Ferromagnetic and antiferromagnetic order in bacterial vortex lattices', *Nature physics* **12**, 341–345 (2016).

[258] A. W. Woods, 'Melting and dissolving', *Journal of Fluid Mechanics* **239**, 429–448 (1992).

[259] J. K. Wróbel et al., 'Regularized image system for Stokes flow outside a solid sphere', *Journal of Computational Physics* **317**, 165–184 (2016).

[260] T. Wu, C. J. Brokaw and C. Brennen, 'Swimming and flying in nature', Vol. 2 (Springer, 1975).

[261] B. H. Wunsch et al., 'Nanoscale lateral displacement arrays for the separation of exosomes and colloids down to 20 nm', *Nat. Nanotechnol.* **11**, 936 (2016).

[262] Z. Ye and M. Sitti, 'Dynamic trapping and two-dimensional transport of swimming microorganisms using a rotating magnetic microrobot', *Lab Chip* **14**, 2177 (2014).

[263] I. M. Young and J. W. Crawford, 'Interactions and self-organization in the soil-microbe complex', *Science* **304**, 1634–1637 (2004).

[264] L. Zhang et al., 'Characterizing the swimming properties of artificial bacterial flagella', *Nano letters* **9**, 3663–3667 (2009).

[265] Y. Zhang, D. Walker and C. E. Lesher, 'Diffusive crystal dissolution', *Contributions to Mineralogy and Petrology* **102**, 492–513 (1989).

[266] B. Zhao, E. Lauga and L. Koens, 'Method of regularized Stokeslets: flow analysis and improvement of convergence', *Physical Review Fluids* **4**, 084104 (2019).

[267] L. H. Zhao, L. Zhang and Y. Ding, 'Analysis of micro-fluidic tweezers in the Stokes regime', *Phys. Fluids* **30**, 032006 (2018).

[268] Q. Zhou et al., 'Dumbbell fluidic tweezers for dynamical trapping and selective transport of microobjects', *Adv. Funct. Mater.* **27**, 1604571 (2017).